The Excited-State Chemistry of Molecular Assemblies and Novel Aromatic Chromophores

by

© Prateek Dongare

A Dissertation Submitted to the School of Graduate Studies in Partial

Fulfillment of the Requirements for the Degree of

Doctor of Philosophy

May, 2014

Department of Chemistry

Memorial University, St. John's, Newfoundland

Canada

ABSTRACT

This dissertation explores the spectroscopic characterization, excited-state behavior and mechanistic analysis of systematically designed molecules. Excited-states are modular in nature, they can be utilized to study electron transfer, proton transfer and concerted electron proton transfer. Furthermore, the excited-state of a molecule has an ability to respond to specific stimuli which can be detected as fluorescence quenching or enhancement. Therefore, the reactivity of an excited-state can be utilized in a variety of applications.

This dissertation starts with investigation of the excited-state properties of strained pyrenophanes. The absorption and emission spectra of three inherently chiral pyrenophanes were analyzed using Franck-Condon band shape analysis and emission spectral fitting procedures. The study tested the applicability of the one-mode spectral fitting procedure and provided detailed quantitative understanding of structural, vibronic and electronic parameters.

With the increased understanding of ground and excited-state properties of pyrene, effect of protonation on constrained pyridine appended pyrene based macrocycles and their half cycle counterparts was studied. Global analysis of the absorption and emission spectral data reveals sequential 1:1 and 1:2 binding equilibria in macrocycles and direct 1:2 binding equilibria in their truncated segments bearing only one pyrene chromophores.

In chapter 5, the applicability of the excited-state in detection of analytes such as saccharides and metal ions was investigated. Systematically designed molecules comprised

of triazole rings were utilized as sensors to detect saccharides and metal ions by employing fluorescence spectroscopy. The study reveals that triazole rings play a major part in the ground and excited-state properties of these molecules and teaches us how to design new sensors to be used in opto-electronic devices.

In chapter 6, concerted electron proton transfer using Re(I) based MLCT excited-states was studied. A sterically bulky phenol was employed as a combined electron/proton donor and the reductive quenching of three analogous Re(I) polypyridyl complexes was studied. Owing to the significant oxidizing power of Re(I) MLCT excited-states the concerted electron proton transfer in these molecular assemblies is feasible. Chapter 7 lists the major conclusions drawn from the individual chapters. In the end, some recommendations for the future work are outlined.

This work is dedicated to my Parents

ACKNOWLEDGEMENT

First of all, I would like to thank my supervisor Prof. David W. Thompson (Dave) for his guidance, support and encouragement throughout this project. Dave is very approachable and easy to communicate supervisor and has always been understanding and patient with me. I am grateful to my co-supervisor and supervisory committee member Prof. Peter Pickup for very patiently reading the earlier versions of this work and many helpful discussions. Special thanks go to my supervisory committee member Prof. Yuming Zhao for all the insightful discussions and a very fruitful collaboration. I always felt welcomed in Prof. Zhao's office to either have a discussion on a manuscript or to have a chat on an ongoing project.

I am very grateful to Prof. Graham Bodwell for providing the opportunities to take part in number of curricular activities (SOCCER and colloquium) and allowing me to be a part of the research collaborative projects between Prof. David Thompson and Prof. Graham Bodwell research groups.

Thanks to all the present and past group member of Thompson group, especially Brent (for all the interesting discussions in the laser lab and sharing his technical expertise with me), Steve Smith and Mohammad Rahaman. I would also like to thank Zhao and Bodwell group members especially, Karimulla Mulla, Yousef Pourghaz (Zhao group), Penchal Reddy and Venkatramana for letting me use high purity compounds they made by

putting so much hard work.

Thanks to all the members of the chemistry department, Memorial University who helped me in some manner. I would like to extend my gratitude to the school of graduate studies for providing me the financial support and Memorial University for hosting my PhD.

I am indebted to my mom, dad and my brothers for their love, constant support and encouragement. I would not be the person I am today without them. In the end, a huge thanks to my wife Poorva for her everlasting patience, love, care, support and encouragement.

Prateek Dongare

December 2013

TABLE OF CONTENTS

LIST OF FIGURES

LIST OF TABLES

LIST OF SCHEMES

LIST OF ABBREVIATIONS

4,4’-bpy	4,4’-bipyridine
A	Acceptor
AIE	Aggregation induced emission
bpy	2,2’-bipyridine
C-hmer	Closed hmer
CT	Charge Transfer
CEPT	Concerted electron proton transfer
D	Donor
DFT	Density functional theory
DGG	Delay gate generator
DMA	*N,N*-dimethylaniline
D_{OP}	Optical dielectric constant
*D*s	Static dielectric constant
E	Energy
EA	Electron affinity
EDA	Electron-donor-acceptor complex
E_{em}	Emission energy in cm^{-1}
EGL	Energy gap law
E_NT	Energy transfer
EPT	Electron proton transfer

ESIPT	Excited-state intramolecular proton transfer
ET	Electron transfer
EWG	Electron withdrawing group
F	Fluorophore
FC	Franck-Condon
f_{osc}	Oscillator strength
fwhm	Full width at half maximum
h	Planck's constant
$\hbar$	Planck's constant/2π
H'	Hamiltonian operator
H_{AB}	Donor/acceptor electronic coupling factor
HAT	Hydrogen atom transfer
hb	Hot bands
HOMO	Highest occupied molecular orbital
HOTF	Trifluoromethane sulfonic acid
ICT	Intramolecular charge transfer
ILET	Interligand electron transfer
IP	Ionization potential
IRF	Instrument response function
K_A	Association constant
k_B	Boltzmann constant
k_{CR}	Charge recombination

k_{diff}	Rate constant of diffusion
KIE	Kinetic isotope effect
k_{nr}	Rate constant for non radiative decay
k_{obs}	Observed rate constant
k_r	Rate constant for radiative decay
k_q	Bimolecular quenching
K_{SV}	Stern-Volmer constant
LE	Localized excited-state
LUMO	Lowest unoccupied molecular orbital
mg	Milligram
MLCT	Metal to ligand charge transfer
mL	Millilitre
MS-EPT	Multiple site electron proton transfer
N_A	Avogadro's number
Nd:YAG	Neodymium-doped yttrium aluminum garnet
OLED	Organic light emitting diode
O-hmer	Open hmer
OPE	Oligo(phenylene ethynylene)
OPV	Oligo-phenylene vinylene
PAH	Poly aromatic hydrocarbons
PBS	Potassium phosphate buffer
PCET	Proton coupled electron transfer

Pd	Photodiode
PES	Potential energy surface
PT	Proton transfer
PTI	Photon technology international
PMT	Photomultiplier tube
PPE	Poly(*p*-phenylene ethynylene)s
Py	Pyridine
Pyr	Pyrene
Pyr_{ben}	Pyrene benzene macrocycle
Pyr_{in}	Pyrene in macrocycle
Pyr_{in}-half	Pyrene in half cycle
Pyr_{out}	Pyrene out macrocycle
Pyr_{out}-half	Pyrene out half cycle
Q_k	Displacement of nuclear coordinates
R	Distance between D and A
RET	Resonance energy transfer
S_M	Electron-vibrational coupling constant or Huang-Rhys factor
SVD	Single value decomposition
SWNT	Single wall carbon nanotube
TA	Transient absorption
$(tBu)_2PhOH$	2,6-di-tert-butylphenol

TD-DFT	Time dependent density functional theory
TFA	Trifluoroacetic acid
Thexi	Thermally equilibrated excited-state
TRS	Time-resolved spectroscopy
TTF	Tetrathiafulvelene
V_k	Vibrationally induced electronic coupling matrix element
$\hbar\omega$	Quantum spacing of averaged coupled vibrational modes of medium frequency
$\rho(E)$	Density of states
$w(v)$	Probability for single photon absorption
$\vec{M}$	Transition moment
$\vec{\mu}$	Transition dipole moment
v	Frequency in wavenumber
τ	Fluorescence lifetime
Φ_{em}	Emission quantum yield
β_0	Electronic coupling element
ω_k	Vibrational angular frequency
ΔQ	Nuclear displacement
λ_0	Solvent reorganization energy
λ_i	Vibrationally induced reorganization energy
λ_t	Total reorganization energy
ΔG^o	Free energy difference between final and initial states

Γ_λ	Nuclear tunneling factor
ρ_{mn}	Boltzmann's population of the initial level in the excited-state
ε	Extinction coefficient

Chapter – 1

Introduction to the Fundamentals of Photochemistry

1.1. Preamble

The primary goal of this chapter is to introduce the theory and underlying principles that are directly related to this dissertation. Fundamental concepts such as radiative and non-radiative decay, energy-gap law, Fermi Golden Rule, electron-and energy transfer and electron-proton transfer constitute the building blocks of the majority of photophysical processes. Therefore, before studying the excited-state and dynamic properties of chromophores it is important to review the theory and background that is essential to the understanding and discussion of the research described in this dissertation.

1.2. Fermi Golden Rule

The Fermi Golden Rule operates under the Franck-Condon and Born-Oppenheimer principles and provides a basic formulation for the quantitative understanding of photophysical processes.[4] The Fermi Golden Rule dictates the probability of a transition between states, Equation 1.1.[4]

$$P_{if} = \frac{2\pi}{\hbar}\rho(E)\left|\psi_{el,f}|H'|\psi_{el,i}\right|^2 \qquad [1.1]$$

Where, $\psi_{el,i}$ and $\psi_{el,f}$ are the wavefunctions for the initial and final electronic states respectively, H' is the operator that describes the perturbation inducing the probability of a transition between weakly interacting states, $\rho(E)$ is the density of states in the product at energy E which also defines the energy distributions in the initial and final states. It is valid in the weak coupling limit, weak perturbation and low transition probability. The probability of transition between two states depends upon the "perturbation forces" which change the position or motion of the electrons in their initial and final states. For different transitions, the perturbation forces can be represented separately and are mathematically modelled by the Hamiltonian operator (H'). For a radiative process such as absorption and/or emission, the form of the operator is the product $e\sum_n \vec{r}_n$. Where e is the unit electron charge which is summed over the vectorial displacement of all the electrons affected.

The Franck-Condon and Born-Oppenheimer approximations assume that electron motion (10^{-15} s^{-1}) is faster than nuclear motion (10^{-13} s^{-1}) and allows for the separation of nuclear and electron dynamics. Immediately following photon capture, the molecule has the electronic coordinates of the excited-state. However, the molecule retains the ground-state nuclear and solvent coordinates. In the time scale where electron kinesis >> vibrational motion, application of the Born-Oppenheimer approximation allows the separation of the electronic and nuclear wavefunctions yielding Equation 1.2.[4]

$$P_{if} = \frac{2\pi}{\hbar}\rho(E)\left|\langle\psi_{el,f}|H'|\psi_{el,i}\rangle\right|^2\left|\langle\psi_{vib,f}|\psi_{vib,i}\rangle\right|^2 \qquad [1.2]$$

Where, $\psi_{vib,i}$ and $\psi_{vib,f}$ are the total vibrational wavefunctions of the initial and final states, respectively. Equation 1.2 is gien by the transitions between weakly coupled states and can be applied to radiative and non-radiative processes such as absorption, emission, electron transfer and excited-state decay. Subsequent dynamic events after photon capture may involve transitions between states which are dictated by the ensemble of vibrations available to the molecule.

1.2.1. Absorption

Application of the Fermi Golden Rule for a single photon capture event is given by Equation 1.3.[4, 5]λ

$$w(v) = \frac{2\pi}{3\hbar^2 n^2} \left|\vec{M}\right|^2 W(v) \qquad [1.3]$$

Where, $w(v)$ is the probability for single photon absorption, n is the refractive index and $W(v)$ is the energy density of the electromagnetic field at frequency, v.

The transition moment ($\vec{M}$) and the transition dipole moment ($\vec{\mu}$) are given by Equations 1.4 and 1.5, respectively.

$$\vec{M} = \langle\psi'_{el}|e\sum_n \vec{r}_n|\psi_{el}\rangle\langle\psi'_{vib}|\psi_{vib}\rangle = \vec{\mu}\langle\psi'_{vib}|\psi_{vib}\rangle \qquad [1.4]$$

$$\vec{\mu} = \langle\psi_{el}|e\sum_n \vec{r}_n|\psi_{el}\rangle \qquad [1.5]$$

The integrated absorption spectrum, $\int \varepsilon(v)dv$ is related to the transition moment by Equation 1.6.[4-6]

$$\int \varepsilon(v)dv = \frac{4\pi^3 N_A v}{3000\ c\ n\ \hbar\ ln10} \left|\vec{M}\right|^2 \qquad [1.6]$$

Where, ε is the extinction coefficient, v is the frequency in wavenumber (cm^{-1}), c is the speed of light, N_A is Avogadro's number, n is the refrective index and $\hbar$ is Planck's constant.

1.3. Radiative Decay

The fluorescence of a molecule arises as a result of light emission due to a transition from an excited-state to the ground-state. The rate constant of radiative decay (k_r) can be calculated by using the experimentally measured fluorescence lifetime (τ) and emission quantum yield (Φ_{em}), given by Equations 1.7 and 1.8.

$$k_r = \Phi_{em}\tau^{-1} \qquad [1.7]$$

$$k_{obs} = k_r + k_{nr} \qquad [1.8]$$

Where, k_{obs} is the rate constant for excited-state decay and k_{nr} is the rate constant of non-radiative decay.

The rate constant for radiative decay of the $S_n \rightarrow S_0$ transition is given by Equation 1.9 and is related to the transition moment ($\vec{M}$).[5, 6]

$$k_r = \frac{64\pi^3 n^2}{3\hbar} \left|\vec{M}\right|^2 \langle \bar{v}^{-3} \rangle^{-1} \qquad [1.9]$$

In Equation 1.9, $\langle \bar{\nu}^{-3} \rangle$ is the cube of the energy gap between the excited and ground-state given by Equation 1.10 and E_{em} is the emission maxima in cm^{-1}, $\bar{\nu}$ is the average emission energy in wavenumber (cm^{-1}), and $I(\tilde{\nu})$ is the emission intensity in quanta per energy interval per second at $\bar{\nu}$.[6]

$$\langle \bar{\nu}^{-3} \rangle^{-1} = \frac{\int I(\bar{\nu}) d\bar{\nu}}{\int \bar{\nu}^{-3} I(\bar{\nu}) d\bar{\nu}} \sim E_{em}^{3} \qquad [1.10]$$

1.4. Non-Radiative Decay

The theory of non-radiative decay was primarily developed by Lin, Freed and Jortner.[7-9] The ground and excited-states electronic wavefunctions are the orthonormal solutions of the same Hamiltonian. The orthogonality of the electronic wavefunctions is diminished by the overlap of the vibrational modes or promoting modes on the excited-state potential energy surfaces (PES) with hot vibrational levels of the ground-state PES and allows mixing of ψ_{el}^{*} and ψ_{el} providing a mechanism for electronic relaxation. For non-radiative decay, electron motion occurs on the time scale of vibrational motion and the Born-Oppenheimer approximation is not valid. As a result of these processes the excess energy is eventually transferred to the solvent and dissipated as heat. The application of the Fermi Golden Rule to non-radiative decay yields Equation 1.11.

$$k_{nr} = \frac{2\pi}{\hbar} |V_k|^2 (FC) \qquad [1.11]$$

FC is the Franck-Condon weighted density of states and V_k is the vibrationally induced electronic coupling matrix element defined in Equation 1.12 for a single mode of

reduced mass, M_{k}. For a single promoting mode of quantum spacing $\hbar\omega_{\mathrm{k}}$, the average mode approximation and V_{k} is given by Equation 1.12.[10]

$$V_{\mathrm{k}} = \frac{\hbar^2}{M_{\mathrm{k}}}\left\langle \psi_{\mathrm{el},f} \middle| \frac{\partial}{\partial Q_{\mathrm{k}}} \middle| \psi_{\mathrm{el},i} \right\rangle \left\langle \chi_{V_{\mathrm{k}},f} \middle| \frac{\partial}{\partial Q_{\mathrm{k}}} \middle| \chi_{V_{\mathrm{k}},i} \right\rangle = \frac{\hbar}{{M_{\mathrm{k}}}^{1/2}}\left\langle \psi_{\mathrm{el},f} \middle| \frac{\partial}{\partial Q_{\mathrm{k}}} \middle| \psi_{\mathrm{el},i} \right\rangle \left(\frac{\hbar\omega_{\mathrm{k}}}{2}\right)^{\frac{1}{2}} = C_{\mathrm{k}}\left(\frac{\hbar\omega_{\mathrm{k}}}{2}\right)^{\frac{1}{2}}$$

[1.12]

In equation 1.12 $\psi_{\mathrm{el},f}$ and $\psi_{\mathrm{el},i}$ are the final and initial electronic wave functions respectively, $\chi_{V_{\mathrm{k}},f}$ and $\chi_{V_{\mathrm{k}},i}$ are the final and initial vibrational wave functions for promoting mode k with quantum spacing $\hbar\omega_{\mathrm{k}}$, Q_{k} is the displacement of nuclear coordinates and C_k is the change in the dominant acceptor vibrational mode for nuclear coordinate.

In logarithmic form k_{nr} is given by Equation 1.13;[4, 10] where β_0 and ln[FC(calc)] are defined in Equations 1.14 and 1.15.

$$\ln k_{\mathrm{nr}} = \ln \beta_0 + \ln[\mathrm{FC(calc)}] \qquad [1.13]$$

$$\beta_0 = \left(\frac{\pi}{2}\right)^{1/2} \omega_{\mathrm{k}} {C_{\mathrm{k}}}^2 = \frac{\sqrt{2\pi}{V_{\mathrm{k}}}^2}{\hbar} \qquad [1.14]$$

Where, β_0 is the electronic coupling element and ω_{k} is the vibrational angular frequency.

$$\ln[\mathrm{FC(calc)}] = -\frac{1}{2}\ln(\hbar\omega_M E_0) - S_M - \frac{\gamma E_{\mathrm{em}}}{\hbar\omega} + \left(\frac{\gamma+1}{\hbar\omega_M}\right)^2 \lambda_{\mathrm{o}} k_{\mathrm{B}} T \qquad [1.15]$$

In Equation 1.15, E_0 is the energy gap for the $v' = 0 \rightarrow v = 0$ transition, λ_o is the solvent reorganization energy, $k_B T$ is the Boltzmann constant and Equation 1.16 gives the electron-vibrational coupling constant or Huang-Rhys factor (S_M) which depends upon the change in equilibrium displacement between the ground and excited-state equilibrium nuclear displacement (ΔQ).

$$S_M = \frac{1}{2}\frac{M\omega}{\hbar}(\Delta Q)^2 \qquad [1.16]$$

Where M is the reduced mass and ω is the angular frequency.

and γ is given by Equation 1.17.

$$\gamma = \ln\left(\frac{E_0}{S_M \hbar \omega_M}\right) - 1 \qquad [1.17]$$

In the single mode approximation Equation 1.13 can be written as following (Equation 1.18).

$$\ln k_{nr} = \ln \beta_0 - S_M - \frac{\gamma E_0}{\hbar \omega_M} + \left(\frac{\gamma+1}{\hbar \omega_M}\right)^2 \lambda_o k_B T \qquad [1.18]$$

In this form, Equation 1.18 is the famous "energy gap law" for non-radiative decay. It relates non-radiative decay dynamics to the energy gap between excited and ground-states.

In the simplest form, the energy gap law (EGL) for excited-state non-radiative decay predicts a linear dependence of rate of ln k_{nr} on the ground-to-excited-state energy

gap (E_0).[11] The EGL has been demonstrated for organic chromophores and closely related polypyridyl complexes of Re(I), Os(II) and Ru(II).[11-13] Most of these complexes exhibit weak quantum yields (Φ_{em}) and fluorescence is dictated by k_{nr}. In non-radiative decay, the vibrational energy of the excited-state is transferred into hot vibrational levels of the ground-state where $v > 0$.

1.5. Emission Spectral Fitting

Emission profiles can be analyzed by using a one-mode, or a two-mode Franck-Condon method. Figure 1.1 provides spectral fitting parameters, their definitions and emission spectral fitting profiles, revealing Gaussian bands.

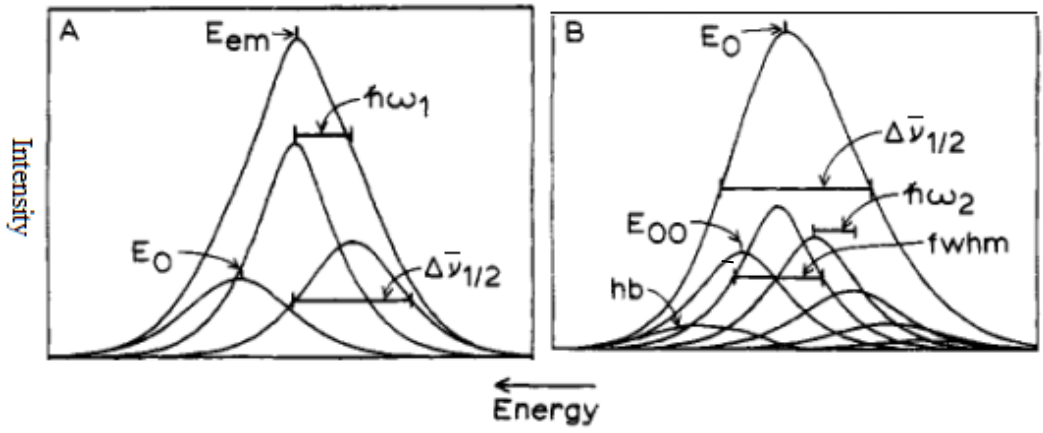

Figure 1.1. Emission spectral fitting profiles revealing Gaussian bands, pertinent emission spectral fitting parameters and their definitions. (A) The complete spectrum is fit to a series of bands with the spacing $\hbar\omega_1 = 1300\ cm^{-1}$. The band shapes have a half-width of $\Delta\bar{\nu}_{1/2}$, and the maximum of the first peak occurs at E_0. The peak maximum of the complete spectra occurs at E_{em}. (B) The band shapes of the $\hbar\omega_1 = 1300\ cm^{-1}$ progression are generated by summing a series of Gaussian bands with spacing $\hbar\omega_2 = 300\ cm^{-1}$. These have a full width at half-maximum of fwhm, and the 0-0 transition occurs at E_{00}. Because thermal population in this mode is allowed, "hot bands" (hb) occur at energies higher than E_{00}. All relative peak heights are constrained to Franck-Condon values. Reprinted with permission from Kober, E. M.; Caspar, J. V.; Lumpkin, R. S.; Meyer, T. J. J. Phys. Chem. 1986, 90, 3722.[13]

1.5.1. One-Mode Fitting

One-mode fitting is based on a weighted-average of all the medium-frequency accepting modes of the molecule under investigation. A one-mode fit can be represented in a one-dimensional potential energy surface (PES) diagram as presented in Figure 1.2.

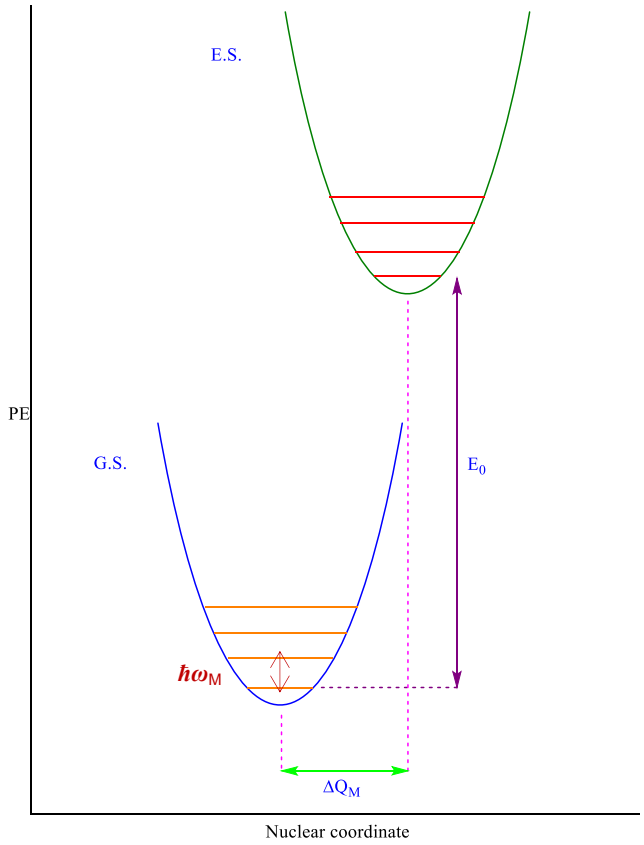

Figure 1.2. Depiction of the one-mode fitting model using a potential energy (PE) surface diagram.[14]

Emission spectral fitting analysis provides valuable information such as the energy difference between states, solvent contributions and distortion between states. A

number of Gaussian bands dictate the shape of the emission band envelope. These broad Gaussian bands suggest contributions of the solvent librations and low-frequency modes. The broadening is usually represented as "full width at half maximum" $\Delta\bar{\nu}_{0,1/2}$. A one-mode fitting equation for the emission bands at a given temperature is given by Equation 1.19.[15-18]

$$I(\bar{\nu}) = \sum_{\upsilon=0}^{\upsilon=5} \left\{ \left(\frac{E_0 - \upsilon\hbar\omega_M}{E_0} \right)^3 \cdot \left(\frac{S^\upsilon}{\upsilon!} \right) \cdot \exp\left[-4\ln 2 \left(\frac{\bar{\nu} - E_0 + \upsilon\hbar\omega_M}{\Delta\bar{\nu}_{1/2}} \right) \right] \right\} \qquad [1.19]$$

Where, $I(\bar{\nu})$ is the emitted light intensity at the energy $\bar{\nu}$ in cm^{-1}, relative to the intensity of the $0 \rightarrow 0$ transition; $\bar{\upsilon}$ is the energy of abscissa in wavenumbers and n is the highest ground-state vibrational level.[15-18] The exponential term in Equation 1.19 defines a Gaussian band with breadth $\Delta\bar{\nu}_{1/2}$ and with the vibrational progressions $E_0 + \upsilon_M\hbar\omega_M$.

1.5.2. Two-Mode Fitting

The two-mode method should be represented in a three-dimensional PES diagram due to the presence of two nuclear coordinates as presented in Figure 1.3.

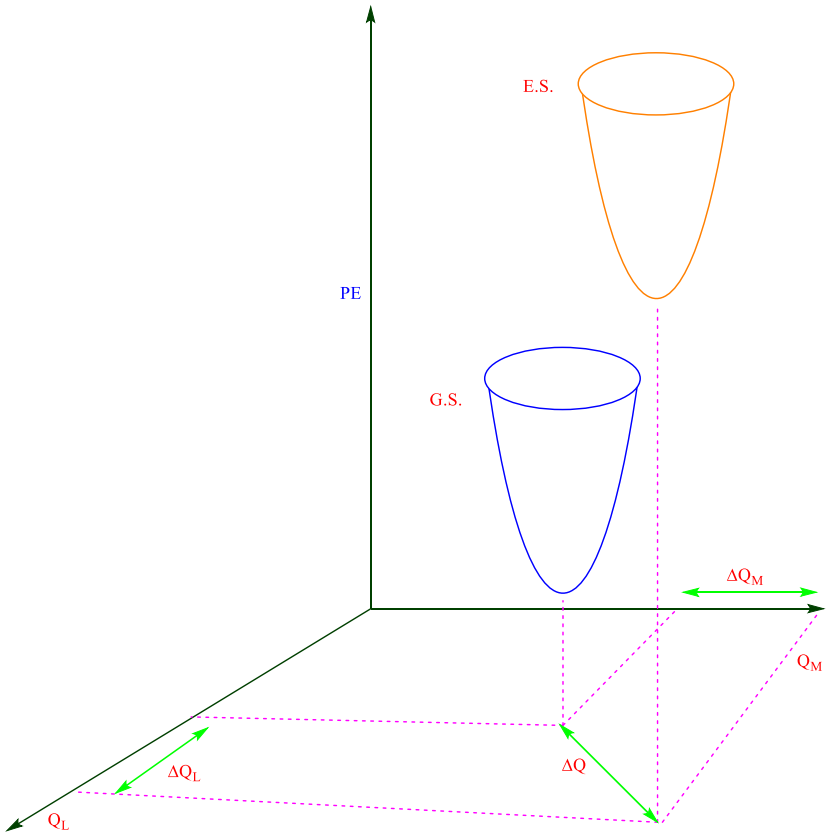

Figure 1.3. Depiction of the two-mode fitting model using potential energy (PE) surface diagrams, where three-dimensional nuclear coordinates are shown (as mentioned in the main text). Parameters shown in the one-mode fitting diagram are eliminated to highlight nuclear coordinates. ΔQ is the displacement between the minima of the ground and excited-state energy surfaces.[14]

In Equation 1.20, ΔQ depicts the displacement between the minima of the ground and excited-state energy surfaces.

$$\Delta Q^2 = \Delta Q_M^2 + \Delta Q_L^2 \qquad [1.20]$$

Two-mode fitting includes the average frequency mode as well as the average low-frequency accepting mode. The energy gap in two-mode fitting is labelled as E_{00} and corresponds to the energy difference between the energy gaps between the zeroth vibrational levels of the ground and excited-states.[13]

Equation 1.21 describes the fitting model for an emission within a two-mode model (usually for emission spectra acquired at low temperature or where a visible vibronic progression is present).[13, 19-21]

$$I(v) = \sum_{v_M=0}^{5} \sum_{v_L=0}^{15} \left\{ \left(\frac{E_{00} - v_M \hbar\omega_M - v_L \hbar\omega_L}{E_0} \right)^3 \cdot \left(\frac{S_M^{v_M}}{v_M!} \right) L(v_L) \, . \, \exp\left[-4\ln 2 \left(\frac{\bar{v} - E_{00} + v_M \hbar\omega_M + v_L \hbar\omega_L}{\Delta\bar{v}_{1/2}} \right) \right] \right\} \qquad [1.21]$$

$\hbar\omega_L$ is the quantum spacing for the coupled vibrations in the low frequency mode, S_L is the Huang-Rhys factor reflecting the nuclear distortion along the low frequency quantum modes. This effect is taken into account by the time-dependent function $L(v_L)$ (Equation 1.22), which is a series of Laguerre polynomial.[22] [19, 20]

$$L(v_L) = S_L^{v_L} \left(\frac{X^m m!}{(m + v_L)!} \right) \left[\sum_{l=0}^{\infty} \frac{(m + v_L)! \, (-S_L)^l}{(m - l)! \, (l + v_L)! \, m!} \right]^2, (v_L \geq 0) \qquad [1.22]$$

and term X is given by Equation 1.23

$$X = exp\left(\frac{-\hbar\omega_L}{k_B T} \right) \qquad [1.23]$$

At low temperature, where $\hbar\omega_L \gg k_B T$, the function $L(v_L)$ converges to an expression equivalent to one corresponding to the medium frequency mode.

Equation 1.24 gives the energy gap in two-mode spectral fitting. E_0 corresponds to the energy gap as determined by the displaced vibrational coordinates used to calculate factors such as $\hbar\omega_M$, whereas E_{00} includes the contributions from low-frequency intramolecular and solvent modes.[23]

$$E_{00} = E_0 + \left[\frac{(\bar{\nu}_{0,1/2})^2}{16 \ln 2 \, k_B T}\right] \qquad [1.24]$$

The effect of change in both E_0 and ΔQ on the vibrational overlap (therefore on k_{nr}) is represented in Figure 1.4 using a model showing coupling between the isoenergetic vibrational levels of the ground and excited-state potential energy surfaces (PES).

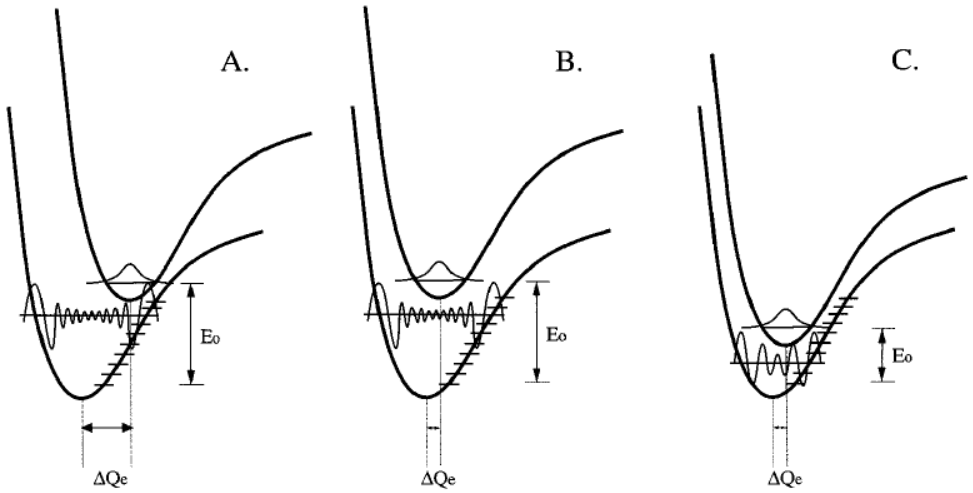

Figure 1.4. Diagrams illustrating the factors that affect the vibrational overlap in the rate of non-radiative decay. Note the change of ΔQ_e or ΔQ (nuclear displacement) with E_0 (energy gap).[23] Reprinted with permission from Damrauer, N. H.; Boussie, T. R.; Devenney, M.; McCusker, J. K. J. Am. Chem. Soc, 1997, 119, 8253. Copyright © 1997, American Chemical Society.

A decrease in the energy gap at constant ΔQ_e (from Figure 1.4 B to C) results in an increase in the vibrational overlap between the lowest energy vibrational levels (an increase in k_{nr}). On the other hand, an increase in the energy gap brings a decrease in vibrational overlap (therefore a smaller k_{nr}). A larger nuclear displacement favours the effective vibrational overlap between the lowest energy vibrational states of the excited-state surface and the ground-state surface (Figure 1.4 A). The effective overlap is therefore responsible for a larger k_{nr} in the case A.[23]

1.6. Mechanisms for Quenching

Excited-states can be quenched in several ways. They can emit or "dump" the excess energy in the form of heat through vibrational cooling i.e. excited-state decay or get quenched by another molecule. The quenching can be through electron transfer, charge transfer or energy transfer. In this section some of these quenching mechanisms will be discussed to illustrate the fates of excited-states following photon capture.

1.6.1. Electron Transfer

According to the energetic requirements needed to initiate an electron-transfer (ET) process, an electron-transfer reaction can be divided into three types: thermal, optical and photoinduced electron transfer. The potential energy surface diagrams of reactants and products in a two-state system are shown in Figure 1.5. In Figure 1.5 (a), the free energy of the reactant is higher than the free energy of the product i.e. ET from donor (D) to acceptor (A) is thermodynamically favored ($\Delta G^o < 0$). Figure 1.5 (b)

presents the case of optical electron transfer, where the free energy change between reactant and product is greater than zero ($\Delta G^{o} > 0$) and the reaction is thermodynamically uphill. Therefore additional energy is required for reactant ($D^{+}-A$) to get converted into the product ($D-A^{+}$). Once product is formed, the system relaxes from $D-A^{+}$ to $D^{+}-A$ and releases energy to the surroundings. The third mechanism is the photoinduced electron-transfer mechanism (Figure 1.5 c). In this mechanism, formation of an excited-state species D^{*}-A takes place following the capture of photons. The ensuing excited-state species then undergo ET to form D^{+}-A^{-} charge-separated species a thermodynamically favoured process. The charge-separated spices then relaxes back to the ground-state radiatively, or non-radiatively.

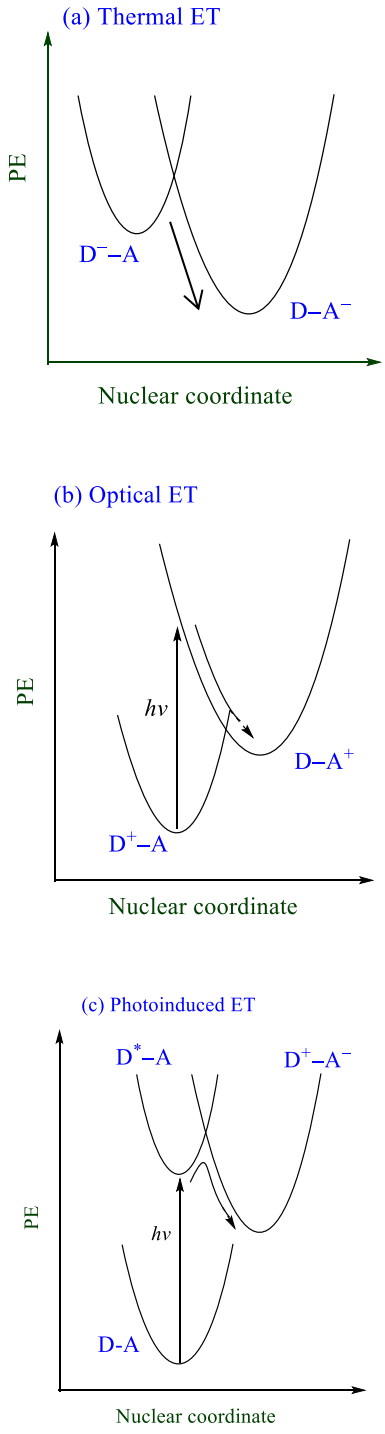

Figure 1.5. (a) Reactant and product potential energy surface (PES) diagrams for thermal electron transfer ($\Delta G^o < 0$) (b) optical electron transfer ($\Delta G^o > 0$) and (c) photoinduced electron transfer process.

The first model of electron transfer (ET) was proposed by Libby in the 1950's.[24] Libby explained his electron-transfer model in terms of the Franck-Condon principle.[25, 26] However, this model neglected the role of inner-and outer-sphere solvent reorganization energy. Furthermore, Libby suggested that electron transfer occurs in the first step followed by solvent reorganization (Figure 1.6)[26] Although the Franck–Condon part was correct, this approach led to a violation of the law of energy conservation. Libby suggested large changes in the energy before and after the electron transfer, changes in equilibrium bond lengths and hence a large energy barrier to the electron transfer but he failed to explain where the extra energy will come from.[25] Marcus and Sutin recognized both inner-and outer-sphere solvent contributions and proposed a theory of electron transfer, eliminating the drawbacks of Libby's model.[24, 27, 28]

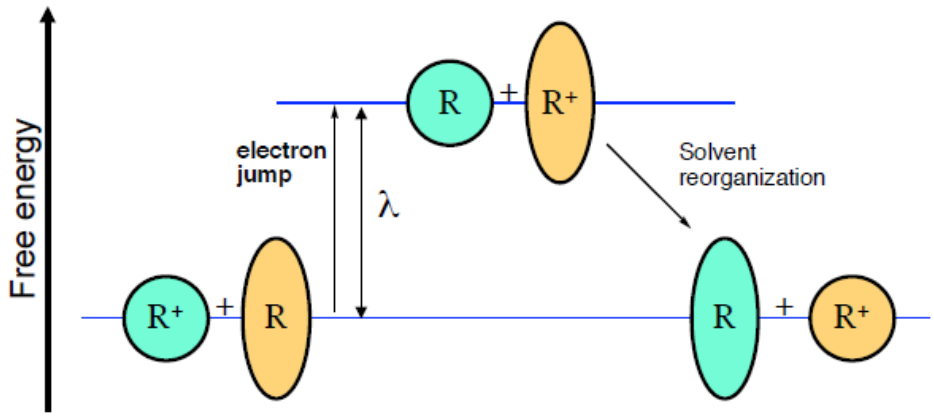

Figure 1.6. Libby's ET model showing that electron transfer is a step- wise process where ET reaction occurs without solvent reorganization. In the second step, solvent reorganization takes place. In the scheme R represents metal ions undergoing ET reaction.

Scheme 1.1 describes the self-exchange reaction between the reduced and oxidized forms of a metal complex, via an outer-sphere electron transfer mechanism.

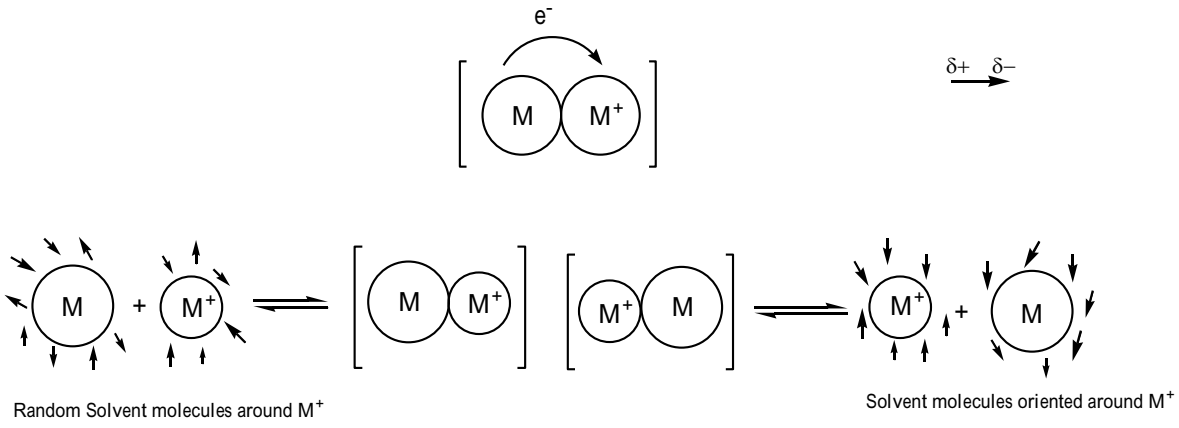

Scheme 1.1. A self-exchange reaction via the inner-and outer-sphere electron transfer mechanism of a metal complex, M and M^+.

The metal-ligand bond length decreases after electron transfer. In addition, the solvent reorganizes itself to accommodate the new electrostatic field created after electron transfer. The reorganization of solvent dipoles arises at the expanse of energy and this energy requirement creates an energy barrier for the electron transfer reactions.

1.6.1.1. Classical Theory of Electron Transfer

From Scheme 1.1 it can be assumed that the highest contribution to the rate of electron transfer comes from the short-range interaction of a reactant pair. Marcus also predicted that the ET process is diabatic and occurs only on one potential energy surface (PES). In this discussion, the term "non-adiabatic" is used for the ET reactions which occur on more than one PES. The observed rate constant for an outer-sphere electron transfer reaction in a non-adiabatic limit (weak coupling between two potential energy surfaces, Figure 1.7) is given by Equation 1.25 and the first-order rate constant for the electron transfer within the reactant pair is given by Equation 1.26.[29, 30]

$$k_{obs} = K_A k_{et} \qquad [1.25]$$

$$k_{et} = v_n \kappa_{el} \Gamma_\lambda exp\left(-\frac{\Delta G^\ddagger}{RT}\right) \qquad [1.26]$$

Where, κ_{el} is the electronic factor, ranging from zero to unity, K_A is the association constant for the formation of the reactant adduct, v_n is the effective nuclear frequency, β_{el} is the electronic factor, Γ_λ is the nuclear tunneling factor and $\Delta G^\ddagger$ is the free energy of the reaction.

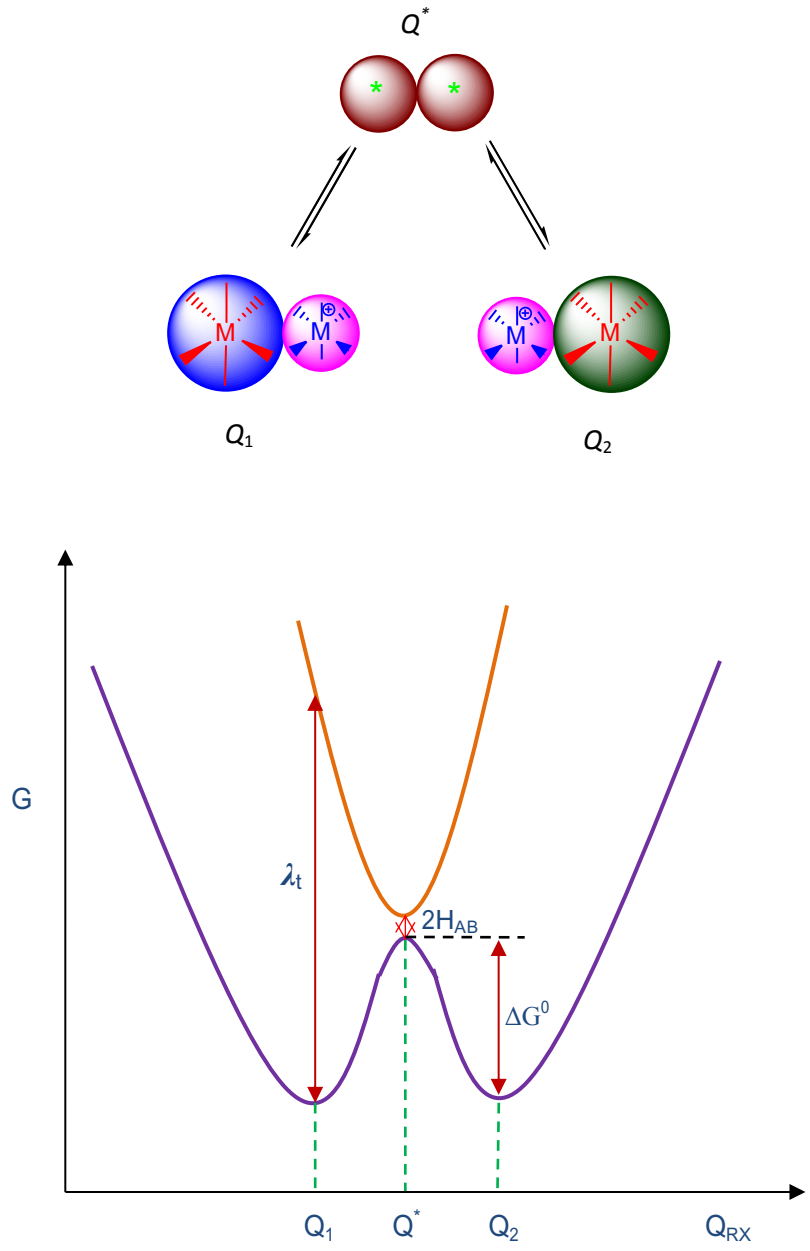

Figure 1.7. Potential energy surface diagram for a self-exchange reaction. The colored spheres on the top depict the reactant pair reaching the activation complex and relaxing to the product pair.[29]

The potential energy surfaces for a self-exchange reaction (where overall $\Delta G^0 = 0$) are shown in Figure 1.7. The PESs are a function of the nuclear coordinate Q_{RX} that describes the reaction. So Q_1 corresponds to reactant and Q_2 corresponds to product. Q^* is the junction point where the energy surfaces split due to the electronic coupling between D and A states. The coupling is indicated as $2H_{AB}$ and this coupling dictates how adiabatic the reaction will be. The conditions for adiabatic (weakly coupled) and diabatic (strongly coupled) are as follows.[31]

$$H_{AB} >> k_BT \text{ ; adiabatic}$$

$$H_{AB} << k_BT \text{ ; non-adiabatic}$$

$\Delta G^{\ddagger}$ is the free energy of activation (Equation 1.27) which th e system must achieve in order to reach the product energy surface, λ_t is the total reorganizational energy that is required by the system if the electron transfer occurs at point Q_1, and ΔG^0 is the difference in free energies of the reactant and product.[26, 32]

$$\Delta G^{\ddagger} = \frac{\lambda_t}{4}\left(1 + \frac{\Delta G^0}{\lambda_t}\right)^2 \qquad [1.27]$$

The total reorganizational energy (λ_t) is given as Equation 1.28

$$\lambda_t = \lambda_o + \lambda_i \qquad [1.28]$$

Where, λ_o is the outer-sphere solvent reorganizational energy and λ_i is the inner-sphere or vibrational reorganizational energy associated with the solvent trapping.[33] Figure 1.8

describes the effect of change in the solvent reorganization energy on the thermal electron transfer process.

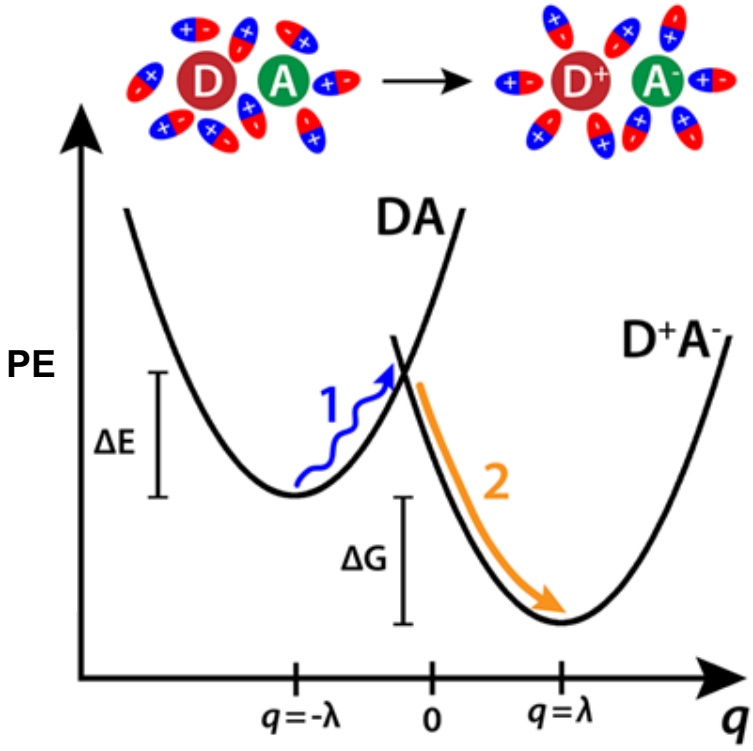

Figure 1.8. Visualization of change in solvent reorganization (top) and schematic illustration of potential energy surfaces of donor (D) and acceptor (A) (bottom). It is assumed that the two potential energy surfaces have the same curvature or have same force constants. As a result, the nuclear configuration, q, is linear in energy. In the figure, a thermally activated electron transfer process is shown where only the solvent contribution (outer-sphere) is considered. First, solvent fluctuations alter the nuclear geometry randomly until the nuclear configuration, q is "appropriate" for the donor and acceptor surfaces to cross. Once this occurs, the electron transfers from D to A surface, which subsequently relaxes to the most stable nuclear configuration of the oxidized D and reduced A state.[34] Modified and reproduced from Barthel, E. R.; Martini, I. B.; Schwartz, B. J. J. Phys. Chem. B 2001, 105, 12230.

According to Marcus theory the outer-sphere reorganizational energy can be approximated using the Born equation in which reactant and products are depicted as hard non-interpenetrating spheres and the solvent is treated as a continuum with bulk solvent dielectric constants. This form of reorganizational energy is given by Equation 1.29.[31, 35]

$$\lambda_o = (\Delta e)^2 \left(\frac{1}{2a_d} + \frac{1}{2a_a} - \frac{1}{r}\right)\left(\frac{1}{D_{op}} - \frac{1}{D_s}\right) \qquad [1.29]$$

Where, D_{op} and D_s are the optical and static dielectric constants, a_d and a_a are the radii of D and A which are separated by a distance r and Δe is the charge transferred from the donor to the acceptor. On the other hand λ_i can be estimated from the harmonic oscillator model as given in Equation 1.30.[29, 36]

$$\lambda_i = \frac{1}{2}\sum_i k_i (d_d^0 - d_a^0)_i^2 \qquad [1.30]$$

Where k_i is the reduced force constant for the i-th inner shell vibration, d_d^0 and d_a^0 are the bond lengths of D and A respectively, $(d_d^0 - d_a^0)_i^2$ is the difference in the equilibrium bond distance in the two oxidation states and summation is over all the molecular vibrations.

1.6.1.2. The Inverted Region

According to Equation 1.26, with an increase in the driving force, an increase in the rate of electron transfer (k_{et}) is expected until a maximum is reached for $\Delta G^0 = -\lambda$ and at this point the electron transfer process is activationless. Marcus predicted that after

this point k_{et} is expected to decrease with increase in driving force because the activation barrier reappears. This particular regime is called the "inverted region".[37, 38] Equation 1.26 relates the rate of electron transfer (k_{et}) with the driving force (ΔG^o) and the implications of this equation are illustrated in Figure 1.9. In the case of Figure 1.9 b, where $-\Delta G^o < \lambda$, increasing $-\Delta G^o$ and holding λ constant, k_{et} increases with increasing $-\Delta G^o$. For $-\Delta G^o = \lambda$, k_{et} reaches its maximum, $k_{et} = \kappa_{el}\nu_N$ (Figure 1.9 c), and k_{et} is independent on $-\Delta G^o$. Figure 1.9 d shows the existence of the Marcus inverted region in which k_{et} decreases with increasing driving force $-\Delta G^o > \lambda$.

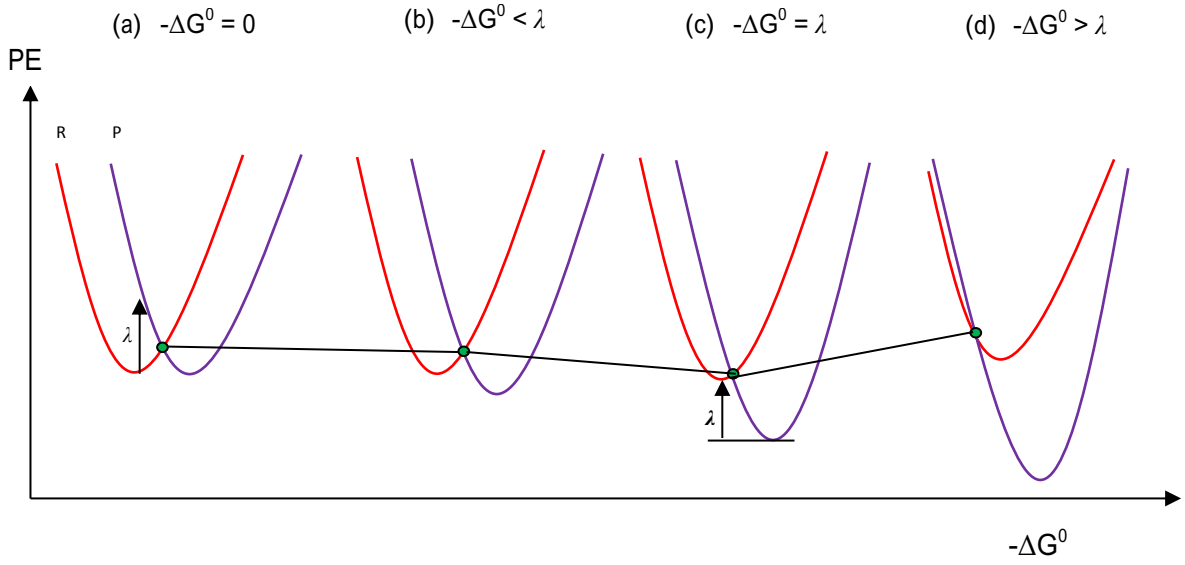

Figure 1.9. Illustrating the influence on the classical barrier to electron transfer of increasing $-\Delta G^o$ at fixed reorganization energy, λ, according to Equation 1.26. The green dot indicates the energy of the transition state as ΔG^0 becomes more negative. R describes the reactant potential energy surface and P describes the product potential energy surface.[29]

The prediction of the inverted region spurred several controversies until Closs and Miller experimentally proved the existence of Marcus inverted region.[35]. The inverted region lies well below the diffusion limit i.e. the diffusion (k_{diff}) can be very much smaller than the maximum rate of electron transfer (k_{et}), therefore, it is very difficult to discover this regime for bimolecular reactions due to the "diffusional masking" (Figure 1.10).[39] Nocera has described that under the diffusion masking conditions, k_{obs} can be given by Equation 1.31.[40]

$$\frac{1}{k_{obs}} = \frac{1}{k_{et}} + \frac{1}{k_D} \qquad (1.31)$$

Furthermore, if $k_{et} >> k_D$, $k_{obs} = k_D$, the diffusion limit imposes an upper limit on the k_{obs}. However, Closs and Miller were able to circumvent this problem by freezing the medium.

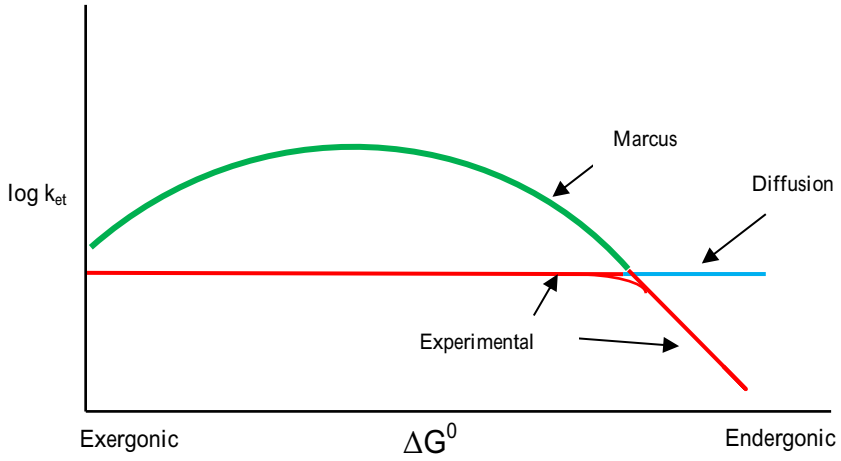

Figure 1.10. Parabolic dependence of the ET rate constant on the free energy driving force. The diffusion limit, signified by the horizontal solid line, truncates the parabola predicted by a plot of the logarithm of the electron transfer rate constant vs.the free energy.

Figure 1.11 shows the experimental plot from the original work performed by Closs and Miller where they observed the inverted region for intramolecular ET reactions in which diffusion limit no longer exists. In this experiment, the rate of ET is plotted vs. the free energy. It was observed that, as the driving force reaches maimum the rate constant for ET decreases.

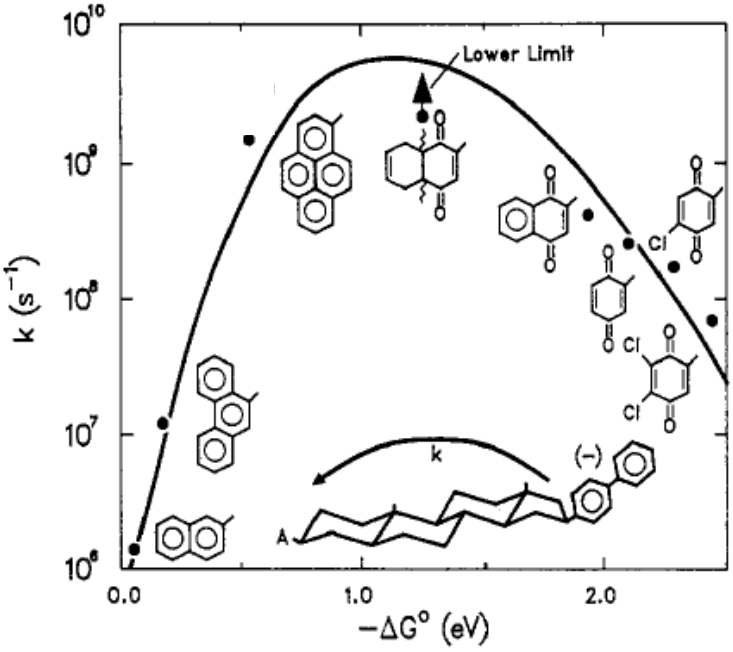

Figure 1.11. The plot of data from original work performed by Closs and Miller to disclose the physical existence of the inverted region.[31] Reprinted with permission from Closs, G. L.; Calcaterra, L. T.; Green, N. J.; Penfield, K. W.; Miller, J. R. J. Phys. Chem. 1986, 90, 3673.

1.6.2. Quantum Mechanical Theory of Electron Transfer

The quantum mechanical theory has evolved for nonadiabatic systems. In this model, an effective vibrational overlap between the vibrational wavefunctions of D and A is predicted rather than a thermal crossing point. According to this model, a vibrational tunneling though a barrier is possible if the vibrational overlap is not effective and this makes thermal energy irrelevant for ET processes.

The quantum mechanical theory relies on the Golden Rule which makes it analogous to electronic transitions as per the following equation (Equation 1.32).[36]

$$k_{et} = k_{m\to n} = \frac{2\pi|H_{AB}|^2}{\hbar}\prod_{k=1}^{3N-6}\langle\chi_v^m(\xi_k)\chi_{v'}^n(\xi_k)\rangle\,\rho_{mn} \qquad [1.32]$$

Where, H_{AB} is the electronic coupling between two potential energy surfaces if the D molecule is in its vibrational ground state, and the A molecule is in a higher vibrational level. If only one vibrational mode with quantum spacing $\hbar\omega$ is considered, $\chi_{v'}^n(\xi_k)$ are the associated vibrational wavefunctions with quantum number v, ξ_k is the internal coordinate for the acceptor mode k and ρ_{mn} is the Boltzmann's population of the initial level in the excited-state. The ET rate with this model is given by the following equation (Equation 1.33).[30, 31, 35]

$$k_{ET} = \sqrt{\frac{\pi}{\hbar^2\lambda_o k_B T}}\,|H_{AB}|^2\sum_{v'=0}^{\infty} exp\,(-S)\frac{S^{v'}}{v'!}exp\left\{-\left[\frac{(\lambda_o+\Delta G^0+v')^2}{4\lambda_o k_B T}\right]\right\} \qquad [1.33]$$

Equation 1.33 is a good approximation for highly exothermic reactions with weak electronic coupling.

1.7. Energy Transfer

Energy transfer in a supramolecular framework is a non-radiative transition between two excited-states but localized on different units. There are three main mechanisms that define the energy transfer process: (1) Trivial mechanism (2) Förster energy transfer (3) Dexter, or exchange mechanism.

1.7.1. Trivial Mechanism

In the trivial mechanism, a direct interaction between D and A molecule is not required for energy transfer to occur. In this case, the excited donor (D^*) may emit a photon (photoemission) or an electron (photoionization) and A may capture the photon or electron resulting in a overall energy transfer between D and A. The radiative energy transfer occurs by the two-step sequence as presented in Equations 1.34 and 1.35.

$$D^* \rightarrow D + hv \qquad [1.34]$$

$$A + hv \rightarrow A^* \qquad [1.35]$$

In the trivial mechanism, the absorption spectrum of D^* must overlap the absorption spectrum of A and the rate or probability of energy transfer per unit time depends upon the following factors: (i) The quantum yield of emission by D^*; (ii) the concentration of A molecule in the path of photons emitted by D^*; (iii) the light absorbing ability of A. The extent of energy transfer maximizes when these factors are satisfied. The overall spectral overlap integral is given by Equation 1.36, where, I_0 is the emitted light intensity for D as a function of frequency.

$$J = \int_0^\infty I_0(\bar{v})\varepsilon(\bar{v})d\bar{v} \qquad [1.36]$$

1.7.2. Förster Energy Transfer

For the Förster mechanism to operate, the absorption spectrum of the acceptor must overlap with the emission spectrum of donor (Figure 1.12) and the distance between D and A should be less than 100-300 Å.[41] Considering D^* as an excited donor and A as an acceptor, the following energy transfer (E_NT) event can be predicted (Equation 1.37):

$$D^* + A \longrightarrow D + A^* \qquad [1.37]$$

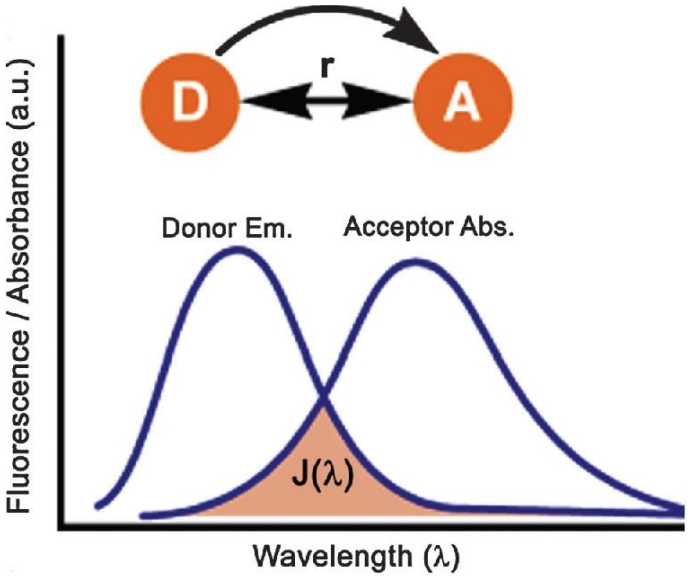

Figure 1.12. The spectral overlap between absorption and emission spectra of D and A as an indication of Förster E_NT, here, J is the overlap integral and r is the distance between D and A.[42] Reprinted from Freeman, R.; Willner, I. Chem. Soc. Rev. 2012, 41, 4067. Copyright ©2012 Royal Society of Chemistry. All Rights Reserved.

This process decreases the fluorescence intensity and lifetime of the D molecule but enhances the fluorescence and lifetime of the A molecule. Resonance E_NT was first observed by Perrin in 1918[43] and many years after that Förster proposed the theory of

fluorescence resonance energy transfer (FRET) in 1940s.[44] FRET occurs from a dipole-dipole interaction of the D and A electronic states. Furthermore, the extent of FRET depends upon the magnitude of the dipole-dipole interaction.

E_NT from Coulombic interaction is referred to as Förster E_NT. In this mechanism, the excited molecules behave like oscillating dipoles due to the presence of an electric field. The transition dipole of these excited molecules then oscillates the electron to the ground-state. In Figure 1.31, A "D" is excited by photon capture and undergoes suseqent relaxation to its lowest excited singlet state, S_1. If the acceptor group is in the close proximity, the energy released as a consequence of transition from excited to ground-state (S_0) may simultaneously excite "D".

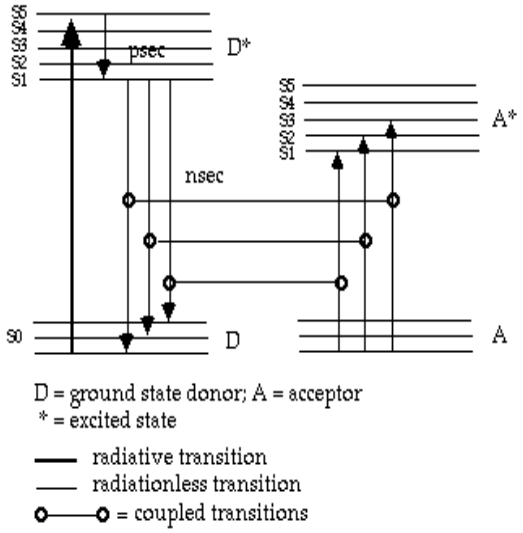

Figure 1.13. The coupled transitions of D and A during a Förster E_NT process.[45]

The rate of Förster E_NT is given by Equation 1.38, Φ_{em} is the quantum yield of the donor, n is the refractive index of the solvent, r is the distance between D and A in nm, ε is the molar extinction coefficient of the acceptor and $\bar{\nu}$ is the energy in wavenumber.[46]

$$k_{en}^{Coul} = 1.25 \times 10^{17} \left(\frac{\Phi_{em}}{n^4 \tau r^6}\right) \int_0^{\infty} \varepsilon(\bar{\nu}) \, \frac{d\bar{\nu}}{\bar{\nu}^4} \qquad [1.38]$$

Förster distance (R_0) is the distance at which the energy transfer efficiency is 50%. A large Förster radius (R_0 > 25 Å) is indicative of a very efficient Förster E_NT process, while, a short Förster radius ($R_0 \leq 10$ Å) indicates that very short donor-acceptor distances are needed to allow the E_NT process, which increases the probability of non-Förster and quenching processes to occur. In order to obtain k_{obs}, fast spectroscopic measurements of the decay of the excited-state are required. If this is known, the actual D-A distance (R) can be estimated.

The Förster distance, R_0, can be calculated from the spectral properties of the donor and acceptor, by Equation 1.39, where κ^2 is a factor governed by the relative orientation in space of the transition dipoles of D and A, with values between 0 and 4; for collinear and parallel dipoles κ^2 = 4. For parallel dipoles κ^2= 1, for perpendicular dipoles κ^2= 0, and for random orientation of dipoles κ^2 = 2/3.[44, 47]

$$R_0^6 = \frac{9000 \ln 10 \kappa^2 \phi_{em}}{128 \pi^5 N_A n^4} \int \frac{F_D(\bar{\nu}) \varepsilon_A(\bar{\nu})}{\bar{\nu}^4} d\bar{\nu} \qquad (1.39)$$

In Eqution 1.39, n is the refrective index of the solvent, ϕ_{em} is the fluorescence quantum yield of the donor, $F_D(\bar{\nu})$ is the normalized donor fluorescence spectrum, $\varepsilon_A(\bar{\nu})$ is the normalized acceptor's absorption spectrum and N_A is the Avogadro number.

The integral in Equation 1.39 describes the degree of spectral overlap between the donor emission and the acceptor absorption spectra and is known as the overlap integral for resonance interaction $J(\lambda)$, which must be nonzero for FRET to occur. Equation 1.40 can be simplified by using known physical constants and $J(\lambda)$ in units of M^{-1} cm^{-1} nm^4 to give the Förster distance in angstroms, where n, ϕ and κ are dimensionless, and λ, is given in nm.[44]

$$R_0 = 0.211[\kappa^2 n^{-4} \Phi_{em} J(\lambda)]^{1/6} \quad \text{(in Å)} \qquad [1.40]$$

Using the calculated R_0 from Equation 1.40 and the experimental spectroscopic values for τ and k_{obs}, the donor-to-acceptor distance R can be estimated. In many studies, FRET is used solely to detect changes in distance as a result of conformational change and not to measure absolute distance between fluorophores, so Equation 1.40 suffices for such studies.

1.7.3. Dexter or Exchange Mechanism

The Dexter mechanism was proposed by Dexter in the 1950s, where this the exchange of electrons between excited D and A was proposed.[48] Unlike Förster energy transfer, this mechanism operates over short distances (less than 10 Å) and the rate constant decays exponentially as the distance between D and A increases.[49, 50] Figure 1.14 shows the spin conservation and difference between the Förster and Dexter mechanisms.[51]

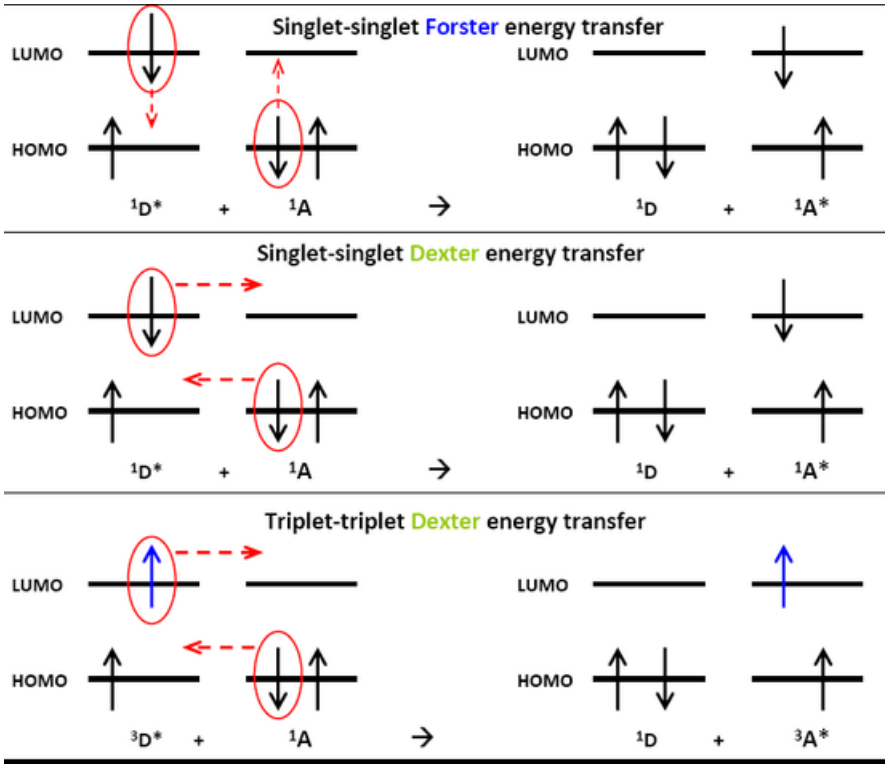

Figure 1.14. Showing electronic distributions and spin conservation during Förster and Dexter energy transfer processes.[52]

In order for exchange to occur, D electrons must be transferred to the empty orbitals of A and so the overlap of wavefunctions must take place. As a result of this orbital overlap, an electron cloud forms between D and A and this is referred to as "collision" in this mechanism. The rate of Dexter energy transfer (k_{obs}) is given by Equation 1.41.[46]

$$k_{obs} = KJ_{ex}\left(\frac{-2r}{L}\right) \qquad [1.41]$$

Where, K is an experimental constant, r is the distance between D and A and L is the sum of the Van der Walls radii and J_{ex} is the normalized spectral overlap given by Equation 1.42.

$$J_{ex} = \int_0^\infty F_D\,(\bar{v})\varepsilon_A(\bar{v})d(\bar{v}) \qquad [1.42]$$

Therefore, the rate for energy transfer decreases exponentially with increasing distance between donor and acceptor.

1.7.4. Differences between Dexter and Förster Energy Transfer

Förster and Dexter mechanisms are the two most common photophysical models used in order to explain the nonradiative energy transfer process in bimolecular systems. Table 1.1 shows some of the characteristics and differences between the two models.

Table 1.1. Characteristic parameters for Dexter and Förster energy transfer.

Förster	Dexter
Dipole-Dipole interaction.	Double electron exchange interaction.
Transfer over large distances (R_0 = 10-100 Å).	Transfer over short distances ($R_0 \leq 10$ Å).
No physical contact required.	Requires near-collisional contact which ensures good molecular orbital overlap.
Only singlet-singlet interactions.	Singlet and triplet interactions allowed.
Only bands for A should be in emission spectra.	Bands for D and A should be present in absorption and emission spectra.
J(λ) should be large as a result of good spectral overlap, which contributes to larger Förster radius.	J(λ) should be low as a result of poor spectral overlap.
Good dipole alignment (geometry factor) for allowing effective resonance dipole interaction.	No geometric requirements for orbital overlap.
No rigid molecular structures.	Rigid molecular structures.
High ε values ~10^4 M^{-1} cm^{-1}.	Independent of ε.

Using some of the parameters described in Table 1.1, it is possible to predict if a muitichromophoric or bichromophoric system will undergo Förster or Dexter ET preferentially. However, when the distance between chromophores is short, less than about 10 Å, the photophysical interpretation by pure Förster or Dexter models becomes

difficult, and new models to explain the experimental results are still in debate (especially for conjugated polymers), and it becomes difficult to predict or interpret ET results.[53, 54]

1.8. Theory of Electron-Proton Transfer (EPT)

The theory of electron transfer is much more evolved as compared to the theory of EPT. Pioneering work by Taube and later by Marcus led to a working understanding of the dynamics of electron transfer.[26-28, 55, 56] The theory of EPT is still in its infancy as compared to ET because of the complications arising from PT and ET coupling. The experimental work of Babcock, Krishtalik, Hammarström, Mayer, Nocera and Meyer, among others, coupled with the development of the associated EPT theory by Cukier[57] and Hammes-Schiffer, have lent insight into the EPT process.[58, 59] Since Hammes-Schiffer theory explains EPT in terms of four diabatic regimes which cover ET, PT and EPT events, hence this theory will be elaborated below.

This theory is an extension of electron transfer theory introduced by Marcus. In this theory both the transferring electron and proton are treated quantum mechanically. Furthermore, three-dimensional vibronic free energy surfaces as stacked paraboloids have been used to depict the potential energy surfaces of EPT process. Reactants can be represented as one set of paraboloids, and products can be represented as a second set of paraboloids (Figure 1.15).

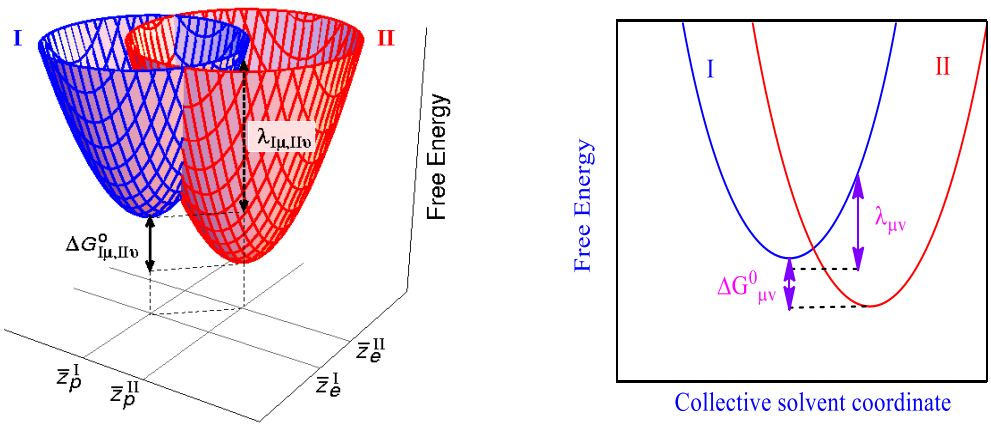

Figure 1.15. (Left) Multidimensional stacked potential energy surface paraboloids for the reactant (I), mixture of 1a and 1b states and product (II), mixture of 2a and 2b states as a function of collective solvent coordinates, Z_p (PT coordinates) and Z_e (ET coordinates). (Right) A slice of potential energy surface of the reactant (I) and product (II) showing reaction free energy ($\Delta G^0_{\mu\nu}$) and reorganizational energy ($\lambda_{\mu\nu}$), where μ and ν are vibrational states.[60] Adapted with permission from Hammes-Schiffer, S.; Soudackov, A. V. J. Phys. Chem. B 2008, 112, 14108.

PCET processes occur in the following three typical regimes:[61-64]

(1) Adiabatic ET and PT: In this regime, the vibronic coupling between pairs of the above-described four diabatic states is very strong.

(2) Non-adiabatic ET and PT: In this regime, the vibronic coupling between pairs of the above-mentioned four diabatic states is very weak.

(3) Adiabatic PT and non-adiabatic ET: where vibronic coupling between the pair of PT diabatic states is strong but coupling between the pair of ET diabatic states is weak.

As described earlier, the theory of EPT follows Marcus theory formulations with inclusion of PT transfer coordinates. In this treatment, the wavefunctions for ET and PT are represented as the following four diabatic electronic states.

$$(1a)\ D_e^- \text{——} {}^+D_pH \text{ ------ } A_p \text{——} A_e$$

$$(1b)\ D_e^- \text{——} D_p \text{ ------ } HA_p^+ \text{——} A_e$$

$$(2a)\ D_e \text{——} {}^+D_pH \text{ ------ } A_p \text{——} A_e^-$$

$$(2b)\ D_e^- \text{——} D_p \text{ ------ } HA_p^+ \text{——} A_e^-$$

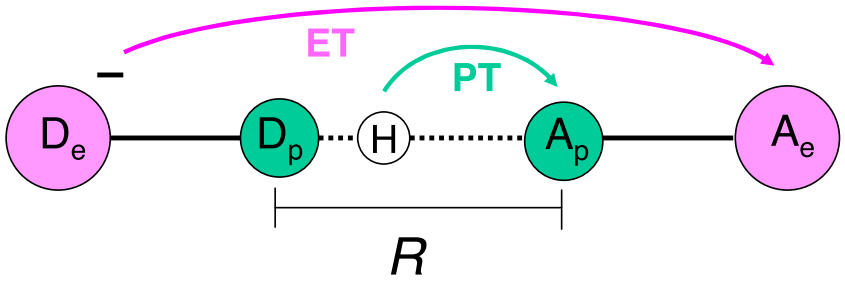

Scheme 1.2. Schematic of electron transfer from D_e to A_e and PT from D_p to A_p

Here, D_e and A_e are electron donor and acceptor, respectively, and D_p and A_p are the proton donor and proton acceptor, respectively (Scheme 1.2). In the above, diabatic electronic states 1 and 2 depict ET states and (a) and (b) depict PT states. A transition from (1a) → (1b) will be PT, (1a) → (2a) will be ET and (1a) → (2b) will be EPT. Both 1b and 2a diabatic states are usually much higher in energy than the 1a and 2b diabatic states for EPT reactions.

In the limit of nonadiabatic electron transfer, Hammes-Schiffer has applied the Fermi Golden Rule to derive a rate expression for nonadiabatic transition from the reactant state to the product set of vibrational states (Equation 1.43).[61-64]

$$k_{12} = \frac{2\pi}{\hbar}|V_{12}|^2(4\pi\lambda k_B T)^{-1/2} \times \sum_\mu P_{I\mu} \sum_v S^2_{1\mu,2\mu} \exp\left\{\frac{-(\Delta G^0_{1\mu,2\mu}+\lambda)^2)}{4\lambda k_B T}\right\} \qquad [1.43]$$

Where, Σ_μ and Σ_v indicate summations over the vibrational states for diabatic states 1 and 2, respectively, V_{12} is the coupling between the two diabatic states, λ is the reorganizational energy, $S^2_{1\mu,2\mu}$ is the overlap of the vibrational wavefunctions 1μ and 2v, $\Delta G^0_{1\mu,2\mu}$ is the equilibrium free energy difference between solvated vibrational states 1μ and 2v and $P_{I\mu}$ is the Boltzmann factor for the state 1μ. Furthermore, Hammes-Schiffer and Soudackov have also derived the rate expression in the limit of adiabatic proton transfer and nonadiabatic electron transfer by the application of the Fermi Golden Rule.[65] Application of the Fermi Golden Rule on the two sets of paraboloids shown in Figure 1.15 gives the following rate expression (Equation 1.44).

$$\mathrm{k} = \frac{2\pi}{\hbar}\sum_\mu P_{I\mu} \sum_v V^2_{\mu v} (4\pi\lambda_{\mu v} k_B T)^{-1/2} \exp\left\{-\frac{(\Delta G^0_{\mu v}+\lambda_{\mu v})^2)}{4\lambda_{\mu v} k_B T}\right\} \qquad [1.44]$$

Where, $V^2_{\mu v}$ is the nonadiabatic coupling between the reactant and product vibronic states μ and v, respectively, $\Delta G^0_{\mu v}$ is the equilibrium free energy change and $\lambda_{\mu v}$ is the total reorganizational energy. In this expression the reorganization energy ($\lambda_{\mu v}$) is given as Equation 1.45[61]

$$\lambda_{\mu v} = \epsilon_{\mu}^{I}\left(\bar{Z}_p^{II_v}, \bar{Z}_e^{II_v}\right) - \epsilon_{\mu}^{I}\left(\bar{Z}_p^{I_\mu}, \bar{Z}_e^{I_\mu}\right) = \epsilon_{v}^{II}\left(\bar{Z}_p^{I_\mu}, \bar{Z}_e^{I_\mu}\right) - \epsilon_{v}^{II}\left(\bar{Z}_p^{II_v}, \bar{Z}_e^{II_v}\right) \qquad [1.45]$$

and the free energy deference is defined as Equation 1.46.

$$\Delta G_{\mu v}^{0} = \epsilon_{v}^{II}\left(\bar{Z}_p^{II_v}, \bar{Z}_e^{II_v}\right) - \epsilon_{\mu}^{I}\left(\bar{Z}_p^{I_\mu}, \bar{Z}_e^{I_\mu}\right) \qquad [1.46]$$

Where, $\left(\bar{Z}_p^{I_\mu}, \bar{Z}_e^{I_\mu}\right)$ and $\left(\bar{Z}_p^{II_v}, \bar{Z}_e^{II_v}\right)$ are the solvent coordinates for the minima of $\epsilon_{\mu}^{I}(Z_p, Z_e)$ and $\epsilon_{v}^{II}(Z_p, Z_e)$ respectively. These quantities are shown in Figure 1.15 for a pair of paraboloids. The coupling $V^2_{\mu v}$ is defined as a quantity $V(r_p, Z_p)$ averaged over the reactant and product proton vibrational wavefunctions I_μ and II_v, where $V(r_p, Z_p)$ is a linear combination of coupling between the four diabatic states with weightings dependent upon proton coordinates r_p. Equation 1.44 provides the rate expression for EPT and Equation 1.43 provides the rate constant for single-electron transfer in a solute mode uncoupled to the solute. The most discernible features between Equations 1.43 and 1.44 are the reorganization energies, equilibrium free energy differences and the coupling between two states. Equation 1.44 is presented in terms of two-dimensional paraboloids instead of one-dimensional parabolas. Furthermore, reorganization energy (λ) in Equation 1.43 is the same for all pairs of intersecting parabolas. Conversely, the reorganization energies ($\lambda_{\mu v}$) in Equation 1.44 are different for each pair of intersecting electron-transfer diabatic surfaces.

1.9. Scope of this Thesis

This dissertation is divided into 7 chapters. Chapter 1 includes the theroeis behind the basic concepts used throughout this dissertation. Chapter 2 describes the experimental and synthetic techniques employed during the data acquisition and analysis.

Chapter 3 accounts the "Effect of Torsional Strain on the Photophysics of Symmetric Pyrenophanes". In this Chapter, the study of three inherently-chiral pyrenophanes with varying tether lengths is described. The change in tether length is associated with a change in the bend angle across the pyrene moiety and the effect of change in the bend angle on the photophysical properties of these pyrenophanes is described.

Chapter 4 describes the "Proton Transfer Dynamics in Rigid Pyrene Macrocycles". The goal of the work described in this chapter is to study the effect of protonation on the photophysical properties of pyridine-appended pyrene macrocycles. Chapter 5 describes the "Sensing Mechanisms in Triazole Based Oligomers". This chapter describes the efforts to delineate the sensing mechanism in various triazole - based oligomers. The role of a triazole unit as a linker and ligand is also explored in brief in this Chapter. Chapter 6 reports the "Concerted Electron Proton Transfer Using Re(I) MLCT Excited-States" which a sterically-bulky phenol is used to reductively quench the MLCT excited-state of three distinct Re polypyridyl complexes. Chapter 7

lists the major conclusions drawn from the individual chapters. In the end, some recommendations for the future work are outlined.

References

[1] Holten, D.; Bocian, D. F.; Lindsey, J. S., Acc. Chem. Res., (2001) 35, 57.

[2] He, L.; Wang, M.; Ge, J.; Yin, Y., Acc. Chem. Res., (2012) 45, 1431.

[3] Liu, J. M., Photonic Devices, Cambridge University Press: London, (2009); Vol. 2.

[4] Ito, A.; Meyer, T. J., Phys. Chem. Chem. Phys., (2012) 14, 13731.

[5] Chen, P.; Meyer, T. J., Chem. Rev., (1998) 98, 1439.

[6] Alstrum-Acevedo, J. H.; Brennaman, M. K.; Meyer, T. J., Inorg. Chem., (2005) 44, 6802.

[7] Freed, K. F.; Jortner, J., J. Chem. Phys., (1970) 52, 6272.

[8] Freed, K. F., Curr. Top. Chem., (1972) 31, 65.

[9] Lin, S. H., J. Chem. Phys., (1966) 44, 3759.

[10] Thompson, D. W.; Ito, A.; Meyer, T. J., Pure Appl. Chem., (2013) 85, 1257.

[11] Caspar, J. V.; Kober, E. M.; Sullivan, B. P.; Meyer, T. J., J. Am. Chem. Soc., (1982) 104, 630.

[12] Caspar, J. V.; Meyer, T. J., J. Phys. Chem., (1983) 87, 952.

[13] Kober, E. M.; Caspar, J. V.; Lumpkin, R. S.; Meyer, T. J., J. Phys. Chem., (1986) 90, 3722.

[14] Kestell, J. D.; Williams, Z. L.; Stultz, L. K.; Claude, J. P., J. Phys. Chem. A, (2002) 106, 5768.

[15] Claude, J. P.; Meyer, T. J., J. Phys. Chem., (1995) 99, 51.

[16] Claude, J. P.; Omberg, K. M.; Williams, D. S.; Meyer, T. J., J. Phys. Chem. A, (2002) 106, 7795.

[17] Claude, J. P.; Williams, D. S.; Meyer, T. J., J. Am. Chem. Soc., (1996) 118, 9782.

[18] Graff, D.; Claude, J. P.; Meyer, T. J., Adv. Chem. Ser., (1997) 253, 183.

[19] Caspar, J. V.; Meyer, T. J., J. Am. Chem. Soc., (1983) 105, 5583.

[20] Caspar, J. V.; Westmoreland, T. D.; Allen, G. H.; Bradley, P. G.; Meyer, T. J.; Woodruff, W. H., J. Am. Chem. Soc., (1984) 106, 3492.

[21] Caspar, J. V.; Meyer, T. J., Inorg. Chem., (1983) 22, 2444.

[22] Ballhausen, C. J. Ed. Molecular Electronic Structures of Transition Metal Complexes, McGraw Hill : New York: (1979); Vol. 2.

[23] Damrauer, N. H.; Boussie, T. R.; Devenney, M.; McCusker, J. K., J. Am. Chem. Soc., (1997) 119, 8253.

[24] Libby, W. F., J. Phys. Chem., (1952) 56, 863.

[25] Marcus, R. A., Pure Appl. Chem., (1997) 69, 13.

[26] Marcus, R. A., Phys. Chem. Chem. Phys., (2012) 14, 13729.

[27] Marcus, R. A., J. Chem. Phys., (1965) 43, 3477.

[28] Marcus, R. A., Rev. Mod. Phys. (1996) 65,

[29] Sutin, N.; Creutz, C., J. Chem. Ed., (1983) 60, 809.

[30] Kestner, N. R.; Logan, J.; Jortner, J., J. Phys. Chem., (1974) 78, 2148.

[31] Closs, G. L.; Calcaterra, L. T.; Green, N. J.; Penfield, K. W.; Miller, J. R., J. Phys. Chem., (1986) 90, 3673.

[32] Marcus, R. A., J. Chem. Phys., (1956) 24, 966.

[33] Balzani, V., Electron Transfer in Chemistry, WILEY-VCH Verlag GmbH, D-69469 Weinheim (Federal Republic of Germany): (2001).

[34] Barthel, E. R.; Martini, I. B.; Schwartz, B. J., J. Phys. Chem. B, (2001) 105, 12230.

[35] Closs, G. L.; Miller, J. R., Science, (1988) 240, 440.

[36] Meyer, T. J.; Taube, H., Comp. Coord. Chem., (1987) 1, 331.

[37] Gould, I. R.; Moody, R.; Farid, S., J. Am. Chem. Soc., (1988) 110, 7242.

[38] Gould, I. R.; Moser, J. E.; Armitage, B.; Farid, S.; Goodman, J. L.; Herman, M. S., J. Am. Chem. Soc., (1989) 111, 1917.

[39] Rosspeintner, A.; Koch, M.; Angulo, G.; Vauthey, E., J. Am. Chem. Soc., (2012) 134, 11396.

[40] Turró, C.; Zaleski, J. M.; Karabatsos, Y. M.; Nocera, D. G., J. Am. Chem. Soc., (1996) 118, 6060.

[41] Forster, T., Chem. Phys. Lett., (1 972) 17, 309.

[42] Freeman, R.; Willner, I., Chem. Soc. Rev., (2012) 41, 4067.

[43] Lackowicz, J. R. Ed. Principles of Fluorescence Spectroscopy, Springer: (2009); Vol. 3.

[44] Főrster, T., Farad. Discuss. , (1959) 27, 7.

[45] http://www.labautopedia.org/mw/index.php,

[46] Nicholas J. Turro; V. Ramamurthy; Scaiano, J. C., Principles of Molecular Photochemistry: An Introduction, In University Science Books.: (2009).

[47] Forster, T.; Kasper, K. Z., Elektrochem., (1955) 59, 976.

[48] Dexter, D. L., J. Chem. Phys., (1953) 21, 836.

[49] Bolinger, J. C.; Traub, M. C.; Brazard, J.; Adachi, T.; Barbara, P. F.; Vanden Bout, D. A., Acc. Chem. Res., (2012) 45, 1992.

[50] Speiser, S., Chem. Rev., (1996) 96, 1953.

[51] Hsu, C. P., Acc. Chem. Res., (2009) 42, 509.

[52] http://chemwiki.ucdavis.edu/Theoretical_Chemistry/Fundamentals/Dexter

[53] Wong, K. F.; Bagchi, B.; Rossky, P. J., J. Phys. Chem. A, (2004) 108, 5752.

[54] Murphy, C. B.; Zhang, Y.; Troxler, T.; Ferry, V.; Martin, J. J.; Jones, W. E., J. Phys. Chem. B, (2004) 108, 1537.

[55] Marcus, R. A., J. Chem. Phys., (1989) 93, 3078.

[56] Taube, H.; Myers, H.; Rich, R. L., J. Am. Chem. Soc., (1953) 75, 4118.

[57] Cukier, R. I.; Nocera, D. G., Annu. Rev. Phys. Chem., (1998) 49, 337.

[58] Huynh, M. H. V.; Meyer, T. J., Chem. Rev., (2007) 107, 5004.

[59] Weinberg, D. R.; Gagliardi, C. J.; Hull, J. F.; Murphy, C. F.; Kent, C. A.; Westlake, B. C.; Paul, A.; Ess, D. H.; McCafferty, D. G.; Meyer, T. J., Chem. Rev., (2012) 112, 4016.

[60] Hammes-Schiffer, S.; Soudackov, A. V., J. Phys. Chem. B, (2008) 112, 14108.

[61] Decornez, H.; Hammes-Schiffer, S., J. Phys. Chem. A, (2000) 104, 9370.

[62] Hammarstrom, L.; Styring, S., Phil. Trans. R. Soc. B, (2008) 363, 1283.

[63] Hammes-Schiffer, S., Acc. Chem. Res., (2009) 42, 1881.

[64] Hammes-Schiffer, S.; Iordanova, N., Biochim. Biophys. Acta, (2004) 1655, 29.

[65] Soudackov, A.; Hammes-Schiffer, S., J. Chem. Phys., (2000) 113, 2385.

Chapter - 2

Experimental Techniques and Methodology

This chapter describes the synthesis of Re polypyridyl complexes and includes an overview of experimental techniques associated with measuring the ground and excited-state properties. As well, the methodology of single value decomposition analysis to extract association constants is explained.

2.1. Materials

The complexes fac-$[(CO)_3Re(4,4'\text{-}(X)_2\text{-}bpy)(4,4'\text{-}bpy)]^+$ (X = H, CH_3, NH_2) were prepared according to previously published procedures.[1-7] $Re(CO)_5Cl$ was purchased from Strem Chemicals, 4,4'-bpy, 2,2'-bpy and 4,4'-dimethyl-2,2'-bpy were purchased from Sigma Aldrich and 4,4'-diamino-2,2'-bpy ligand (Figure 2.1) was purchased from Carbosynth Inc. (U.K.) in 99% purity and was used as received.

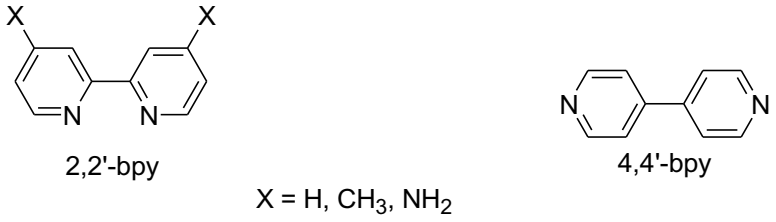

Figure 2.1. Structures of the pyridyl ligands.

De-ionized water was obtained from a Sybron/Barnstead apparatus. Aqueous potassium phosphate (PBS) buffer solutions were prepared by mixing 80.2 mL of aqeous 1.0 M K_2HPO_4 (Sigma Aldrich) and 19.8 mL of aqeous 1.0 M KH_2PO_4 (Sigma Aldrich)

and diluted to 1.00 L with de-ionized water giving a 0.1 M PBS buffer with a pH of 7.41.

Spectral grade THF and DMSO solvents (Sigma Aldrich > 99% pure) and spectral grade chloroform (Fisher) were used as received. Spectral grade CH_3CN was purchased from Burdick and Jackson and was used for the photophysical measurements. For the synthesis of metal complexes reagent grade (ACS) ethanol, CH_2Cl_2 and acetone were used as sovents.

2.2. Methods

The following methods/protocols were employed for the sample preparations, synthesis of metal complexes and photophysical data acquisitions.

2.2.1. Sample Preparation

For the majority of photophysical measurements, samples were prepared gravimetrically. Solid samples were dissolved in a fixed volume of the appropriate spectral-grade solvent to produce stock solutions of desirable concentration. Using a microsyringe the aliquots from the stock solution were then injected into a 1.0-cm pathlength screw-top quartz cuvette containing 2.5 mL (for some cases 3.0 mL) of spectral grade solvent and the resulting spectra were recorded. UV-Vis spectra referenced vs. air to determine if there were any absorbing impurities present, and fluorescence spectra of the solvents were acquired prior to titration to ensure that the solvents were spectroscopically clean, showing no intrinsic emission at excitation

wavelength. In addition, almost all the samples (unless otherwise stated) were degassed by slowly bubbling N_2 into the sample cuvette for approximately 15 minutes. A UV-Vis spectrum of the sample was acquired immediately after degassing to ensure the purity and concentration of the sample.

2.2.2. Synthesis

The Synthesis of all the metal complexes have been published previously and all the manipulations were carried out as described before for the same complexes.[5,7,8] Synthesis was carried out in a nitrogen atmosphere and using nitrogen-purged solvents (unless otherwise stated). Equations 2.1 and 2.3 summarize the synthetic schemes for the preparation of fac-$[(CO)_3Re^{I}(4,4'\text{-}(X)_2\text{-bpy})(4,4'\text{-bpy})]^+$ (X = H, CH_3, NH_2) complexes.

$$(CO)_5ReCl + 4,4'\text{-}(X)_2\text{-bpy} \xrightarrow[\text{reflux/Toluene}]{\text{2 hrs./}N_2} [(CO)_3Re(4,4'\text{-}(X)_2\text{-bpy})(Cl)] + 2CO \qquad [2.1]$$

$$[(CO)_3Re(4,4'\text{-}(X)_2\text{-bpy})(Cl)] \xrightarrow[\text{rt/}CH_2Cl_2]{CF_3SO_3H} [(CO)_3Re(4,4'\text{-}(X)_2\text{-bpy})(CF_3SO_3)] + HCl \qquad [2.2]$$

$$[(CO)_3Re(4,4'\text{-}(X)_2\text{-bpy})(CF_3SO_3)] + 4,4'\text{-bpy} \xrightarrow[\text{4hrs./}N_2\text{/reflux}]{\text{3:1 v/v EtOH/}H_2O}$$

$$[(CO)_3Re(4,4'\text{-}(X)_2\text{-bpy})(4,4'\text{-bpy})]^+ + CF_3SO_3^- \qquad [2.3]$$

2.2.3. fac-$[(CO)_3Re^{I}$(**4,4'**-$(X)_2$-bpy)(**4,4'**-bpy)$]^+$ (X = H, CH_3, NH_2)

The complexes were prepared by using the methods published elsewhere.[1, 6, 9-11] fac-$[(CO)_3Re^{I}(4,4'-(X)_2$-bpy)$(CF_3SO_3)]$ was prepared according to the published literature procedures (Equations 2.1 and 2.2)[7, 12] and the details for the preparation of the final product fac-$[(CO)_3Re^{I}(4,4'-(X)_2$-bpy)$(4,4'$-bpy)$]^+$ (X = H, CH_3, NH_2) is described here. In a representative preparation 180 mg (0.31 mmol) of fac-$[(CO)_3Re^{I}(4,4'-(X)_2$-bpy)$(CF_3SO_3)]$ was added to 20 mL of 3:1 v/v mixture of ethanol/water, 82 mg (0.52 mmol) of 4,4'-bpy was added to the mixture which was heated at reflux under N_2, for 4 h. The reaction was allowed to cool to room temperature, the solvent was removed by rotary evaporation and the remaining bright yellow solid was re-dissolved in minimum amount of acetone. A aqueous saturated solution of $[NH_4](PF_6)$ was added drop-wise into the ice-cold acetone solution containing the Re complex, to yield a yellow precipitate. The precipitate was filtered off and dried in vacuum. For further purification, the product was dissolved in distilled CH_2Cl_2 and was reprecipitated in cold isooctane.

The purification of fac-$[(CO)_3Re^{I}(4,4'-(CH_3)_2$-bpy)$(4,4'$-bpy)$]^+$ was done by column chromatography as per following procedure. The dried product was dissolved in a minimum amount of acetone and was loaded to a silicagel (75/230 mesh) column. The product was eluted using a 1:4 v/v CH_3CN/CH_2Cl_2 solvent mixture. The collected final product was dried in vacuum to yield a yellow product. ^{1}H NMR spectra were measured on a 500 MHz spectrometer and chemical shifts are reported in ppm downfield from the signal of the internal reference, Me_4Si. Extinction coefficients of all the complexes so

obtained were calculated to verify if the complexes contained any absorbing impurity. ^{1}H NMR, IR, extinction coefficients, luminescence lifetimes, Φ_{em} and λ_{MLCT}^{abs} were found to be in good agreement with the literature values.[5, 7, 8]

X = H:

96.2 mg (0.16 mmol), 53% yield.

^{1}H NMR (CD_3CN-d_3, 500 MHz) δ 9.29 (d, J = 5.3 Hz, 2H), 8.72 (d, J = 6.1 Hz, 2H), 8.37-8.42 (m, 6H), 7.84 (dt, J = 5.0 and 1.5 Hz, 2H), 7.60-7.84 (m, 4H).

ν_{CO}: 2028, 1930, 1900 cm^{-1}

$\varepsilon \times 10^3$ M^{-1} cm^{-1} = 4.3 and λ_{MLCT}^{abs} = 350 nm.

X = CH_3:

82.4 mg (0.13 mmol), 45% yield.

^{1}H NMR (DMSO-d_6, 500 MHz): 9.14 (d, J = 5.6 Hz, 2H), 8.55 (s, 2H), 8.49 (d, J = 6.8 Hz, 2H), 8.28 (s, 4H), 7.71 (t, J = 6.7 Hz, 4H), 2.50 (s, 6H).

ν_{CO}: 2035, 1922 cm^{-1}

$\varepsilon \times 10^3$ M^{-1} cm^{-1} = 5.0 and λ_{MLCT}^{abs} = 340 nm.

X = NH_2:

66.3 mg (0.10 mmol), 36% yield.

^{1}H NMR (CD_3CN-d_3, 500 MHz) 8.22 (d, J = 6.3 Hz, 2H), 8.03 (d, J = 5.3 Hz, 2H), 7.52 (s, 2H), 7.12 (s, 4H), 6.66 (d, J = 4.8 Hz, 2H), 6.45 (d, J = 5.4 Hz, 2H) 6.03 (s, 4H).

ν_{CO}: 2041, 1935 and ν_{NH}: 3350 cm^{-1}

$\varepsilon \times 10^3$ M^{-1} cm^{-1} = 3.0 and λ_{MLCT}^{abs} = 343 nm.

2.2.4. Instrumentation

In this section, an overview of the instrumental techniques described in this thesis to record absorption, steady-state fluorescence, time-resolved fluorescence and transient absorption of the samples will be presented. The descriptions are presented in the following manner: UV-Vis spectrophotometer, steady-state fluorescence spectrofluorometer, time-resolved fluorescence and transient absorption spectroscopy.

2.2.4.1. UV-Vis Spectrophotometer

Absorption spectra were acquired using an Agilent 8453A diode array UV-visible spectrophotometer with a wavelength range of 190 to 1100 nm (<± 0.5 nm precision). Manipulations of the UV-visible spectroscopic data were conducted using ChemStation software provided by Agilent or by exporting the data and utilizing Origin 8.0 (Origin Lab Corporation) for the analysis.[13]

2.2.4.2. Steady-State Fluorescence Spectrometer

The fluorescence measurements were performed on a Photon Technology International (PTI) Quantamaster 6000 photon-counting spectrofluorometer equipped with a 75 W Ushio Xenon arc lamp as the excitation source, with excitation wavelength selection provided by a Czerny-Turner f/3.4 grating monochromator. The emitted light was collected at 90^o to the excitation beam and detected by a Hammamatsu R-928 photomultiplier tube (PMT). The PMT was housed in a water-cooled PMT housing

supplied by Products for Research Inc. Emission spectra were corrected for the instrument response and light loss using correction factors supplied by the manufacturer.

2.2.4.2.1. Measurement of Fluorescence Quantum Yield

The fluorescence quantum yields were measured in N_2-saturated solutions using relative actinometry. The emission spectrum of the sample under study was acquired along with the emission spectrum of a standard of known quantum yield (actinometer). The choice of an actinometer depends upon the wavelength region in which the sample under investigation emits. In order to measure the quantum yield accurately, the emission of the actinometer and the sample should be in the same wavelength range and the absorbance should be < 0.2 a.u. at the excitation wavelength in order to minimize the self absorption. One of the widely-used actinometers is a solution of quinine bisulphate (λ_{exc} = 350 nm and Φ_{em} = 0.54) prepared in aqueous 0.10 M H_2SO_4.[14] Relative quantum yields were calculated by using Equation 2.4.

$$\Phi_{em} = \Phi_{std}\left(\frac{A_{std}}{A_{un}}\right)\left(\frac{I_{un}}{I_{std}}\right)\left(\frac{n_{un}}{n_{std}}\right)^2 \qquad [2.4]$$

Where, Φ_{std} is the quantum yield of the standard of known quantum yield, A_{std} and A_{un} are the absorbances of the standard and unknown sample, respectively, at the excitation wavelength; n_{std} and n_{un} are the refractive indices of the solvents for the standard and unknown samples, and I_{un} and I_{std} are the integrated emission intensities of the unknown and standard samples.

2.2.4.3. Time-Resolved Fluorescence

Fluorescence decay measurements were performed by using a PTI LaserStrobe TM-3 fluorescence lifetime spectrofluorometer equipped with an automated emission monochromator and a standard PMT that can detect from 200 to 900 nm. Sample excitation is afforded by PTI's own GL-3300 nitrogen laser coupled to a high-resolution GL-302 dye laser with PTI-302 dye laser module which provides 337.2 nm excitation. Selective wavelength excitations can be achieved by using two identical quartz cells filled with fluorescent dyes. The laser was allowed to pulse at the rate of 10 Hz repetition rate and sent to the compartment containing the sample via a 12-meter long optical fibre cable, where it strikes the sample. Wavelength selection was done with a Czerny-Turner f/3.4 grating monochromator while the laser that triggers the data collection was controlled by using a delay gate generator (DGG). A block diagram of an N_2 dye laser-based time-resolved spectrofluorometer is presented in Figure 2.2.

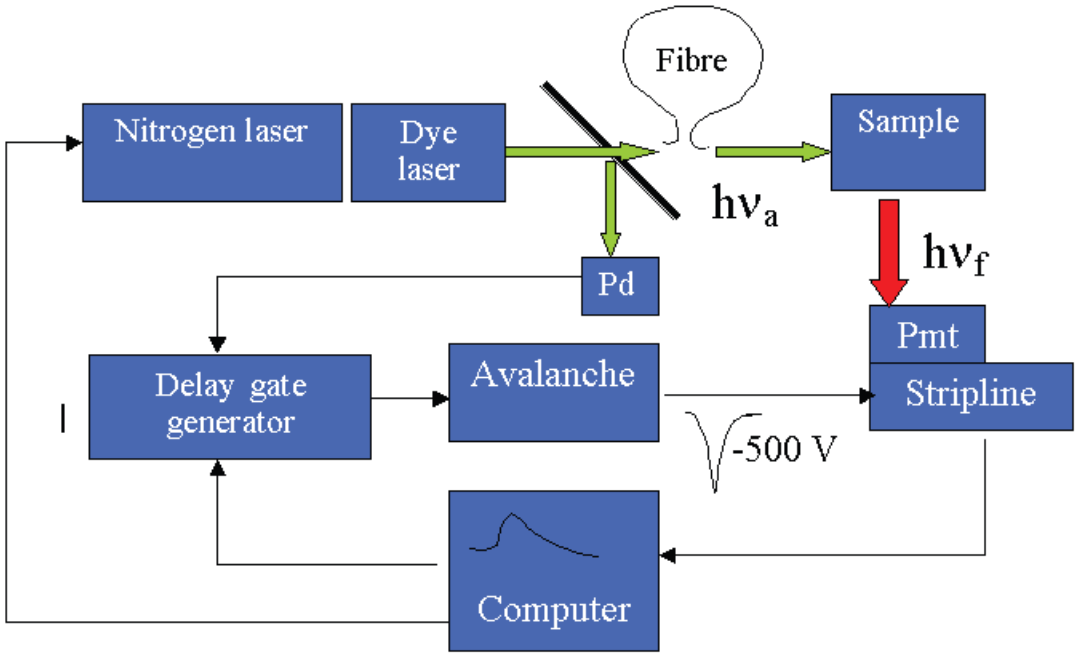

Figure 2.2. A block diagram of an N_2 dye laser-based time-resolved spectrofluorometer, reprinted from Photon Technology International, Inc, copyright © 2013, Birmingham, NJ, United States, All rights reserved.[15]

2.2.4.3.1. Data Acquisition

The LaserStrobe system is based on the stroboscopic technique which utilizes a pulsed N_2 laser which measures fluorescence intensity at different time delays right after the trigger. The fundamental wavelength for the N_2 laser is a 337.2 nm with a pulse width of 450 ± 50 ps. The output of the dye laser goes to a beam splitter where one port of the beam is directed towards a photodiode to initiate the timing of data acquisition. The other part of the beam goes through a 12 m fibre optical delay line. The collection data uses a proprietary stroboscopic technique from PTI.

2.2.4.3.2. Deconvolution of Data

In a typical time-resolved experiment, two curves are acquired, an IRF and a sample decay curve. Analysis is then performed by deconvoluting the IRF with a model function provided in the data processing software. The software provides single exponential, bi-exponential and multiple exponential model functions. A comparison of results with the experimental decay can be done by an iterative numerical procedure until the best agreement with the experimental decay curve is achieved. The time-dependent fitting function is denoted by D(t) and can be considered as time-dependent fluorescence, where the excitation laser pulse is treated as a delta function. In a simple case, D(t) is represented by a single exponential function as per Equation 2.5.

$$D(t) = Ae^{(-\frac{t}{\tau})} \qquad [2.5]$$

Where A is the amplitude of the decay trace and τ is the lifetime acquired at time t. In any pulsed excitation fluorescence lifetime instrument, the finite width of the excitation pulse will distort the free decay of fluorescence as described by D(t). This distortion is known as convolution, which can be expressed as Equation 2.6.

$$F(t) = \int_0^t R\,(t - t')\,D(t')dt' \qquad [2.6]$$

where R(t) is the IRF and F (t) is the experimentally-determined decay intensity at time t. To extract meaningful kinetic data, the IRF R(t) must be recorded as described above. The decay F(t) is then used to extract the lifetime of D(t) by employing a Marquardt algorithm for iterative deconvolution. The calculated values are optimized by

minimizing the weighted sum of the squares of deviations of the calculated points, $I(i)_{calc}$, from the experimental ones, $I(i)_{exp}$, according to Equation 2.7, for all i channels of data, the reduced chi-square (χ^2), is minimized.[15]

$$\chi^2 = \frac{1}{N-n-1}\sum_1^N \frac{(I(i)_{calc}-I(i)_{exp})^2}{s(i)^2} \qquad [2.7]$$

where N is the number of data channels, n is the number of fitting parameters, s is the standard deviation, $I(i)_{calc}$ is the weighted sum of the squares of deviations of the calculated points and $I(i)_{exp}$ is the weighted sum of the squares of deviations of the experimental points for all i channels of data.

2.2.5. Transient Absorption Spectroscopy

2.2.5.1. Introduction

Many of the elementary processes in nature proceed very rapidly. The detection of these rapid processes was made possible when Porter and Norrish developed flash photolysis in 1949.[16, 17] Time-resolved spectroscopy (TRS), widely known as flash photolysis or pump-probe spectroscopy, offers a new twist to standard spectroscopic techniques. Furthermore, it is a powerful tool to observe transient species such as radicals, electron transfer, ions, ion-pair and even back electron-transfer in chemical and biological systems.[17]

2.2.5.2. Experimental Set-up

Transient absorbance measurements were performed using an Applied Photophysics LKS80 laser flash photolysis spectrometer, The excitation light used was the third harmonic (355 nm) of a neodymium-doped yttrium aluminum garnet (Nd:YAG) laser (Quantel, Brilliant ω) with a duration of 5-8 ns, repetition rate of 20 Hz. The intensity of the pump light was 9.5 mJ/cm^2 and the excitation beam was 90° with respect to the monitoring beam. The probe beam utilized a Ushio 150 W pulsed Xe arc lamp; detection was obtained by using an f/3.4 variable slit-width Czerny-Turner f/3.4 grating monochromator and a five-stage Homamatsu R-928 PMT. The most common excitation wavelength used was 355 nm; however a 532 nm excitation wavelength can be achieved by using non-linear optical crystals.

2.2.5.3. Data Acquisition

In time-resolved laser spectroscopy, a laser is used to populate the excited-state, and radiation from a strongly emitting lamp is used to probe the relaxation of the ensuing exited-state species. The sample is excited by a laser pulse and the changes it induces in the sample are probed by the lamp, which is suitably delayed with respect to the excitation source.

In a typical experiment, light strikes the sample under investigation and transient spectra can be recorded. The observations can be assigned to a variety of processes, such as electron transfer,[18] proton transfer,[19] solvated electrons,[20] formation of radicals,[16, 17] triplet states and many other remarkable processes.[16] Furthermore, it is very

important to keep the sample degassed (O_2 free) for experiments because O_2 quenches the triplet state to a great extent and weaker absorbing triplet species could be very difficult to resolve from laser shot noise. To circumvent this problem the samples were degassed by purging with N_2 for 15-20 minutes.

In the nanosecond transient absorption spectrometer, the output from a pulsed laser is directed onto a sample cuvette at right angles or co-linear with an analysing beam (probing light from Xe lamp). The optical system is equipped with aperture stops to maximise collection of analysing light and minimize the stray light.[21] After the sample is excited, it is probed by the Xe lamp pulse and gets directed to a Czerny-Turner, f/3.4 monochromator through adjustable apertures located in the sample holder compartment. After the analysing light passes through the monochromator, it gets directed to the PMT. The current from the PMT is then transferred to an Agilent Infinium 54830B 600 MHz digitalizing oscilloscope and conversion of signals to absorption data takes place. The data was then exported into programs such as Origin 8.0 (Origin Lab Corporation). Ground-state absorption and emission spectra were recorded regularly to check the photo-stability of the sample after ~50 laser shots.

2.2.6. Global Kinetic Analysis

The systematic study of a series of emission, electronic or transient absorption spectra is an integral part of many chemical and biological analyses. Single value decomposition (SVD) offers a very reliable and efficient tool to analyze multi-

wavelength data. It has the ability to extract predicted spectra of unknown intermediates and provides more reliable parameter estimates than single-wavelength fits alone. In addition, it has the ability to constrain fits with known molar absorptivity spectra.

2.2.6.1. Theoretical Background

All the spectral data analyses in this thesis were performed using the SPECFIT/32 program. The SPECFIT program was developed by Binstead[22] and is based on an algorithm written by Maeder and Zuberbuhler.[23-27] It can be viewed as an efficient and quite reliable tool to satisfy many of the above-mentioned criteria. The number of contributing species to spectral variations, equilibrium constants and the rate constants for chemical reactions can be extracted by SVD methodology with minimum error. Systematic analysis of such information can lead to a full understanding of the underlying mechanisms and the corresponding equilibrium constants.[28]

The Beer-Lambert law shows that the absorbance of a solution at a particular wavelength and time t, is the sum of all contributing species. In addition, the contribution of each species depends upon the pathlength and concentration. If all the spectra are arranged in a two-dimensional matrix denoted by Y, containing the number of spectra in rows denoted by M, and the measured wavelengths denoted by W in columns, matrix Y can be represented as Equation 2.8:

$$Y = M \times W \qquad [2.8]$$

Matrix Y can be decomposed into concentration (C), molar absorptivity (A) and a residual (R), as shown in Equation 2.9,

$$Y = C \times A \times R \qquad [2.9]$$

where, $C = (M \times N)$ and N is the number of absorbing components and; $A = (W \times N)$. Due to the presence of instrumental noise, Y can't be represented precisely, so a residual, R, needs to be taken into consideration as well, as shown in Equation 2.10

$$R = CA - Y \qquad [2.10]$$

Factor analysis can be performed to extract the number of contributing species. With factor analysis, the total number of data points can be fitted. $Y = M \times W$ can be replaced by $Y = M \times N$ and non-linear least square fitting can be performed. The single value decomposition matrix Y can be decomposed into three separate matrices namely V, U and S (Equation 2.11)

$$Y = USV \qquad [2.11]$$

The matrices comprise the following properties: $U(M \times N)$; created by significant eigen vectors of YY^t and $V(N \times W)$ created by Y^tY columns, where U and V are orthonormal (linearly dependent) sets of vectors. U is an evolutionary or wavelength eigen vector, V is a spectral eigen vector and matrix S is; $S(N \times N)$ hence S is a set of singular (weighting) vectors.

However the number of M is much higher than N so replacing Y by SVD in Equation 2.10, we get the following (Equation 2.12).

$$R = CA - USV \qquad [2.12]$$

Multiplying Equation 2.12 by transpose of V,V^t we get Equations 2.13 and 2.14

$$RV^t = CAV^t - US \qquad [2.13]$$

$$R' = CA' - Y' \qquad [2.14]$$

Comparison of Equation 2.13 with Equation 2.14 shows that there is a significant reduction in the size of elements Y, A and R from W and N.

Depending upon the number of spectra, SVD determines the number of eigen vectors which belong to U (evolutionary), V (spectral) and product of U and S $(U \times S)$ (temporal) properties. SVD reveals number of vectors equal to the number of spectra or abscissa points in the original data set. Out of all the vectors, arise from the lamp, instrumental noise or non-random instrument response. With each eigen vector, the eigen value drops and almost reaches to instrumental noise. Depending upon the noise level, vectors can be discarded without analysis and only significant vectors having no or little noise are considered without loss of any valuable information.[29, 30] To further discern the significant and non-significant eigen vectors, they can be plotted separately and the noise level can be observed more clearly. One can then use the significant eigen vectors to reconstruct the data by using Equation 2.15.

$$Y = USV^t \qquad [2.15]$$

Sometimes due to non-random instrumental noise, insignificant eigen vectors appear to be significant and can only be eliminated by observation of other supportive information

such as the number of colored species involved and the number of dominating species and Levenberg- Marquardt fitting obtained as a result of SVD. Analysis of individual U, V and $U \times S$ plots also helps in eliminating insignificant eigen vectors which appear as colored species.

2.2.6.2. Fitting Methodology

The SPECFIT program employs a singular value decomposition (SVD) method to get the orthonormal sets of U and V vectors. The program also rectifies the values of initial parameters by the Levenberg- Marquardt algorithm and hence minimizes the least square residuals.

The fitting was done by taking account of structural and chemical properties of the chemical system under investigation. After careful analysis of the spectroscopic data, a user-defined value was provided to set the fitting model. The value may or may not comply with the stoichiometry of the binding motif.

It was assumed that all the species except $[M_0L_1]$ (M = host and L = guest) were colored (absorbing). User-defined values for association constants (log β_{xy}) need to be given arbitrarily according to the system properties. After running the global fit, specfit gives the relevant global spectra, Levenberg-Marquardt fitting, colorful species, U, $U \times S$ and V vectors, correlation matrix, and a stability constant with estimated errors to define whether the given indices and β_{xy} comply with binding motif or not. Each spectrum yields an eigenvector as a result of SVD, which then further can be plotted separately to see the colored species involved. The useful eigenvectors are only those

which belong to the colored species, while the rest of them appears as noise and does verifies whether the given model was appropriate or not. Moreover, the reckoned values of initial parameters are rectified by Levenberg - Marquardt algorithm and hence minimize the least square residuals between the 3D data and the model system. The colored species extracted by SVD procedure arise from numerical integration of a user-defined differential rate equation and as a result, simulated values of equilibrium or rate constants are obtained.

The main advantages of SPECFIT methodology and multi-wavelength data analysis include the extraction of colored species involved in the binding event, the deconvolution of unknown dominating species, their extinction coefficients and corresponding spectra. The analysis also yields the non-linear fitting of single wavelength data using Levenberg – Marquardt least square fitting analysis. Furthermore, it validates the number of steps involved in the binding equilibrium. In summary, SPECFIT provides information on several contributing factors in one analysis.

References

[1] Chen, P.; Danielson, E.; Meyer, T. J., J. Phys. Chem., (1988) 92, 3708.

[2] Chen, P. Y.; Curry, M.; Meyer, T. J., Inorg. Chem., (1989) 28, 2271.

[3] Stewart, D. J.; Brennaman, M. K.; Bettis, S. E.; Wang, L.; Binstead, R. A.; Papanikolas, J. M.; Meyer, T. J., J. Phys. Chem. Lett., (2011) 2, 1844.

[4] Strouse, G. F.; Schoonover, J. R.; Duesing, R.; Meyer, T. J., Inorg. Chem., (1995) 34, 2725.

[5] Tapolsky, G.; Duesing, R.; Meyer, T. J., Inorg. Chem., (1990) 29, 2285.

[6] Tapolsky, G.; Duesing, R.; Meyer, T. J., J. Phys. Chem., (1991) 95, 1105.

[7] Worl, L. A.; Duesing, R.; Chen, P.; Della Ciana, L.; Meyer, T. J., J. Chem. Soc., Dalton Trans.: Inorg. Chem. (1972-1999), (1991), 849.

[8] Lin, R.; Fu, Y.; Brock, C. P.; Guarr, T. F., Inorg. Chem., (1992) 31, 4346.

[9] Kleverlaan, C. J.; Stufkens, D. J.; Clark, I. P.; George, M. W.; Turner, J. J.; Martino, D. M.; van, W. H.; Vlcek, A., Jr., J. Am. Chem. Soc.., (1998) 120, 10871.

[10] Liard, D. J.; Vlcek, A., Inorg. Chem., (2000) 39, 485.

[11] Jones, W. E.; Chen, P.; Meyer, T. J., J. Am. Chem. Soc., (1992) 114, 387.

[12] Sullivan, B. P.; Meyer, T. J., J. Chem. Soc., Chem. Comm., (1984), 403.

[13] Origin Lab Corporation, 8.0 Northampton, MA, 01060, USA, (2008).

[14] Melhuish, W. H., J. Phys. Chem., (1961) 65, 229.

[15] http://www.pti-nj.com/products/Fluorescence-Lifetime-Spectrofluorometers/LaserStrobe/LaserStrobe.html, Photon technology international, USA, In.

[16] Norrish, R. G. W.; Porter, G., Nature, (1949) 164, 658.

[17] Porter, G., Farad. Discuss. , (1950) 9, 60.

[18] Barbara, P. F.; Meyer, T. J.; Ratner, M. A., J. Phys. Chem., (1996) 100, 13148.

[19] Tolbert, L. M.; Solntsev, K. M., Acc. Chem. Res., (2001) 35, 19.

[20] Ottolenghi, J. J. M.; Stein, G., J. Am. Chem. Soc., (1963) 85, 2712.

[21] Operating Manual, Applied photophysics,

[22] Stultz, L. K.; Binstead, R. A.; Reynolds, M. S.; Meyer, T. J., J. Am. Chem. Soc., (1995) 117, 2520.

[23] Gampp, H.; Maeder, M.; Meyer, C. J.; Zuberbuhler, A. D., Talanta, (1985) 32, 95.

[24] Gampp, H.; Maeder, M.; Meyer, C. J.; Zuberbuhler, A. D., Talanta, (1985) 32, 257.

[25] Gampp, H.; Maeder, M.; Meyer, C. J.; Zuberbuhler, A. D., Talanta, (1985) 32, 1133.

[26] Gampp, H.; Maeder, M.; Meyer, C. J.; Zuberbuhler, A. D., Talanta, (1986) 33, 943.

[27] Maeder, M.; Zuberbuhler, A. D., Anal. Chem., (1990) 62, 2220.

[28] http://www.hi-techsci.com/products/specfitglobalanalysis/,

[29] Binstead, R. A.; Stultz, L. K.; Meyer, T. J., Inorg. Chem., (1995) 34, 546.

[30] Lebeau, E. L.; Binstead, R. A.; Meyer, T. J., Abstracts of Papers of the American Chemical Society, (1995) 209, 244.

Chapter – 3

Photophysics of Strained Pyrenophanes

The effect of torsional strain and bent angle on the photophysical properties of three inherently chiral pyrenophanes was studied, using Franck-Condon band-shape analysis and the emission spectral fitting procedures.

3.1. Introduction

Pyrene is a polycyclic aromatic hydrocarbon (PAH) with conjugated double bonds. Owing to its attractive ground-and excited-state properties, pyrene and its derivatives have been extensively studied.[1] Accordingly, several reviews have been published on the synthetic, photophysical, and electrochemical attributes of pyrene.[1, 2] Figure 3.1 shows the structure of pyrene.

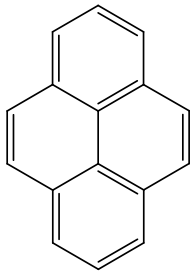

Figure 3.1. The structure of pyrene

For a long time, pyrene was used in the synthetic dye industry.[3] The first milestone in the photochemistry of pyrene was achieved in 1954, when Förster and Kesper found excimer emission from a pyrene solution.[4] Since then, pyrene chemistry has been an area of extensive theoretical and experimental research.[1, 2] More specifically, this is because pyrene exhibits a set of very significant electrochemical and photophysical properties that can be exploited in a variety of areas, and has widespread utility such as: fluorescence labelling of oligonucleotides for DNA assays;[5, 6] carbon nanotube functionalization;[7] study of proteins;[8, 9] chemosensors to detect organic compounds,[10] metals,[11, 12] explosives[13] and gases.[14] As well, the excimer emission of pyrene is very frequently used in the sensing of physical quantities such as pH,[15] temperature,[16] and pressure.[17] The sensing or recognition properties are observed as a change in the pyrene fluorescence.

3.1.1. Pyrene Derivatives

Pyrene is characterized by having a well-resolved UV-Vis band at 310 – 340 nm and fluorescence between 360 – 380 nm.[18] The electronic structure of pyrene can be fine tuned by derivatizing it with various substituents, which is observed as a change in its optical properties. Depending on the substituent, i.e. electron-withdrawing or electron- donating, the optical properties of the resulting molecule may be exploited in applications such as organic light-emitting diodes (OLED) and organic photovoltic devices.[19] Therefore, the existence of extended conjugation in pyrene also brings a limitation that some highly π – extended, pyrene-based molecules form π – aggregates in solution at high concentrations (~0.01 M). Although this results in an extra feature in the

emission and absorption spectra and makes data interpretation complicated, this problem can be circumvented through the addition of aliphatic chains to the pyrene ring.[18]

The photophysics of pyrene and its derivatives has been studied extensively.[1, 2] At this juncture, it is useful to review the factors that govern the photophysical properties of pyrene. Figure 3.2 provides the structure of a pyrene molecule with the associated vertical and horizontal transitions.

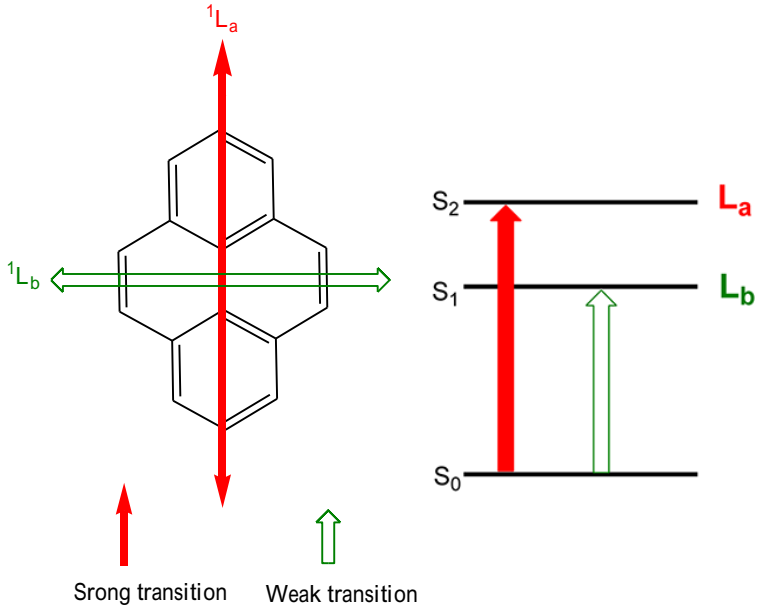

Figure 3.2. The orientation of the associated transitions in pyrene. Reprinted in part with permission from Lambert, C.; Ehbets, J.; Rausch, D.; Steeger, M. J. Org. Chem. 2012, 77, 6147.[20]

Pyrene is a highly-symmetrical molecule with D_2h symmetry, and the electronic spectrum of pyrene is dominated by four singlet-singlet transitions. These transitions produce four well-defined vibrational progressions with constant spacings, while the absorption and emission spectra are revealing of the complexity of the electronic structure. Transitions which are formally disallowed, gain intensity when a suitable solution of pyrene is placed in a magnetic field.[21] Using the nomenclature developed by Platt, these transitions can be assigned as follows: [22] the y-axis-polarized weak transition at 370 nm as ^1L_b ($S_0 \rightarrow S_1$); the z-axis-polarized strong transition at 333 nm is assigned as ^1L_a ($S_0 \rightarrow S_2$); a strong y-axis-polarized transition at 270 nm as ^1B_b ($S_0 \rightarrow$

S_{10}); and, finally, a very strong z-polarized transition at 243 nm as ^1B_a ($S_0 \rightarrow S_7$).[21, 23-25] Figure 3.3 provides an energy-level diagram for pyrene and its respective spectral assignments. In addition to the above-mentioned bands, several other transitions exist which do not appear because they are symmetry-forbidden.[24, 26]

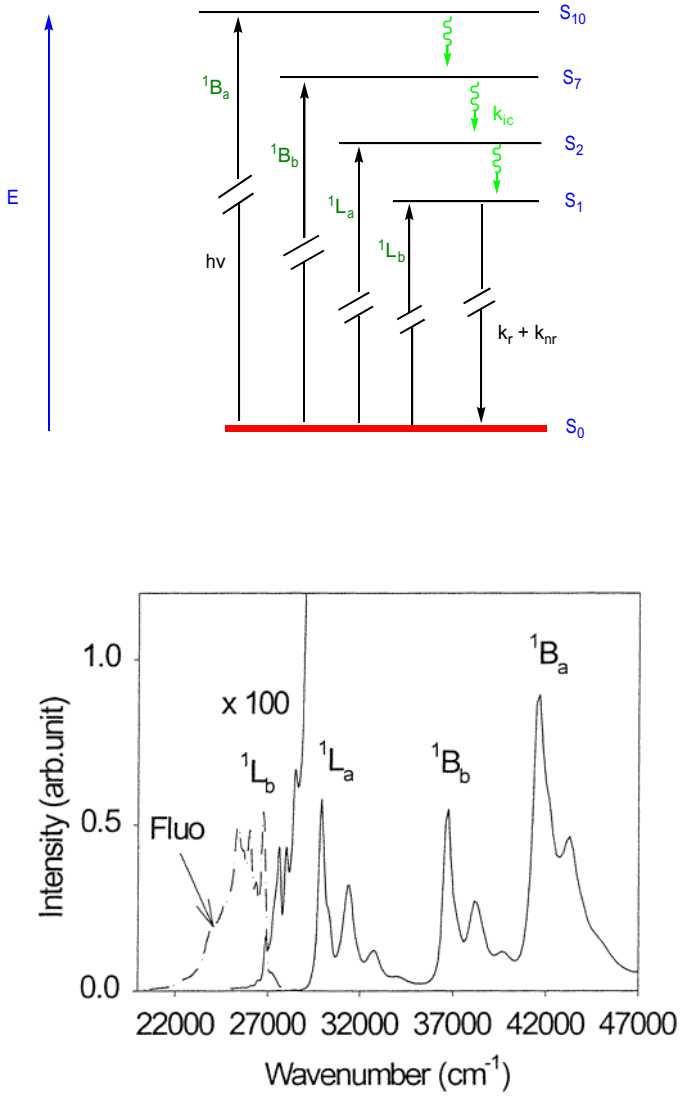

Figure 3.3. A schematic illustration of the origin of various transitions in pyrene, using an energy level diagram (top) and the assignments of the transitions in an electronic spectrum of pyrene (bottom) acquired in n-hexane. Reproduced in part with permission from Tran-Thi, T. H.; Prayer, C.; Millié, P.; Uznanski, P.; Hynes, J. T. J. Phys. Chem. A 2002, 106, 2244.[24]

The assignments of the absorption bands in the absorption spectrum of pyrene reported by Thulstrup and Hynes are described as follows.[24, 26, 27] The direction of the

transition dipole of ^1L_a is parallel to ^1B_a and roughly orthogonal to the ^1B_b state; since the ^1L_a state is orthogonal to ^1L_b, this transition remains hidden in the strong ^1L_a transition. If the ^1L_b state has a change in the dipole moment, however, it can bring a substantial change to the spectral properties of pyrene-based molecules.[24, 28] The ^1L_b transition is weak, furthermore, the transition moment of B_{2u} possesses the opposite sign and cancels their resulting transition moments consequently making the overall transition moment of ^1L_b negligible. Nonetheless, due to a vibrational mixing between the ^1L_a and ^1L_b transitions, ^1L_b gains intensity from the ^1L_a state and appears as a weak transition in the form of vibronic structures, in optical and fluorescence spectra.[26] Because the $^1L_b \rightarrow S_0$ transition is disallowed, the excited-state lifetime of pyrene is long-lived, i.e. 430 ns.[24]

3.1.2. Excimers

Supramolecular interactions are ubiquitous in biological systems, bio-inspired materials, and novel-synthetic constructs.[29-31] Aromatic interactions via π-π stacking are an integral part of supramolecular interactions, as well especially in highly conjugated materials.[32] Sanders has presented a detailed theory on the nature of π-π interactions.[33] According to Sanders' theory, π-π interactions are actually the result of σ-π interactions that overcome the repulsions due to π-π interactions. Nevertheless, depending on the size of a molecule and the extent of conjugation, the propensity of forming supramolecular assemblies via π-π interactions varies. The identification of such interactions, moreover, will expand our ability to rationally design and construct a system having desirable electronic and optical properties. Of course, pyrene is well-known for its aggregation

behaviour and the resulting properties. Figure 3.4 provides the emission spectra of a growing pyrene excimer.

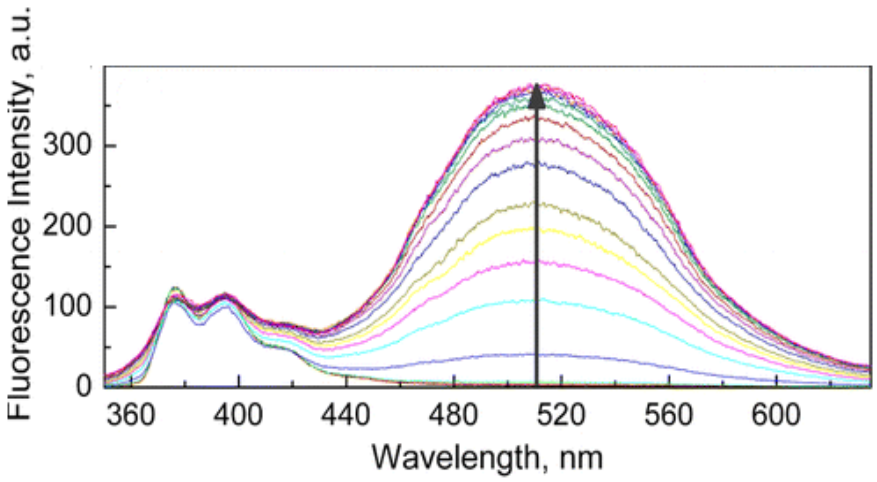

Figure 3.4. Fluorescence spectra of a growing pyrene excimer emission due to formation of pyrene aggregates upon increasing the concentration of glucose. Reprinted with permission from Huang, Y.-J.; Ouyang, W.-J.; Wu, X.; Li, Z.; Fossey, J. S.; James, T. D.; Jiang, Y.-B. J. Am. Chem. Soc. 2013, 135, 1700.[34]

Aggregation is not always a disadvantage in pyrene photochemistry, however, the photophysical properties of pyrene change dramatically upon aggregation. Moreover, excimer emission involves the formation of an adduct between an excited pyrene (Pyr^*) and a ground-state pyrene (Pyr), a dimer which forms an association in the electronic excited-state and dissociates in the ground-state.[2] The excimer emission band arises when two pyrene rings are ~4 Å (in pyrene crystal) from each other.[2] At this distance, the overlap integral between key orbital pairs are aligned in the most symmetric fashion.[35]

The electronic stabilization of the pyrene excimer is ca. $\Delta H^0 \sim -10\ \text{kcal mol}^{-1}$ while the entropy of formation is ca. $\Delta S^0 = -20$ eu and $-T\Delta S^0 = 6\ \text{kcal mol}^{-1}$ at 298 K.[35] This indicates that, at room temperature, the formation of a pyrene excimer is favourable by $\Delta G^0 \sim -4\ \text{kcal mol}^{-1}$. Hence, the band increases in intensity as the concentration of pyrene is increased. Figure 3.5 shows potential energy surface diagrams for the formation of a pyrene excimer in two scenarios: one in which a ground-state adduct forms and secondly when association occurs only in the excited-state.

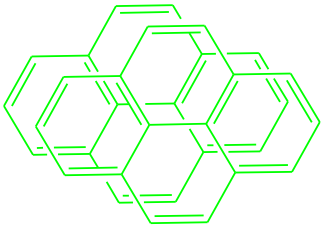

Offsetting interaction

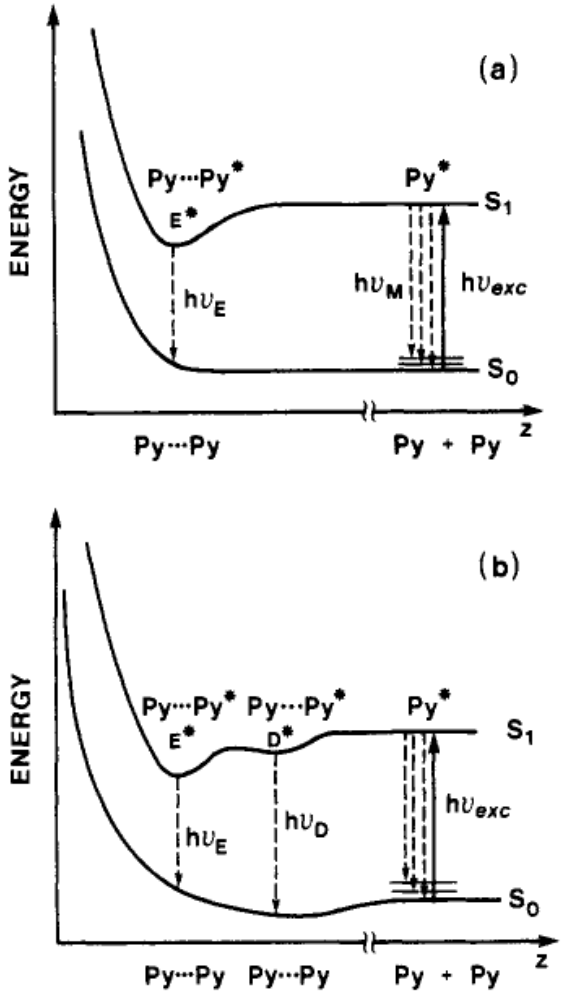

Figure 3.5. Schematic illustration of pyrene excimer formation using potential energy surface diagrams. (a) Formation of an excimer in the absence of a ground-state adduct (b) formation of an excimer in the presence of a ground-state adduct. In the figure, E* is a dynamic excimer, D^* is a dimer in first excited singlet state, $h\nu_E$ is the excimer fluorescence, $h\nu_D$ is the excited dimer fluorescence and $h\nu_M$ is the monomer fluorescence.[2] Reprinted in part with permission from Winnik, F. M. Chem. Rev. 1993, 93, 587.

The pyrene excimer equilibrium is of a dynamic nature, e.g. when a cyclohexane solution of pyrene (~1.0 mM) is excited for a very short time (~1 ns) using time-resolved emission spectroscopy, only monomer emission is attenuated.[36] If the same solution however is excited using a prolonged pulse of light (~20 ns), the monomer emission decreases and excimer emission is observed: this indicates that the diffusion of excited monomer towards a ground-state pyrene adduct is required for an excimer to form. After a prolonged length of time (~20 ns), sufficient diffusion occurs such as both monomer and excimer are present in equal concentrations. If the sample is excited for hundreds of nanoseconds, then, the excimer emission can be seen even in steady-state fluorescence spectra in which both monomer and excimer stay in a dynamic equilibrium or in a photo-stationary state, as shown in Equation 3.1.

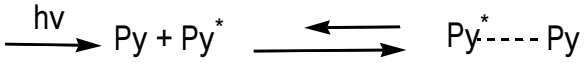

[3.1]

3.1.3. Non-Planar Aromatics

The chemistry of non-planar PAHs is a widely-documented discipline, in particular for cyclophanes. Cyclophanes consist of an aromatic unit (pyrene in the case of a pyrenophane) and an aliphatic chain that forms a bridge between two non-adjacent positions of an aromatic ring. Since the 1970s, cyclophanes have been an active area of investigation.[37, 38] Moreover, cyclophanes exhibit interesting spectral, chemical, and electrochemical properties. The emergence of single-wall nano-tube (SWNT) and

fullerene chemistry, and their homology to non-planar aromatics evoke the need to study small non-planar aromatics in detail.

It was reported that tethering the adjacent sides of pyrene and creating a curvature in an aromatic molecule does not perturb the aromatic character, i.e. does not attenuate the magnetic anisotropy effect (direction dependence of a material's magnetic properties).[39-41] As well, it is also documented that the magnetic anisotropy is only slightly perturbed upon increasing the bend angle from 0° to 109.2°.[42] The term aromatic is used by chemists in a rather different way thatn its noramally applied, however in simple terms, aromaticity is an extra stability achived by a molecule due to delocalization of electrons. Accordingly, the pyrene-based cyclophanes (pyrenophanes) containing non-planar pyrene moieties shown in Figure 3.6 were synthesized and reported by Aprahamian et al.[43] The molecules were reduced with lithium metal to observe the effect of non-planarity in a two-electron reduction process whose progress was monitored by NMR spectroscopy.

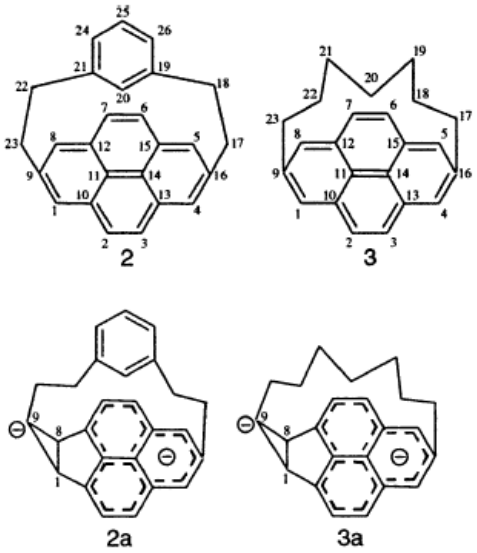

Figure 3.6. The strained pyrenophanes examined by Aprahamian et al. Molecules 2 and 3 are pyrenophanes before reduction, and 2a and 3a are new pyrenophanes formed after reduction. Reprinted with permission from Aprahamian, I.; Bodwell, G. J.; Fleming, J. J.; Manning, G. P.; Mannion, M. R.; Sheradsky, T.; Vermeij, R. J.; Rabinovitz, M. J. Am. Chem. Soc. 2003, 125, 1720.[43]

Initial NMR observations suggested a possible change in the symmetry of the molecules. Detailed examination using 2-D NMR spectroscopy reveals that the reduction should produce anti-aromatic species. According to Breslow, if a cyclic conjugated system has π-electron energy higher than that of a suitable reference compound which is not cyclically delocalized it is considered as antiaromatic.[44] Nevertheless, when compound 2 is subjected to two-electron reduction and transforms into 2a (Figure 3.6), it undergoes an intramolecular cyclization reaction which forms a new σ – bond between carbon C1 and C8, and the new system avoids forming an unfavourable strained anti-aromatic analogue by keeping the two charges separate. In an extension of this study, Aprahamian

et al. prepared a series of pyrenophane analogues with varying tether length in order to control the strain and non-planarity (Figure 3.7).[45]

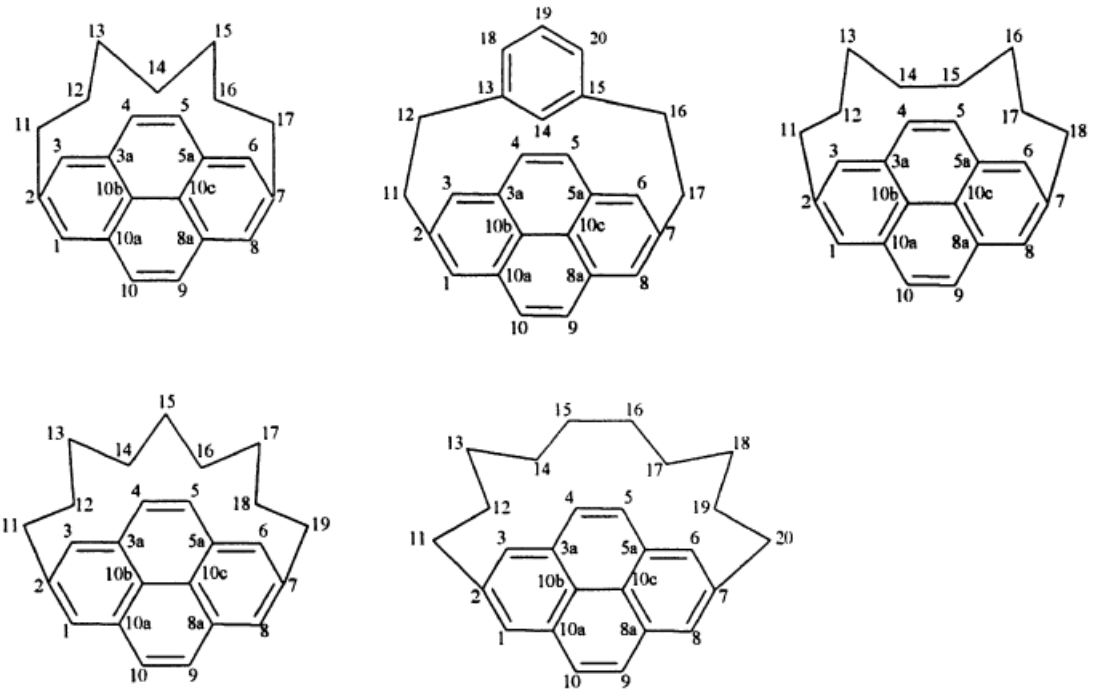

Figure 3.7. The series of pyrenophanes studied and reported by Aprahamian et al., where a systematic variation in the tether length was made in order to analyze the effect of tether length on the reduction process of pyrenophane. Reprinted with permission from Aprahamian, I.; Bodwell, G. J.; Fleming, J. J.; Manning, G. P.; Mannion, M. R.; Merner, B. L.; Sheradsky, T.; Vermeij, R. J.; Rabinovitz, M. J. Am. Chem. Soc. 2004, 126, 6765.[45]

The main goal of this study was to understand the effect of strain on the reduction process using different pyrenophanes, which was again monitored using NMR spectroscopy. It was observed, that all the pyrenophanes in the series undergo dimerization via one-electron reduction. Following dimerization, depending upon the tether length, these pyrenophanes undergo chemical deformations such as bond cleavage with the formation of anti-aromatic anions. Nevertheless, no indication of a two-electron reduction process was observed in the reaction when the tether length exceeded eight carbons (Figure 3.7).[45]

A series of bent pyrenophanes have been synthesized and their bend angles (θ) have been reported.[41, 46, 47] The bend angle is defined as the angle formed by two terminal planes of the atoms in the pyrene system. Figure 3.8 lists the pyrenophanes with their bend angles. Indeed, a combination of computational and experimental studies suggests that the bend angle of the pyrene moiety depends upon the number and position of substituents. For example, when benzylic groups were absent from the tether or bridge the bend angle remained enlarged and, in the presence of benzylic moiety, the bend angle was compressed. As shown in Figure 3.8, the bend angle was also enlarged when a hetroatom was present in the tether. However, the study was primarily focused on the systhesis of strained pyrenophaes and a discussion leading to this selective bending behaviour was not provided.

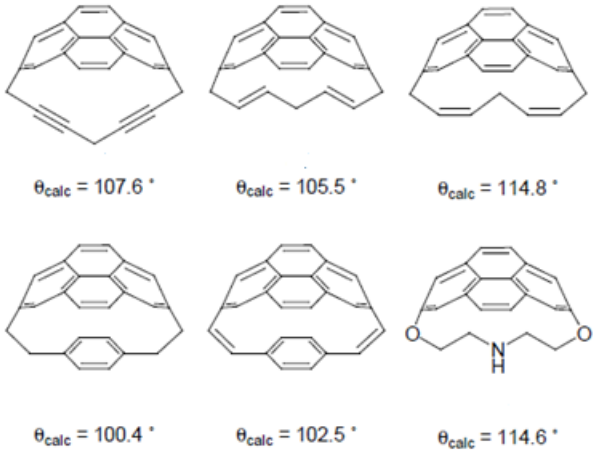

Figure 3.8. Pyrenophanes and their bend angles reported by Bodwell et al. Reprinted with permission from Bodwell, G. J.; Fleming, J. J.; Miller, D. O. Tetrahedron 2001, 57, 3577. Copyright Elsevier Ltd. 2001, all rights reserved.[46]

Similarly, Merner et al. recently reported a bent pyrenophane similar to a segment of a single wall nanotube (SWNT) (Figure 3.9).[47]

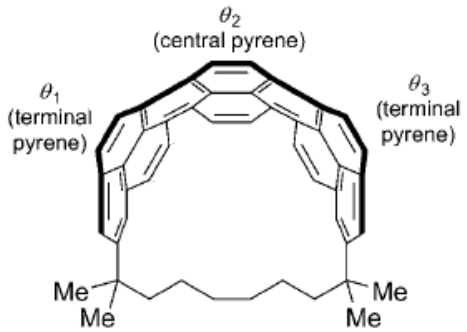

Figure 3.9. The half-segment of an aromatic belt consisting of a severely bent fused pyrene molecule, as reported by Merner et al. Reprinted from Merner, B. L.; Dawe, L. N.; Bodwell, G. J. Angew. Chem. Int. Ed. 2009, 48, 5487. Copyright 2009 © John Wiley & Sons, Inc. All Rights Reserved.[47]

The two terminal pyrene units in the half-aromatic belt were bent by angles of θ_1 and θ_3 = 67.5 – 60.4°, while the central pyrene unit was bent by an angle of θ_2 = 92.8 – 95.9°. Furthermore, the spectral properties were also analyzed briefly, where highly structured bands were observed with a very small Stokes shift.[47] Hence, a systematic analysis of the bend angle, deformity and non-planarity is particularly illustrative to study.

3.2. Objectives and Methodology

A detailed and systematic study on the photophysical properties of bent pyrenophanes has not been reported yet. In the present chapter the following issues have been addressed:

1. What is the overall effect of variation in tether length on the photophysical properties of three C_2-symmetric pyrenophanes (Figure 3.10).
2. Investigation of the effect of bend angle on the photophysical properties of these pyrenophanes i.e effect of bend angle on the vertical ^1L_a and horizontal ^1L_b transitions.
3. What is the nature of the excited-state, and what are the main factors which govern the excited-state properties?
4. How do the photophysical properties of the bent pyrenophanes differ from pyrene itself?

In order to address the above-mentioned issues, Franck-Condon band shape analysis and emission spectral fitting procedures were employed to extract detailed quantitative

understanding of structural, vibronic and electronic parameters. The study also tested the applicability of the one-mode spectral fitting procedure.

3.3. Results

Three C_2-symmetric, chiral pyrenophane molecules of varying tether length were synthesized by Prof. Graham Bodwell's group (Department of Chemistry, Memorial University) and the structures of these molecules are shown in Figure 3.10.[48]

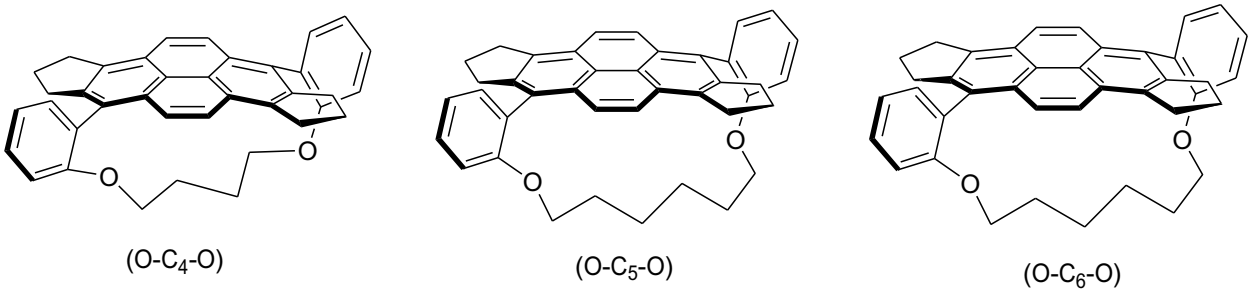

Figure 3.10. Structures and abbreviations of the three symmetric pyrenophanes of varying tether length studied in this chapter.[48]

3.3.1. Electronic Spectra

Based on the linearity of the Beer's law plots (e.g. Figure 3.11), it can be considered that aggregation does not occur in the (O-C_n-O) (n = 4, 5, 6) pyrenophane series below concentrations of 60 μM.

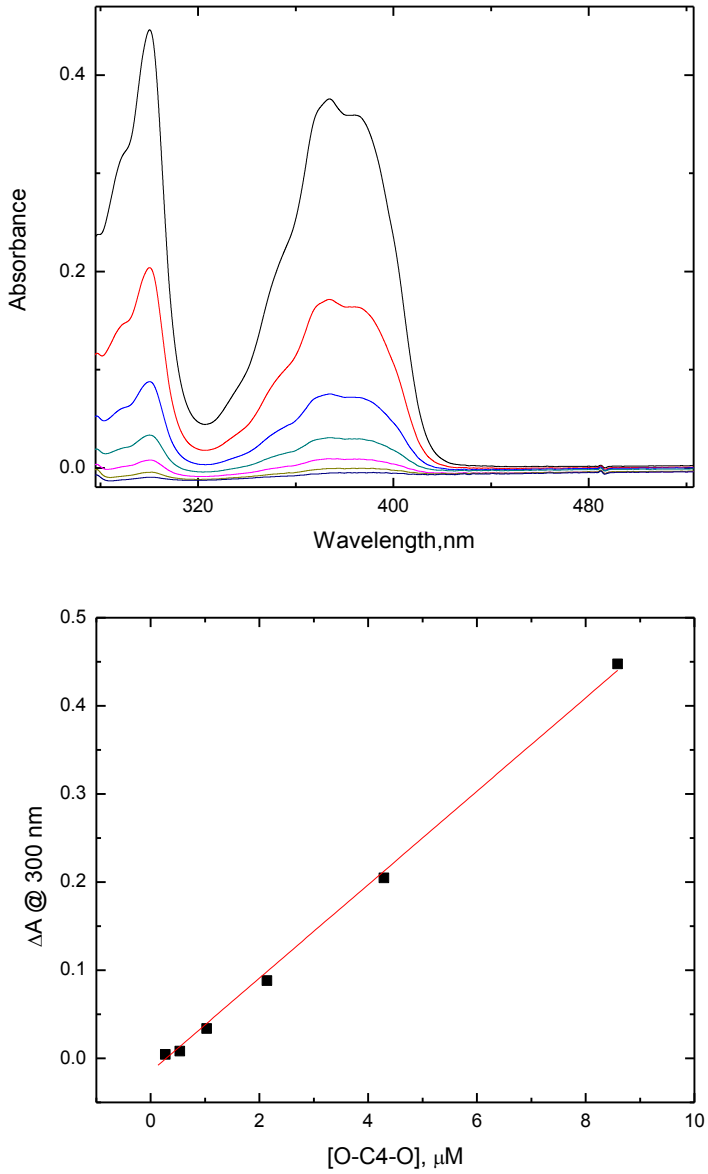

Figure 3.11. (a) Absorption spectral data obtained as a function of [O-C_4-O] in $CHCl_3$ at 298 ± 3 K. (b) Beer's law plot of the absorbance at λ = 300 nm as a function [O-C_4-O]. The red line is the result of a linear least-squares analysis of the data, yielding a slope of 5.3 (± 0.1)× 10^4 M^{-1} cm^{-1} with an intercept = -0.01 (± 0.1), R^2 = 0.995.

In Figure 3.12, the normalized absorption and emission spectra of the (O-C_n-O) compounds are shown. The absorption spectra of the (O-C_n-O) compounds show considerable complexity in the low-energy absorption manifold, and consist of characteristic pyrene-based transitions between 270 to 320 nm.[48] For (O-C_4-O), the absorption band at 300 nm is red-shifted by 5 nm (337 cm^{-1}) as compared to the other two pyrenophanes. For pyrenophanes n = 5, 6 the high energy absorption manifold (270 to 320 nm) was found to be similar to that of pyrene itself indicating the similarity of these two pyrene moieties with the planar pyrene. Low-energy shoulders for (O-C_5-O) and (O-C_6-O) at ca. 395 nm (25320 cm^{-1}) and 392 nm (25510 cm^{-1}), respectively, are apparent in the absorption spectra. On the other hand, the absorption band at 385 nm (25980 cm^{-1}) in (O-C_4-O) is barely resolved and the absorption manifold was found to be more structured than for the other two pyrenophanes in the series. The origin of these bands is due to several overlapping transitions and their vibronic progressions.

Table 3.1 lists details of the photophysical properties for the (O-C_n-O) pyrenophane series. The values of k_r and k_{nr} were calculated as described in Section 1.3 and the fluorescence lifetimes (τ) were acquired according to the procedure described in Section 2.2.4.3.

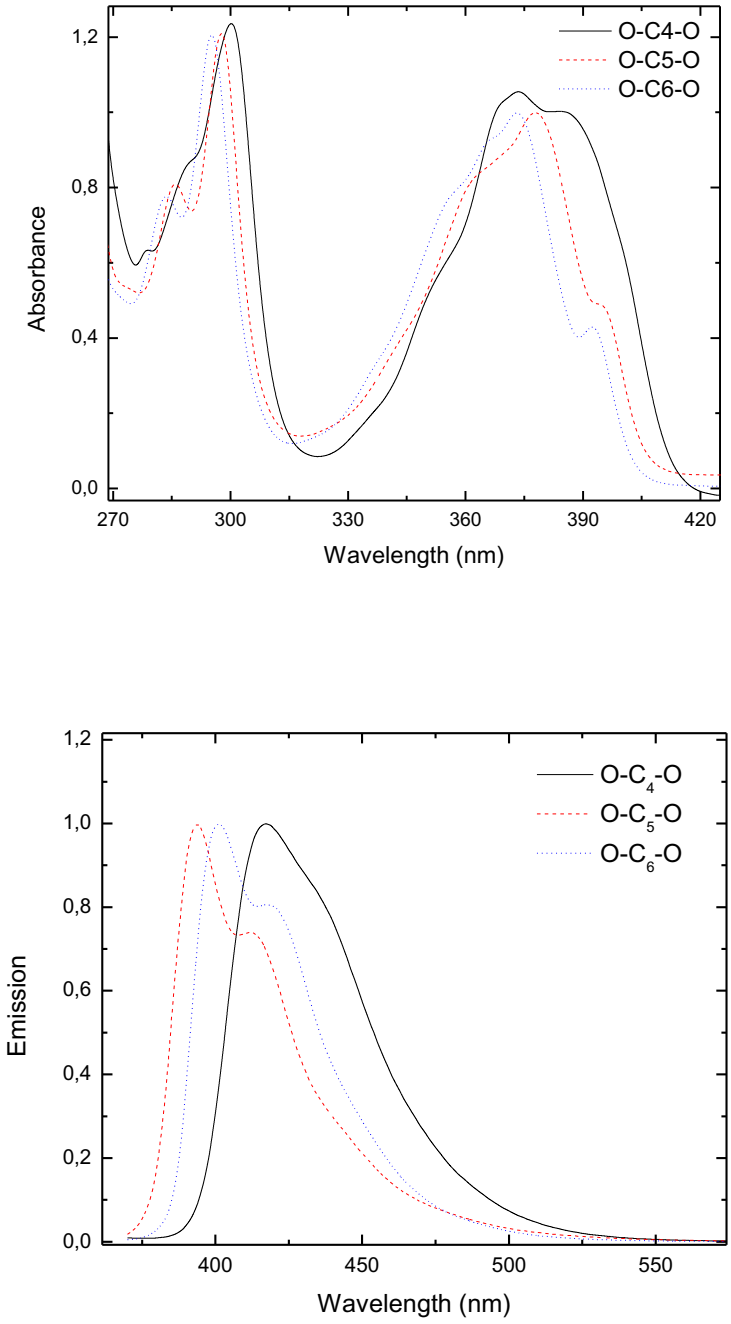

Figure 3.12. Normalized absorbance (top) and emission spectra (bottom) of (O-C_n-O) pyrenophanes. The data was acquired in $CHCl_3$ (1 atm N_2) at 298 ± 3 K by exciting at 350 nm, the concentration of all three pyrenophanes was maintained at 1.3 μM.

Table 3.1. Photophysical data and radiative and non-radiative rate constants for (O-C_n-O) pyrenophane series, acquired in $CHCl_3$ (1 atm N_2) at 298 ± 3 K, λ_{exc} = 350 nm and [O-C_n-O] = 1.3 μM.

Compound	λ_{max}^{abs}, nm ($\varepsilon \times 10^5 M^{-1}cm^{-1}$)	E_{op}, cm^{-1}	λ_{max}^{em}, nm	τ, ns	Φ_{em}	k_r, s^{-1}	k_{nr}, s^{-1}
Pyrene[b]	373 333 276 245	^1L_b: 26800 ^1L_a: 29500 ^1B_b: 36200 ^1B_a: 26800	373	480	0.63	1.3×10^6	7.8×10^5
(O-C_6-O)	392 (1.4) 373 (3.2) 365^{sh} (3.0) 355^{sh} (2.5) 295 (3.9) 283 (2.5)	25510 26810 27400 28170 33400 35340	400 419	1.7	0.40	2.3×10^8	3.5×10^8
(O-C_5-O)	395^{sh} (1.4) 377 (3.1) 362^{sh} (2.6) 349^{sh} (1.3) 297 (3.9) 285 (2.5)	25320 26530 27625 28650 33670 35090	404 422	1.5	0.40	2.9×10^8	6.9×10^8
(O-C_4-O)	385 (0.4) 373 (0.4) 353^{sh} (0.2) 300 (0.5) 290^{sh} (0.3)	25980 26810 26800 33330 34500	417 436	1.2	0.80	6.9×10^8	1.7×10^8

(b) In 3-methylpentane, only the maxima of the first vibronic progression is reported. Data for pyrene is taken from Tran-Thi, T. H.; Prayer, C.; Millié, P.; Uznanski, P.; Hynes, J. T. J. Phys. Chem. A 2002, 106, 2244.[24]

In (O-C_6-O), the lower-energy transitions at 373 nm (26810 cm^{-1}) and corresponding shoulders at 355 nm (28170 cm^{-1}) and 365 nm (27400 cm^{-1}) are previously assigned to a $S_0 \rightarrow {}^1L_b$ transition which are originally forbidden but picks up intensity as a result of vibrational mixing with the $S_0 \rightarrow {}^1L_a$ state and becomes allowed.[24, 26, 48] Another noticeable feature, as well, is that the bands in the high energy absorption manifold (270 – 320 nm) are more split in the case of (O-C_5-O) and (O-C_6-O) as compared to (O-C_4-O). In (O-C_4-O), the split is more like a shoulder which appears at 290 nm (34500 cm^{-1}), while in (O-C_5-O) and (O-C_6-O) the split posses a well-resolved shoulder at 285 nm (35090 cm^{-1}) and 295 nm (33400 cm^{-1}), respectively. Given the complexity of absorption band envelopes, assignment of the individual transitions is difficult and awaits detailed TD-DFT calculations.

3.3.2. Fluorescence Spectra

It is noticeable that the absorption and emission spectra lack the mirror-image symmetry that is expected for a two-state system (Figure 3.12). Emission of (O-C_4-O) is broad and centered at 417 nm with a weak shoulder at 436 nm, while the emission bands of (O-C_5-O) and (O-C_6-O) are very similar to each other in terms of well resolved vibronic progressions thus indicating a similar vibronically structured, thermally equilibrated excited (thexi) state. Both (O-C_5-O) and (O-C_6-O), moreover, have bands centered at ~400 nm with well-resolved shoulders at 422 and 419 nm, respectively. Table 3.1 presents a summary of the detailed spectral properties of (O-C_4-O), (O-C_5-O) and (O-C_6-O).

Another interesting feature of these pyrenophanes is the notable similarities in the photophysical properties of the (O-C_n-O) series, in which all the pyrenophanes were found to be highly fluorescent (Table 3.1). In addition, there does not appear to be a great difference in the fluorescence lifetimes τ of the (O-C_n-O) pyrenophanes. Nevertheless, a cursory glance of the data in Table 3.1 suggests very little difference between the three strained pyrenophanes, but a detailed analysis reveals many aspects of the photophysics of these systems.

The analysis of the spectroscopic data is expected to provide information regarding the structure-dynamical relationships for the (O-C_n-O) (n = 4, 5, and 6) series as a function of increasing torsion across the pyrenophane chromophore. While the series is limited to three compounds precluding a detailed statistical analysis, a quantitative analysis of the data to assess the impact of increasing the torsion on the photophysical properties is tenable. Moreover, in order to make comparisons, pyrene will be utilized as the reference compound.

3.3.3. The Franck-Condon Band-Shape Analysis

Absorption and emission band envelopes may enclose any number of bands (depending upon the solvent and molecule), with the broad, "Gaussian" bands, including contributions from solvent librations and low-frequency modes. Gaussian deconvolution analyses were performed to determine the number of transitions that comprised the total envelope. In addition, deconvolution of peaks is also important because it will provide such necessary information as position, height, and full-width at half-maximum ($\Delta\bar{\nu}_{1/2}$) for the

individual bands. These parameters will be used within the context of existing theory, described as below.

Overlapping peaks are usually resolved into first-and second-derivative components, with the assumption that both functions are independent of each other. This procedure is required to minimize the number of parameters in the absorption spectral fitting analysis. Therefore, the deconvolution procedure starts with extracting the first-and second-derivatives from the experimental data. A multi-peak, non-linear, least-square minimization is used to extract the individual Gaussian components of an absorption spectrum (Equation 3.2), to produce a deconvoluted spectrum with a good fit to the experimental results.

$$A = y_0 + \sum_{j=1}^{n} \alpha_j \frac{A_{jmax}}{\left(\Delta\bar{\nu}_{1/2}\right)^2 \cdot \sqrt{\frac{\pi}{2}}} exp\left[-\frac{2\left(\bar{\nu} - b_j\right)^2}{\left(\Delta\bar{\nu}_{1/2}\right)^2}\right] \qquad [3.2]$$

In Equation 3.2, A is absorbance, α_j is the fraction of the jth component, A_{jmax} is the absorbance of a particular band under investigation. The center, b_j, represents the "mean", $\Delta\bar{\nu}_{1/2}$ is the full-width at half-maximum (fwhm), and $\bar{\nu}$ is the frequency in wavenumbers.

In general, OriginPro 8.0 was used as the software platform to process the analysis.[49] Gaussian deconvolution of the absorption manifold for the (O-C_n-O) series is presented in Figures 3.13 to 3.15. For clarity, the first-and second-derivatives are not shown in the deconvolution spectra and are provided in the appendix (Figure S1-S3).

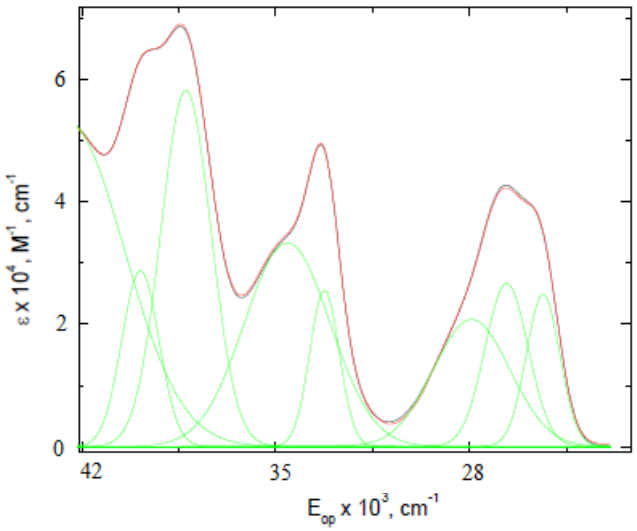

Figure 3.13. Deconvolution of the absorption spectrum of (O-C_4-O). The green bands are the deconvoluted spectral components, calculated using the procedure described earlier. The red line is the calculated spectrum from summation of the individual transitions (green), and the black line is the observed spectrum.

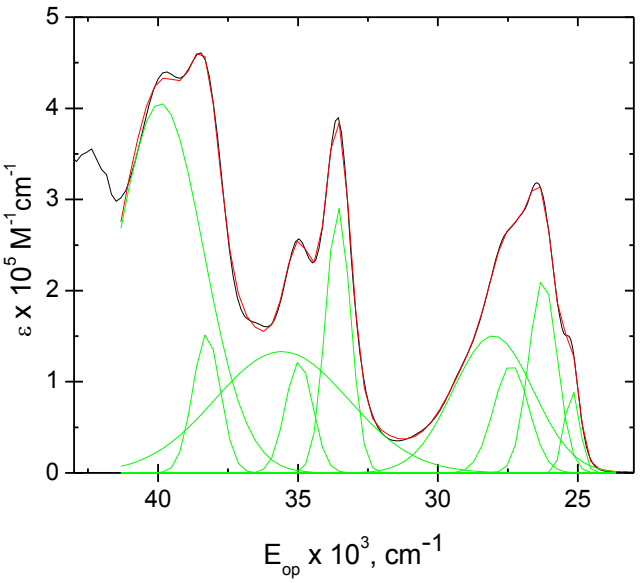

Figure 3.14. Deconvolution of the absorption spectrum of (O-C_5-O). The green bands are the deconvoluted spectral components calculated using the procedure described above. The red line is the calculated spectrum from summation of the individual transitions (green), and the black line is the observed spectrum.

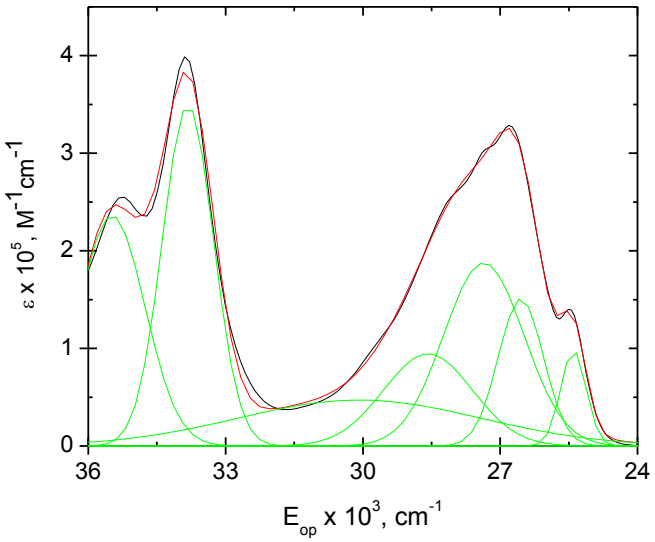

Figure 3.15. Deconvolution of the absorption spectrum of (O-C_6-O). The green bands are the deconvoluted spectral components calculated using the procedure described above. The red line is the calculated spectrum from summation of the individual transitions (green), and the black line is the observed spectrum.

In the classical, Gaussian limit, absorption spectral bandwidths are related to the band energy and the free-energy difference between the thexi and ground-states by Equation 3.3.

$$(\Delta\bar{\nu}_{1/2})^2 = 16(E_{op} - \Delta G^0)k_B T\ ln\ 2 \qquad [3.3]$$

In Equation 3.3 $\bar{\nu}_{1/2}$ is the half-width-at-full maximum, E_{op} is the energy of the optical transition in cm^{-1}, ΔG is the free-energy change between the thermally equilibrated ground- and excited-states in cm^{-1}, k_B is the Boltzmann constant and T is temperature.

Pyrene-based compounds possess significant charge-transfer character.[50-52] The π-π^* transitions are dipole-allowed and possess significant charge transfer character, meaning

that the absorptions occur with relatively high absorptive cross sections. As such, integrated intensities vary with the oscillator strength (f_{osc}), as illustrated in Equation 3.4.

$$f_{osc} = \int e(\bar{\nu})d\bar{\nu} = \frac{4\pi N_A \nu}{3000cn\hbar \ln 10}\left|\vec{M}\right|^2 \qquad [3.4]$$

In Equation 3.4, $\int e(\bar{\nu})d\bar{\nu}$ is the integrated absorptivity; $\vec{M}$ is the transition moment; N_A is Avogadro's number; ν and c are the frequency and speed of light, respectively; n is the refractive index of the solvent and $\hbar$ = h/2π. The oscillator strength (f_{osc}) is related to the transition dipole moment by Equation 3.5.[53]

$$f_{osc} = \int \varepsilon(\bar{\nu})d\bar{\nu} = \frac{8\pi m_e \bar{\nu}_{max}}{3he^2}|\vec{\mu}|^2 \qquad [3.5]$$

In Equation 3.5, m_e is the mass of the electron, $\bar{\nu}_{max}$ is the energy of the band maximum, h is Planck's constant, e is the unit electron charge, and $\vec{\mu}$ is the transition dipole moment. For a Gaussian-shaped band, f_{osc} is given by Equation 3.6.[53]

$$f_{osc} = 4.61 \times 10^{-9}\left(\varepsilon_{max}\Delta\bar{\nu}_{1/2}\right) \qquad [3.6]$$

In Equation 3.6, ε_{max} is the extinction coefficient in M^{-1} cm^{-1} at $\bar{\nu}_{max}$. The transition dipole moment is given by Equation 3.7.[53]

$$|\vec{\mu}|^2 = (1.08 \times 10^{-5})f_{osc}\bar{\nu}_{max} \qquad [3.7]$$

The parameters extracted from the deconvolution of the lowest-energy band envelope are summarized in Tables 3.2 to 3.4. The major perturbation to the (O-C_n-O) system is a substituent effect in the 1,7 positions on the pyrene due to the presence of a σ donating phenoxyl group, which has been documented to electronically alter the ^1L_a more than the ^1L_b states.[23]

The oscillator strengths for the ~375 nm bands, meanwhile, are roughly twice as large than those found for the ~ 390 nm bands across the series, with the exception of n = 4. Similar trends are seen for the transition at 365 nm, 362 nm and 353 nm for n = 6, 5 and 4, respectively.

Table 3.2. Summary of λ_{max}, energies, ($\Delta\bar{\nu}_{1/2}$), oscillator strengths (f_{osc}), and transition dipole moments derived from the absorption spectral fits for (O-C_4-O) shown in Figure 3.14.

λ_{max}, nm (ε, M^{-1} cm^{-1})	Energy, cm^{-1}	$\Delta\bar{\nu}_{1/2}$, cm^{-1}	f_{osc}	$\vec{\mu}$, eÅ
385 (4.06×10^4)	25980	550	0.10	0.027
373 (4.39×10^4)	26810	1010	0.20	0.056
353 (2.41×10^4)	26800	1263	0.14	0.041
300 (5.08×10^4)	33330	2850	0.66	0.199
290 (3.38×10^4)	34500	890	0.13	0.047
250 (6.42×10^4)	39920	3080	0.91	0.392

Table 3.3. Summary of λ_{max}, energies, bandwidths ($\Delta\bar{\nu}_{1/2}$), oscillator strengths (f_{osc}), and transition dipole moments derived from the absorption spectral fits for (O-C_5-O) shown in Figure 3.15

λ_{max}, nm (ε, M^{-1} cm^{-1})	Energy, cm^{-1}	$\Delta\bar{\nu}_{1/2}$, cm^{-1}	f_{osc}	$\vec{\mu}$, eÅ
395 (3.12×10^4)	25320	555	0.079	0.021
377 (3.12×10^5)	26530	984	1.41	0.40
362 (2.63×10^5)	27625	1752	0.21	0.062
349 (1.34×10^5)	28650	1945	1.20	0.064
297 (3.90×10^5)	33670	1115	2.00	0.73
285 (2.50×10^5)	35090	1440	2.31	0.88

Table 3.4. Summary of λ_{max}, energies, bandwidths ($\Delta\bar{\nu}_{1/2}$), oscillator strengths (f_{osc}), and transition dipole moments derived from the absorption spectral fits for (O-C_6-O) shown in Figure 3.16.

λ_{max}, nm (ε, M^{-1} cm^{-1})	Energy, cm^{-1}	$\Delta\bar{\nu}_{1/2}$, cm^{-1}	f_{osc}	$\vec{\mu}$, eÅ
392 (1.43×10^4)	25510	485	0.031	0.008
373 (3.21×10^5)	26810	786	1.16	0.33
365 (3.07×10^5)	27400	1614	2.43	0.71
355 (2.54×10^5)	28170	1910	2.15	0.66
295 (3.92×10^5)	33400	1440	1.59	0.60

3.3.4. The Torsional Angle

The torsion angles (δ_{tor}) of (O-C_6-O) and (O-C_4-O) were calculated from the X-ray crystal structures and are: (O-C_6-O), $\delta_{tor} = 10^{\circ}$ and (O-C_4-O), $\delta_{tor} = 22^{\circ}$.[54] For (O-$C_5$-O), the torsion angle ($\delta_{tor}$) was calculated using molecular modeling (AM1 level theory) and $\delta_{tor} = 16^{\circ}$ was extracted.[54, 55] The torsional angle can be related to the underlying transitions of the (O-C_n-O) series pyrenophanes. It is evident from the deconvoluted plots presented in Figures 3.13 - 3.15, that the number of underlying transitions in the low energy absorption manifold varies across the (O-C_n-O) series, where five transitions for n = 6 make up the lowest-energy spectral manifold. As well, the numbers of deconvoluted transitions for n = 5 is four and for n = 4, there are three apparent transitions.

The observation that increasing δ_{tor} reduces the number of underlying transitions is difficult to rationalize at the present time. Time-dependent density functional theory (TD-DFT) calculations predict that the band energies should move to lower energy as the tether is shortened.[55]. A more definitive analysis of this, however, requires a larger data set and higher level TD-DFT calculations.

3.3.5. Excited-States

Although the data are limited, the following trends are observed as the tether is shortened: (1) τ decreases, (2) ϕ_{em} increases, (3) k_r decreases, (4) and k_{nr} increases (Table 3.1). The trends outlined above can be understood within the theoretical frameworks for radiative and non-radiative decay as described below.

3.3.5.1. Radiative Decay

The equations that relates the rate constant for radiative decay (k_r), transition moment ($\overrightarrow{M}$) and the cube of the emission energy, $\langle\vec{\nu}^{-3}\rangle^{-1}$ have been described in Section 1.3 and are presented here for convenience.

The rate constant for radiative decay for the $S_n \rightarrow S_0$ transition is given by Equation 3.8.[56]

$$k_r = \frac{64\pi^4\eta^3}{3\hbar}\left|\overrightarrow{M}\right|^2\langle\vec{\nu}^{-3}\rangle^{-1} \qquad [3.8]$$

The transition moment $\overrightarrow{M}$ is given by Equation 3.9,[56]

$$\vec{M} = \langle\psi_{el}|e\sum_n \vec{r}\,|\psi_{el}\rangle\langle\psi_{vib}|\psi_{vib}\rangle = \vec{\mu}\langle\psi_{vib}|\psi_{vib}\rangle \qquad [3.9]$$

and $\langle\bar{\nu}^{-3}\rangle^{-1}$ is the cube of the energy gap between the excited and ground-state, given by Equation 3.10 where E_{em} is the emission maxima in cm^{-1}.[56]

$$\langle\bar{\nu}^{-3}\rangle^{-1} = \frac{\int I(\bar{\nu})d\bar{\nu}}{\int \bar{\nu}^{-3}I(\bar{\nu})d\bar{\nu}} \sim E_{em}{}^3 \qquad [3.10]$$

A plot of k_r vs. $E_{em}{}^3$ is shown in Figure 3.16 (a), where linear least squares analysis of the data yields a negative slope of $-2.5(\pm0.3)\times10^{-4}$ cm^{-3}. Furthermore, the observation of a negative dependence of $\overrightarrow{M}$ (Figure 3.16 (b), calculated by Equation 3.8) as a function of E_{em} represents a dramatic effect that is not consistent with observations made previously for other systems.[57, 58]

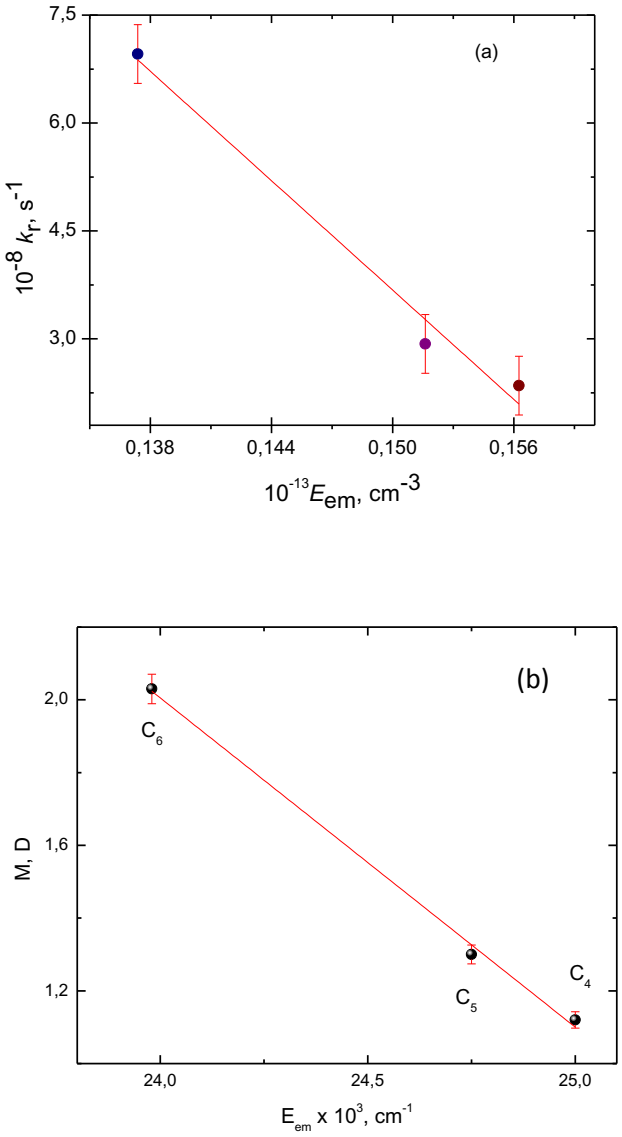

Figure 3.16. (a) A plot of k_r vs. E_{em}^3 for (O-C_n-O) n = 6, 5, and 4 with R^2 = 0.97 and slope = $-2.5(\pm 0.3) \times 10^{-4}$ (b) A plot of the transition moment ($\vec{M}$) vs. emission energy (E_{em}) of (O-C_n-O) pyrenophanes, with R^2 = 0.99 and slope = $-9.03(\pm 0.4) \times 10^{-4}$. Symbols represent the data points and the red line is a linear least square fit to the data points.

It has been reported for 3-H indole derivatives that if $\vec{M}$ is independent of the E_{em}, the slope of a plot between $\vec{M}$ and E_{em} should be linear with a positive slope.[59, 60] Such changes

were primarily attributed to changes in the extent of charge delocalization and solvent systems.[60] This deviation observed in this study could be due to some offsetting effects leading to a change in the wavefunctions, so that the intensity is dictated by the L_b transition and not by L_a. However, the verification and proof for this needs to be scientifically addressed.

A plot of the transition moment $\vec{M}$ as a function of torsion angle is particularly revealing, as shown in Figure 3.17. There is a non-linear dependence of $\vec{M}$ on δ_{tor} as the tether is shortened, and as per Equation 3.9, the transition moment is a product of the transition dipole moment $\vec{\mu}$ and the integral of the vibrational wavefunctions $\langle\psi_{vib}|\psi_{vib}\rangle$ between the ground and the excited-states. Therefore, the graph reaveals that transition moment varies systematically with the torsion accros these molecules and nearly display quadratic dependence.

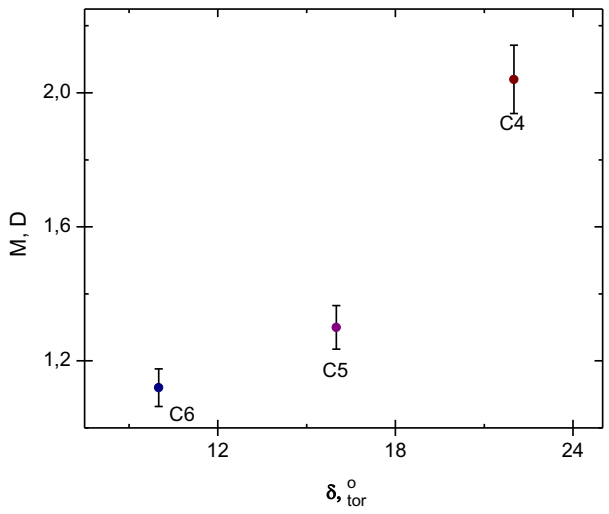

Figure 3.17. A plot of the transition moment $\vec{M}$ vs. the torsion angle (δ_{tor}) for (O-C_n-O).

3.3.5.2 Application of the Strickler-Berg Equation

In contrast to the absorption spectral data, where the energetics of the absorption bands are relatively constant for the (O-C_n-O) series, there is a clear dependence of the emission energy on the tether length with λ_{em}^{max} = 400 nm for (O-C_6-O), λ_{em}^{max}= 404 nm for (O-C_5-O) and λ_{em}^{max} = 417 nm for (O-C_4-O). Similar to the fluorescence spectral data, the radiative rate constant can also be calculated from the absorption spectral data using the Strickler-Berg equation, Equation 3.11.[61]

$$k_r = (3.05 \times 10^{-9})\eta^2 \langle \bar{\nu}^{-3} \rangle^{-1} \left(\frac{\varepsilon_{max}\, \Delta\bar{\nu}_{1/2}\,(abs)}{E_{abs}} \right) \qquad [3.11]$$

In Equation 3.11, η is the refractive index of the solvent, ε_{max} is the extinction coefficient at λ_{max}, E_{abs} is the energy of the absorption band at λ_{max}, $\langle \bar{\nu}^{-3} \rangle^{-1} \approx E_{em}^3$, and $\Delta\bar{\nu}_{1/2}\,(abs)$ is given by Equation 3.12.[62]

$$\left(\Delta\bar{\nu}_{1/2}(abs) \right)^2 = 16\lambda_o' k_B T ln2 \qquad [3.12]$$

In Equation 3.12, $\lambda_o' = \lambda_o + \lambda_{iL}$, with λ_o is solvent reorganization energy and λ_{iL}, the low-frequency vibrational modes treated classically.

The application of the Strickler-Berg equation is only valid for broad molecular bands and the transitions that are strongly allowed.[61, 63] It is also valid only in the absence of solvent interaction, difference in the refractive index of solvent for absorption and emission, and large changes in the system geometry between ground and excited-state.[61, 63] Although this equation makes a number of simplifying assumptions, the results of the

analysis can be useful in identifying the presence of complicated behaviours, such as the involvement of transitions between states of different electronic symmetry. Furthermore, in the case of (O-C_n-O) pyrenophanes a mirror image relationship between absorption and emission is absent suggesting a change in the structural geometry upon excitation. However, the trend of calculated k_r (Table 3.5) values can be related to the experimental values (Table 3.5). Moreover, the calculated values corroborate with the experimentally calculated values of k_r calculated from absorption spectral data using the Strickler-Berg equation.

Table 3.5. Calculated and Experimental Quantities for Radiative Decay, Emission Spectral Fitting Parameters, Franck-Condon Factors, and Reorganization Energies for (O-C_n-O) (n = 4, 5, and 6) in $CHCl_3$ at 298 ± 3 K.

Property	(O-C_6-O)	(O-C_5-O)	(O-C_4-O)
λ_{em}^{max}, nm	400	404	417
$E_{em,}$ cm^{-1}	25000	24750	23980
τ, ns	1.70	1.50	1.15
ϕ_{em}	0.40	0.44	0.80
k_r, s^{-1}	2.3×10^8	2.9×10^8	6.9×10^8
$k_r^{[a]}, s^{-1}$	1.0×10^8	1.3×10^8	2.0×10^8
$\langle \bar{\nu}^{-3} \rangle^{-1}, cm^{-3}$	1.6×10^{13}	1.5×10^{13}	1.4×10^{13}
$\vec{M}, D$	1.12	1.30	2.03
E_o, cm^{-1}	24940	24753	24070
S_M	1.06	1.02	0.97
$\Delta\bar{\nu}_{0,1/2}, cm^{-1}$	1200	1140	1450
$\hbar\omega_M, cm^{-1}$	1200	1200	1300
γ	1.98	2.01	1.98
λ_o, cm^{-1}	620	560	915
λ_{vib}, cm^{-1}	1270	1224	1260
k_{nr}, s^{-1}	5.7×10^8	6.2×10^8	8.6×10^8
$\ln[FC]$	-42.7	-44.1	-38.3
$ln(\beta_0 \times 1s)$	62.5	63.8	57.3

[a] Calculated from the Strickler-Berg Equation.

3.3.5.3. Emission Spectral Fitting, Excited-State Structure and Franck-Condon Factors.

The emission spectra of the pyrenophanes were analyzed using the single, average mode Franck-Condon line-shape analysis. A detailed procedure of emission spectral fitting analysis is provided in Chapter 1. The fitted spectra are shown in Figure 3.18, and the spectral fitting parameters E_0, S_M and $\Delta\bar{\nu}_{1/2}$, with $\hbar\omega_M$, are listed in Table 3.5.

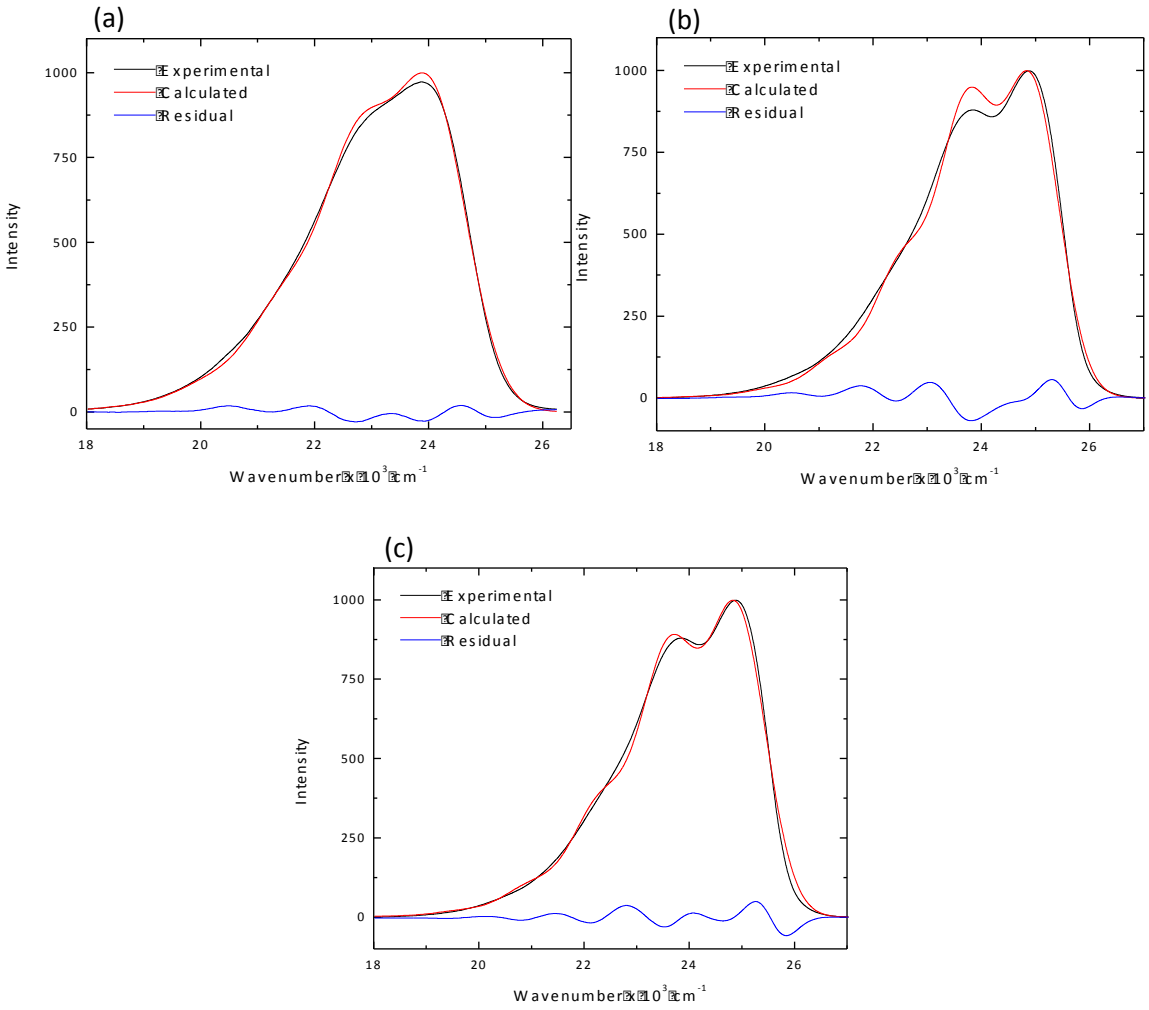

Figure 3.18. One-mode fit emission spectral fitting profiles for (O-C_n-O) series of pyrenophanes in the following order: (a) (O-C_4-O), (b) (O-C_5-O), and (c) (O-C_6-O). The residuals are shown as a blue line and the largest deviation between the calculated fit and the experimental data is ~ 6%.

The spectral fitting parameters can be used to calculate the vibrational overlap factors for the non-radiative decay, $\ln[F(\text{calc})]$, by using Equation 3.13 and the average mode approximation.[64]

$$\ln[\mathrm{FC(calc)}] = -\frac{1}{2}\ln(\hbar\omega_M E_0) - S_M - \frac{\gamma E_{\mathrm{em}}}{\hbar\omega_M} + \left(\frac{\gamma+1}{\hbar\omega_M}\right)^2 \lambda_{\mathrm{o,L}} k_{\mathrm{B}} T \qquad [3.13]$$

In Equation 3.13, E_0, $\hbar\omega_M$ and $\Delta\bar{\nu}_{1/2}$ are in cm^{-1} where γ is given by Equation 3.14.

$$\gamma = ln\left(\frac{E_0}{S_M \hbar_\omega}\right) - 1 \qquad [3.14]$$

This expression is valid in the weak vibrational coupling, $E_0 \gg S_M \hbar\omega$, low-temperature limits, $\hbar\omega >> k_BT$, and assumes equal quantum spacings in the initial and final states, $\hbar\omega_M = \hbar\omega_M$'.[56] For pyrene, meanwhile, S_M and $\hbar\omega_M$ are the average values for contributions from a number of symmetrical ν(Pyr) stretching modes mainly C=C in character. The exact nature of the acceptor modes cannot be delineated for the pyrenophane series in the absence of a detailed analysis of resonance Raman data. The calculated values for $\ln[\mathrm{F(calc)}]$ from Equation 3.13 are listed in Table 3.5, and the electron-vibrational coupling element (β_0) can be calculated by Equation 3.15.[56]

$$ln(k_{nr} \times 1s) = ln(\beta_0 \times 1s) + \ln[F(calc)] \qquad [3.15]$$

The parameters derived from the spectral fitting analysis (Table 3.5) lend insight into the effect of increasing the torsion across the pyrene face on the excited-state structure, the role of solvent, and the non-radiative dynamics of the thexi states.

The first observation is that satisfactory fits to the experimental emission spectra were obtained with $\hbar\omega_M$ values of 1200 - 1300 cm^{-1} for the (O-C_n-O) series and one can expect this for an aromatic system.[65] These values approximately correspond to the quantum spacings observed between consecutive maxima in a structured emission

spectrum. One-mode fit is the weighted average of all the accepting modes of medium frequency available to the molecule. Hence, this shows the success of the one-mode approximation in determining the $\hbar\omega_M$ values in these molecules, and points to a common set of vibrational modes in the (O-C_n-O) pyrenophane series, which accept the excited-state vibrational energy for the $S_n \rightarrow S_o$ transition.[66]

The Huang-Rhys factor (S_M), furthermore, is seen to increase with increasing emission energy. This is an expected trend based on the argument that as the energy gap between the ground and excited-state increases, the extent of ground and excited-state electronic mixing decreases thus increasing the charge-transfer character which, in turn, increases the bond distortions between states.[62]

The values of k_r and k_{nr} are approximately constant for n = 5 and 6 while n = 4 shows a smaller value for k_{nr} and a larger value for k_r, as compared to the other two pyrenophanes in the series. Similarly, the solvent reorganizational energy (λ_0) is similar for n = 5 and 6 but is significantly larger for n = 4, presumably due to the increased transition moment and increased CT character. This suggests that the reorganization energies are influenced by the magnitude of CT across the pyrenophane.

The molecules of pyrenophane series are relatively strong emitters whose excited-state lifetimes are dictated by the radiative decay processes described above, and by non-radiative decay. There is extensive literature on both organic and inorganic choromophores where there is a linear correlation between $\ln(k_{nr} \times 1s)$ and E_{em}, which forms the basis of the "Energy Gap Law".[57, 67-69] With the spectral fitting results in hand,

one can correlate between $\ln(k_{nr} \times 1s)$ and E_{em} and relate the result to the effect of tether length with the predictions from radiationless decay theory. Such a correlation is provided in Figure 3.19, where, with an increase in emission energy k_{nr} drops and this is in line with the Energy Gap Law, which predicts a linear dependence of k_{nr} on the emission energy which is reflected in the Figure 3.19.[67, 68]

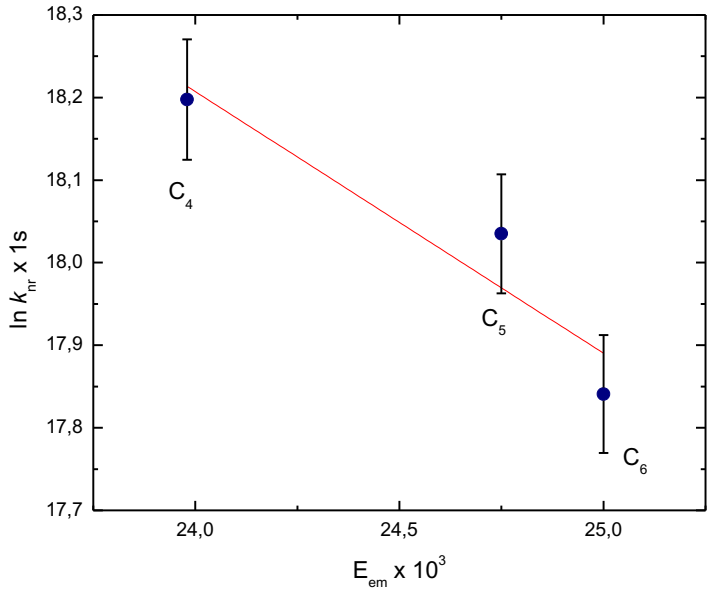

Figure 3.19. A plot of $k_{nr} \times 1s$ vs. E_{em}^3 for (O-C_n-O), n = 6, 5, and 4.

Furthermore, k_{nr} was also found to be dependent upon the tether length i.e. k_{nr} values increased upon decrease in strap length in the following order: n = 4 > n = 5 > n = 6.

3.4. Concluding Remarks

Several of the properties of bent pyrenophanes that are important to their photophysics have been explored in this Chapter. The spectral data was subjected to Franck-Condon band shape analysis and emission spectral fitting analysis. The key findings are outlined below.

1. The Beer's law plots suggest that (O-C_n-O) pyrenophanes are not self-aggregating.
2. The mirror image symmetry between absorption and emission spectra is absent, as is to be expected for a two-state system. This observation and the Franck-Condon band shape analysis suggests that the lowest energy band envelope consists of transitions which lead to emission as well as non-radiative decay.
3. The results provided in Tables 3.2 – 3.4 indicate to the presence of significant dipole moment and charge-transfer character in the (O-C_n-O) pyrenophanes.
4. A cursory analysis of the spectral data presented in Tables 3.2 – 3.4 and 3.5 suggests very little difference between the three strained pyrenophanes but a detailed analysis reveals that the Pyrenophane (O-C_4-O), exhibits properties that are quite different from the remaining two pyrenophanes in the series. The behavior of (O-C_4-O) can be attributed to its more bent structure than those of (O-C_5-O) and (O-C_6-O) pyrenophanes.
5. Application of the Strickler-Berg equation compares the calculated rates of radiative decay (k_r) with the experimentally determined k_r.

6. The $\hbar\omega_M$ values calculated from the emission spectral fitting procedure are consistent for an aromatic system and confirms the success of the one-mode spectral fitting procedure for a structured emission band.

References

[1] Figueira-Duarte, T. M.; Mullen, K., Chem. Rev., (2011) 111, 7260.

[2] Winnik, F. M., Chem. Rev., (1993) 93, 587.

[3] Welham, R. D., J. Soc. Dyes Colour (1963) 79, 98.

[4] Forster, T.; Kasper, K. Z., Elektrochem., (1955) 59, 976.

[5] Lewis, F. D.; Zhang, Y.; Letsinger, R. L., J. Am. Chem. Soc., (1997) 119, 5451.

[6] Tong, G.; Lawlor, J. M.; Tregear, G. W.; Haralambidis, J., J. Am. Chem. Soc., (1995) 117, 12151.

[7] Martin, R. B.; Qu, L.; Lin, Y.; Harruff, B. A.; Bunker, C. E.; Gord, J. R.; Allard, L. F.; Sun, Y.-P., J. Phys. Chem. B, (2004) 108, 11447.

[8] Goedeweeck, M.; Van der Auweraer, M.; De Schryver, F. C., J. Am. Chem. Soc., (1985) 107, 2334.

[9] Sahoo, D.; Narayanaswami, V.; Kay, C. M.; Ryan, R. O., Biochemistry, (2000) 39, 6594.

[10] Ikeda, H.; Nakamura, M.; Ise, N.; Oguma, N.; Nakamura, A.; Ikeda, T.; Toda, F.; Ueno, A., J. Am. Chem. Soc., (1996) 118, 10980.

[11] Yang, R.-H.; Chan, W.-H.; Lee, A. W. M.; Xia, P.-F.; Zhang, H.-K., J. Am. Chem. Soc., (2003) 125, 2884.

[12] Valeur, B.; Leray, I., Coord. Chem. Rev., (2000) 205, 3.

[13] He, G.; Yan, N.; Yang, J.; Wang, H.; Ding, L.; Yin, S.; Fang, Y., Macromolecules, (2011) 44, 4759.

[14] Lee, E. D.; Werner, T. C.; Seitz, W. R., Anal. Chem., (1987) 59, 279.

[15] Pokhrel, M. R.; Bossmann, S. H., J. Phys. Chem. B, (2000) 104, 2215.

[16] Birks, J. B.; Munro, I. H.; Lumb, M. D., Proc. R. Soc. A, (1964) 280, 289.

[17] Templer, R. H.; Castle, S. J.; Curran, A. R.; Rumbles, G.; Klug, D. R., Discuss. Faraday, (1998), 41.

[18] Birks, J. B., Organic Molecular Photophysics, John Wiley & Sons Ltd: (1975).

[19] Netzel, T. L.; Nafisi, K.; Headrick, J.; Eaton, B. E., J. Phys. Chem., (1995) 99, 17948.

[20] Lambert, C.; Ehbets, J.; Rausch, D.; Steeger, M., J. Org. Chem., (2012) 77, 6147.

[21] Andersen, K. B.; Waluk, J.; Thulstrup, E. W., Photochem. Photobiol., (1999) 69, 158.

[22] Platt, J. R., J. Chem. Phys., (1949) 17, 484.

[23] Spry, D. B.; Goun, A.; Bell, C. B., III; Fayer, M. D., J. Chem. Phys., (2006) 125,

[24] Tran-Thi, T. H.; Prayer, C.; Millié, P.; Uznanski, P.; Hynes, J. T., J. Phys. Chem. A, (2002) 106, 2244.

[25] Langkilde, F. W.; Thulstrup, E. W.; Michl, J., J. Chem. Phys., (1983) 78, 3372.

[26] Thulstrup, E. W.; Michl, J., Spectrosc. Lett., (1977) 10, 435.

[27] Spanget-Larsen, J.; Waluk, J.; Eriksson, S.; Thulstrup, E. W., J. Am. Chem. Soc., (1992) 114, 1942.

[28] Heng, W. Y.; Hu, J.; Yip, J. H. K., Organometallics, (2007) 26, 6760.

[29] Sivakova, S.; Rowan, S. J., Chem. Soc. Rev., (2005) 34, 9.

[30] Cooke, G.; Rotello, V., Chem. Soc. Rev., (2003) 32, 56.

[31] Cooke, G.; Rotello, V. M., Chem. Soc. Rev., (2002) 31, 275.

[32] Meyer, E. A.; Castellano, R. K.; Diederich, F., Angew. Chem. Int. Ed., (2003) 42, 1210.

[33] Hunter, C. A.; Sanders, J. K. M., J. Am. Chem. Soc., (1990) 112, 5525.

[34] Huang, Y.-J.; Ouyang, W.-J.; Wu, X.; Li, Z.; Fossey, J. S.; James, T. D.; Jiang, Y.-B., J. Am. Chem. Soc., (2013) 135, 1700.

[35] Nicholas J. Turro; V. Ramamurthy; Scaiano, J. C., Principles of Molecular Photochemistry: An Introduction, University Science Books.: (2009).

[36] Yoshihara, K.; Kasuya, T.; Inoue, A.; Nagakura, S., Chem. Phys. Lett., (1971) 9, 469.

[37] Cram, D. J.; Cram, J. M., Acc. Chem. Res., (1971) 4, 204.

[38] Nishimura, J.; Nakamura, Y.; Hayashida, Y.; Kudo, T., Acc. Chem. Res., (2000) 33, 679.

[39] Bühl, M.; Hirsch, A., Chem. Rev., (2001) 101, 1153.

[40] Bodwell, G. J.; Bridson, J. N.; Houghton, T. J.; Kennedy, J. W. J.; Mannion, M. R., Angew. Chem.Int. Ed., (1996) 35, 1320.

[41] Bodwell, G. J.; Bridson, J. N.; Houghton, T. J.; Kennedy, J. W. J.; Mannion, M. R., Chem. Eur. J., (1999) 5, 1823.

[42] Bodwell, G. J.; Bridson, J. N.; Cyrañski, M. K.; Kennedy, J. W. J.; Krygowski, T. M.; Mannion, M. R.; Miller, D. O., J. Org. Chem., (2003) 68, 2089.

[43] Aprahamian, I.; Bodwell, G. J.; Fleming, J. J.; Manning, G. P.; Mannion, M. R.; Sheradsky, T.; Vermeij, R. J.; Rabinovitz, M., J. Am. Chem. Soc., (2003) 125, 1720.

[44] Breslow, R., Acc. Chem. Res., (1973) 6, 393.

[45] Aprahamian, I.; Bodwell, G. J.; Fleming, J. J.; Manning, G. P.; Mannion, M. R.; Merner, B. L.; Sheradsky, T.; Vermeij, R. J.; Rabinovitz, M., J. Am. Chem. Soc., (2004) 126, 6765.

[46] Bodwell, G. J.; Fleming, J. J.; Miller, D. O., Tetrahedron, (2001) 57, 3577.

[47] Merner, B. L.; Dawe, L. N.; Bodwell, G. J., Angew. Chem.Int. Ed., (2009) 48, 5487.

[48] Nandaluru, P. R.; Dongare, P.; Kraml, C. M.; Pascal, R. A.; Dawe, L. N.; Thompson, D. W.; Bodwell, G. J., Chem. Commun., (2012) 48, 7747.

[49] Origin Lab corporation, Origin Lab corporation, 8.0 In Northampton, MA, 01060, USA, (2008).

[50] Dierksen, M.; Grimme, S., J. Chem. Phys., (2004) 120, 3544.

[51] Li, J.; Liu, Y.; Qian, Y.; Li, L.; Xie, L.; Shang, J.; Yu, T.; Yi, M.; Huang, W., Phys. Chem. Chem. Phys., (2013) 15, 12694.

[52] Yang, S.-W.; Elangovan, A.; Hwang, K.-C.; Ho, T.-I., J. Phys. Chem. B, (2005) 109, 16628.

[53] Mines, G. A.; Roberts, J. A.; Hupp, J. T., Inorg. Chem., (1992) 31, 125.

[54] Nandaluru, P. R., Ph.D. Thesis Memorial University of Newfoundland St. Johns, (2013).

[55] Zhao, Y.; Bodwell, G. B., In Unpublished observations, Memorial University of Newfoundland: St. Johns.

[56] Chen, P.; Meyer, T. J., Chem. Rev., (1998) 98, 1439.

[57] Chen, P.; Duesing, R.; Tapolsky, G.; Meyer, T. J., J. Am. Chem. Soc., (1989) 111, 8305.

[58] Chen, P. Y.; Curry, M.; Meyer, T. J., Inorg. Chem., (1989) 28, 2271.

[59] Belletete, M.; Durocher, G., J. Phys. Chem., (1992) 96, 9183.

[60] Gould, I. R.; Mueller, J. L.; Farid, S., Z. Phys. Chem. (Munich), (1991) 170, 143.

[61] Strickler, S. J.; Berg, R. A., J. Chem. Phys., (1962) 37, 814.

[62] Alstrum-Acevedo, J. H.; Brennaman, M. K.; Meyer, T. J., Inorg. Chem., (2005) 44, 6802.

[63] Claude, J. P.; Williams, D. S.; Meyer, T. J., J. Am. Chem. Soc., (1996) 118, 9782.

[64] Thompson, D. W.; Ito, A.; Meyer, T. J., Pure Appl. Chem., (2013) 85, 1257.

[65] Graff, D.; Claude, J. P.; Meyer, T. J., Adv.Chem. Ser., (1997) 253, 183.

[66] Kober, E. M.; Caspar, J. V.; Lumpkin, R. S.; Meyer, T. J., J. Phys. Chem., (1986) 90, 3722.

[67] Caspar, J. V.; Kober, E. M.; Sullivan, B. P.; Meyer, T. J., J. Am. Chem. Soc., (1982) 104, 630.

[68] Caspar, J. V.; Meyer, T. J., J. Phys. Chem., (1983) 87, 952.

[69] Lin, R.; Fu, Y.; Brock, C. P.; Guarr, T. F., Inorg. Chem., (1992) 31, 4346.

Chapter – 4

Proton Transfer in Pyridine-Appended Pyrene Macrocycles

The effect of protonation on the photophysical properties of pyridine-appended pyrene macrocycles and their half-cycle counterparts were studied through comprehensive spectral studies. The reference compound bearing no appended pyridine was also analyzed for comparisons.

4.1. Introduction

Highly conjugated, carbon-rich macrocycles have been extensively examined in the recent years.[1-3] Owing to their rigid frameworks, such macrocycles are discernible from other 1D, 2D and 3D supramolecular structures in terms of electronic and magnetic properties.[4] This rigidity significantly attenuates the conformational flexibility of macrocycles and results in a decrease in the rate of non-radiative decay (k_{nr}).[5, 6] The opto-electronic properties originating from conjugated and carbon-rich compounds can be systematically analyzed to obtain insight about the electronic environment within the framework.[1]

4.1.1. Charge Transfer (CT) in Pyrene Based Donor-Acceptor Systems

CT in a system containing an electron-rich donor (D) and electron-poor acceptor (A) where D and A interact to form a [D,A] complex has been a subject of intense investigation over the years, [7] Such complexes absorb at specific wavelengths and can be

easily detected by several spectroscopic methods for example, UV-Vis, fluorescence and transient absorption (TA) spectroscopy.

Pyrene has been recognized as an excellent chromophore.[3, 8, 9] The ground-state redox potential of bare pyrene is E_{ox} = 1.16 V vs. SCE and the excited-state of pyrene is a potent oxidizing agent.[10, 11] Numerous literature reports have been published to date on pyrene-based D−A systems. However, the excited-state dynamics of pyrene are still not completely understood.

Sung et al. have reported the ultrafast CT dynamics and solvent dependence of CT in pyrene-acetylene based systems.[12] Figure 4.1 shows the molecules prepared by Sung et al. where the number and position of the peripheral substituents were systematically varied to study the CT dynamics.

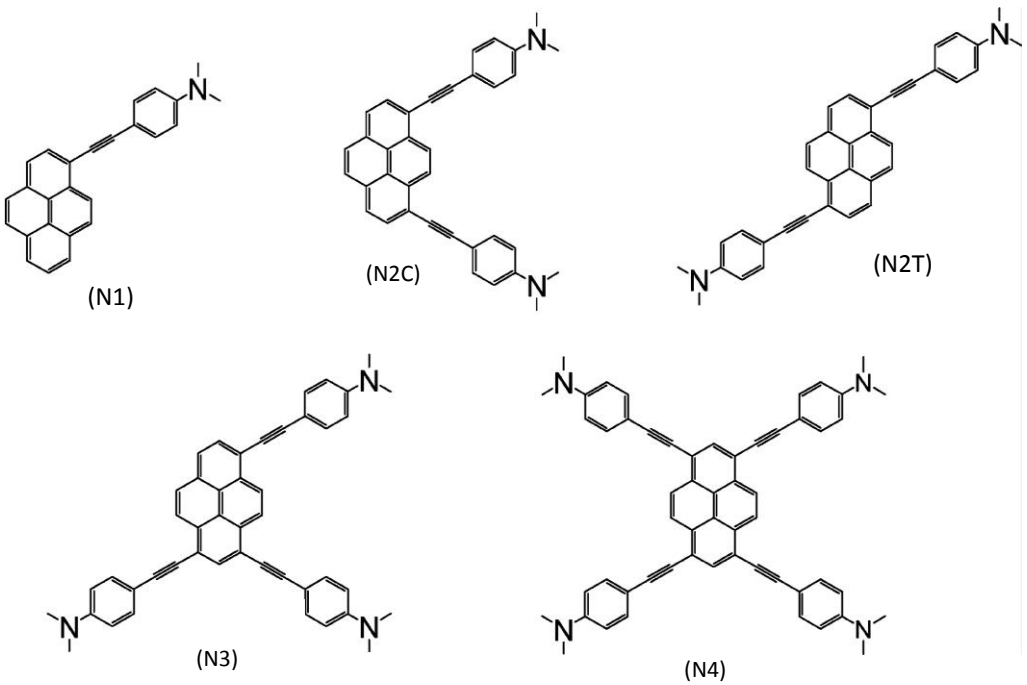

Figure 4.1. The molecules reported by Sung et al. to study the effect of change in molecular symmetry and donor groups on the charge transfer character. The letters C and T in the compound labels denote cis and trans geometries, respectively.[12]

The molecules were studied by increasing the number of N,N-dimethylaniline (DMA) electron-donor groups. Systematic variation of the number of substituents and their positions not only changes the symmetry but also shows a strong solvent dependence. Sung et al. utilized the femtosecond fluorescence up-conversion technique to get better understanding of solvent effects on CT interactions. Furthermore, the Lippert-Mataga equation (Equation 4.1) was employed to study the excited-state dipole moments by fitting the plot of changes in the Stokes shift vs. calculated Lippert function.

$$\bar{\nu}_A - \bar{\nu}_F = \frac{2}{hc}\left(\frac{\epsilon-1}{2\epsilon+1} - \frac{n^2-1}{2n^2+1}\right)\frac{(\mu_E-\mu_G)^2}{a^3} \qquad [4.1]$$

In Equation 4.1, n is the refractive index, ϵ is the dielectric constant of the static property, h is Planck's constant, a is the radius of the cavity in which the fluorophore resides, $\bar{\nu}_A$ and $\bar{\nu}_F$ are the energies of absorption and emission, respectively in cm^{-1}, μ_E and μ_G are the excited-and ground-state dipole moments, respectively, and c is the speed of light.

It was determined that for N2T and N4 (Figure 4.1) their dipole moments were smaller than those of N1, N2C and N3. Since N2T and N4 are symmetrical, it was therefore concluded that the CT character depends upon the molecular symmetry and the number of donor groups. Figure 4.2 shows the ground-and excited-state potential energy surfaces for the N1, N2C, N3, N2T and N4 systems. As shown in Figure 4.2, the ground-state of the pyrene-DMA dyad absorbs a photon, forming a Franck-Condon (FC) excited-state. After vibrational relaxation it can either decay to the ground-state in the form of fluorescence from the localized excited (LE) state or it can undergo a thermally-activated surface crossing from LE to the CT excited-state manifolds.

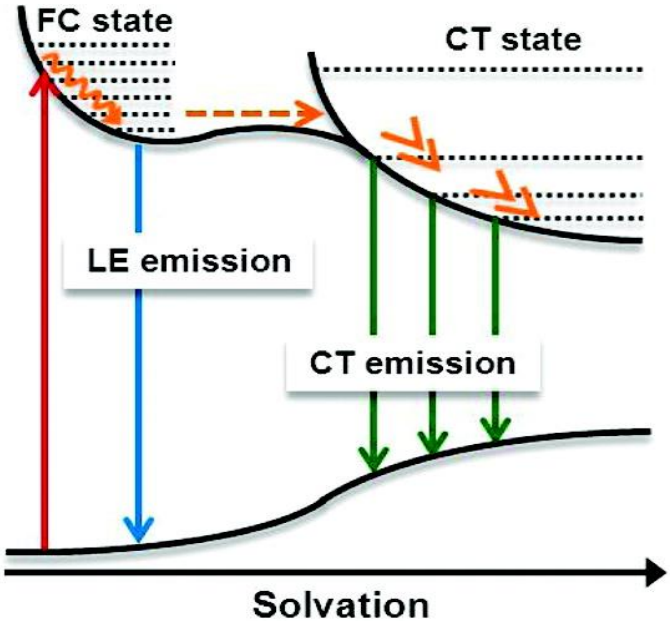

Figure 4.2. A schematic illustration of the mechanism of charge transfer in pyrene-DMA donor-acceptor systems. The red line shows the vertical excitation of the ground-state, the blue line represents the relaxation of the FC excited state as a localized excited (LE) state, and the green arrows indicate the emission from the CT excited-state.[12] Reprinted with permission from Sung, J.; Kim, P.; Lee, Y. O.; Kim, J. S.; Kim, D. J. Phys. Chem. Letters 2011, 2, 818.

4.1.2. Shape-Persistent Macrocycles

A plethora of literature examples are available in which the excited-state properties of pyrene-based systems have been studied.[13] However, the excited-state dynamics involving pyrene-based shape-persistent macrocycles have largely remained unexplored. Recently, Venkataramana et al.[1] reported 1,8-ethylnyl pyrenylene macrocycles. Although the study mainly focuses on the macrocyclic ring current in these macrocycles, the photophysical properties were also documented. The structures of the 1,8-ethylnyl pyrenylene macrocycles are shown in Figure 4.3.

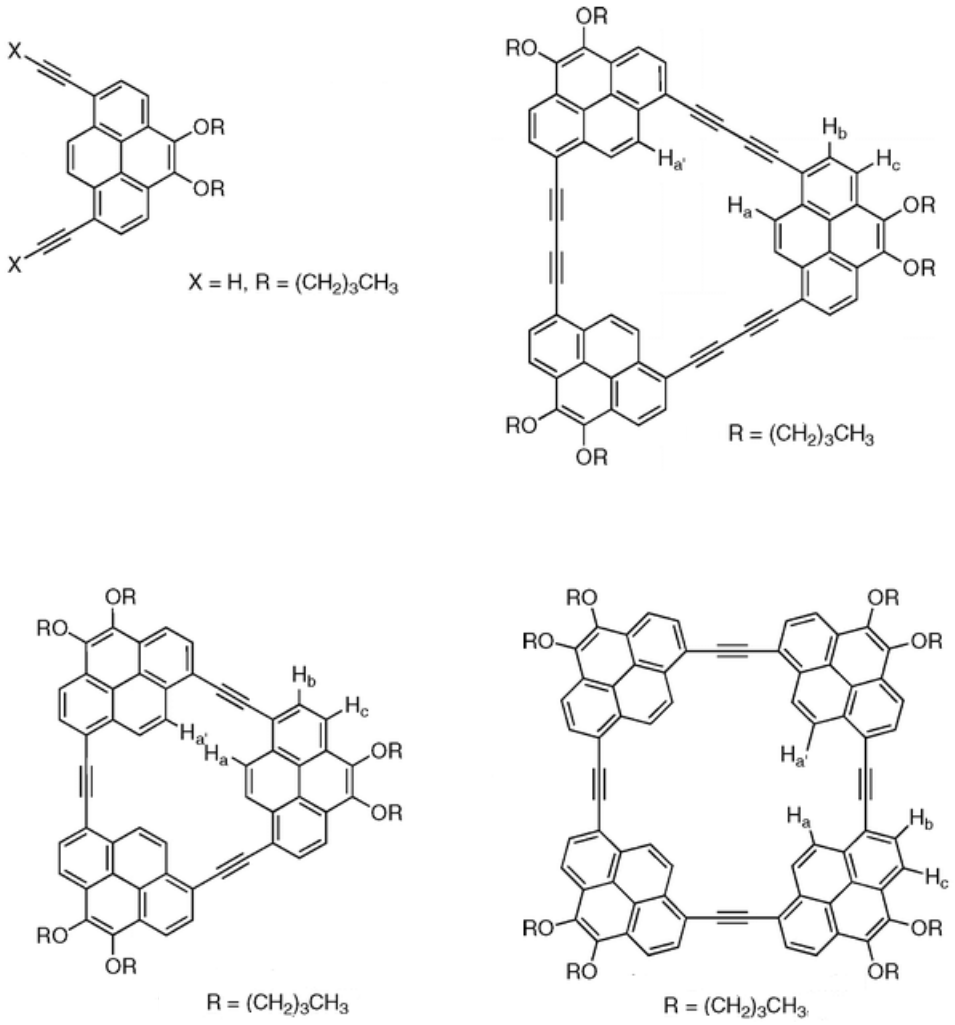

Figure 4.3. The 1,8-ethylnyl pyrenylene shape-persistent macrocycles.[1]

The UV-Vis spectra of these 1,8-ethylnyl pyrenylene macrocycles show $S_0 \rightarrow S_1$ (mainly $\pi \rightarrow \pi^*$ in nature) low-energy transitions which are not observed in the unsubstituted pyrene molecule.[14] Thus, it was concluded that the ethynyl and alkoxy substituents are responsible for the asymmetry in these molecules which leads to the

mixing of ground and excited-state electronic wavefunctions. It was also demonstrated that the fluorescence quantum yields (Φ_{em}) of these macrocycles are much smaller than those of the corresponding diynes. This result indicates that alkoxy and ethynyl substitution also result in an increase in the rate constant for non-radiative decay (k_{nr}) in the 1,8-ethylnyl pyrenylene macrocycles.

Similarly, Baxter et al. have reported the nitrogen heterocyclic dehydroannulene macrocycles shown in Figure 4.4.[15] All macrocycles exhibited a reversible proton-triggered fluorescence quenching behaviour. The brief spectroscopic analysis reveals that all the macrocycles are highly absorbing in the UV-Vis spectrum ($\varepsilon \sim 10^5$ M^{-1} cm^{-1}).

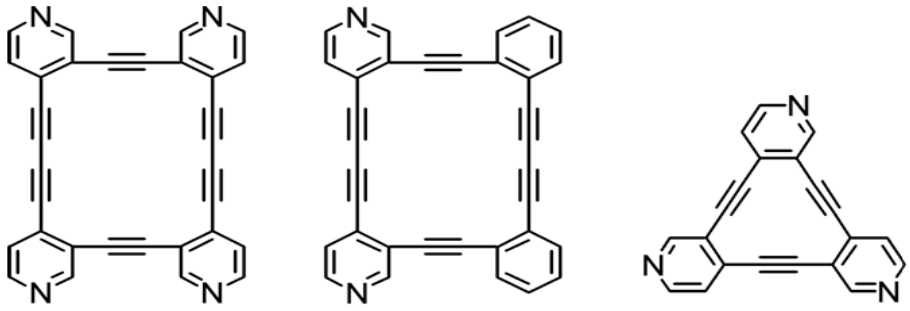

(a) (b) (c)

Figure 4.4. The nitrogen heterocyclic dehydroannulene macrocycles.[15]

The absorption spectra were found to be very sensitive towards acids, such as CF_3SO_3H (HOTf). Addition of HOTF to macrocycle b leads to a red-shift in the absorption spectrum. However, the treatment of the acidified solution with a base, such as,

aqueous Na_2CO_3 reproduces the original, non-protonated spectrum. Similarly, the fluorescence spectrum of macrocycle b was also found to be sensitive towards HOTF. The addition of HOTF was found to attenuate the fluorescence intensity along with a significant red-shift. No further analysis was reported to delineate the origin of such effects. However, the observations suggest a sequential binding of HOTF with the basic pyridinic nitrogen sites.

In a relevant study, Giansante et al. have analyzed and reported the effects of protonation on the shape-persistent macrocycles, an example of which is shown in Figure 4.5.[16] Each macrocycle is composed of 2,2'-bipyridine (bpy) and coumarin units attached on the opposite sides. The two bpy units exhibit independent protonation to form mono-protonated and di-protonated species, and further addition of acid results in the protonation of the coumarin units, leading to four-step equilibria. The effect of protonation was observed in the absorption and fluorescence spectra (as fluorescence quenching) of the macrocycles and the origin of such effects were assigned to an electron transfer from the un-protonated form to the protonated form, of the bpy.

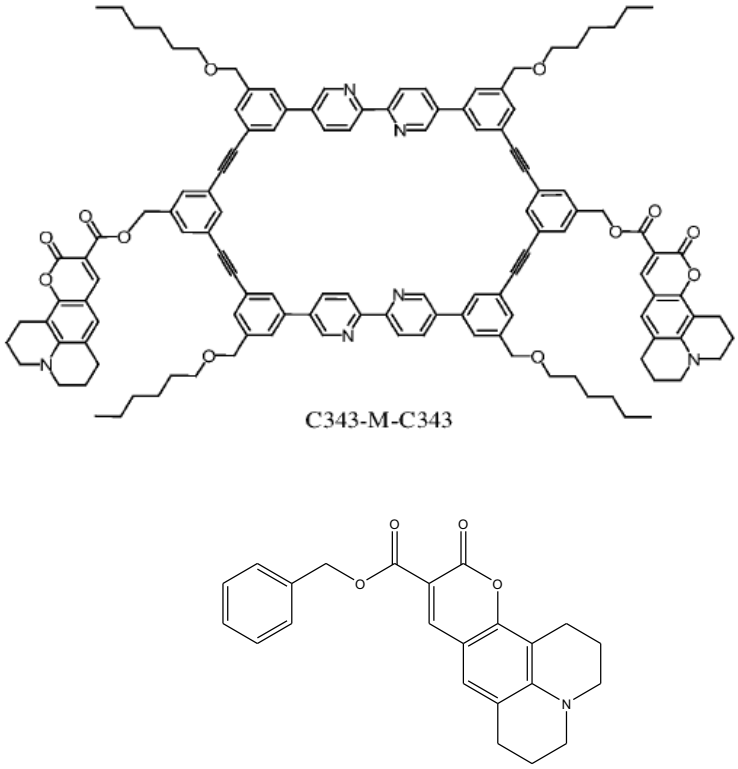

Figure 4.5. An example of the bipyridine-based shape-persistent macrocycles reported by Giansante et al., M and C343 denotes the macrocycle and coumarin (shown at the bottom), respectively.[16]

From an analysis of the absorption spectral data, Giansante et al. predicted that the excited-states of C343 lie at the lower energy than the diprotonated macrocycle, so the emission quenching should be from an ET process. Based on this, two possible excited-state pathways were predicted. In one pathway, the ET quenching of the excited protonated macrocycle ($M.2H^{+*}$) by C343 and in the second pathway, E_NT sensitization of C343 by $M.2H^{+*}$ followed by an ET from the excited $C343^{*}$ moiety to the protonated

species of the macrocycles was predicted. Giansante et al. indicated that the E_NT sensitization is the most probable mechanism because the quenching of the C343 emission is observed when this unit was directly excited. Scheme 4.1 illustrates these events and can be explained as follows: The photoexcitation of the macrocycle is followed by the E_NT to the peripheral moieties (Scheme 4.1 a). Meanwhile, the protonation of the macrocycle sensitizes the C343 coumarin unit followed by an inter-molecular charge-transfer (ICT) to the protonated species of the macrocycle (Scheme 4.1 b). A complete protonation of the macrocycle is achieved and as a result, the energy transfer from the excited macrocycle to the protonated C343 occurs leading to a characteristic low energy, weak emission of C343 upon addition of HOTf (Scheme 4.1 c).[16]

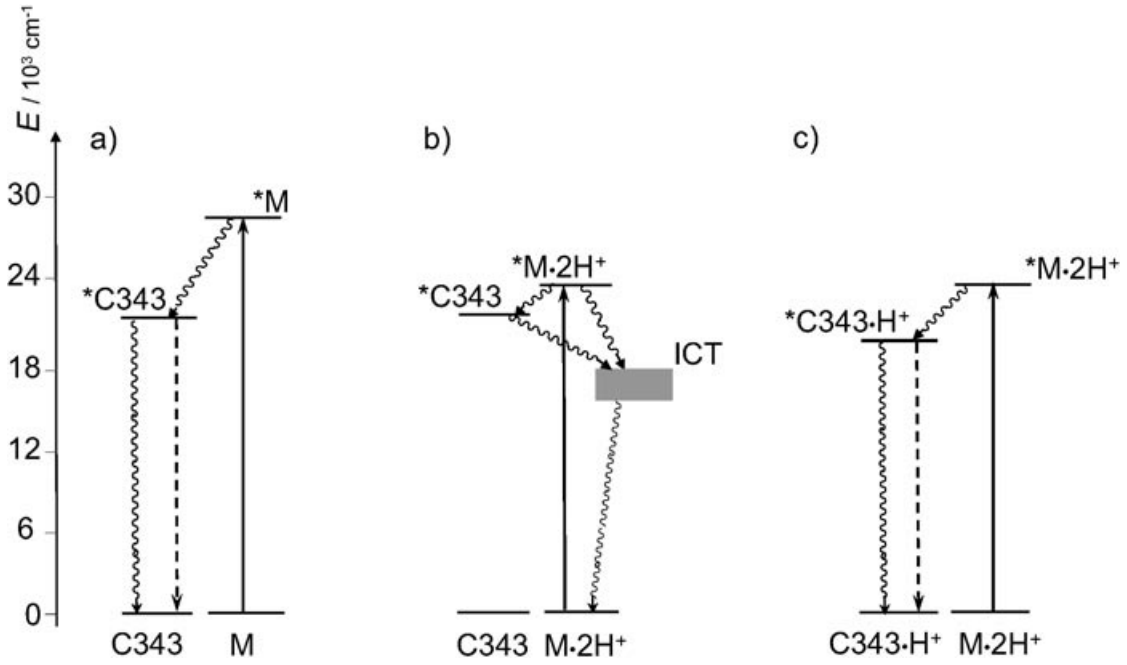

Scheme 4.1. An illustration of the electron-and $E_N T$ mechanism in the C343-M-C343 macrocycle and its protonated version using an energy level diagram. The wavy lines represent non-radiative transitions, the dashed lines represent radiative transitions and the solid lines show the selective excitation.[16] Reprinted from Giansante, C.; Ceroni, P.; Venturi, M.; Balzani, V.; Sakamoto, J.; Schlüter, A. D. Chem. Eur. J. 2008, 14, 10772.

4.2. Objectives

The main objectives of the work described in this Chapter are to investigate the spectral properties of shape-persistent pyrene-based macrocycles, and the effect of protonation on their spectral properties. Proton binding mechanisms and the resulting equilibrium constants for the protonation of macrocycles were to be investigated employing SVD methodology.

4.3. Results and Discussion

4.3.1. Macrocycles

Pyrene macrocycles were synthesized and were provided by Prof. Graham Bodwell's group, and are shown in Figure 4.6.[17] All three macrocycles constitute structurally different members of a new class of pyrene-based shape-persistent macrocycles. Moreover, the macrocycles consist of acetylene bridges between two aromatic systems (pyrene and pyridine or benzene) making the molecules relatively rigid as compared to other similar pyrene-based molecules.[3] Pyr_{out} and Pyr_{in} macrocycles incorporate nitrogen heterocyclic rings and are designed in such a way that the orientation of the pyridinic nitrogens is different.

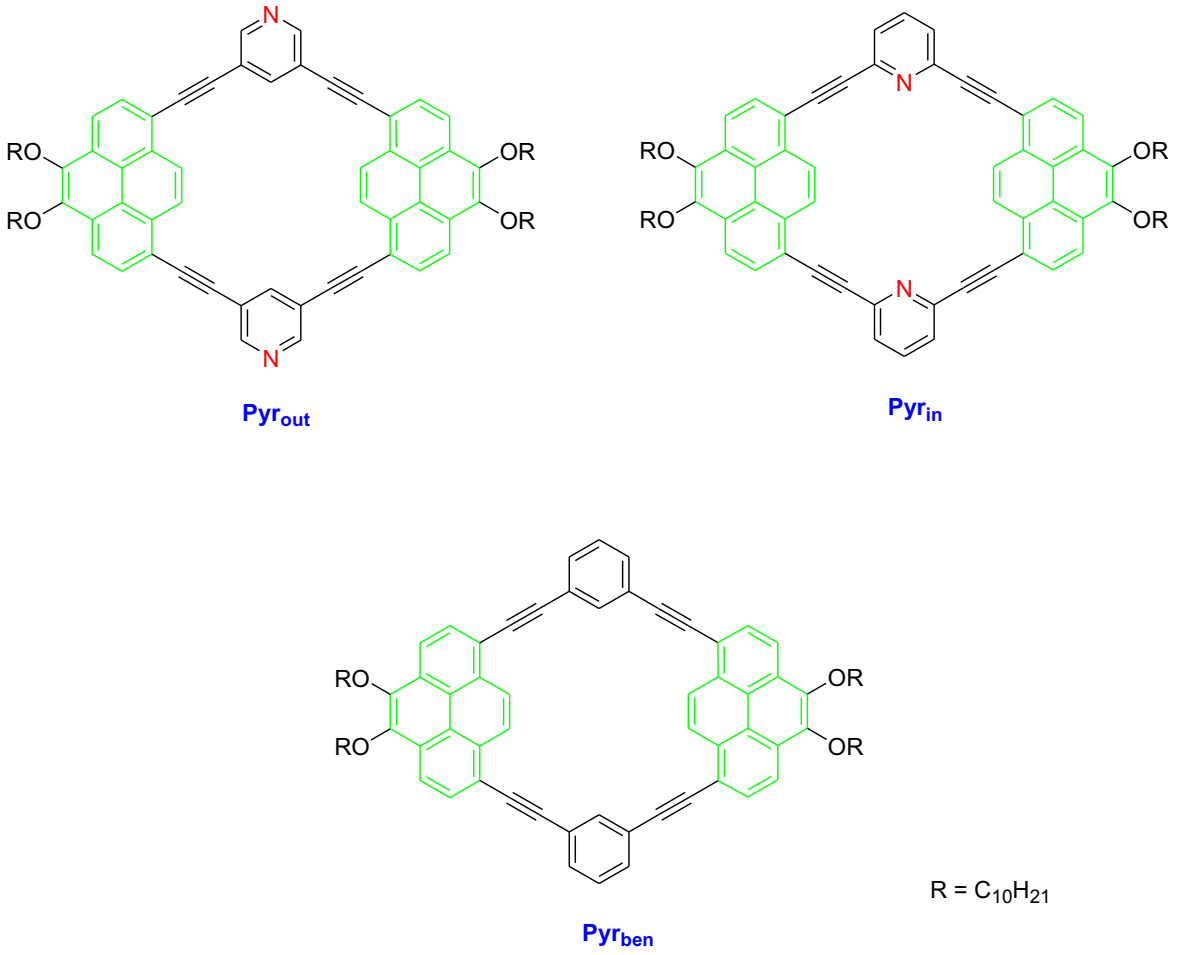

Figure 4.6. Molecular structures and abbreviations for the pyrene macrocycles described in this Chapter.[17]

4.3.1.1. Steady-State Absorption and Emission Spectra

Normalized absorption and emission spectra of Pyr_{in}, Pyr_{out} and Pyr_{ben} are shown in Figure 4.7 and the data are summarized in Table 4.1. The absorption spectra of these macrocycles are characterized by the presence of intense bands with λ_{max} ($\varepsilon \times 10^4\ \mathrm{M^{-1}cm^{-1}}$) at 333 (11.2), 351 (7.9) and 326 (17.1) for Pyr_{out}, Pyr_{in} and Pyr_{ben},

respectively. From the higher extinction coefficient values and previously-studied pyrene-based systems, these transitions can be assigned to $\pi \rightarrow \pi^*$ transitions.[14, 18] As discussed in Chapter 3, the electronic transitions in the pyrene-based molecules arise from the vertical ^1L_a transition and vibrational mixing between ^1L_a and ^1L_b states.[14, 18] Noticeably, the high-energy shoulder at 322 nm (31055 cm^{-1}) in Pyr_{in} is more resolved than in those of the other two macrocycles, where this band appears only as a shoulder.[19]

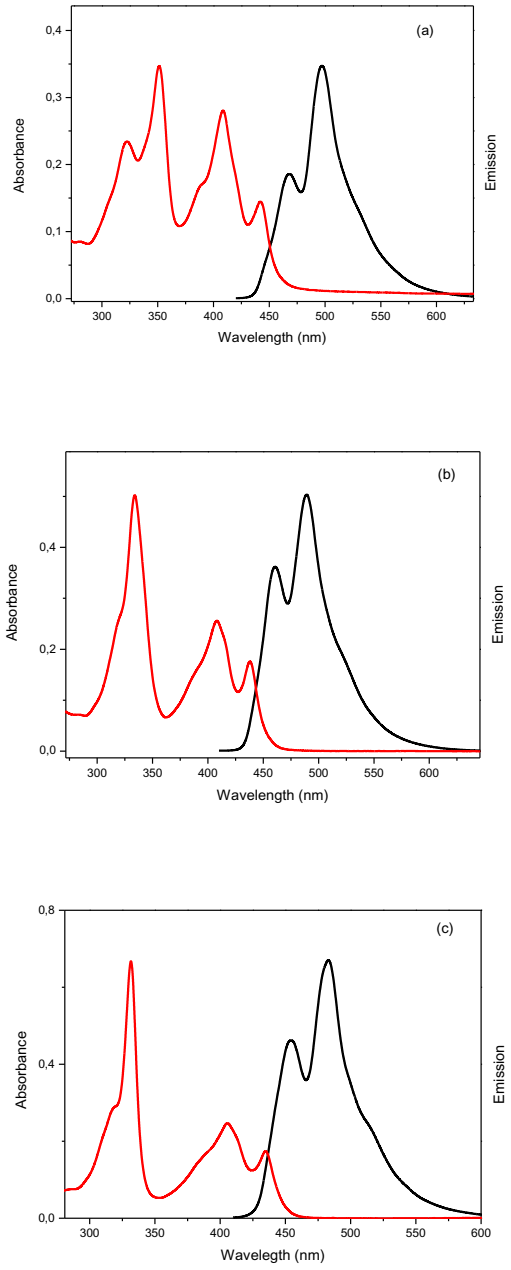

Figure 4.7. Normalized absorption and emission spectra of pyrene macrocycles; (a) [Pyr_{in}] = 6.2 μM (b) [Pyr_{out}] = 6.4 μM and (c) [Pyr_{ben}] = 6.5 μM. Red and black curves are absorption and emission spectra, resepectively. Spectra were acquired by exciting (λ_{exc} = 400 nm) a N_2 saturated CH_2Cl_2 solution of the particular macrocycles at 298 ± 3 K.[17]

Table 4.1. The photophysical properties of pyrene macrocycles acquired in CH_2Cl_2 (1 atm N_2) at 298 ± 3 nm. Emission spectra were acquired by exciting at 400 nm.

Compound	λ_{abs} (nm)	$\varepsilon \times 10^4$ (M^{-1} cm^{-1})	E_{op} (cm^{-1})	λ_{em}, nm (cm^{-1})	E_{SS} (cm^{-1}) [a]	τ, ns	k_r, s^{-1}	k_{nr}, s^{-1}	ϕ_{em}
Pyr_{out}	320[s]	6.2	31250	460	1144	4.0	9.2×10^7	3.4×10^7	0.37
	333	11.2	30030	(21739)					
	388[s]	3.4	25773	489					
	407	5.9	24570	(20449)					
	437	4.0	22883						
Pyr_{in}	322	5.2	31055	468	1257	4.7	6.7×10^7	2.1×10^7	0.32
	351	7.9	28490	(21367)					
	387	3.7	25839	496					
	408	6.4	24509	(20161)					
	442	3.1	22624						
Pyr_{ben}	317[s]	6.6	31545	454	962	3.7	8.6×10^7	2.7×10^7	0.32
	326	17.1	30674	(22026)					
	407	3.6	24570	482					
	428	5.8	23364	(20746)					
	474	4.2	21097	514					
				(19455)					

[a] Stokes shift and [s]shoulder

The lower energy bands in ca. 345 – 385 nm region were found to be similar in all three macrocycles. These bands arise due to several overlapping transitions and vibrational coupling between highly allowed ^1L_a and disallowed ^1L_b transitions.[20] The high extinction coefficient (ε) values of $S_0 \rightarrow S_1$ transitions indicates that such transitions are allowed in these macrocycles while the same transitions were found to be disallowed in pyrene itself.[21] Presumably, these variations arise from the increased rigidity in the macrocyclic framework, resulting in a small Δq in the potential energy surface (PES) for S_0 and S_1 states.[22] Furthermore, the transition dipole changes are expected due to the presence of a "cavity" in the macrocycles (Figure 4.6).[23]

4.3.1.2. Dilution Experiment

Since aggregation has been a common phenomenon in the π-conjugated macrocycles, dilution experiments were carried out to see if absorption profiles deviate from the Beer-Lambert law. However, the linearity of the Beer's-law plot (Figure 4.8) suggests that these macrocycles are not aggregating below a concentration of 40 μM i.e. under our experimental conditions. The results obtained from a linear regression analysis of Beer's law plots are provided in Table 4.2. As well, sample titration spectra of Pyr_{out} and a plot of absorbance vs. [Pyr_{out}] are given in Figure 4.8 (titration spectra and Beer's law plots of Pyr_{in} and Pyr_{in} are shown in the Appendix, Figures S4-S5).

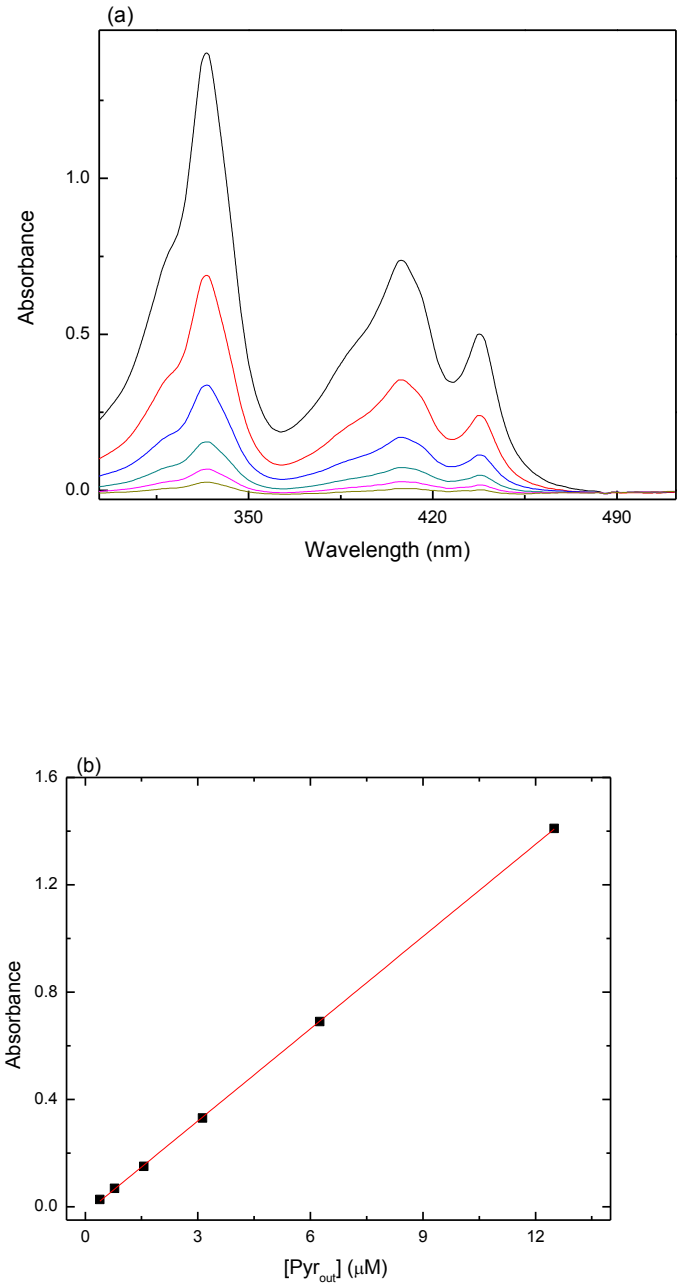

Figure 4.8. (a) Absorption spectral data obtained as a function of [Pyr_{out}] in CH_2Cl_2 at 298 ± 3 K. (b) Beer's law plot of the absorbance at λ = 333 nm as a function [Pyr_{out}]. The red line is the result of a linear least squares analysis of the data yielding a slope of 1.14 (± 0.1) × 10^5 M^{-1} cm^{-1}, R^2 = 0.995.

Table 4.2. The results obtained from a linear regression analysis of Beer's law plots for pyrene macrocycles, monitored at 333 nm.

Macrocycle	Slope, $M^{-1}cm^{-1}$	Intercept	R^2
Pyr_{in}	$7.8(\pm 0.2) \times 10^4$	$5.0(\pm 0.002) \times 10^{-3}$	0.99
Pyr_{out}	$1.1(\pm 0.1) \times 10^5$	$0.024(\pm 0.002)$	0.99
Pyr_{ben}	$1.6(\pm 0.2) \times 10^5$	$7.0(\pm 0.002) \times 10^{-3}$	0.99

4.3.1.3. Changes in Absorption Profiles after Addition of TFA

Absorption spectra of Pyr_{in}, Pyr_{out} and Pyr_{ben} as a function of increasing TFA (trifluoroacetic acid) acquired in CH_2Cl_2 at 298 ± 3 K are shown in Figure 4.9. Dramatic changes appear in the electronic spectra of all the macrocycles after addition of aliquots of TFA. It is evident from Figure 4.9 that the extinction coefficients of the macrocycles drop considerably suggesting that the protonated macrocycles are less absorbing than in the precursors. Noticeably, the appearance of isosbestic points is indicative of perturbation of the electronic environment within the macrocyclic framework. Furthermore, red shifts in the spectra of Pyr_{in} and Pyr_{out} were observed due to the build up of an intermediate. As well, loss of isosbestic points in the concentration region of ~10 - 22 mM in the case of Pyr_{in} and Pyr_{out} and ~119 – 280 mM in Pyr_{ben} was observed. Furthermore, the appearance of a weak and low energy band at ca. 535 nm (18690 cm^{-1}) in Pyr_{in} and 465 nm (21500 cm^{-1}) in Pyr_{out} can be observed with addition of aliquots of TFA. Interestingly, Pyr_{ben} also shows noticeable changes in the absorption profile after TFA addition. The intensity of the absorption envelope of Pyr_{ben} is attenuated and a new transition appeared at 285 nm (35085 cm^{-1}) while the remaining transitions are slightly shifted to higher energy.

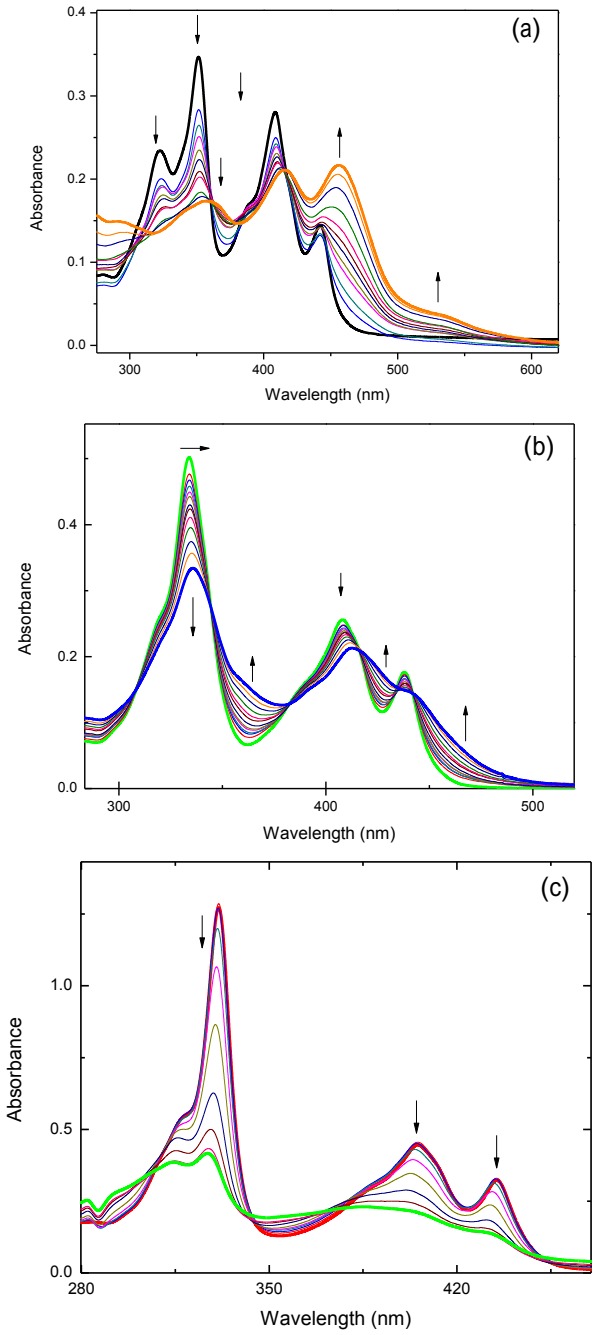

Figure 4.9. Absorption spectra of: (a) Pyr_{in} at 0.0, 1.90, 2.70, 3.50, 4.30, 5.10, 5.90, 6.70, 8.70, 10.7, 14.7, 14.7 and 22.7 mM; (b) Pyr_{out} at 0.0, 0.40, 0.80, 1.20, 1.60, 2.0, 2.80, 3.60, 4.80, 6.80, 10.0, 14.0 and 22.0 mM; (c) Pyr_{ben} at 0.0, 2.0, 9.90, 20.0, 50.0, 80.0, 119, 240 and 280 mM of TFA acquired in CH_2Cl_2 at 298 ± 3 K. [Pyr_{in}] = 2.6 μM, [Pyr_{out}] = 4.0 μM and [Pyr_{ben}] = 7.4 μM. The arrows indicate changes in the spectral response after the stepwise additions of TFA.[17]

In all three macrocycles, the alkoxy groups are connected to the pyrene double bond, making it a perfect enol ether moiety. It is well-documented that upon protonation, enol ethers prefer to be protonated on the sp^2 carbon end, instead of on the oxygen end (Scheme 4.2).[24-28] Therefore, the changes in the absorption spectra of Pyr_{in} and Pyr_{out} are attributed to protonation of the pyridinic nitrogens[15, 29] and the "enol ether" moities. In enol ether, the double bond is in conjugation with the oxygen lone pair. If the R group is hydrogen then the molecule is called a simple enol. The analogous of enol is known as enol ether. Nevertheless, the changes in the absorption spectra of Pyr_{ben} are presumably due to the protonation of the "enol ether" moieties. These results are indicative of significant equilibrium constants for protonation of the "enol ether" moiety. However, in the absence of any experimental evidence at the present time, the protonation of other sites such as pyrene double bonds is also possible and cannot be overruled.

Scheme 4.2. An illustration of the protonation of "enol ether" moiety.

The appearance of a weak-and low-energy band at ca. 535 nm (18690 cm^{-1}) in Pyr_{in} and 465 nm (21500 cm^{-1}) in Pyr_{out} is indicative of a CT transition from pyrene to protonated pyridine (Pyr → Py $2H^+$) initiated by protonation of the pyridinic nitrogens.[30]

The absence of a new low-energy transition in the case of Pyr_{ben} supports this assignment. Figure 4.10 shows the absorption spectra of macrocycles before and after the addition of TFA (~20 mM for Pyr_{in} and Pyr_{out} and ~128 mM for Pyr_{ben}) acquired in CH_2Cl_2. The experimental data show that the absorption spectra of Pyr_{in} and Pyr_{out} undergo noticeable redshift with a drop in the extinction coefficient.

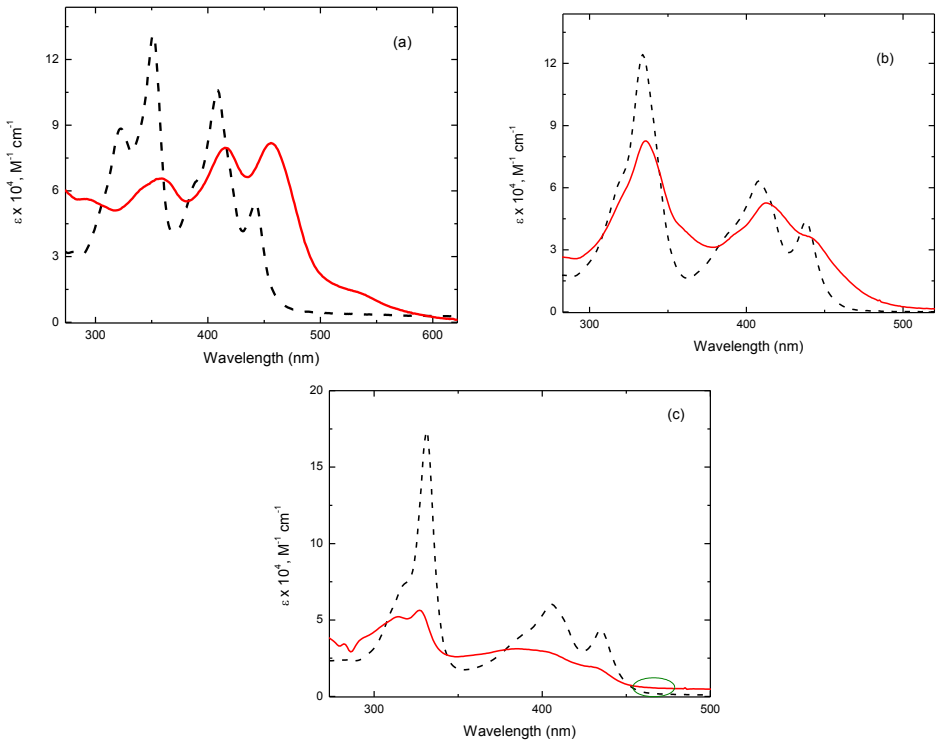

Figure 4.10. The effect of addition of TFA on the absorption spectra of (a) Pyr_{in}, (b) Pyr_{out} and (c) Pyr_{ben}. In each case, the broken line spectrum is the absorption spectrum of pure macrocycle and the solid line spectrum is that of the the corresponding protonated spectrum. Note the redshifts in the protonated spectra as compared to the non-protonated spectra in Pyr_{in} and Pyr_{out}. The green circle in Pyr_{ben} indicates the absence of a new weak intensity band. [Pyr_{in}] = 2.6 μM, [Pyr_{out}] = 4.0 μM and [Pyr_{ben}] = 7.4 μM. Data was acquired in $CHCl_2$ at 298 ± 3 K.

The largest redshift was observed for Pyr_{in} where the pyridinic nitrogens are present inside the cavity and the highest perturbation of the electronic environment is expected. In several literature reports, the redshift upon protonation in the absorption spectra of macrocycles comprised of pyridine rings has been assigned to an increase in the anti-aromatic character of the system.[31, 32]

4.3.1.4. Fluorescence

The fluorescence profiles of the macrocycles studied herein were found to posses similar band envelopes (Figure 4.7). It is clear from Figure 4.7 that the absorption and emission band profiles of all three macrocycles exhibit mirror image relationships, which is expected for a two-state system.[1, 20] The emission profiles consist of two major bands centered at 468 (21367 cm^{-1}) and 496 nm (20161 cm^{-1}) in Pyr_{in}, 460 (21739 cm^{-1}) and 489 nm (20449 cm^{-1}) in Pyr_{out} and 454 (22026 cm^{-1}) and 482 nm (20746 cm^{-1}) in Pyr_{ben} (Table 4.1). Clearly, the emission profile of Pyr_{in} is slightly red-shifted as compared to the other two macrocycles.

The fluorescence quantum yields (Φ_{em}) are comparable for the three macrocycles, with values of 0.37 (Pyr_{out}), 0.32 (Pyr_{in}) and 0.32 (Pyr_{ben}), respectively. The fluorescence lifetimes (τ) were also found to be similar with 4.0 ns (Pyr_{out}), 4.7 ns (Pyr_{in}) and 3.7 ns (Pyr_{ben}). This compares to Φ_{em} = 0.64 and τ = 480 ns for pyrene.[18] Since the ground-and excited-state properties are quite related in these macrocycles, it is worthy to conclude that the calculated rate of radiative decay (k_r), rate of non-radiative decay (k_{nr}), fluorescence quantum yield (Φ_{em}) and fluorescence lifetime (τ) are similar across the series (Table 4.1).

The lack of flexibility in the macrocyclic framework may attenuate the magnitude of k_{nr} and is responsible for the high Φ_{em} of these macrocycles as compared to some of the similar reported systems.[3, 22] Nevertheless, the largest Stokes-shift was calculated for the Pyr_{in} (E_{SS} = 1257 cm^{-1}) while the energy of emission was very similar across the series.

4.3.1.5. Changes in the Emission Profile after TFA Addition

Noticeable changes appear in the emission profile of macrocycles upon addition of TFA. Figure 4.11 shows the emission titration data of pyrene macrocycles as a function of increasing TFA acquired in CH_2Cl_2 at 298 ± 3 K. Once TFA is added $\pi \rightarrow \pi^*$ emission is attenuated and a low-energy band appears. The attenuation of Φ_{em} can be tentatively assigned to an increase in k_{nr} due to the CT from pyrene to the protonated pyridine, leading to fluorescence quenching. In the case of Pyr_{ben} the binding of TFA occurs at the "enol ether" directly attached to the chromophore (pyrene) and as a result, the fluorescence properties of the chromophore are altered.[1] This alteration is observed as attenuation in the fluorescence intensity, and consequently Φ_{em} of the Pyr_{ben}.

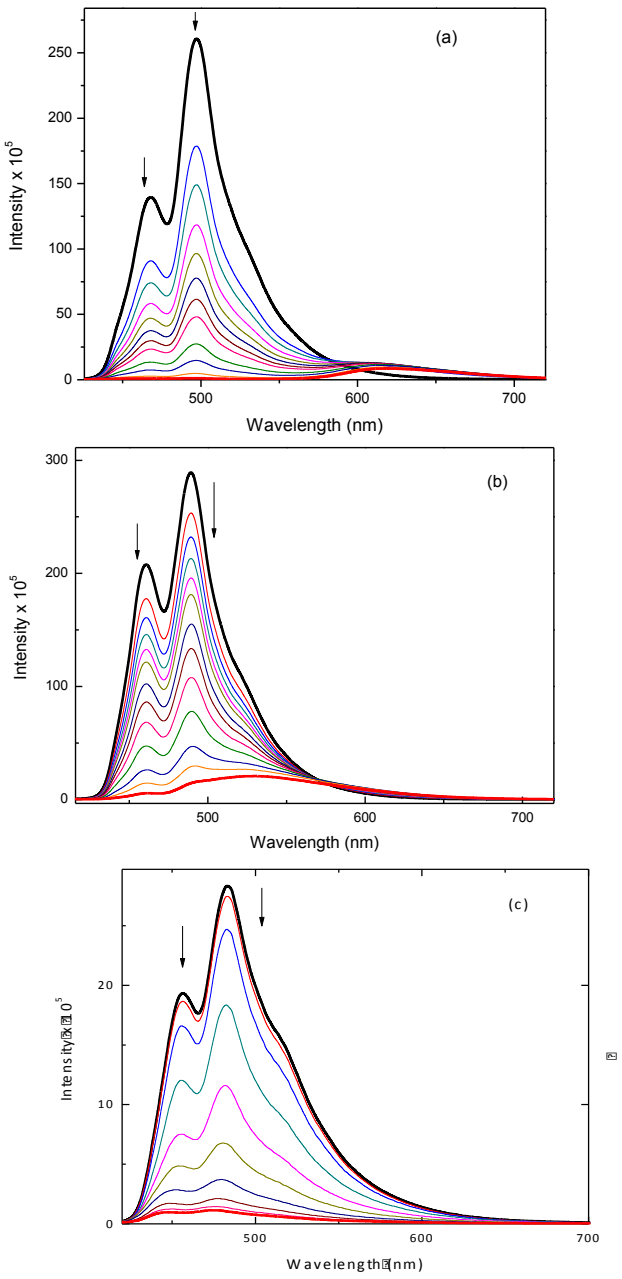

Figure 4.11. The fluorescence spectra of: (a) Pyr_{in} at 0.0, 1.90, 2.70, 3.50, 4.30, 5.10, 5.90, 6.70, 8.70, 10.7, 14.7, 14.7 and 22.7 mM; (b) Pyr_{out} at 0.0, 0.40, 0.80, 1.20, 1.60, 2.0, 2.80, 3.60, 4.80, 6.80, 10.0, 14.0 and 22.0 mM and (c) Pyr_{ben} at 0.0, 2.0, 9.90, 20.0, 50.0, 80.0, 119, 240 and 280 mM of TFA acquired in CH_2Cl_2 at 298 ± 3 K by exciting at 400 nm. The arrows indicate the spectral responses after the addition of TFA. Note the new broad and featureless, low-energy emission bands appearing in Pyr_{in} and Pyr_{out}. [Pyr_{in}] = 2.6 μM, [Pyr_{out}] = $4.0\ \mu M$ and [Pyr_{ben}] = $7.0\ \mu M$.

Appearance of a new broad and featureless band centred at 625 nm (16000 cm^{-1}) and 545 nm (18350 cm^{-1}) in the fluorescence spectra of Pyr_{in} and Pyr_{out}, respectively is evident (Figure 4.11 a and b). The emission profile of Pyr_{ben} appears to be similar to the other two macrocycles. However, upon addition of trifluoroacetic acid (TFA) to Pyr_{ben} no new bands in the fluorescence spectra were observed. Figure 4.12 shows the fluorescence spectra of the macrocycles after addition of TFA (20 mM for Pyr_{in} and Pyr_{out} and 128 mM for Pyr_{ben}) acquired in CH_2Cl_2. It is noticeable that both Pyr_{in} and Pyr_{out} (Figure 4.12 a and 4.12 b) display no vibronic progressions which are characteristic of a $\pi \rightarrow \pi^*$ transition and instead a new broad and featureless band characteristic of a $\mathrm{Pyr} \rightarrow \mathrm{Py} \cdot 2\mathrm{H}^+$ CT is observed. In the case of Pyr_{ben} (Figure 4.12 c) the same vibronic progressions can be observed and no new band appears.

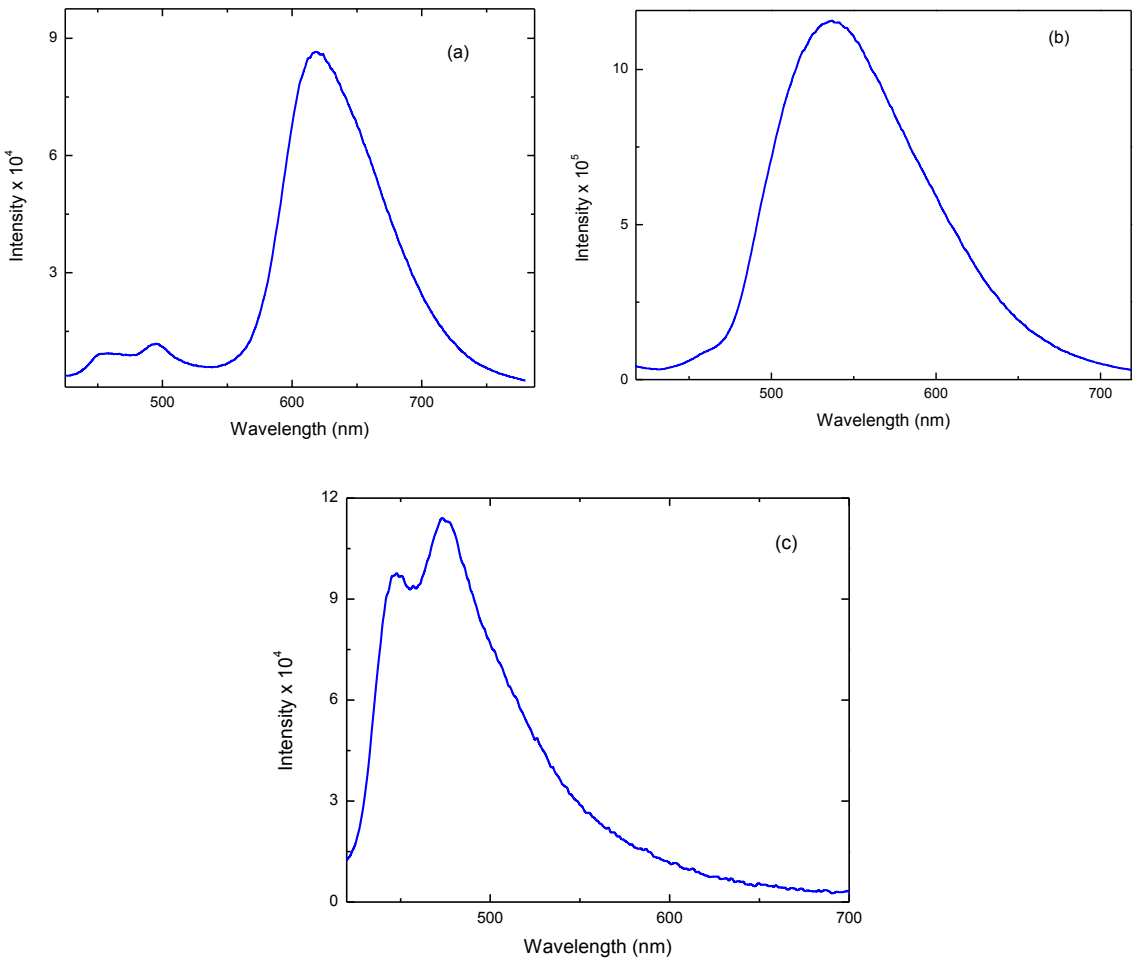

Figure 4.12. The fluorescence spectra of pyrene macrocycles: (a) Pyr_{in} after adding 20 mM of TFA(b) Pyr_{out} after adding 20 mM of TFA and (c) Pyr_{ben} upon addition of 128 mM of TFA. Spectra reveal the CT bands in Pyr_{in} and Pyr_{out} while Pyr_{ben} shows pyrene $\pi \rightarrow \pi^*$ emission and vibronic bands. The spectra were acquired in N_2 saturated CH_2Cl_2 at 298 ± 3 K by exciting at 400 nm.

4.3.1.6. Single-Value Decomposition (SVD) Analysis of the Absorption and Emission Spectra of the Macrocycles

It is quite evident from the absorption spectral data that there is formation of a ground-state adduct between the macrocycles and TFA (Figure 4.9). This ground-state adduct captures a photon of light and reaches the excited-state. A cursory analysis of the structures of Pyr_{in} and Pyr_{out} suggests two probable binding sites (pyridinic nitrogens) for the incoming H^+ based on pKa arguments and it is highly probable that incoming H^+ will preferably bind to the pyridinic nitrogens.[33] Based on this, sequential 1:1and 1:2 type of binding equilibria were predicted and the model (Scheme 4.3) was tested by analysis of the absorption and emission spectra using SPECFIT/32, to extract association constants.

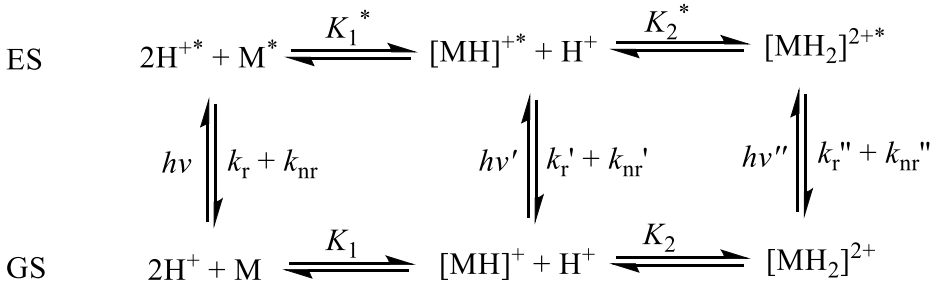

Scheme 4.3. A Förster cycle for sequential binding of H^+ with Pyr_{in} and Pyr_{out} macrocycles (M). Here, GS is the ground-state and ES is the excited-state.

Unfortunately, this model did not produce good fits to the single wavelength data or meaningful eigen vectors. Furthermore, this model ignores the "enol ether" binding and fails to explain all the binding events taking place in the Pyr_{in} and Pyr_{out} systems.

Therefore a new model was proposed (Scheme 4.4). In this model the first step belongs to a single-step protonation of both the pyridinic nitrogens and the second step to the binding of two "enol ether" moieties tethered to the pyrenes.

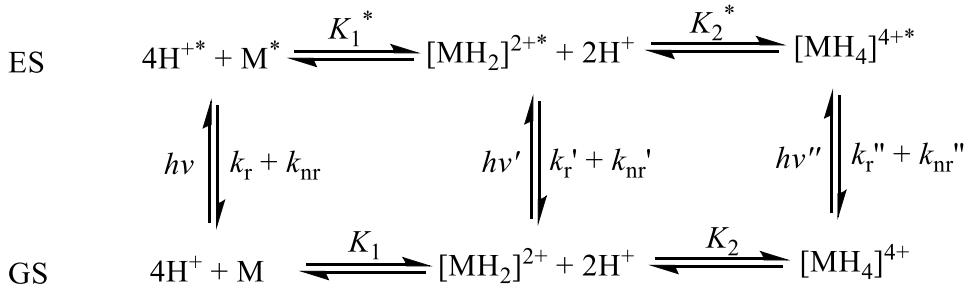

Scheme 4.4. A Förster cycle for overall binding of H^+ with Pyr_{in} and Pyr_{out} macrocycles. The first step in the binding event is the major contributing step and the second step contributes very small.

Based on the thermodynamic process depicted in Scheme 4.4, the absorption (Figure 4.9) and emission (Figure 4.11) titration curves were subjected to a single-value decomposition (SVD) procedure using the SPECFIT/32 program to extract the absorbing species and binding constants. The SVD procedure yielded satisfactory single wavelength fits and meaningful eigen vectors with a 1:2 and 1:4 binding model for Pyr_{in} and Pyr_{out}, in addition, the model also returned the global minimum. The concentration profiles shown in Figures 4.13-4.16 are consistent with a two-step mechanism for Pyr_{in} and Pyr_{out} macrocycles. The presence of the first three spectral eigen vectors V and the first three temporal eigen vectors from $U \times S$ (Figures S12-S18, in the appendix), as a result of the SVD of the spectral data matrix Y, also confirms the presence of three dominating spectral

species. The remaining curves in both the plots of V as well as $U \times S$ arise from the lamp, non-random instrument response and instrumental noise. The eigen values of V and $U \times S$ reach almost to zero and close to instrumental noise and they can be eliminated without further analysis.[34, 35] On the other hand, the first three eigen vectors show considerable eigen values and contain valuable information.

For Pyr_{ben} the analysis shows the presence of 1:2 type of binding equilibria (step 2 in Scheme 4.4). The concentration profile for Pyr_{ben} shown in Figure 4.17 a is consistent with a single-step mechanism. The proton binding in the Pyr_{ben} originates only from the interaction of H^+ with the "enol ether" moieties. This idea can be further confirmed by comparing the equilibrium constants of Pyr_{ben} and the last binding step of Pyr_{in} and Pyr_{out}, Expectedly, the equilibrium constant values are very close to each other, suggesting a similar binding event.

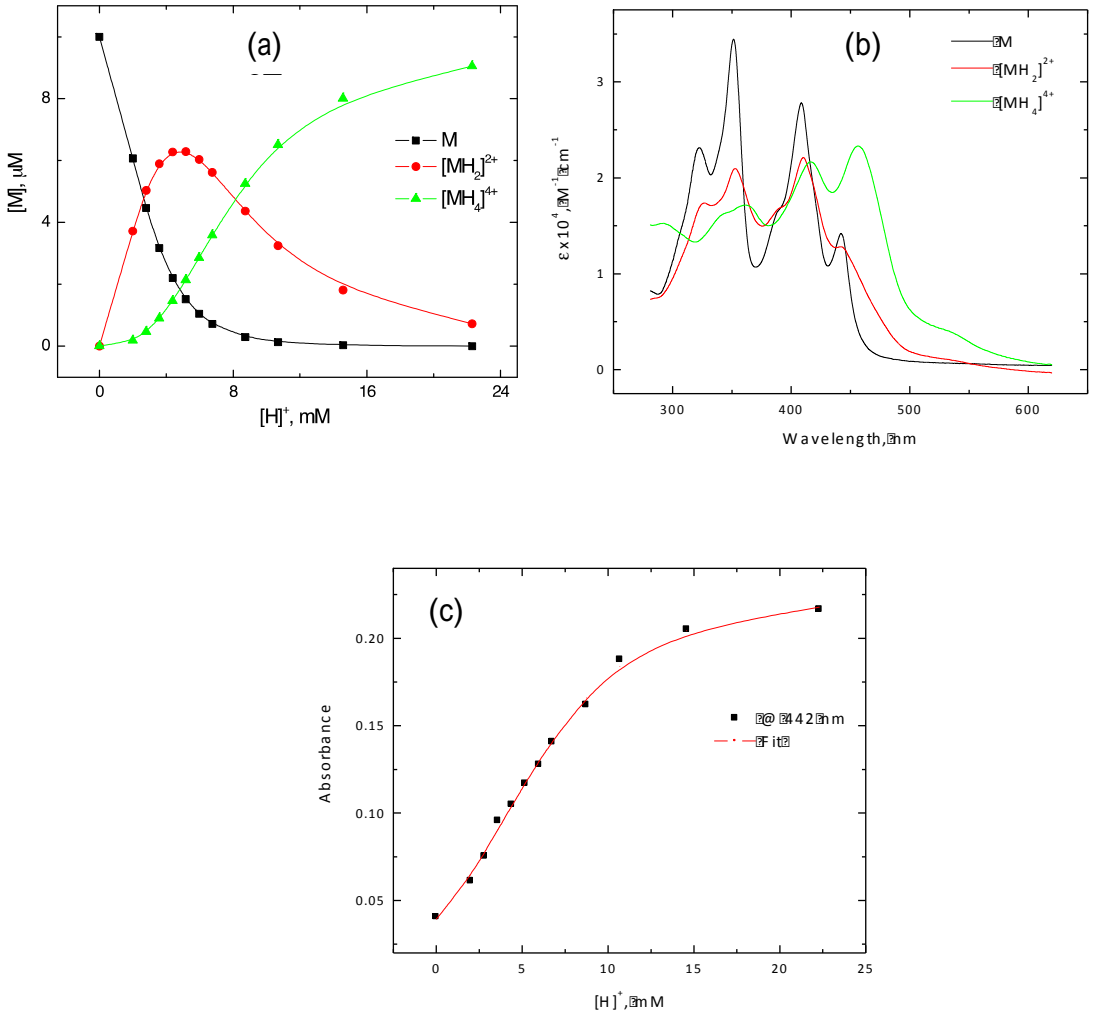

Figure 4.13. The SVD analysis of UV-Vis absorption titration data of Pyr_{in} macrocycle (M) with TFA using the SPECFIT/32 program. The data was fit to the model presented in Scheme 4.4; (a) the deconvoluted absorbing species and their concentrations; (b) deconvoluted spectra of the dominating species and their extinction coefficients, and (c) single-wavelength fit extracted as a result of SVD (λ = 442 nm), the black symbols are the experimental data and the red line is corresponding fit.

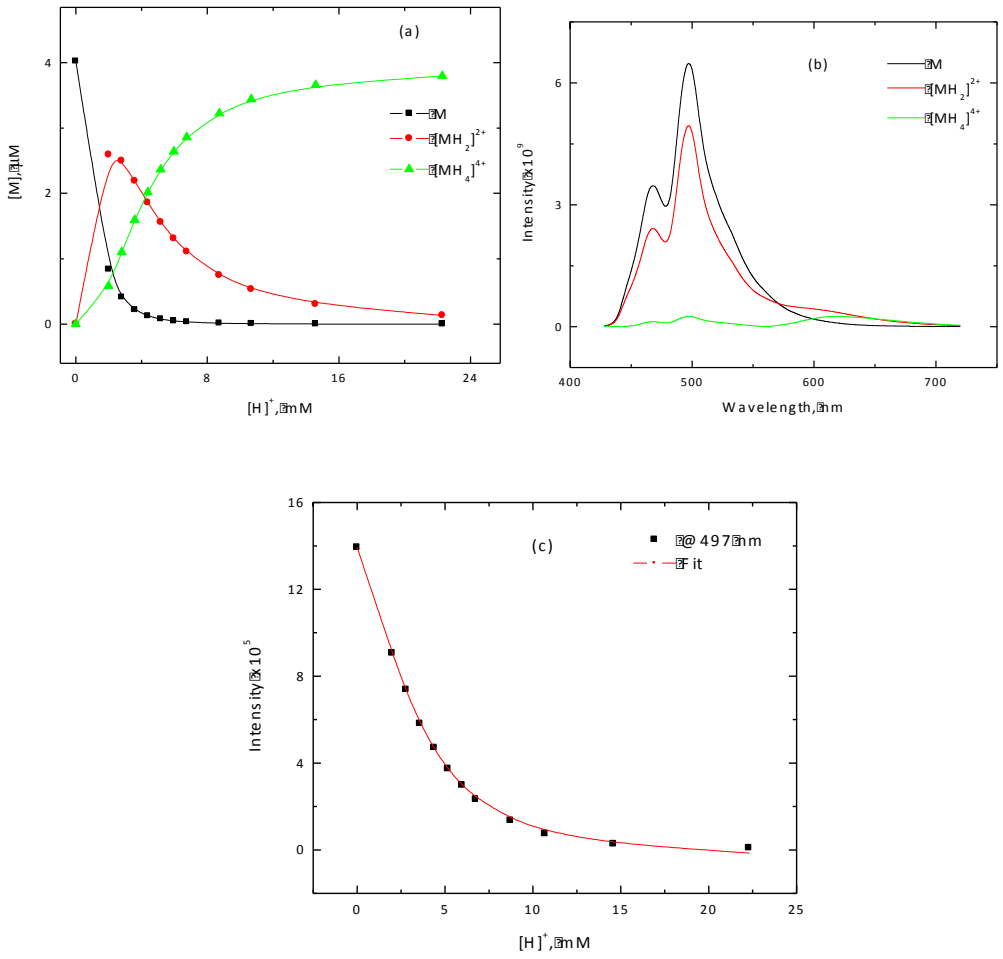

Figure 4.14. The SVD analysis of emission titration data of the Pyr_{in} macrocycle (M) with TFA using the SPECFIT/32 program. The data was fit to the model presented in Scheme 4.4: (a) The deconvoluted absorbing species and their concentrations (b) The deconvoluted spectra of the dominating species and (c) single-wavelength fit extracted as a result of SVD (λ = 497 nm). The black symbols are the experimental data and red line is the corresponding fit.

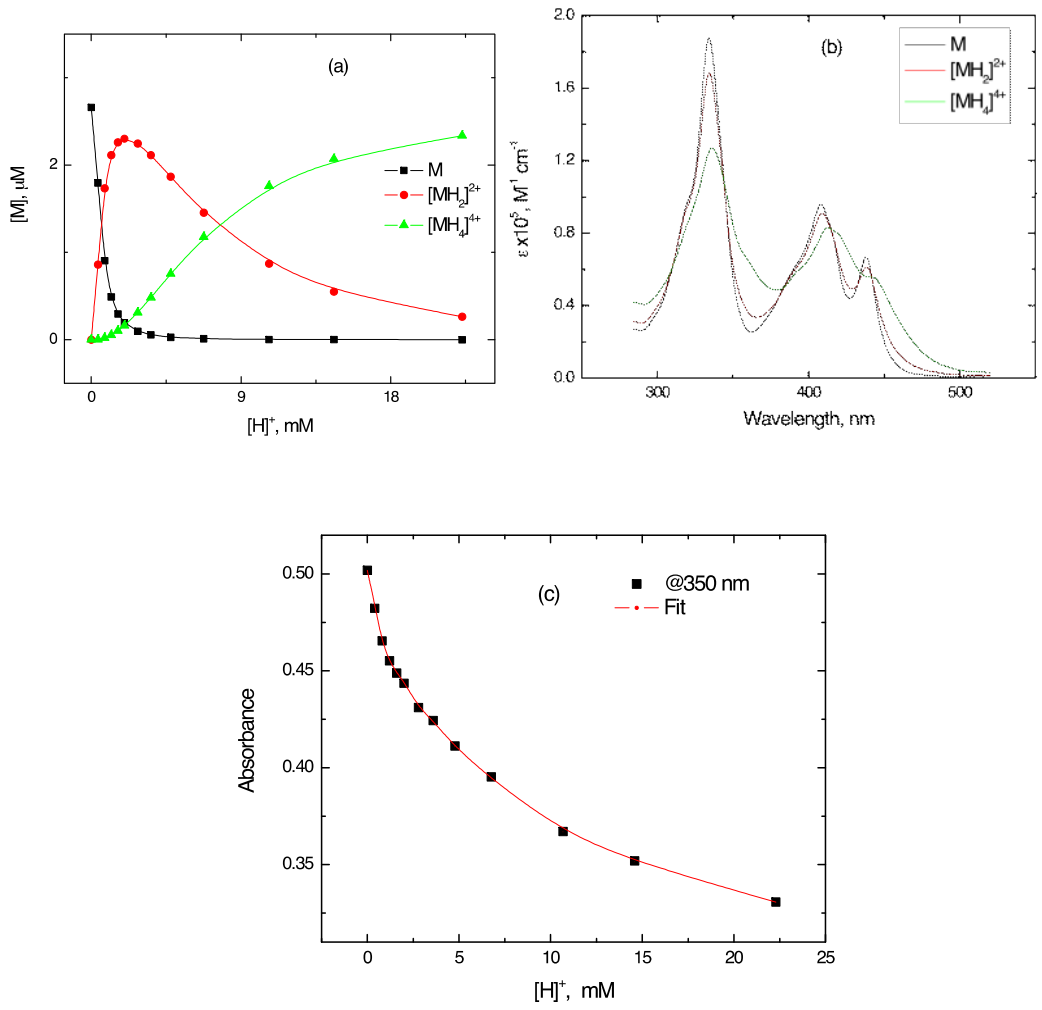

Figure 4.15. The SVD analysis of emission titration data of the Pyr_{out} macrocycle (M) with TFA using the SPECFIT/32 program. The data was fit to the model presented in Scheme 4.4: (a) The deconvoluted absorbing species and their concentrations (b) deconvoluted spectra of the dominating species and their extinction coefficients and (c) single-wavelength fit extracted as a result of SVD (λ = 350 nm). The black symbols are the experimental data and red line is the corresponding fit.

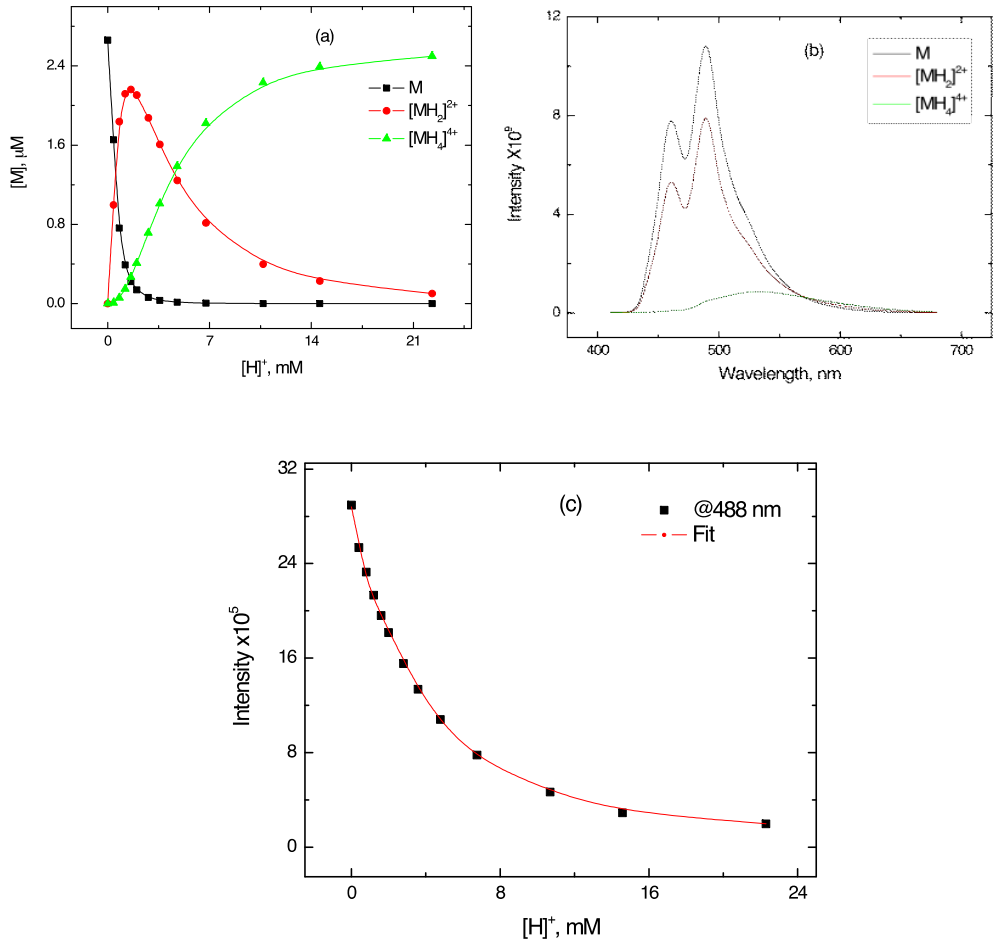

Figure 4.16. The SVD analysis of emission titration data of the Pyr_{out} macrocycle (M) with TFA using the SPECFIT/32 program. The data was fit to the model presented in Scheme 4.4: (a) The deconvoluted absorbing species and their concentrations (b) The deconvoluted spectra of the dominating species and (c) single-wavelength fit extracted as a result of SVD (λ = 488 nm). The black symbols are the experimental data and red line is the corresponding fit.

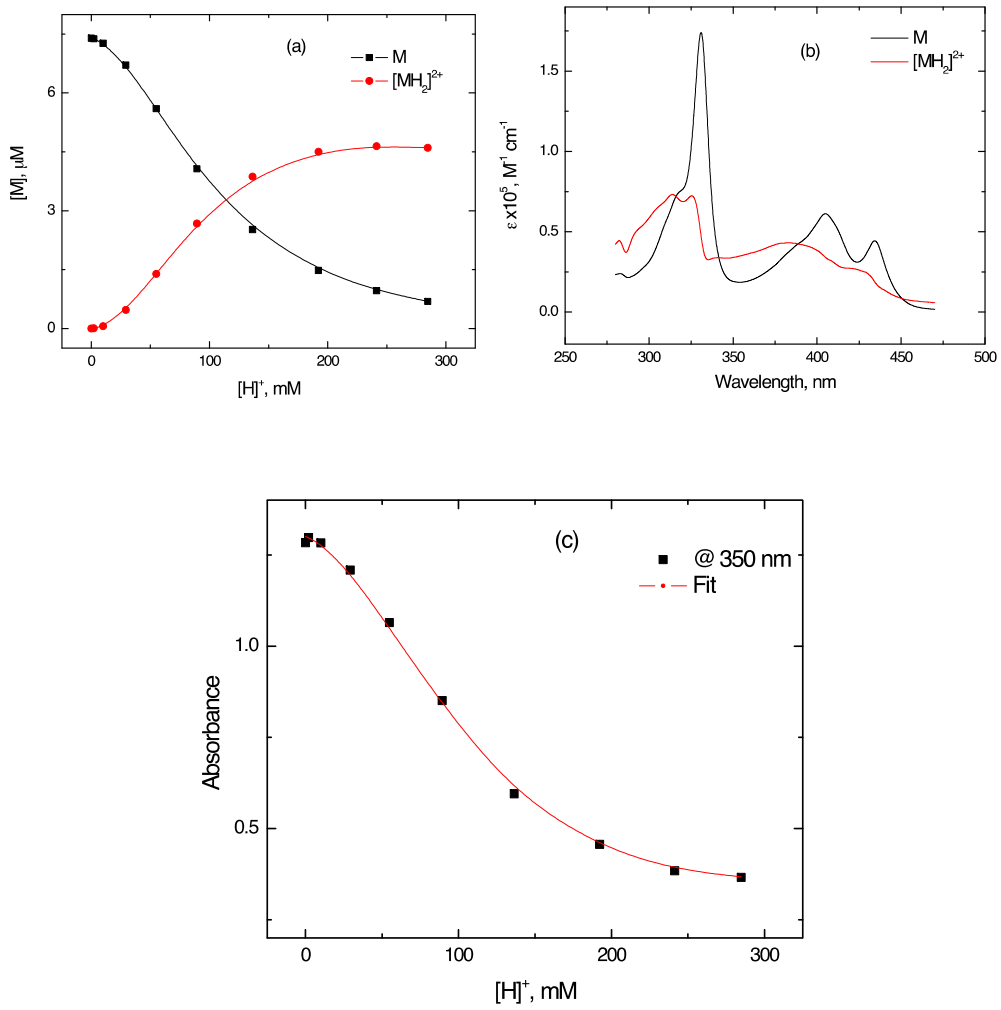

Figure 4.17. The SVD analysis of emission titration data of the Pyr_{ben} macrocycle (M) with TFA using the SPECFIT/32 program. The data was fit to the model presented in Scheme 4.4: (a) The deconvoluted absorbing species and their concentrations (b) deconvoluted spectra of the dominating species and their extinction coefficients and (c) single-wavelength fit extracted as a result of SVD (λ = 350 nm). The black symbols are the experimental data and red line is the corresponding fit.

Similar observations were made by Zhang et al. where the binding equilibria and the binding motif vary according to the availability of the binding sites. Figure 4.18 shows the macrocycles studied by Zhang et al.[36]

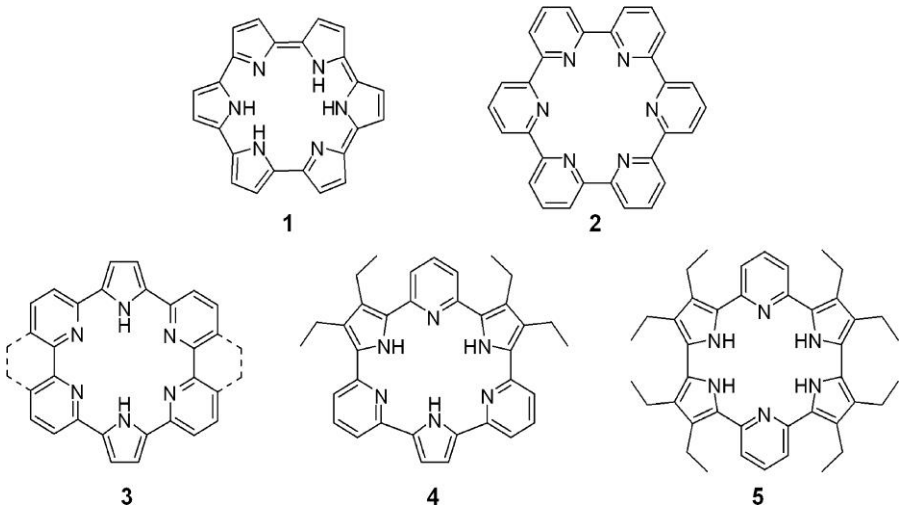

Figure 4.18. The macrocycles having varying proton binding sites investigated and reported by Zhang et al.[36]

A detailed list of thermodynamic parameters for both ground-and excited-state bindings of the pyr macrocycles are given in Table 4.3. The association constants were found to be in good-agreement with the previously reported values for similar systems.[37-40] The ground-state association constants for Pyr_{in} display values of $K_1 = 4.3(\pm 1.2) \times 10^3$ M^{-2} and $K_2 = 160 \pm 1.5$ M^{-2}. Pyr_{out} shows association constants of $K_1 = 3.3(\pm 1.2) \times 10^3$ M^{-2} and $K_2 = 182 \pm 1.2$ M^{-2}. As mentioned earlier, Pyr_{ben} shows a relatively smaller value of $K_1 = 109 \pm 0.1$ M^{-2}. In addition, the calculated values of ΔG^0 were very similar for both Pyr_{in} and Pyr_{out}.

Table 4.3. Thermodynamic parameters for sequential binding of the pyrene macrocycles with H^+.

Parameter	Pyr_{in}	Pyr_{out}	Pyr_{ben}
K_1, M^{-2}	$4.3(\pm 1.2) \times 10^3$	$3.3(\pm 1.2) \times 10^3$	109 ± 0.1
K_2, M^{-2}	160 ± 1.5	182 ± 1.2	
K_1^*, M^{-2}	$7.7(\pm 1.5) \times 10^3$	$6.2(\pm 1.2) \times 10^3$	
K_2^*, M^{-2}	182 ± 1.2	215 ± 5.0	
$\Delta G^0_{1,}\mathrm{cm}^{-1}$[a]	-899 ± 7.0	-871 ± 7.0	-504 ± 1.0
$\Delta G^0_{2,}\mathrm{cm}^{-1}$[a]	-545 ± 1.0	-559 ± 2.0	

[a] calculated by using $\Delta G^0 = -RTlnK$.

4.3.2. The Half Cycles of Pyrene-Pyridine Macrocycles

The Pyr_{in}-half and Pyr_{out}-half molecules were synthesized and analyzed to see how the spectral properties change when the corresponding full macrocycles are formed incorporated into a macrocycle. The "half cycles" were synthesized and provided by Prof. Graham Bodwell's group and their structures are shown in Figure 4.19.[17]

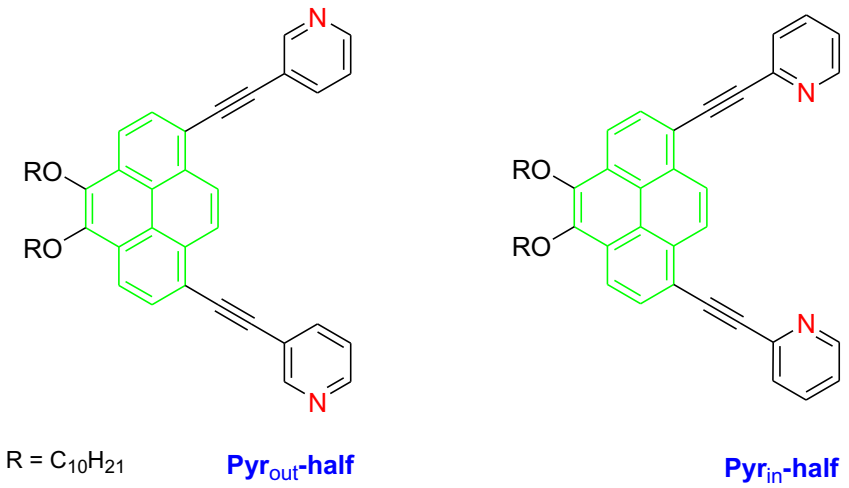

Figure 4.19. The structures of Pyr_{out}-half and Pyr_{in}-half.[17]

4.3.2.1. Absorption and Emission Spectra

The normalized absorption and emission spectra of the half cycles acquired in CH_2Cl_2 at 298 ± 3 K are shown in Figure 4.20, and the data is summarized in Table 4.4. The absorption spectra of both Pyr_{in}-half and Pyr_{out}-half exhibits two distinct absorption manifolds. The higher energy absorption manifold of both Pyr_{in}-half and Pyr_{out}-half exhibits intense bands at 325 nm (30770 cm^{-1} and $\varepsilon = 3.6 \times 10^5$ M^{-1} cm^{-1} for Pyr_{in}-half and $\varepsilon = 9.3 \times 10^4$ M^{-1} cm^{-1} for Pyr_{out}-half).

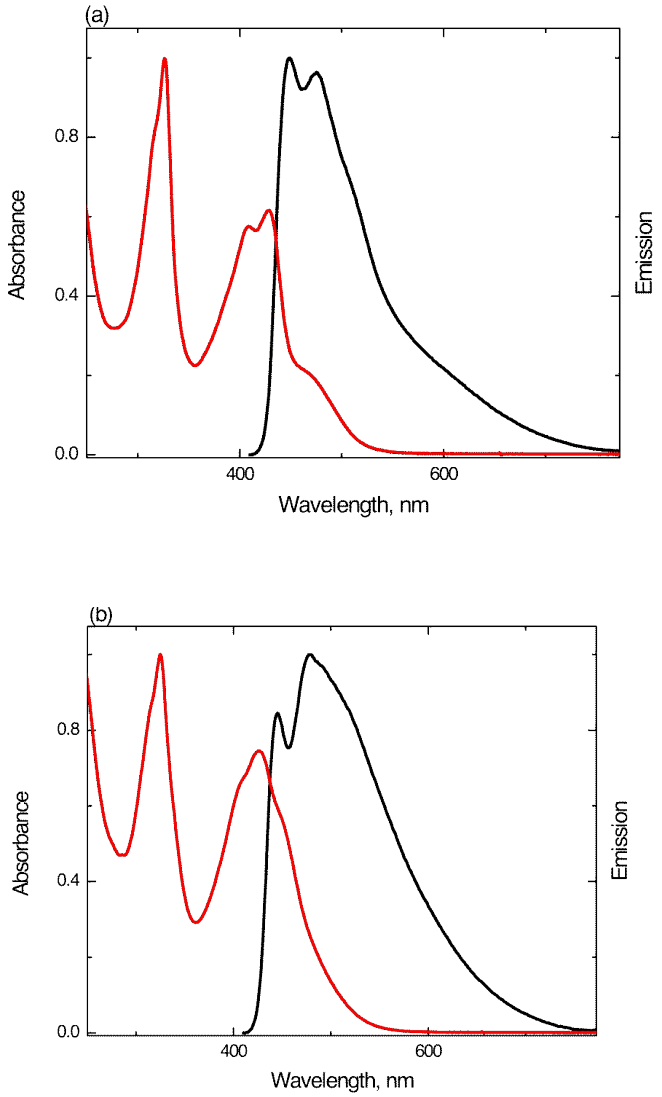

Figure 4.20. Normalized absorption and emission spectra of the pyrene half cycle molecules: (a) [Pyr_{in}-half] = 1.6 μM; and (b) [Pyr_{out}-half] = 3.2 μM. Spectra were acquired by exciting (λ_{exc} = 400 nm) a N_2 saturated CH_2Cl_2 sample solution at 298 ± 3 K.

Table 4.4. The photophysical properties of pyrene half cycles acquired in CH_2Cl_2 (1 atm N_2) at 298 ± 3 nm. Emission spectra were acquired by exciting at 400 nm.

Compound	λ_{abs} (nm)	$\varepsilon \times 10^5$ (M^{-1} cm^{-1})	E_{op} (cm^{-1})	λ_{em}, nm (cm^{-1})	E_{SS} (cm^{-1})[a]	τ, ns	k_r, s^{-1}	k_{nr}, s^{-1}	ϕ_{em}
Pyr_{in}-half	325	3.6	30770	448	1043	1.9	2.4×10^8	2.8×10^8	0.47
	315[s]	3.0	31750	(22320)					
	408	2.1	24505	475					
	428	2.2	23360	(21050)					
	475	0.68	21050						
Pyr_{out}-half	325	0.93	30770	445	1003	2.6	1.6×10^8	2.2×10^8	0.42
	313[s]	0.75	31950	(22470)					
	405[s]	0.59	24690	478					
	426	0.65	23470	(20920)					
	450[s]	0.50	22220						

[a]Stokes shift and [s]shoulder

The lower energy absorption manifold of Pyr_{in}-half exhibits two distinct intense bands at 408 nm (24505 cm^{-1}, ε = 2.1 $\times 10^5$ M^{-1} cm^{-1}) and 428 nm (23360 cm^{-1}, ε = 2.2 $\times 10^5$ M^{-1} cm^{-1}) and a weakly intense band at 475 nm (21050 cm^{-1}, ε = 6.8 $\times 10^4$ M^{-1} cm^{-1}). On the other hand in Pyr_{out}-half the lower energy absorption manifold exhibits only one well-resolved band at 426 nm (23470 cm^{-1}, ε = 6.5 $\times 10^4$ M^{-1} cm^{-1}) with shoulders at 405 nm (24690 cm^{-1}, ε = 5.9 $\times 10^5$ M^{-1} cm^{-1}) and 450 nm (22220 cm^{-1}, ε = 5.0 $\times 10^5$ M^{-1} cm^{-1}) Similar to the macrocycles, these bands can be assigned to $S_0 \rightarrow S_1$ ($\pi \rightarrow \pi^*$ in nature) transitions in the pyrene moiety.

The fluorescence spectra of the two half-cycle molecules are quite distinct from their macrocyclic counterparts. The emission bands are slightly blue-shifted as compared to their macrocyclic counterparts, and can be reasonably assigned to the $S_1 \rightarrow S_0$ transitions and the vibronic progressions leading to intense emission bands. From Table 4.4 it can be concluded that the Stokes shifts, the fluorescence lifetimes, the fluorescence quantum yields, the rates of radiative decay and the rates of non radiative decay are very similar in both half cycle molecules.

4.3.2.2. Protonation with TFA

The optical properties of half cycle molecules undergo dramatic changes upon TFA. The overall titration plots of half-cycle molecules obtained as a function of [TFA] in CH_2Cl_2 at 298 ± 3 K are shown in Figure 4.21.

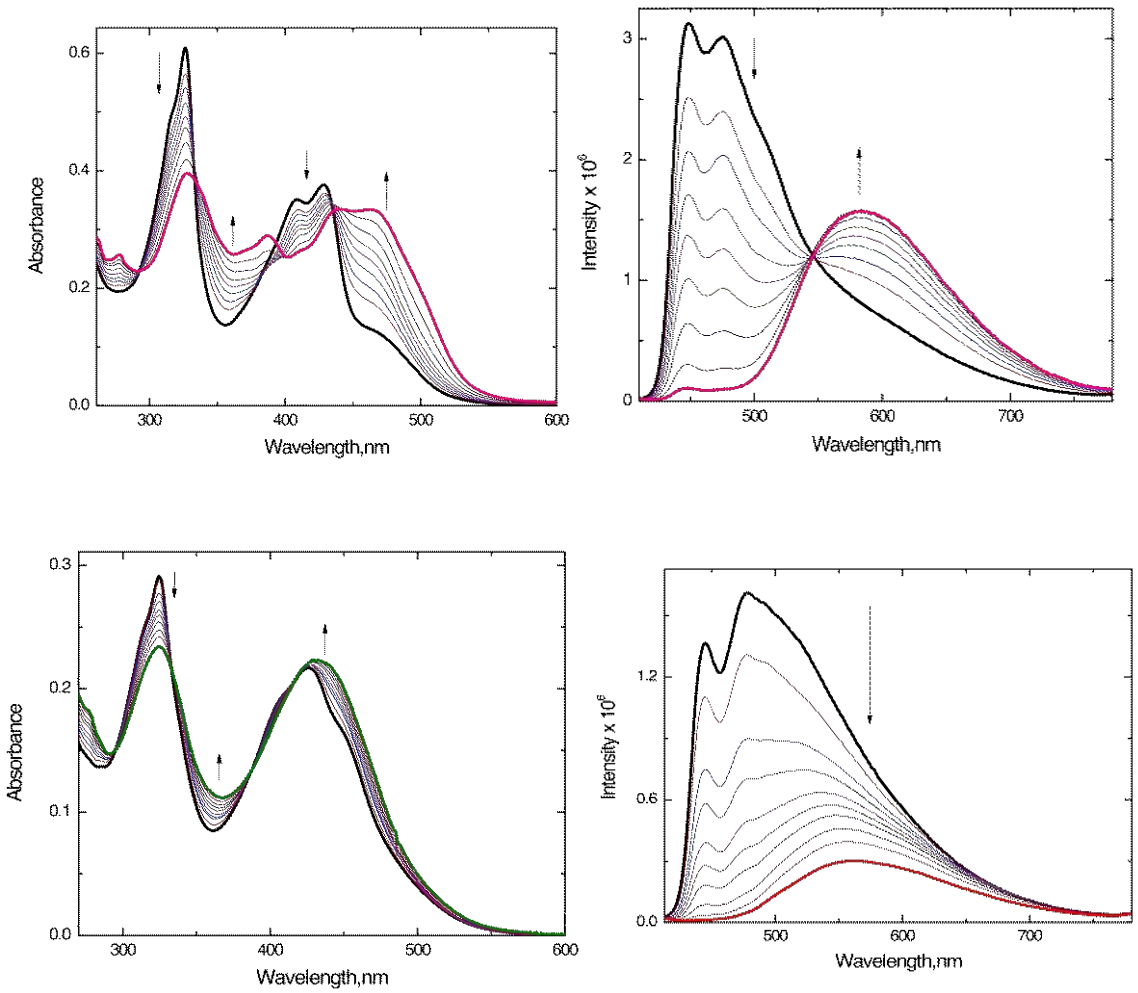

Figure 4.21. The absorption and emission spectra of the Pyr_{in}-half (top) and Pyr_{out}-half (bottom) obtained as a function of increasing TFA in the following manner: 0.0, 0.0018, 0.0039, 0.0059, 0.0071, 0.010, 0.017, 0.032, and 0.060 mM; (b) Pyr_{out}-half at 0.0, 0.0039, 0.0059, 0.0071, 0.010, 0.017, 0.032, and 0.060 mM in CH_2Cl_2 at 298 ± 3 K by exciting at 400 nm. The arrows indicate the spectral response after the addition of TFA. Note the new broad and featureless, low energy emission bands appearing in Pyr_{in}-half and Pyr_{out}-half. [Pyr_{in}-half] = 1.6 μM, [Pyr_{out}-half] = 3.2 μM.

Addition of TFA to the half cycles reveals quite distinct spectral properties than those of their macrocyclic counterparts. With the addition of TFA a blue shift in the absorption spectra with clear isosbestic points at 300 nm (33330 cm^{-1}), 340 nm (29410 cm^{-1}), 440 nm (27725 cm^{-1}) in Pyr_{in}-half and 295 nm (33895 cm^{-1}), 340 nm (29410 cm^{-1}), 395 nm (25315 cm^{-1}) and 420 nm (23810 cm^{-1}) in Pyr_{out}-half is evident. The presence of clear isosbestic points suggests the clean conversion of reactant (unprotonated half cycle) to product (protonated half cycle) with no build-up of an intermediate species. Furthermore, contrary to the macrocycles there is free rotation about the acetylene bonds in the half cycles (Figure 4.22) and an inductive effect through the σ-bond framework may alter the pyrene-based $\pi \rightarrow \pi^*$ transitions.

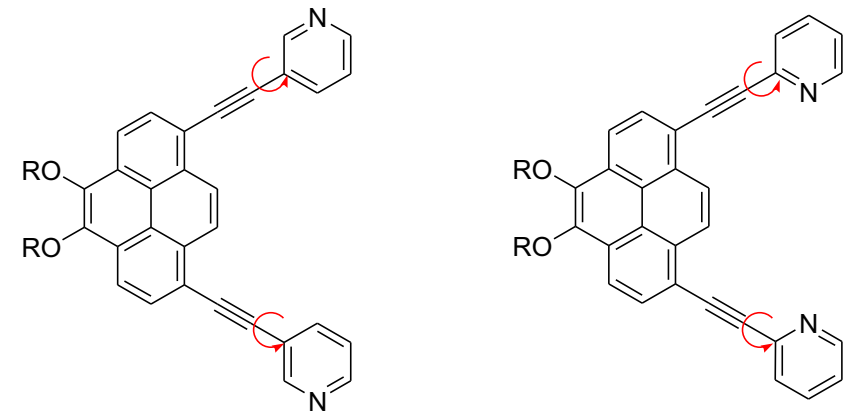

R = $C_{10}H_{21}$ **Pyr_{out}-half** **Pyr_{in}-half**

The single σ bonds allow rotation of the pyridyl fragment

Figure 4.22. A representation of the free rotation of the pyridyl fragment about the single bond that couples the pyridine to the acetylene bond.

The emission intensity of both Pyr_{in}-half and Pyr_{out}-half decreases with each addition of TFA. Furthermore, new low-energy, broad, featureless bands gradually appear at 585 nm (17095 cm^{-1}) and 560 nm (17850 cm^{-1}) for Pyr_{in}-half and Pyr_{out}-half, respectively. Similar to the macrocycles, these new bands can be tentatively assigned to a CT transition from the pyrene to the corrosponding protonated pyridine.[7, 12, 16, 21] A cursory analysis of both the new bands suggests that they are very pronounced in Pyr_{in}-half and Pyr_{out}-half as compared to the their macrocyclic counterparts.

4.3.2.3. Single-Value Decomposition Analysis of the Absorption and Emission Spectra of Half Cycles

In the case of half cycle molecules, any meaningful eigen vectors, single wavelength fits or coloured species were not observed for a model which incorporates the "enol ether". This is presumably due to the smaller amount of TFA added during the titration experiment as compared to that of macrocycles, which is probably not sufficient to protonate the "enol ether" moiety. Zhang et al. has reported similar results where protonation of all the available basic sites does not occur until an excess amount of HOTf is added.[36] This result casts light on the basicity of the pyridine units in the half cycles as compared to the macrocycles and can be further investigated in the future studies.[29, 41, 42]

Nonetheless, the titration data was subjected to single-value decomposition using SPECFIT/32 to extract the association constants using the direct 1:2 binding model shown in Scheme 4.5, and the resulting plots of the coloured (absorbing) species and the deconvoluted dominating species are shown in Figures 4.23 to 4.26.

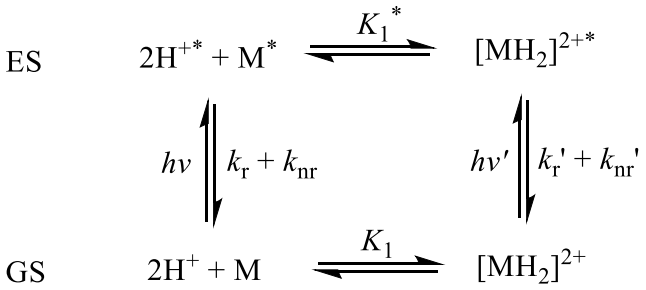

Scheme 4.5. A Förster cycle for the overall binding of H^+ with Pyr_{in}-half and Pyr_{out}-half.

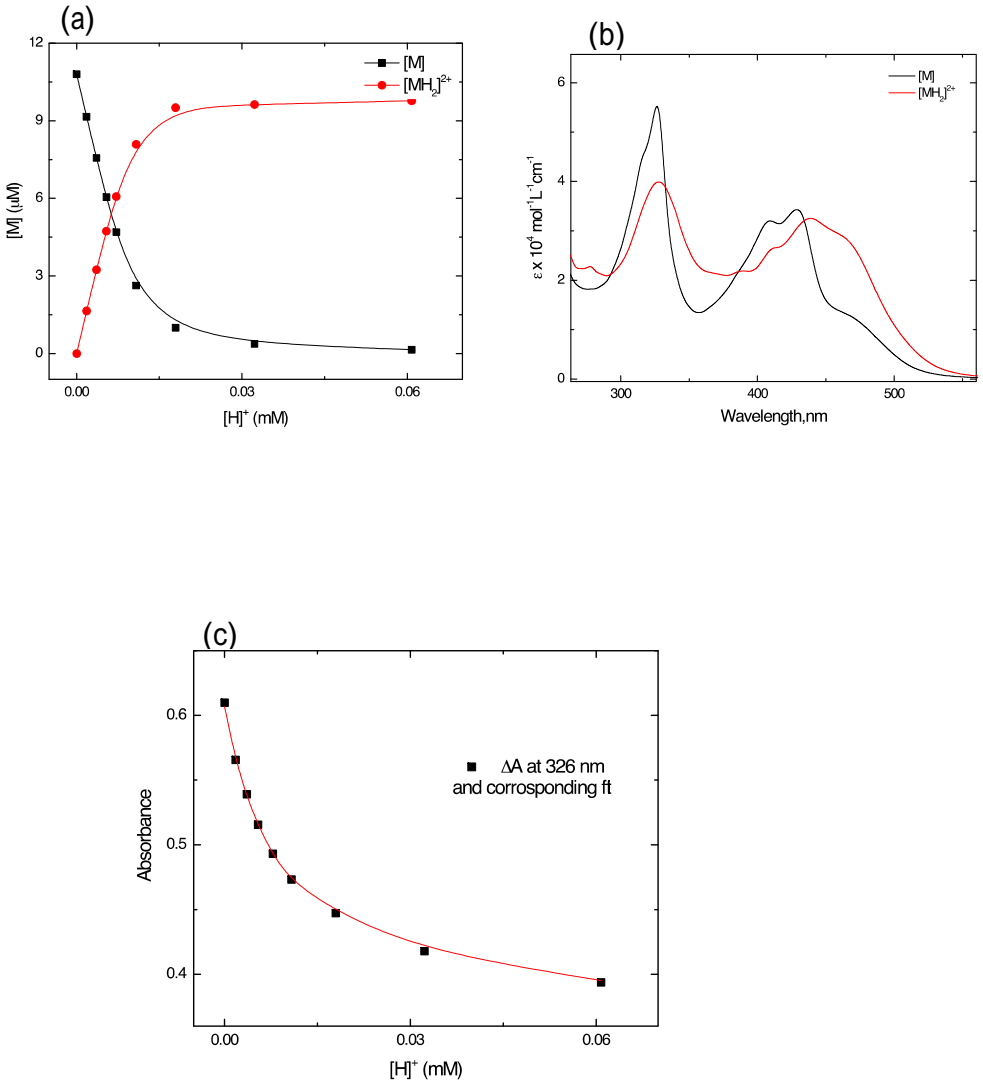

Figure 4.23. The SVD analysis of UV-Vis absorption titration data of Pyr_{in}-half macrocycle (M) with TFA using the SPECFIT/32 program. The data was fit to the model presented in Scheme 4.5; (a) the deconvoluted absorbing species and their concentrations; (b) deconvoluted spectra of the dominating species and their extinction coefficients, and (c) single-wavelength fit extracted as a result of SVD (λ = 326 nm), the black symbols are the experimental data and the red line is corresponding fit.

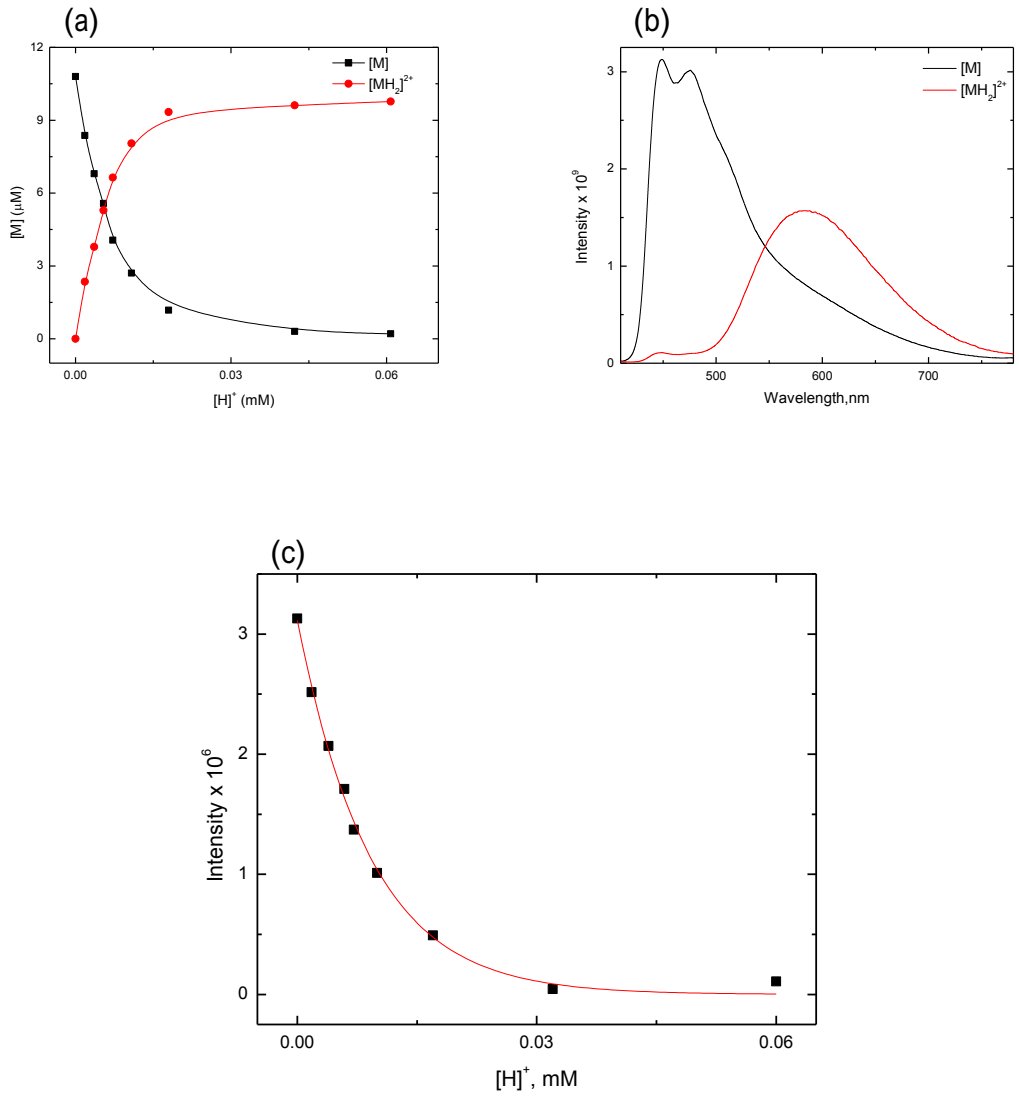

Figure 4.24. The SVD analysis of UV-Vis absorption titration data of Pyr_{in}-half macrocycle (M) with TFA using the SPECFIT/32 program. The data was fit to the model presented in Scheme 4.5; (a) the deconvoluted absorbing species and their concentrations; (b) deconvoluted spectra of the dominating species, and (c) single-wavelength fit extracted as a result of SVD (λ = 448 nm), the black symbols are the experimental data and the red line is corresponding fit.

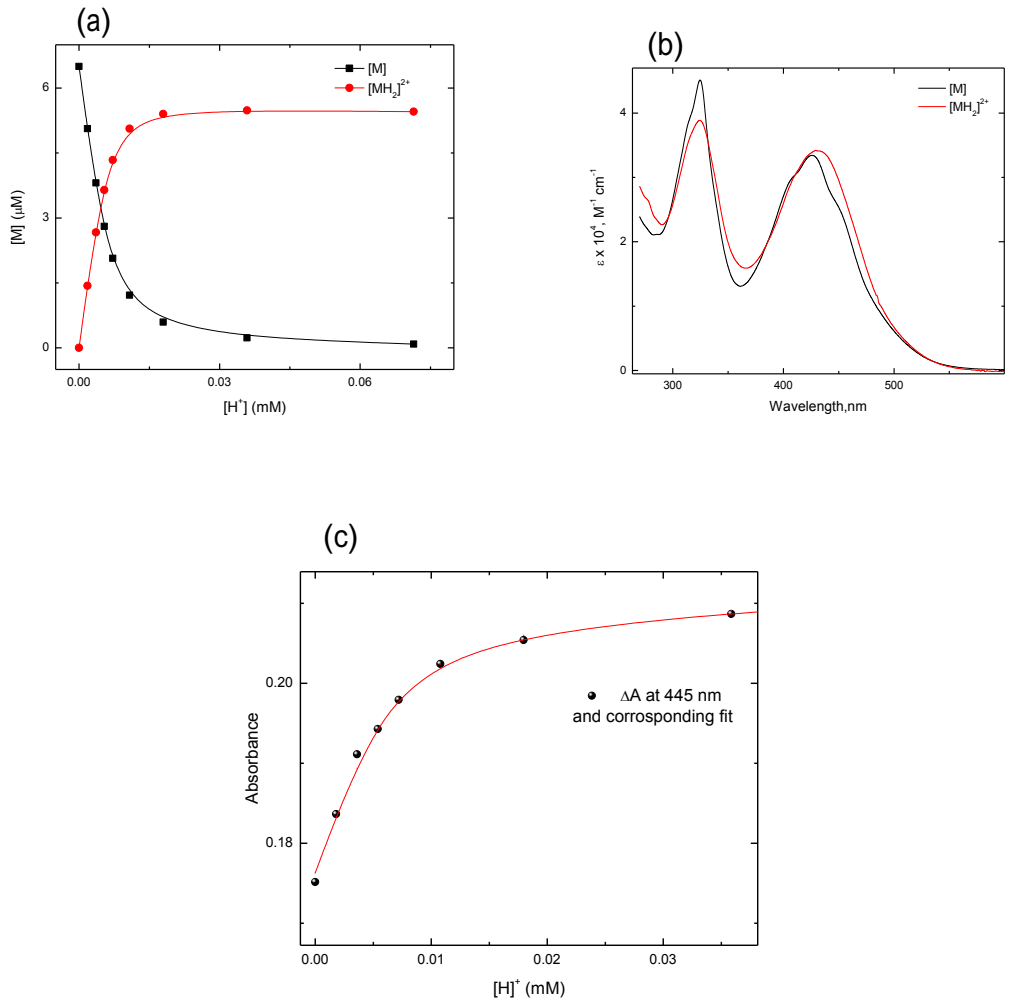

Figure 4.25. The SVD analysis of UV-Vis absorption titration data of Pyr_{out}-half macrocycle (M) with TFA using the SPECFIT/32 program. The data was fit to the model presented in Scheme 4.5; (a) the deconvoluted absorbing species and their concentrations; (b) deconvoluted spectra of the dominating species and their extinction coefficients, and (c) single-wavelength fit extracted as a result of SVD (λ = 445 nm), the black symbols are the experimental data and the red line is corresponding fit.

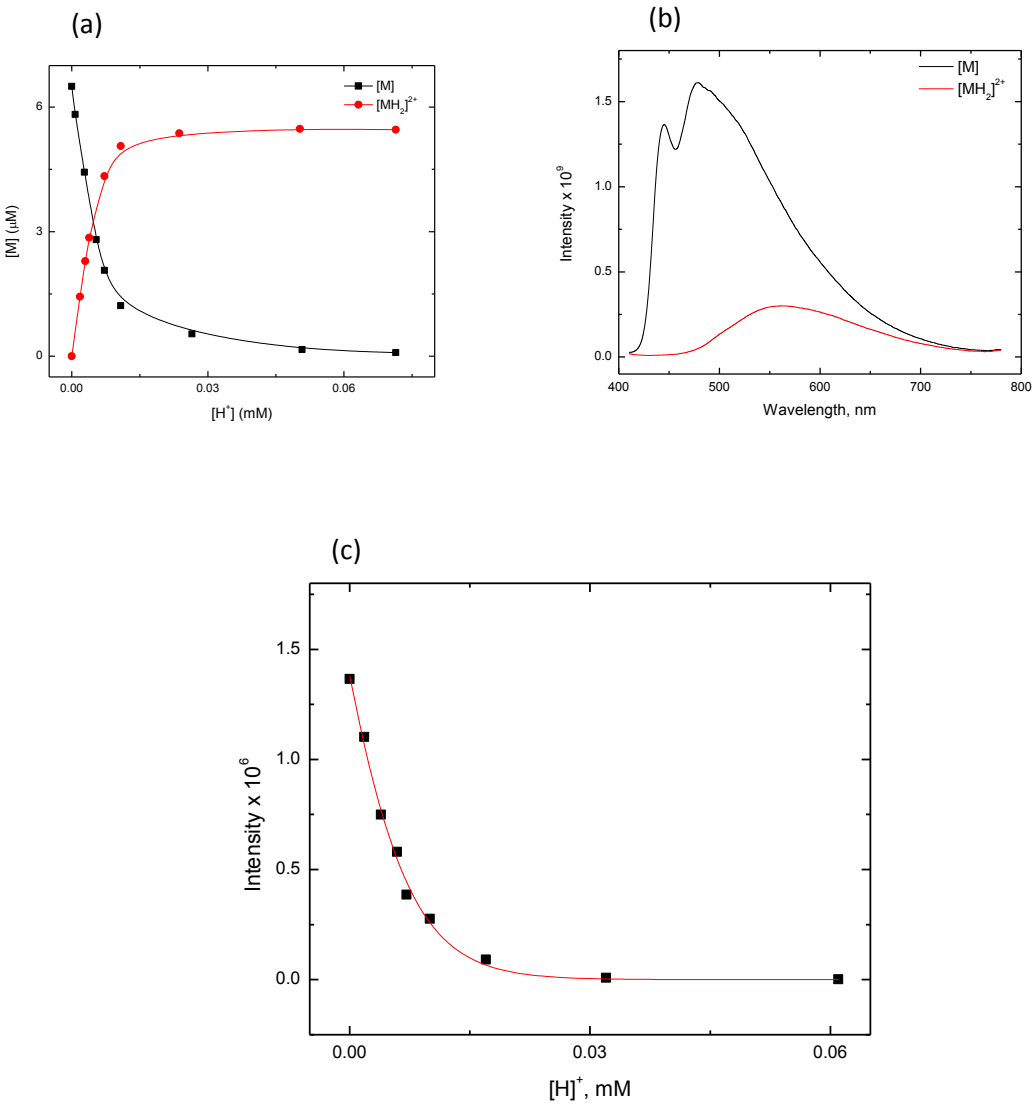

Figure 4.26. The SVD analysis of UV-Vis absorption titration data of Pyr_{out}-half macrocycle (M) with TFA using the SPECFIT/32 program. The data was fit to the model presented in Scheme 4.5; (a) the deconvoluted absorbing species and their concentrations; (b) deconvoluted spectra of the dominating species, and (c) single-wavelength fit extracted as a result of SVD (λ = 480 nm), the black symbols are the experimental data and the red line is corresponding fit.

The coloured (absorbing) species obtained are consistent with the model presented in Scheme 4.5. A detailed list of the thermodynamic parameters is presented in Table 4.5. The association constants for the half cycles were found to be larger than those of the corresponding macrocycles. This suggests a possible role of the cavity present in the case of the macrocycles. The association constants (K) for Pyr_{in}-half were calculated to be $K_1 = 5.82(\pm 1.3) \times 10^4\ \mathrm{M}^{-1}$ from the ground-state and $K_1 = 5.21(\pm 1.1) \times 10^4\ \mathrm{M}^{-1}$ from the excited-state, whereas, for Pyr_{out}-half $K_1 = 8.23(\pm 2.1) \times 10^4\ \mathrm{M}^{-1}$ from the ground-state and $K_1 = 7.11(\pm 2.1) \times 10^4\ \mathrm{M}^{-1}$ from the excited-state were calculated.

Table 4.5. Thermodynamic parameters for the half cycles.

Parameter	Pyr_{in}-half	Pyr_{out}-half
K_1, M^{-1}	$5.82(\pm 1.3) \times 10^4$	$8.23(\pm 2.1) \times 10^4$
K_1^*, M^{-1}	$5.21(\pm 1.1) \times 10^4$	$7.11(\pm 2.1) \times 10^4$
$\Delta G_{1,}^{0}\mathrm{cm}^{-1}$	-117 $\pm$9.5	-123 $\pm$ 10
$\Delta G_{1,}^{0*}\mathrm{cm}^{-1}$	-116 $\pm$9.3	-120$\pm$10

[*] calculated from the fluorescence spectral data

In summary, the addition of TFA to the half cycle molecules causes two major effects: first, the protonation of pyridinic nitrogens in single-step equilibria. Second, as a result of protonation, the pyridine moieties become electron acceptor which inductively polarizes the electron density.

4.4. Concluding Remarks

Based on the spectral analysis of pyrene macrocycles and the half cycle molecules, the following key conclusions can be made:

1. The addition of TFA brings dramatic changes in the spectral properties due to the protonation of the pyridinc nitrogens and the "enol ether" moieties. In the model macrocycle Pyr_{ben}, the spectral changes are mainly associated with the protonation of the "enol ether" moieties in the absence of pyridinic nitrogens.

2. As a result of protonation, new broad and featureless bands appear in all the systems except Pyr_{ben}. The origin of these new bands can be tentatively assigned to an intramolecular charge transfer (ICT) from pyrene to the protonated pyridine. The absence of a new band in the case of Pyr_{ben} further manifests the assumption of ICT. As an extension to this study, these new bands can be analysed using time-resolved spectroscopy to get further insights into the CT dynamics.

3. The SVD analysis of ground and excited-state spectral data of all the systems acquired as a function of [TFA] indicates that the macrocycles Pyr_{in} and Pyr_{out} form 1:2 and 1:4 complexes with H^+, while Pyr_{ben} interacts in a 1:2 fashion through two of its "enol ether" moieties. On the other hand, the half cycles show a direct 1:2 type of binding with comparatively enhanced association constants.

References

[1] Venkataramana, G.; Dongare, P.; Dawe, L. N.; Thompson, D. W.; Zhao, Y.; Bodwell, G. J., Org. Lett., (2011) 13, 2240.

[2] Chirvony, V. S.; van Hoek, A.; Galievsky, V. A.; Sazanovich, I. V.; Schaafsma, T. J.; Holten, D., J. Phys. Chem. B, (2000) 104, 9909.

[3] Figueira-Duarte, T. M.; Mullen, K., Chem. Rev., (2011) 111, 7260.

[4] Iyoda, M.; Yamakawa, J.; Rahman, M. J., Angew. Chem. Int. Ed., (2011) 50, 10522.

[5] Andreasson, J.; Zetterqvist, H.; Kajanus, J.; Martensson, J.; Albinsson, B., J. Phys. Chem. A, (2000) 104, 9307.

[6] Widanapathirana, L.; Zhao, Y., J. Org. Chem., (2012) 77, 4679.

[7] Grabowski, Z. R.; Rotkiewicz, K.; Rettig, W., Chem. Rev., (2003) 103, 3899.

[8] Thomas, K. R. J.; Kapoor, N.; Bolisetty, M.; Jou, J. H.; Chen, Y. L.; Jou, Y. C.,J. Org. Chem., (2012) 77, 3921.

[9] Krotkus, S.; Kazlauskas, K.; Miasojedovas, A.; Gruodis, A.; Tomkeviciene, A.; Grazulevicius, J. V.; Jursenas, S., J. Phys. Chem. C, (2012) 116, 7561.

[10] Perez-Prieto, J.; Perez, L. P.; Gonzalez-Bejar, M.; Miranda, M. A.; Stiriba, S.-E., Chem. Commun., (2005), 5569.

[11] Lu, G.; Shi, G., J. Electro. Anal. Chem., (2006) 586, 154.

[12] Sung, J.; Kim, P.; Lee, Y. O.; Kim, J. S.; Kim, D., J. Phys. Chem. Letters, (2011) 2, 818.

[13] Winnik, F. M., Chem. Rev., (1993) 93, 587.

[14] Thulstrup, E. W.; Michl, J., Spectrosc. Lett., (1977) 10, 435.

[15] Baxter, P. N. W.; Dali-Youcef, R., J. Org. Chem., (2005) 70, 4935.

[16] Giansante, C.; Ceroni, P.; Venturi, M.; Balzani, V.; Sakamoto, J.; Schlüter, A. D., Chem. Eur. J., (2008) 14, 10772.

[17] Venkataramana, G.; Dongare, P.; McKinnon, M.; Thompson, D. W.; Zhao, Y.; Bodwell, G., unpublished results, Memorial University of Newfoundland: St. Johns, (2012).

[18] Tran-Thi, T. H.; Prayer, C.; Millié, P.; Uznanski, P.; Hynes, J. T., J. Phys. Chem. A, (2002) 106, 2244.

[19] Cho, H. S.; Song, J. K.; Ha, J.-H.; Cho, S.; Kim, D.; Yoshida, N.; Osuka, A., J. Phys. Chem. A, (2003) 107, 1897.

[20] Nandaluru, P. R.; Dongare, P.; Kraml, C. M.; Pascal, R. A.; Dawe, L. N.; Thompson, D. W.; Bodwell, G. J., Chem. Commun., (2012) 48, 7747.

[21] Birks, J. B.; Munro, I. H.; Lumb, M. D., Proc. R. Soc. A, (1964) 280, 289.

[22] Nicholas J. Turro; V. Ramamurthy; Scaiano, J. C., Principles of Molecular Photochemistry: An Introduction, University Science Books (2009).

[23] Grave, C.; Lentz, D.; Schäfer, A.; Samorì, P.; Rabe, J. P.; Franke, P.; Schlüter, A. D., J. Am. Chem. Soc., (2003) 125, 6907.

[24] Fagnoni, M.; Dondi, D.; Ravelli, D.; Albini, A., Chem. Rev., (2007) 107, 2725.

[25] Kresge, A. J.; Chen, H. J.; Hakka, L. E.; Kouba, J. E., J. Am. Chem. Soc., (1971) 93, 6174.

[26] Poisson, T.; Gembus, V.; Dalla, V.; Oudeyer, S.; Levacher, V., J. Org. Chem., (2010) 75, 7704.

[27] Reid, C., J. Am. Chem. Soc., (1954) 76, 3264.

[28] Saed, B.; Omidyan, R., J. Phys. Chem. A, (2013) 117, 2499.

[29] Spitler, E. L.; McClintock, S. P.; Haley, M. M., J. Org. Chem., (2007) 72, 6692.

[30] Constable, E. C.; Neuburger, M.; Rösel, P.; Schneider, G. E.; Zampese, J. A.; Housecroft, C. E.; Monti, F.; Armaroli, N.; Costa, R. D.; Ortí, E., Inorg. Chem., (2012) 52, 885.

[31] Mori, S.; Kim, K. S.; Yoon, Z. S.; Noh, S. B.; Kim, D.; Osuka, A., J. Am. Chem. Soc., (2007) 129, 11344.

[32] Roznyatovskiy, V. V.; Lim, J. M.; Lynch, V. M.; Lee, B. S.; Kim, D.; Sessler, J. L., Org. Lett., (2011) 13, 5620.

[33] Brown, H. C., Organic Syntheses via Boranes, Academic Press New York: (1955); Vol. 1.

[34] Binstead, R. A.; Stultz, L. K.; Meyer, T. J., Inorg. Chem., (1995) 34, 546.

[35] Stultz, L. K.; Reynolds, M. S.; Binstead, R.; Meyer, T. J., Abstracts of Papers of the American Chemical Society, (1994) 207, 254.

[36] Zhang, Z.; Lim, J. M.; Ishida, M.; Roznyatovskiy, V. V.; Lynch, V. M.; Gong, H.-Y.; Yang, X.; Kim, D.; Sessler, J. L., J. Am. Chem. Soc., (2012) 134, 4076.

[37] Zapata, F.; Caballero, A.; White, N. G.; Claridge, T. D. W.; Costa, P. J.; Félix, V. t.; Beer, P. D., J. Am. Chem. Soc., (2012) 134, 11533.

[38] Meyer, M.; Fremond, L.; Tabard, A.; Espinosa, E.; Vollmer, G. Y.; Guilard, R.; Dory, Y., New J. Chem., (2005) 29, 99.

[39] Sessler, J. L.; Karnas, E.; Kim, S. K.; Ou, Z.; Zhang, M.; Kadish, K. M.; Ohkubo, K.; Fukuzumi, S., J. Am. Chem. Soc., (2008) 130, 15256.

[40] Granzhan, A.; Teulade-Fichou, M.-P., Tetrahedron, (2009) 65, 1349.

[41] Wilson, J. N.; Bunz, U. H. F., J. Am. Chem. Soc., (2005) 127, 4124.

[42] Zucchero, A. J.; Wilson, J. N.; Bunz, U. H. F., J. Am. Chem. Soc., (2006) 128, 11872.

Chapter – 5

Sensing Mechanism in Triazole-Based Oligomers

This chapter outlines the efforts to delineate the sensing mechanism in various triazole-based oligomers. As well, the role of triazole as a linker and ligand is also briefly explored in this chapter.

5.1. Introduction

Sensors are systems or devices that respond to specific stimuli, which can be physical, biological, or chemical. A chemical sensor, according to IUPAC, is "a device that transforms chemical information ranging from the concentration of a specific sample component to total composition analysis, into an analytically useful signal."[1]

The design and synthesis of opto-chemical sensors (sensor from herein) has been an area of focus for both industrial and academic investigators.[2, 3] Sensor design requires a symbiotic relationship between synthesis and physical measurements. This chapter presents the experimental physical measurement investigations in a collaborative effort with Prof. Yuming Zhao's group (Memorial University, St. Johns) in elucidating the sensing mechanism in various oligomers containing triazole rings.

5.1.1 Overview of Sensing Mechanisms

The use of fluorescence to identify organic chromophores has been in practice since the first observations were reported by Stokes in 1852.[4] Stokes observed that

fluorescence can be used to visibly distinguish some organic compounds; consequently, the ability of fluorescence spectroscopy to detect such compounds in as low as nanomolar (nM) concentrations makes it a very useful probe to be used in molecular sensing.

So far, several sensing mechanisms have been developed which can be studied efficiently by fluorescence spectroscopy: photoinduced electron transfer (PET), intramolecular charge transfer (ICT), metal-to-ligand charge transfer (MLCT), resonance energy transfer (RET), fluorescence resonance energy transfer (FRET), excited-state proton transfer (ESPT), and aggregation-induced emission (AIE) are a few of the most notable.[5, 6]

5.1.2. Saccharide Sensing

Carbohydrates, such as saccharides are involved in numerous physiological processes. Therefore, saccharide sensing has been an active area of investigation during the past three decades,[7] and a variety of sensors have been documented based on various receptor molecules. Among all the other diol receptors, however, boronic acid-based receptors have been most successful for saccharide sensing studies.[7]

The interaction of diols and boronic acid (Scheme 5.1) was first recognized by Lorand and Edwards in 1959, who found that different polyols bind to phenylboronic acids in aqueous media.[8] Generally, boronic acids are weak Lewis acids and by virtue of their deficient valence and vacant p orbitals they exist in equilibrium with the boronate form. The binding event is accompanied by increased Lewis acidity of boronic acid. Unlike Brønsted acids, the pKa of phenylboronic acid does not refer to its deprotonation.

Instead, its a measure of the proton released from a water molecule once its binds to the trigonal boron to from boronate, this process is demonstrated in Scheme 5.1.

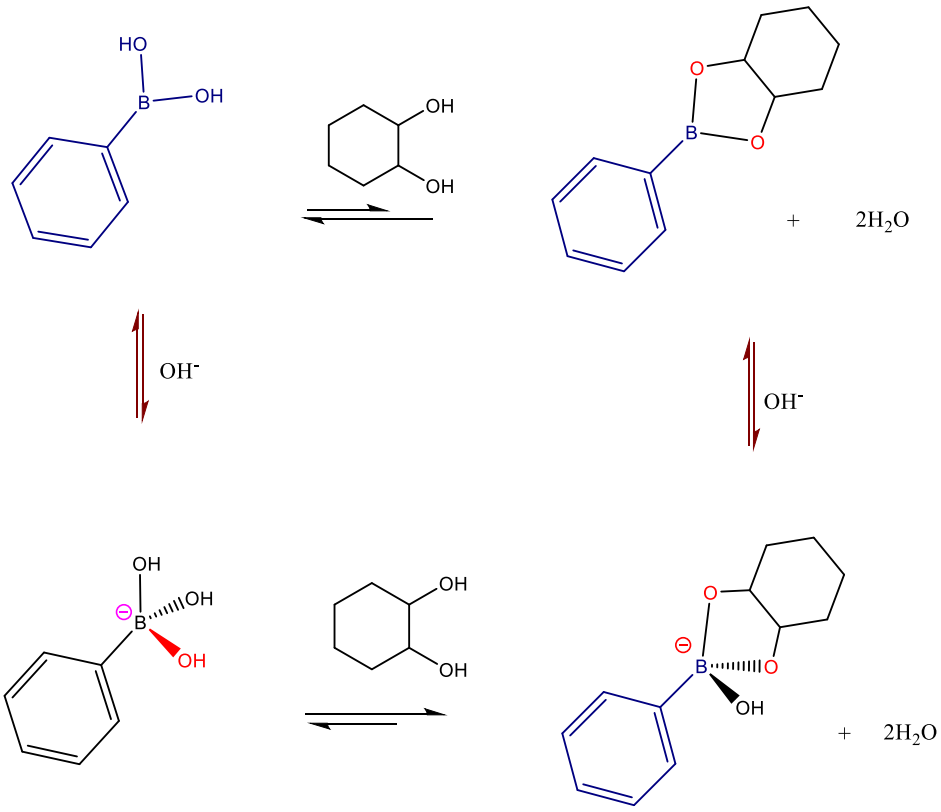

Scheme 5.1. Equilibria of boronic acid-diol interaction in aqueous media.[8]

As depicted in Scheme 5.1, the reaction of the diol with the phenylboronic acid results in the following changes: first, a diol is binds to phenylboronic acid, two equivalents of water are produced, and a boronic ester is formed. The boronic ester is more Lewis acidic than the corrposonding boronic acid because of bond angle strain, and the pKa is lowered. In a buffer solution of appropriate pH the equilibrium will shift from

boronic acid to boronate form. Second, the trigonal planar geometry of the boronic acid becomes tetrahedral in the boronate ion.[9-11] All of these changes (change in geometry, increased negative charge and increased Lewis acidity) can be utilized in producing signals upon the binding of a diol to phenylboronic acid.

5.1.2.1. **Shinkai's** Boronic Acid Receptors

The first boronic acid sensor was reported by Yoon and Czarnik in 1992.[12] However, Shinkai has also contributed immensely in this area[13-24]: Shinkai recognized the importance of Czarnik's reported systems and designed similar boronic-acid appended polyaromatic systems to develop sensors with improved quantum yields upon the saccharide binding.[25] Figure 5.2 shows some of the main boronic-acid based sensors developed by Shinkai.

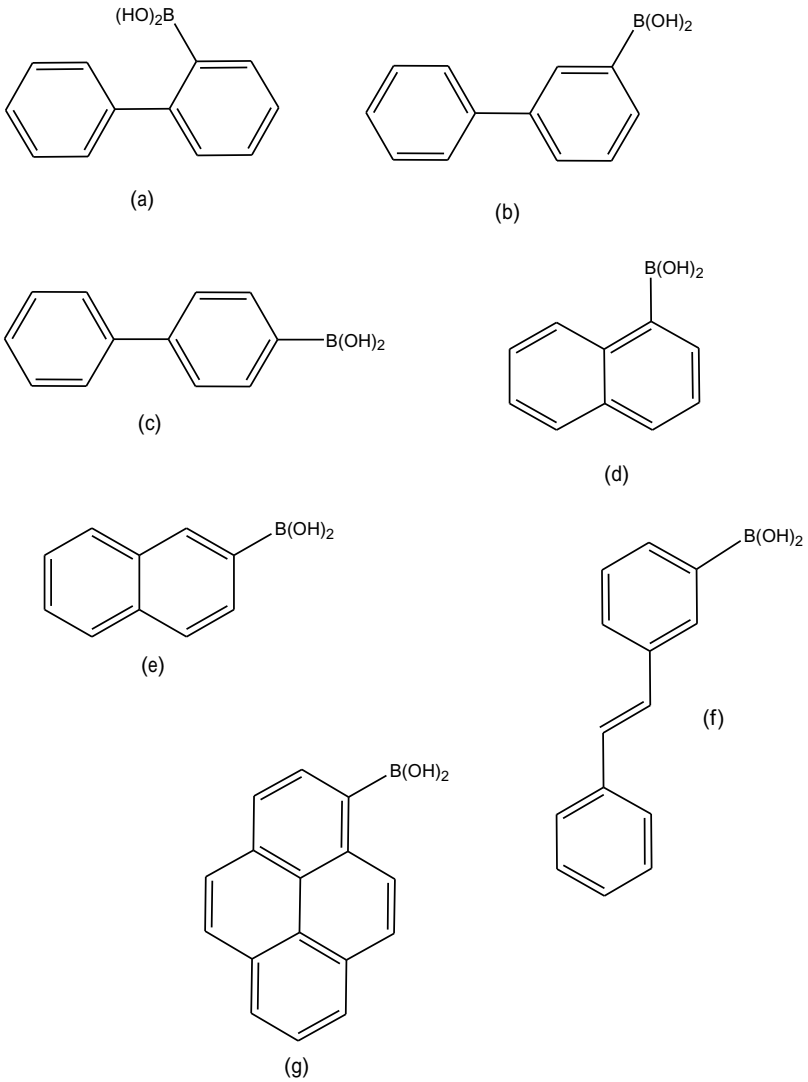

Figure 5.1. The boronic-acid appended polyaromatics screened for saccharide induced detection.[22]

In the presence of fructose, compounds b and e showed the highest fluorescence enhancements under physiological conditions. Scheme 5.2 shows the photoinduced electron transfer (PET) mechanism in the boronic-acid based sensors reported by Shinkai.[26]

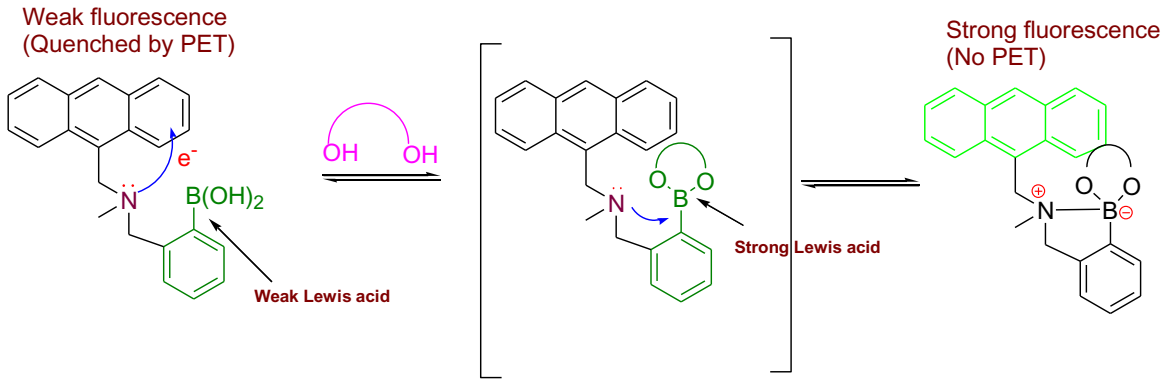

Scheme 5.2. The PET mechanism for a sensor reported by Shinkai. Saccharide binding was demonstrated in methanol/water solution with λ_{exc} = 370 nm and λ_{em} = 423 nm.[26]

Here, the sensor remains weakly fluorescent due to the fluorescence quenching of anthracene by an appended amine through the PET mechanism. Once a diol, such as glucose, binds to the boronic-acid moiety, the corresponding boronic ester forms—which is a stronger Lewis acid than the free boronic acid. Accordingly, the boronic ester then competes with anthracene for the electrons from the amine and, as a result, a coordinate bond forms between B and N. At this stage, the amine can no longer initiate the PET to anthracene (An) and excited-state PET quenching of An^* is attenuated. The fluorescence of the molecule, consequently, is revived. The molecule presented in Scheme 5.2 showed

the highest sensitivity towards the saccharides as compared to all of the other molecules shown in Figure 5.2.

In order to increase the glucose sensitivity over fructose, Shinkai has also developed a diboronic acid version of the molecule as shown in Scheme 5.3.[27] In particular, this advancement was done in order to increase the selectivity towards glucose, and it is proposed that, in a diboronic acid-containing sensor, the boron moieties may be able to align properly with the incoming glucose molecule to allow a cooperative binding ($K_2 > K_1$).[27] Furthermore, Scheme 5.3 depicts the cooperative binding of glucose molecule with diboronic acid sensor which results in an increased fluorescence response as compared to the monoboronic acid counterpart.

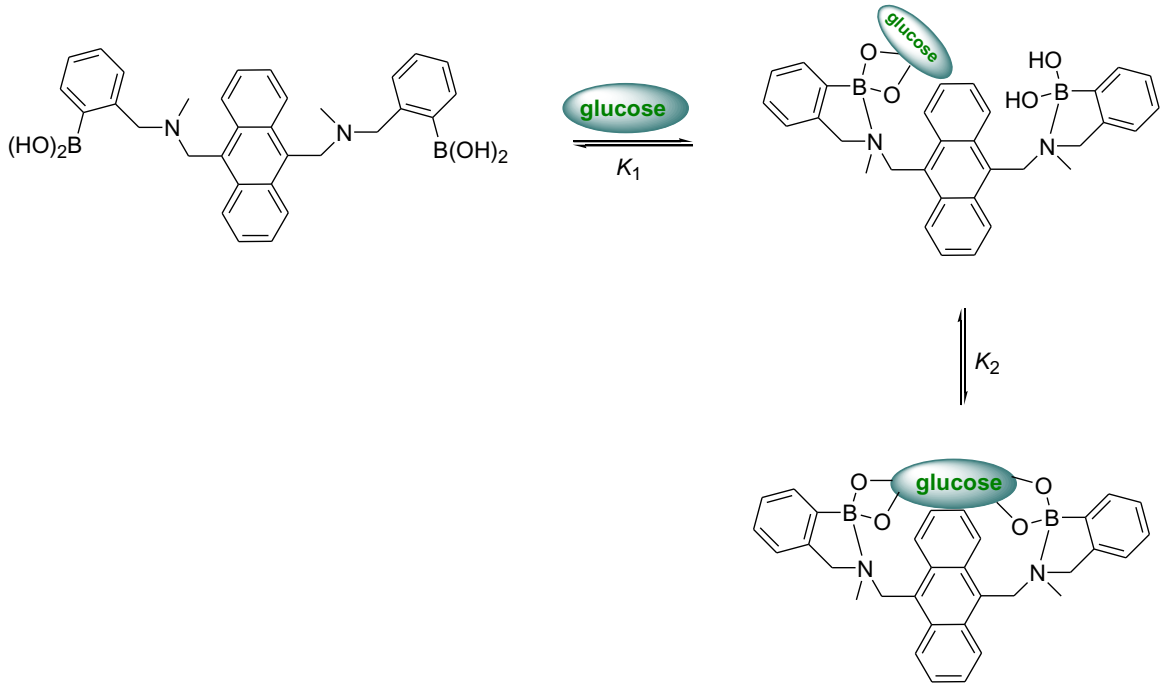

Scheme 5.3. An illustration of the cooperative binding of a diboronic acid to glucose[27]

James et al. subsequently reported a sensor (Figure 5.3), which was shown to have the ability to discriminate between the D- and L-saccharides through a combination of electronic and steric effects. Interestingly, the R form of the sensor displayed a greater chiral recognition for D-fructose and D-glucose over the L-enantiomers.[28]

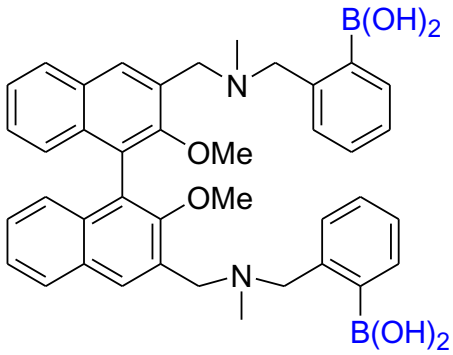

Figure 5.2. A biphenyl-based sensor for chiral discrimination of saccharides.[28]

5.1.2.2. **The "Click Fluor"**

The inception of saccharide sensing using triazole-based sensors arrived with a 1,2,3 triazole ring-based 2-((4-phenyl-1H-1,2,3-triazol-1-yl)methyl)phenylboronic acid molecule, named as "click fluor" by James and co-workers (Figure 5.4).[29] This sensor

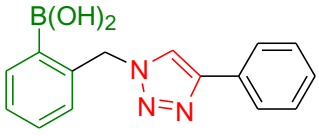

Figure 5.3. The "click fluor" reported by James and Fossey in 2008.[29]

only worked in the presence of an organic co-solvent (52% wt% MeOH/H_2O) and required comparatively alkaline conditions (pH = 8.21): this environment, of course, can't be considered ideal for sensing applications under physiological conditions. In addition to the above limitations, the click fluor provided a very weak detection limit of saccharide such as fructose, ca. 0.01 to 1.0 M, with negligible detection of the biologically most important saccharide, glucose.

5.2. Objective and Methodology

This chapter deals with the design, fabrication and mechanistic aspects of some new triazole based sensors. The first segment of the Chapter is focused on the issue of saccharide binding with triazole-based phenylboronic acid-containing sensors. The second segment is dedicated to the metal ion sensing using triazole-based chromophoric assemblies. Global analysis of the spectral data employed to extract the binding constants.

5.3. Results and Discussion

5.3.1. Ground-and Excited-State Properties

Two H-shaped isomeric oligomers ("hmers"), comprised of four phenylboronic acid moieties and an oligo-phenylene vinylene (OPV) backbone, were synthesized by Mr. Karimulla Mulla in Prof. Yuming Zhao's lab at Memorial University, and the structures of the hmers (closed and open) are presented in Figure 5.5. In the O-hmer, the triazole rings are attached to the terminal phenyl groups of OPV at their 3,5 positions, making it an open arm-type structure. On the other hand in the C-hmer these connections are at the 2,5

positions, making the structure a relatively closed one as compared to the O-hmer. The corrosponding hmer oligomers containing the boronic ester moieties are also presented in Figure 5.5.[30]

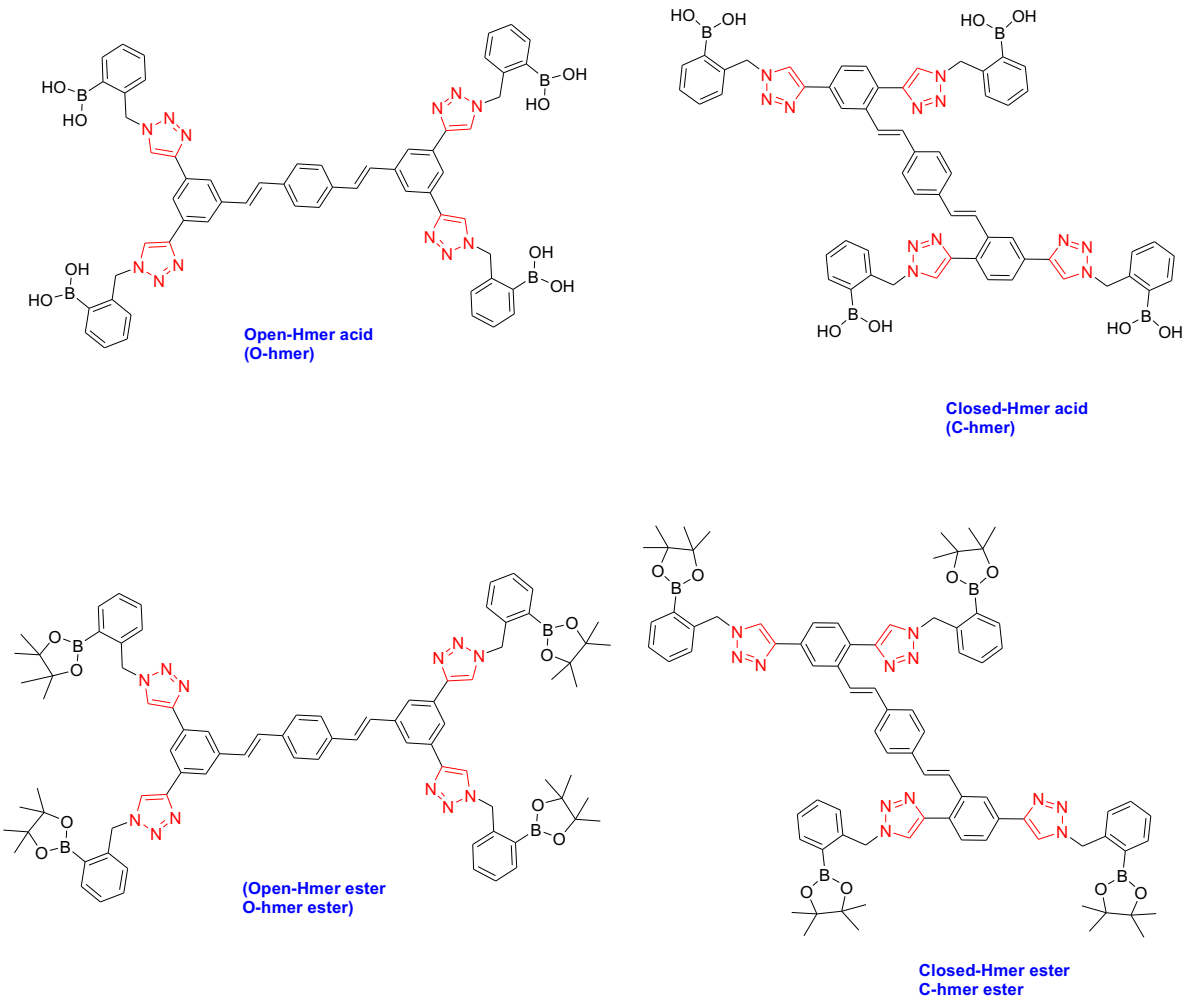

Figure 5.4. The structures and abbreviations of the hmer oligomers studied in this Chapter.[30]

A density functional theory (DFT, B3LYP/6-31G*) analysis suggests that the triazole moiety can energetically stabilize the boron-diol complex by ΔH = -11.2 kcal mol^{-1}.[31] Furthermore, the cruciform-shaped π-conjugated framework, OPV, increased the quantum yield upon saccharide binding.[32]

5.3.2. Absorption and Emission Spectra

The absorption and emission spectra of the hmer oligomers are shown in Figure 5.6 and the data are summarized in Table 5.1. The absorption spectra of hmers are broad with well-resolved bands and shoulders arising from several underlying transitions and their vibronic components. There are two major band envelopes in the hmers: the high-energy absorption manifold at 250-320 nm and the low-energy absorption manifold at 330-400 nm. The absorption spectra of hmers are characterized by $S_0 \rightarrow S_n$ (mainly of $\pi \rightarrow \pi^*$ in nature) transitions. The hmer esters in THF at 298 K display λ_{max}^{abs} at 361 nm (27700 cm^{-1}, ε = 4.2 $\times$ 10^4 M^{-1} cm^{-1}) for the C-hmer ester, and 364 nm (27500 cm^{-1}, ε = 4.1 $\times$ 10^4 M^{-1} cm^{-1}) for the O-hmer ester. On the other hand, the hmer acids in aqueous phosphate buffer (PBS) at 298 K exhibit λ_{max}^{abs} at 365 nm (27400 cm^{-1}, ε = 2.2 $\times$ 10^4 M^{-1} cm^{-1}) in the C-hmer acid and 360 nm (27700 cm^{-1}, ε = 3.2 $\times$ 10^4 M^{-1} cm^{-1}) in the O-hmer acid.

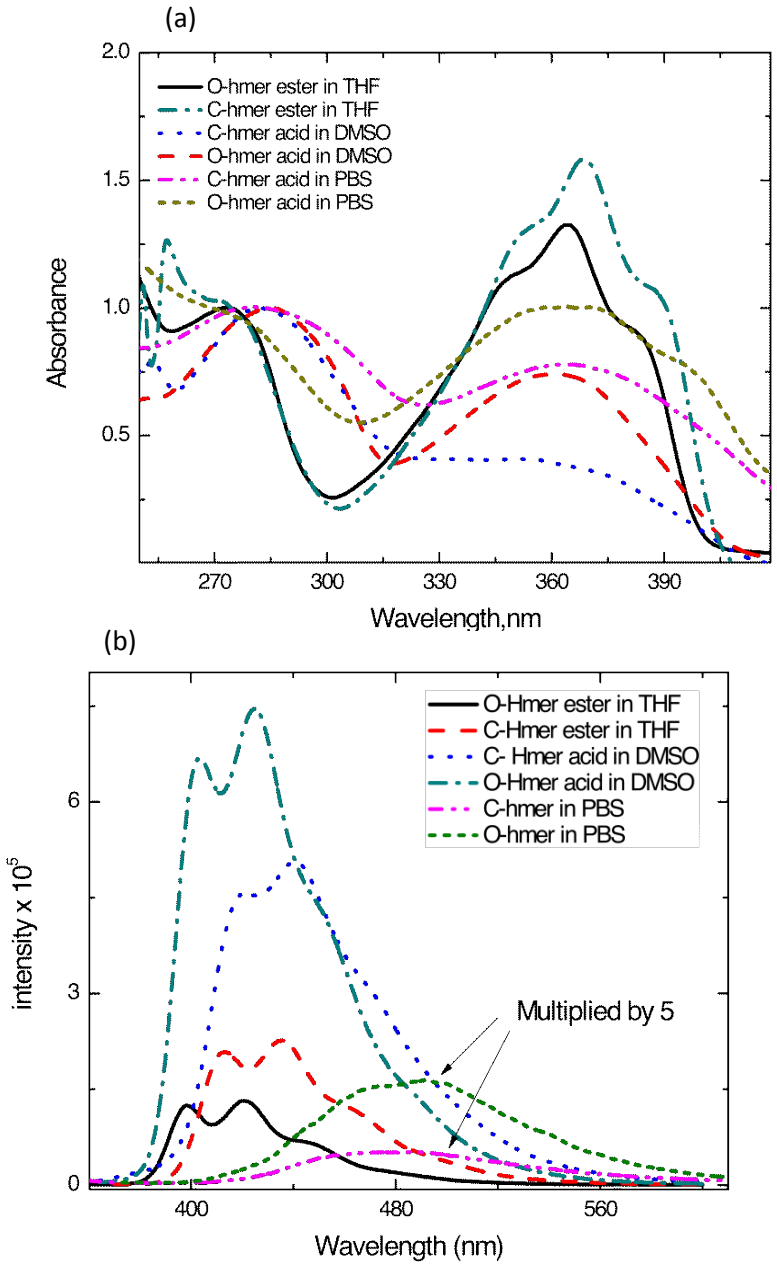

Figure 5.5. (a) UV-Vis absorption spectra, and (b) fluorescence spectra of the hmer oligomers in three different N_2-saturated solvents, namely, THF, DMSO, and aqueous phosphate buffer saline (PBS) (0.1 M, pH 7.4), acquired by exciting the solutions of [C-hmer] = 4.5 μM and [O-hmer] = 6.4 μM at 350 nm at 298 ± 3 K. For clear comparisons, the emission intensity of O-hmer and C-hmer in PBS is presented after multiplying the original data by a factor of five. Of importance, note the solvatochromic shift, broadening of spectra, and the weak emission in aqueous PBS.[30]

Table 5.1. Ground and excited-state photophysical properties of hmer cruciform acids and esters.

Entry	C –hmer ester[a]	O –hmer ester[a]	C –hmer acid[b]	O –hmer acid[b]
λ_{max}, nm	361	364	365	360
$\varepsilon \times 10^4$ $M^{-1}cm^{-1}$	4.2	4.1	2.0	3.2
E_{op}, cm^{-1}	27700	27500	27400	27700
λ_{em}, nm	412	398	482	490
E_{em}, cm^{-1}	24200	25100	20700	20400
E_{SS}, cm^{-1}	3500	2400	6650	7370
ϕ_{em}	0.32	0.34	0.039	0.041
$k_r \times 10^7$, s^{-1}	4.7	2.9	1.2	0.56
$k_{nr} \times 10^7$, s^{-1}	9.9	5.6	29	13
τ, ns	6.7	11.6	3.12	7.23

[a]Acquired in N_2 Saturated THF at 298 ± 3 K. [b] Acquired in N_2 saturated aqueous PBS (pH 7.4) at 298 ± 3 K, λ_{exc} for lifetime data was 337 nm.

When the absorption and emission spectra of the hmer acids acquired in N_2-saturated PBS are compared with those acquired in N_2-saturated DMSO, significant changes can be seen. In PBS, the emission spectra of the hmer acids are broader and structureless, whereas the emission spectra of the hmer acids in DMSO and the hmer esters in THF exhibit distinct vibronic progressions. This is not surprising, however: in water, it is expected that both boronic acid and triazole moieties are expected to perturb the electronic environment of the OPV framework due to possible interactions with water molecules.

Table 5.1 lists some of the main ground-and excited-state properties of the hmer esters and hmer acids. Referring to Table 5.1 it can be deduced that the emission energies and the energies of the optical transition are very similar among the hmer ester and hmer acids. The fluorescence quantum yield (Φ_{em}) of the hmer acids measured in PBS is very weak as compared to the Φ_{em} of the hmer esters acquired in THF—and that the fluorescence lifetimes of the hmer esters are longer than those of the hmer acids.

In the presence of a highly-conjugated environment, the π orbitals can be distributed over many nuclear coordinates, and as such, the ramification of the bonding arrangements are central to the electronic and excited-state properties of a particular molecular assembly.[33, 34] OPV's are known to have a distribution of conformers in solution and, once photo-excited, there is a possibility that they can adopt well-resolved planar conformations.[35, 36] Liu et al. have reported that the presence of OPV brings an asymmetry between absorption and emission spectra and it is attributed to the dramatic changes in the dihedral angles upon excitation, termed "quadratic coupling".[35, 36] In general, it has been reported that the structure of OPV in the excited-state is more planar than in the ground-state, since the excited-state relaxes towards a planar structure, and this influences the fluorescence and electronic spectra. Consequently, the fluorescence spectra of the hmers become narrower than the corrsosponding absorption spectrum.[37] As well, the ground-state energy also depends upon the dihedral angles in the molecule. The energy of the ground-electronic state (E_{GS}) for a given configuration can be modelled as per Equation 5.1.[35]

$$E_{GS}(A) = \frac{V}{2}\sum_{j=1}^{N-1}\left[1 - \cos\left(2\theta_j\right)\right] \qquad [5.1]$$

In Equation 5.1, A is a set of particular torsional configurations for an absorption spectrum, $E_{GS}(A)$ is the energy of the ground electronic state for a given configuration, V is the rotational barrier, i.e. the energy difference between the orthogonal (θ = 90^0), and planar ($\theta = 0$) conformation, summed over N-1 dihedral angles in an oligomer of length N, θ_j is a set of dihedral angles, where j represents the dihedral angle between the j^{th} and (j + 1)th phenylene rings.

5.3.3. Saccharide Sensing in hmer Oligomers

The triazole unit is emerging as a key ligand and spacer component. Moreover, it has been revealed that the triazole is not just a spectator ligand, connector, or spacer[38]—it can also impart significant effects on the mechanism of a photochemical reaction.[39, 40] The hmers are composed of triazole rings and therefore one can expect to observe significant effects due to the triazole rings, on the spectral properties of the hmers.

Due to the presence of tetrakis(phenylboronic acid) groups, the hmers are soluble in PBS with the aid of a small amount of co-solvent, DMSO (0.4% v/v). The fluorescence spectra of C-hmer acid acquired in PBS, as a function of increasing concentration of saccharides (fructose, galactose, ribose and glucose) are shown in Figure 5.7. Once glucose, fructose, or galactose were added, the fluorescence intensity was noticeably enhanced, indicating that these oligomers are sensitive towards the binding of certain saccharides. When C-hmer was titrated with ribose, no significant change in the

fluorescence intensity was observed, but a new emission band appeared at ca. 430 nm (23250 cm^{-1}). Hence, this behaviour with ribose is attributed to a significantly different binding mode relative to the other three saccharides employed in this study. Alternatively, however, when C-hmer was titrated with fructose, galactose, and glucose, a new band appeared at ca. 432 nm (23000 cm^{-1}), 433 nm (23090 cm^{-1}), and 440 nm (22700 cm^{-1}), respectively. The new band includes a well-resolved shoulder at 412 nm (24200 cm^{-1}), in the case of galactose and fructose; while a rather weak shoulder appeared at 402 nm (24800 cm^{-1}) after glucose was added. A cursory inspection of this new high energy emission suggest its origin from $\pi \rightarrow \pi^*$ transitions ($S_n \rightarrow S_0$).

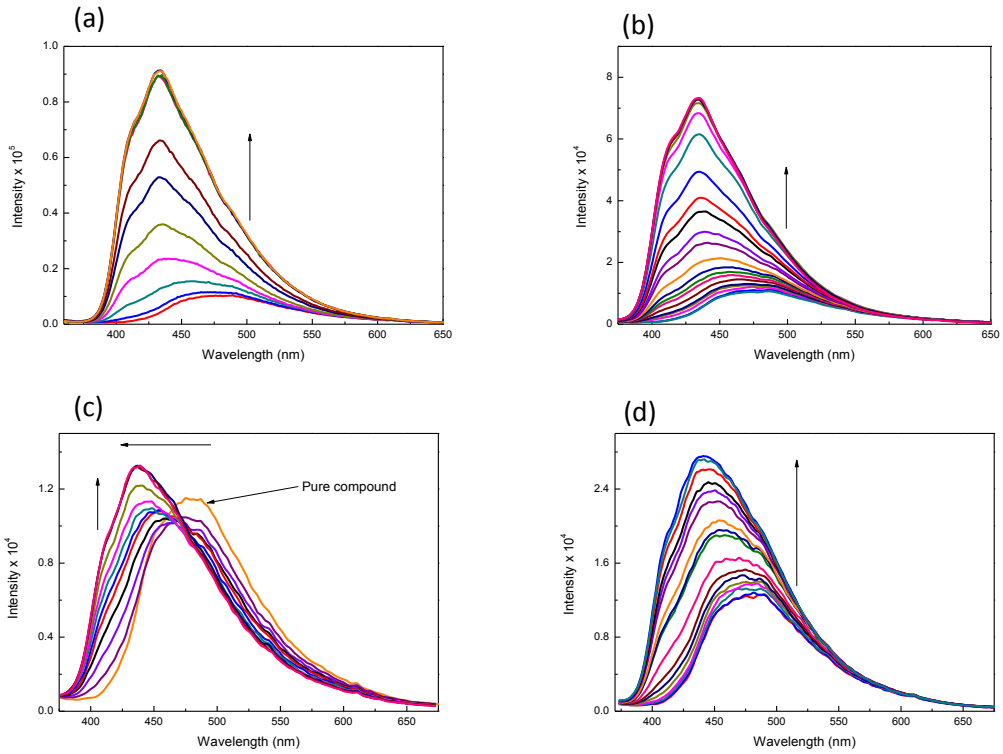

Figure 5.6. Emission spectra (λ_{exc} = 370 nm) of the C-hmer acid (9.8 µM) as a function of increasing concentration of saccharides (a) fructose at 0.00, 0.16, 0.38, 0.61, 0.89, 1.20, 1.50, 1.80, 2.30, 2.80 and 3.40 mM quantities (b) galactose at 0.00, 0.13, 0.33, 0.59, 0.92, 1.30, 1.90, 2.60, 3.40, 4.40, 5.60, 6.80, 8.20, 9.80, 11.60, 13.50, 15.50, 17.70, 20.0 and 24.90 mM quantities (c) ribose at 0.00, 4.4, 13.0, 26.0, 39.0, 57.0, 79.0, 79.0, 79.0, 91.0, 130, 170, 240 and 330 mM quantities (d) glucose at 0.00, 5.5, 20.0, 27.0, 35.0, 46.0, 61.0, 88.0, 100, 120, 140, 170, 190, 230, 270 and 310 mM quantities in aqueous PBS (pH = 7.4) at 298 ± 3 K.[30]

Similar trends were followed when O-hmer was titrated with fructose and galactose. The resulting fluorescent-titration spectra are shown in Figure 5.8. Here, the titration of O-hmer with glucose showed a very weak enhancement. When titrated with the ribose, the emission intensity was attenuated by a factor of four, when compared with the fluorescence enhancement seen with the C-hmer. Moreover, these observations show a significant change in the excited-state properties of the OPV as a function of the saccharide used. In summary, all the saccharides were found to perturb the lowest lying excited-state of the chromophores in a discerning manner. The trends in the spectral response of hmer acids after addition of saccharides are summarized in Table 5.2.

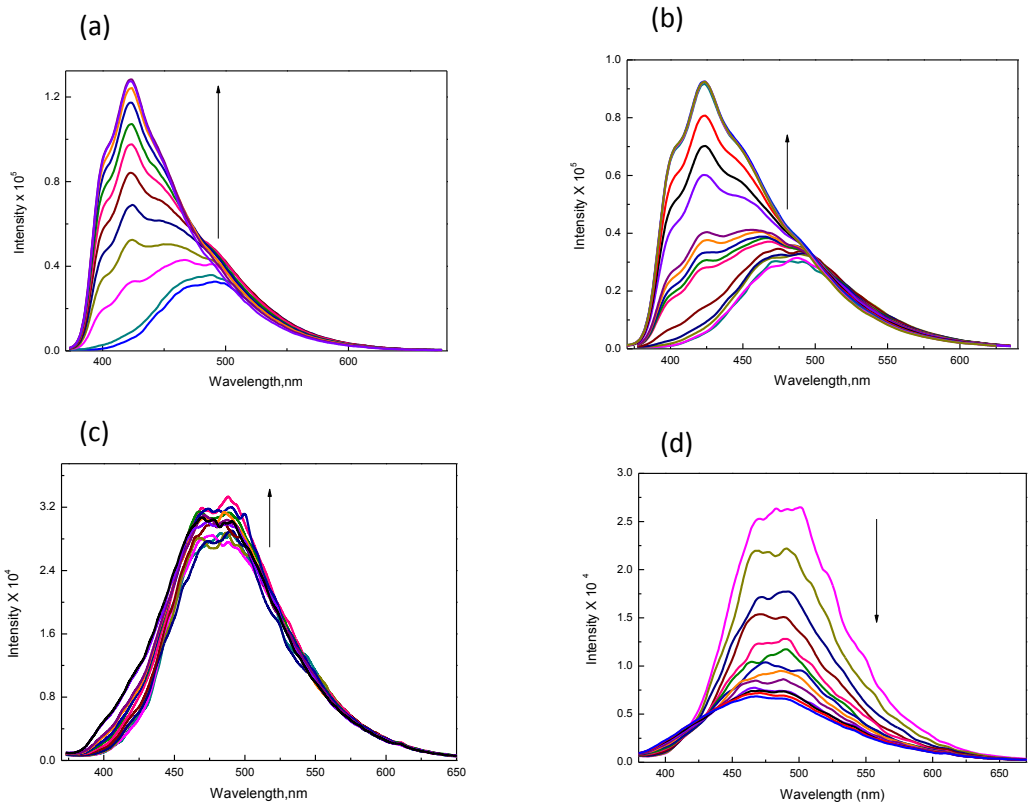

Figure 5.7. Emission spectra (λ_{exc} = 370 nm) of the O-hmer acid (9.8 μM) as a function of increasing concentration of saccharides (a) fructose at 0.00, 0.39, 1.20, 2.00, 2.70, 4.30, 7.50, 13.0, 26.0, 49.0 and 91.0 mM quantities (b) galactose at 0.00, 0.63, 3.60, 7.60, 13.0, 21.0, 32.0, 46.0, 61.0, 79.0, 99.0, 121, 145, 176, 209, 245 and 285 mM quantities (c) glucose at 0.00, 3.37, 12.0, 22.0, 40.0, 40.0, 59.0, 77.0, 100, 130, 170, 220 and 290 mM quantities (d) ribose at 0.00, 0.36, 11.0, 28.0, 52.0, 84.0, 121, 163, 211, 260, 309, 361 and 413 mM quantities in aqueous PBS (pH = 7.4) at 298 ± 3 K.[30]

Table 5.2. The spectral changes observed in hmer acids as a result of saccharide addition. Table is constructed by using the data shown in Figures 5.7 and 5.8.

Oligomer	λ_{max}, I_0 (nm)[a]	λ_{max}, I (nm)[b]	Saccharide	Spectral Change
C–hmer	482	433	Fructose	fluorescence enhancement
	482	434	Galactose	fluorescence enhancement
	482	437	Ribose	weak fluorescence enhancement
	482	440	Glucose	fluorescence enhancement
O–hmer	490	423	Fructose	fluorescence enhancement
	490	423	Galactose	fluorescence enhancement
	490	487	Ribose	fluorescence attenuation
	490	490	Glucose	weak fluorescence enhancement

[a] λ_{max} before the addition of saccharide [b]λ_{max} after the addition of saccharide.

5.3.4. Analysis of Association Constants

It is evident from dramatic changes in the ground-state UV-Vis spectra of hmers obtained as a function of increasing saccharide concentration (presented in the Appendix, Figures S6-S11) and the previously documented NMR-chemical shifts of the triazolyl and phenylic protons (adjacent to the boronic acid group), the binding of saccharides occurs in the ground-state.[30]

The mechanistic model was proposed by taking account all of the possible saccharide binding sites available in the hmers and the changes in the emission spectra upon addition of a saccharide. Initially the data was fit to a model shown in Scheme 5.4. The model was predicted upon the binding sites (i.e. boronic acid groups) available for a diol and assumes that the binding sites are electronically isolated. In this model a direct 1:4 (ML_4) type of binding was proposed.

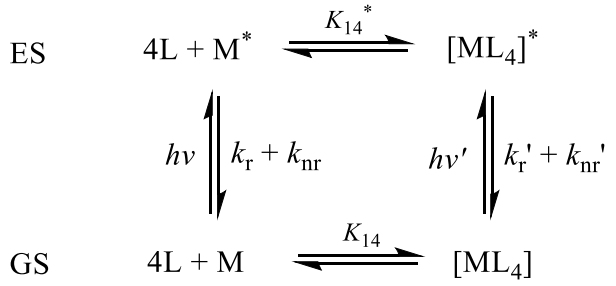

Scheme 5.4. A Förster cycle for the direct binding of saccharides (L) with hmers (M).

Unfortunately, the model did not return satisfactory fits or meaningful eigen vectors. Following these observations, a sequential 1:2 (ML_2) and 1:4 (ML_4) type of binding mechanism for the hmers with a saccharide was proposed (Scheme 5.5). Analysis of the data was successful upon inclusion of the sequential binding model and returned satisfactory fits. Finally, the proposed mechanism for the sequential equilibria, and the relationships between the equilibrium constants in the ground and excited-states of the hmers (M) with the saccharides (L), are shown in Scheme 5.5.

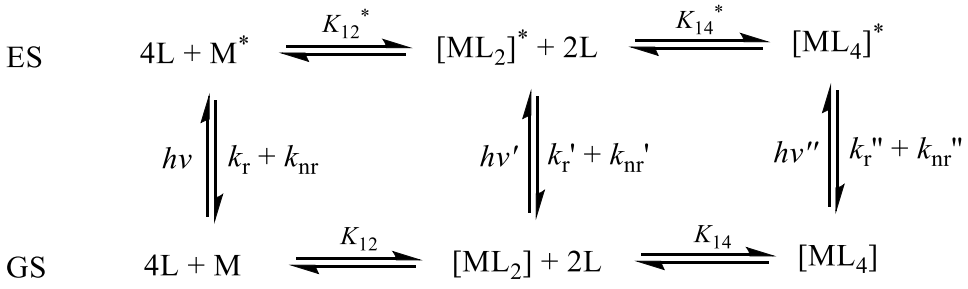

Scheme 5.5. A Förster cycle for the sequential binding of saccharides with hmer oligomers.[30]

To further validate the SVD analysis, the resulting eigen vectors can be taken into account. As described by Binstead et al. depending upon the number of spectra, SVD creates eigen vectors which belong to V (evolutionary), S (spectral), and product of U and S ($U \times S$) (temporal).[41] Moreover, SVD reveals a number of vectors equal to the number of spectra or abscissa points in the original data set. As described in Chapter 2, out of all the vectors, most of arise from the lamp, instrumental noise, or non-random instrument responses. With each eigen vector, then, the eigen value accordingly drops and almost reaches the instrumental noise. Depending upon the noise level, vectors can be discarded without analysis and only significant vectors having little or no noise are considered without the loss of any valuable information. To further discern the significant and non-significant eigen vectors, they can be plotted separately and the noise level can be observed more clearly. Representative plots of the first three temporal eigenvectors ($U \times S$) and first three spectral eigenvectors (V) for the C-hmer binding with fructose and the O-hmer binding with fructose are shown in Figures 5.9 and 5.10, respectively.

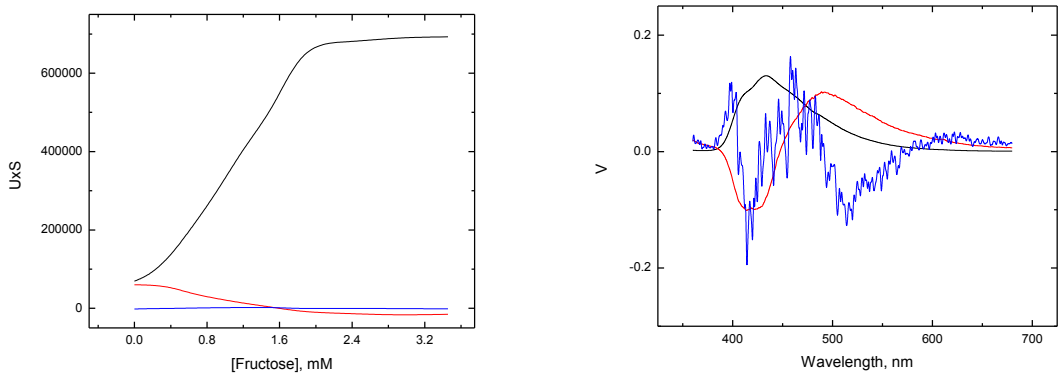

Figure 5.8. The first three temporal eigenvectors from $U \times S$, the remaining curves contains instrumental noise, and noise from the lamp source (left). The first three spectral eigenvectors, and V (right) from the SVD analysis of the data matrix Y of C-hmer and fructose titration data. By definition, the scan data can be reconstructed as $Y = U \times S \times V$.

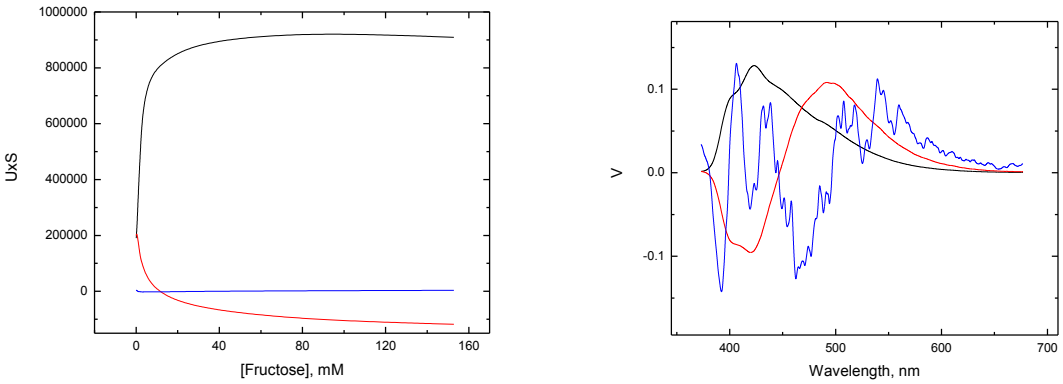

Figure 5.9. The first three temporal eigenvectors from $U \times S$, the remaining curves contains instrumental noise, and noise from the lamp source (left). The first three spectral eigenvectors, and V (right) from the SVD analysis of the data matrix Y of O-hmer and fructose titration data. By definition, the scan data can be reconstructed as $Y = U \times S \times V$.

The presence of the first three spectral eigen vectors V and the first three temporal eigen vectors from $U \times S$ (Figures 5.9 and 5.10), extracted as a result of SVD of the spectral data matrix Y, confirms the presence of three dominating spectral species. Also, the remaining curves in both plots of V as well as $U \times S$ arise from lamp source, non-random instrument response, and instrumental noise.[41-44] On the other hand, however, the first three eigen vectors, as mentioned above show considerable eigen values and contain meaningful information. Thus, this model can be considered plausible and in compliance with Scheme 5.5. The corresponding fits extracted from SPECFIT/32 are shown in Figures 5.11 and 5.12. As well, the quality of fits reflects the validity of the model.

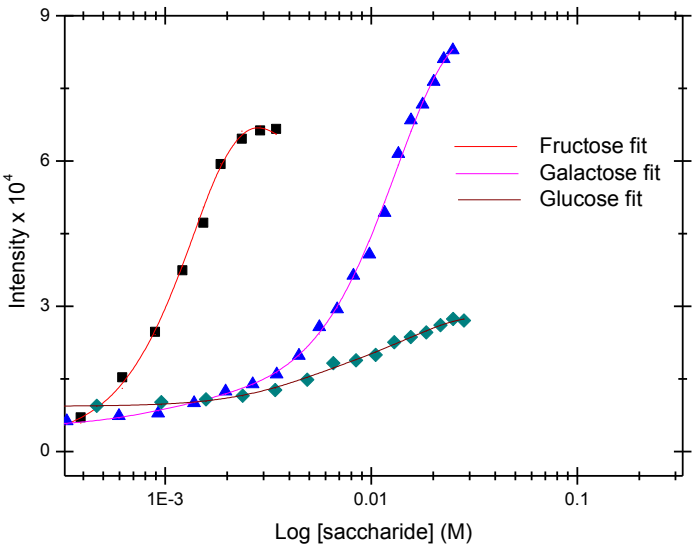

Figure 5.10. A plot of fluorescence enhancement of C-hmer as a function of the log of saccharide concentration. The fits were extracted from SPECFIT at λ = 450 nm.

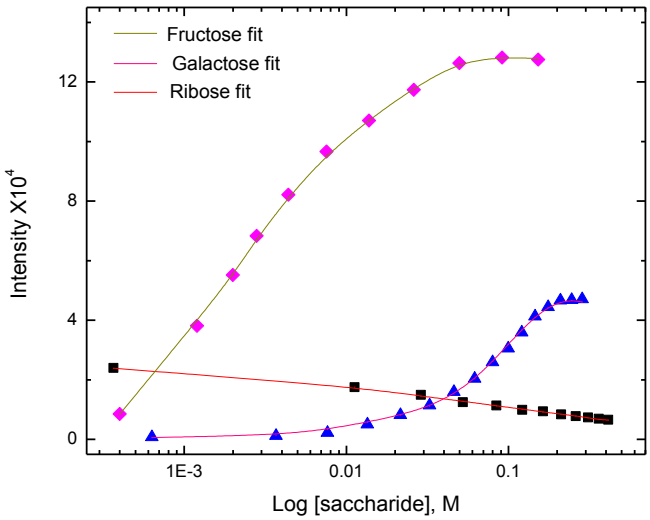

Figure 5.11. A plot of fluorescence enhancement of O-hmer as a function of log of saccharide added. The fitting was extracted from SPECFIT at λ = 450 nm.

The plots extracted from the SPECFIT, as a result of global analysis revealing the concentration profiles and dominating species, are shown in Figures 5.13 to 5.18. This analysis is consistent with a two-step mechanism, for the O-hmer and C-hmer acid, respectively. The coloured (absorbing) species and deconvoluted spectra for C-hmer binding with saccharides are shown in Figures 5.13 to 5.18.

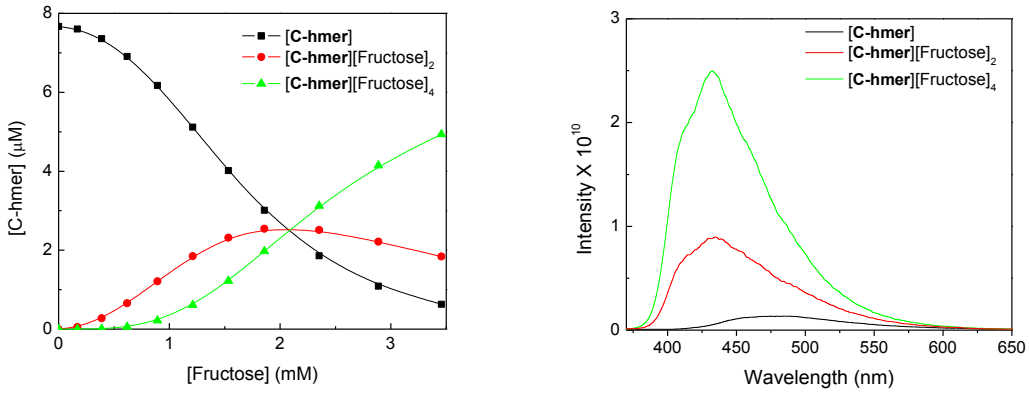

Figure 5.12. The extracted spectra for C-hmer with fructose, showing the coloured species involved (left) and the deconvoluted spectrum of participating species on the bottom (right).

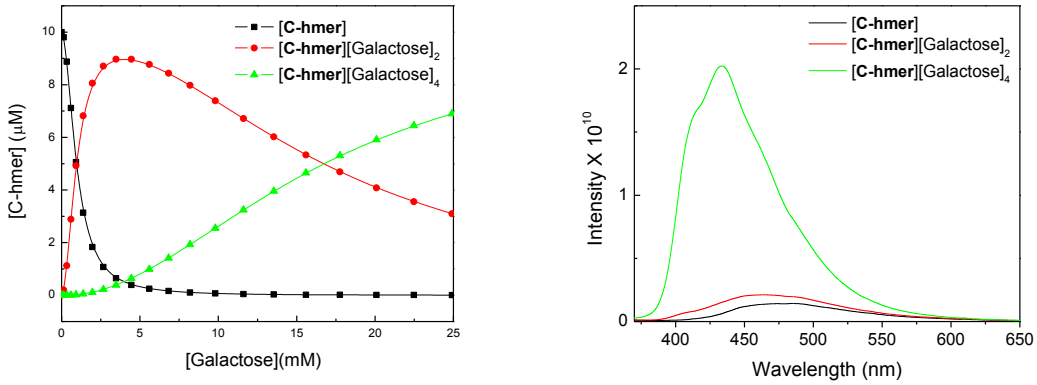

Figure 5.13. The extracted spectra for C-hmer with galactose, showing the coloured species involved (left) and the deconvoluted spectrum of participating species on the bottom (right).

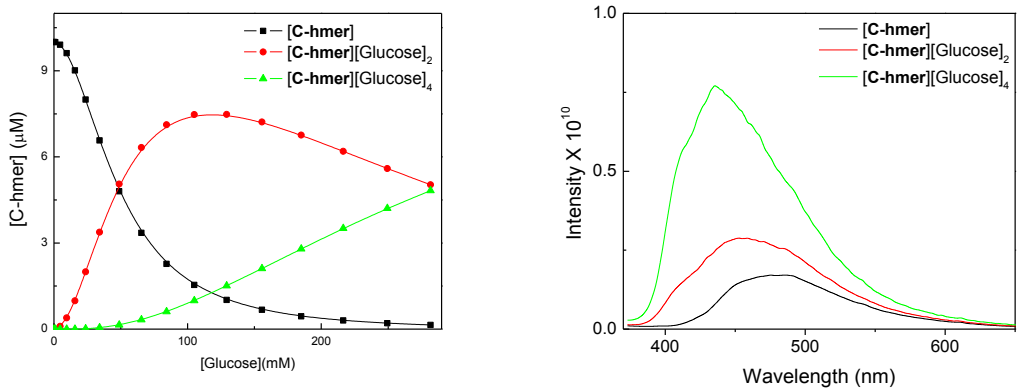

Figure 5.14. The extracted spectra for C-hmer with glucose, showing the coloured species involved (left) and the deconvoluted spectrum of participating species on the bottom (right).

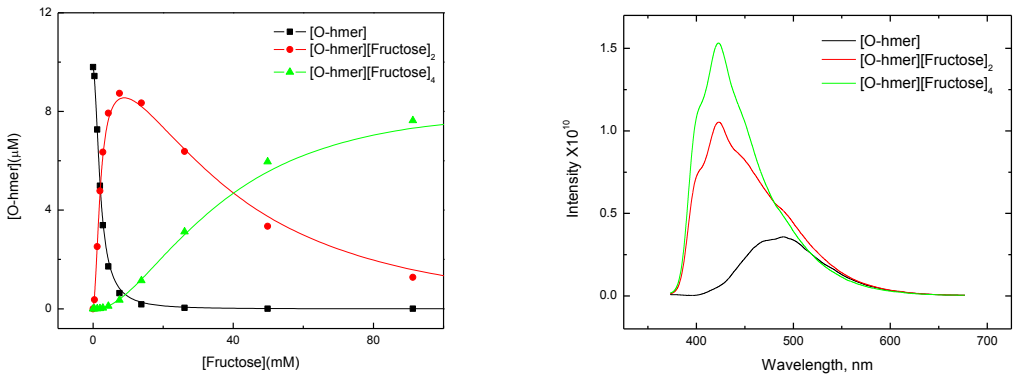

Figure 5.15. The extracted spectra for O-hmer with fructose, showing the coloured species involved (left) and the deconvoluted spectrum of participating species on the bottom (right).

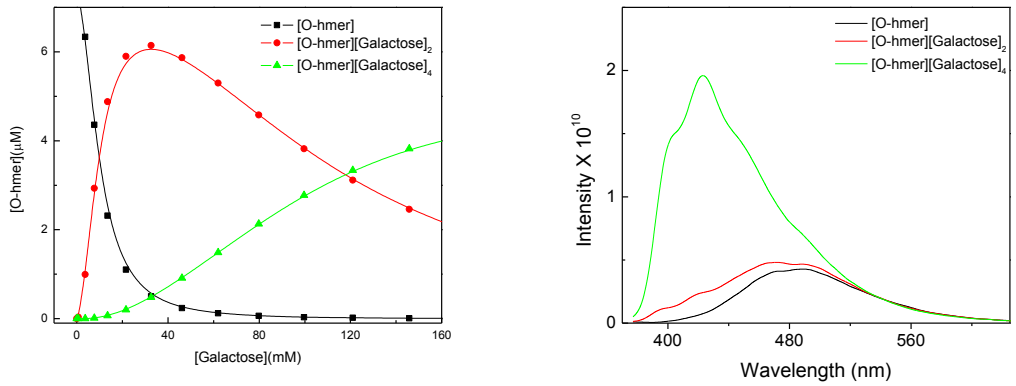

Figure 5.16. The extracted spectra for O-hmer with galactose, showing the coloured species involved (left) and the deconvoluted spectrum of participating species on the bottom (right).

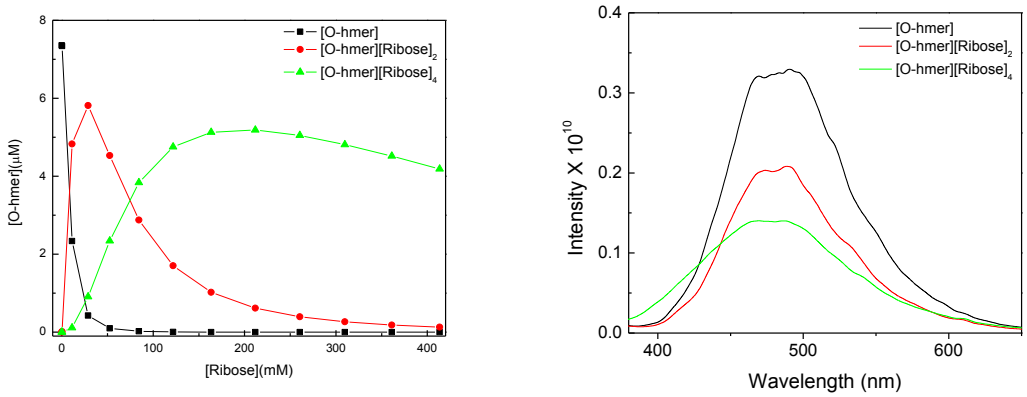

Figure 5.17. The extracted spectra for O-hmer with ribose, showing the coloured species involved (left) and the deconvoluted spectrum of participating species on the bottom (right).

A detailed list of all the association constants (K) is presented in Table 5.3. Overall, with C-hmer acid, fructose shows the highest degree of binding with an association constant $K_{12} = 6.1 \times 10^4$ M^{-2} and $K_{14} = 9.1 \times 10^3$ M^{-2}, while the association constant of galactose was also very similar with $K_{12} = 1.2 \times 10^4$ M^{-2} and $K_{14} = 1.6 \times 10^3$ M^{-2}. Glucose binding shows the weakest association constant with K_{12} = 204 M^{-2} and K_{14} = 169 M^{-2} values. Due to a very weak spectral response with ribose titration data SVD did not return any meaningful association constant values from the analysis. Thus, the association constants of C-hmer acid and saccharides were in the following order: fructose > galactose > glucose. Similarly, the O-hmer association constants for fructose and galactose were found to be very similar. For fructose, $K_{12} = 1.8 \times 10^4$ M^{-2} and $K_{14} = 3.0 \times 10^3$ M^{-2} while for galactose $K_{12} = 1.1 \times 10^4$ M^{-2} and $K_{14} = 7.2 \times 10^3$ M^{-2} values were extracted. The response of glucose was found to be very weak so the glucose data was not analyzed to extract association constant values. The SVD with O-hmer and ribose provided relatively smaller values of K_{12} = 457 M^{-2} and K_{14} = 177 M^{-2}. Thus, the trend for association constants of O-hmer and saccharides is in the following order: fructose > galactose > ribose.

Table 5.3. Binding constants of C-hmer and O-hmer oligomers, with different saccharides as extracted from SPECFIT.

Oligomer	Saccharide	Binding model	Binding constants
C-hmer	D-Fructose	1:2	$K_{12} = 6.1(\pm 1.6) \times 10^4$ M^{-2}
		1:4	$K_{14} = 9.1(\pm 1.4) \times 10^3$ M^{-2}
	D- Glucose	1:2	$K_{12} = 204\ (\pm 1.25)$ M^{-2}
		1:4	$K_{14} = 169\ (\pm 1.25)$ M^{-2}
	D-Ribose		SVD did not return satisfactory results due to very weak spectral response
	D- Galactose	1:2	$K_{12} = 1.2(\pm 2.5) \times 10^4$ M^{-2}
		1:4	$K_{14} = 1.6(\pm 2.5) \times 10^3$ M^{-2}
O-hmer	D-Fructose	1:2	$K_{12} = 1.8(\pm 1.5) \times 10^4$ M^{-2}
		1:4	$K_{14} = 3.0(\pm 2.4) \times 10^3$ M^{-2}
	D-Glucose		SVD did not return satisfactory results due to very weak spectral response
	D- Ribose	1:2	$K_{12} = 457\ (\pm 1.25)$ M^{-2}
		1:4	$K_{14} = 177\ (\pm 1.25)$ M^{-2}
	D- Galactose	1:2	$K_{12} = 1.1(\pm 1.5) \times 10^4$ M^{-2}
		1:4	$K_{14} = 7.2(\pm 2.4) \times 10^3$ M^{-2}

The result attests to the significant influence of molecular shape on binding properties. As evident from Table 5.3, hmer acids bind all four saccharides in a two-step mechanism. It has been reported earlier that the "spatial arrangement" of boronic acid

receptors is in such a way that it facilitates a two step binding.[31] A similar two-step binding has been demonstrated earlier for a similar system (Figure 5.19) and the binding constants presented here are in well-agreement with binding constants reported earlier.[31, 45-47] Although, the presence of SVD data provides an insight into the binding equilibria, a detailed mechanism showing exact binding motif difficult to predict at the present time due to absence of other supporting data such as, detailed ^{1}H NMR titration data and AFM images.

The question that arises, however, is why does fluorescence enhancement occur in hmer oligomers? Although, photoinduced electron transfer (PET) has been widely proposed as a sensing mechanism for saccharide sensors,[5, 6, 48] several other mechanisms can also be considered plausible depending upon the system under study.[6, 14, 49] Similarly, Mulla et al. has proposed that neither PET nor ICT is sufficient to completely explain the turn-on sensing behaviour in system comprised of triazole rings, phenylboronic acid and a conjugated oligomer fluorophore with cruciform and linear π-frameworks (Figure 5.19).[31]

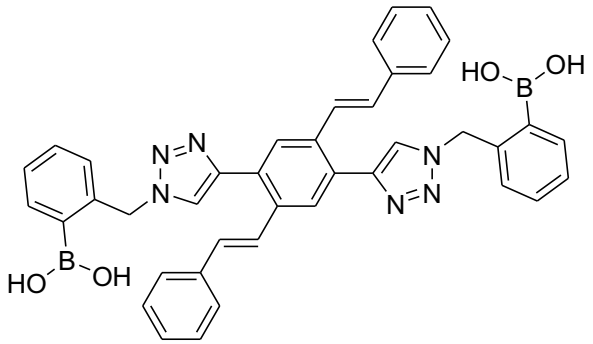

Figure 5.18. A triazole containing phenylboronic acid based saccharide sensor reported by Mulla et al.[31]

Based on AFM images acquired before, and after, adding the saccharides tested, Mulla et al. proposed that the binding of the saccharides reinforces the de-aggregation or solvation of the sensor, preventing its self-quenching behaviour which results in fluorescence enhancements. Since hmers are very closely related to the systems reported by Mulla et al., following the arguments proposed by them, a mechanism for the fluorescence enhancement in these systems can be proposed to be via the de-aggregation-induced emission mechanism.[14, 31, 50]

5.3.5. Metal Sensing Using poly(p-phenylene ethynylene)s (PPE) Polymers

PPE polymers are very interesting to chemists due to their attractive photophysical properties.[51, 52] PPE polymers consist of rigid and highly conjugated units which make them ideal candidates to be used in sensors,[53-58] light emitting diodes (LED),[59] photodiodes,[60] and light-harvesting antennae.[61]

A good example of metal sensing using PPEs has been reported by Jones Jr. et al., who used a poly(p-phenylene ethynylene)-alt-(triethyleneethynylene)] (PPETE) with a N,N,N-triethyleneethynylene diamino receptor (TMEDA-PPETE, Figure 5.20).[62] The polymer itself was very fluorescent and not suitable for turn-on sensing studies.[63] Furthermore, this sensor showed ~98% quenching with Cu^{2+} at a 1:1 ratio of Cu^{2+} to receptor. Therefore, the TMEDA-PPETE sensor was preloaded with Cu^{2+} to achieve a turn-on sensing after addition of an analyte. When $FeCl_2$ was added as an analyte to this TMEDA-PPETE/Cu^{2+} solution, a ~100-fold fluorescence enhancement was observed.

Moreover, it was proposed that Fe^{2+} has displaced Cu^{2+} from the receptor and fluorescence turn-on is observed. This result shows that the TMEDA-PPETE/Cu^{2+} hybrid is a good turn-on Fe^{2+} sensor.

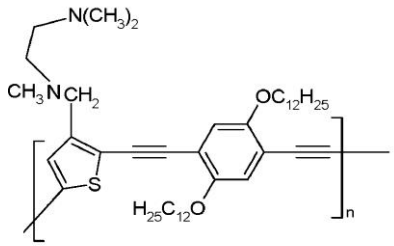

tmeda-PPETE

Figure 5.19. The tmeda-PPETE sensor.

In this work, a series of PPE polymers (Figure 5.21) sysnthesized in Prof. Yuming Zhao's lab (Memorial Unviersity) were analyzed for metal sensing investigations. The results are described in the sections below.

5.3.6. Ground and Excited-State Properties

The photophysical properties of PPEs are characterized by the presence of a relatively small Stokes shift, and a lack of a mirror-image relationship between absorption and emission spectra. Hence, the absorption-band envelope is usually broader than the emission-band envelope: these effects are very similar and are related to these seen with

oligo(phenylene ethynylene) (OPE) and oligo(phenylene vinylene) (OPV) as explained previously for hmer, and can be deduced by using models developed by Berg.[35, 64]

5.3.7. Absorption and Emission Spectra

Figure 5.21 shows the structures of the PPE polymers used in the sensing study. PPE^1 is comprised of two triazole rings with an appended dimethylamino group; PPE^2 also contains two triazole rings, but no amino group is available on the pendent benzene ring and, PPE^3 lacks the triazole rings, while containing the appended dimethylamino group PPE^4, however, contains both triazole rings and amino groups and also has more hydrophilic groups which allows it to dissolve in water with the aid of a co-solvent.

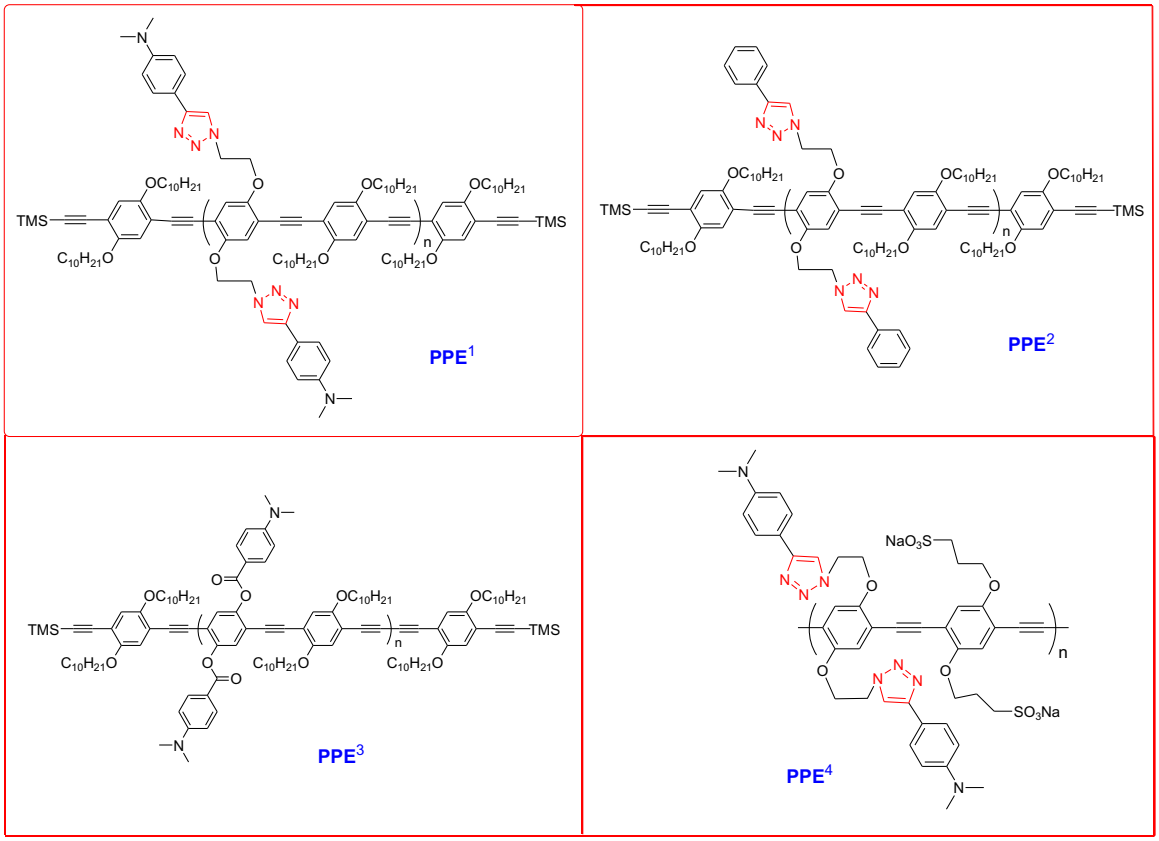

Figure 5.20. The structures of the PPE polymers and the abbreviations used in the metal sensing studies in this chapter.[65]

The subtle changes in the structures significantly alter the ground and excited-state properties of these compounds. Figure 5.22 shows the absorption and emission spectra of PPE^1, PPE^2, and PPE^3. For clarity, the emission of PPE^1 has been scaled by a factor of 15. Table 5.4 lists the main photophysical properties of these polymers. It is evident from Table 5.4 that the polymers in which the triazoles and amino group are both present shows weaker fluorescence as compared to the other PPEs where either triazoles or amino group are present. Ultimately, this indicates a possible role of triazole in the weak and low-intensity emission of PPE^1 and PPE^4.

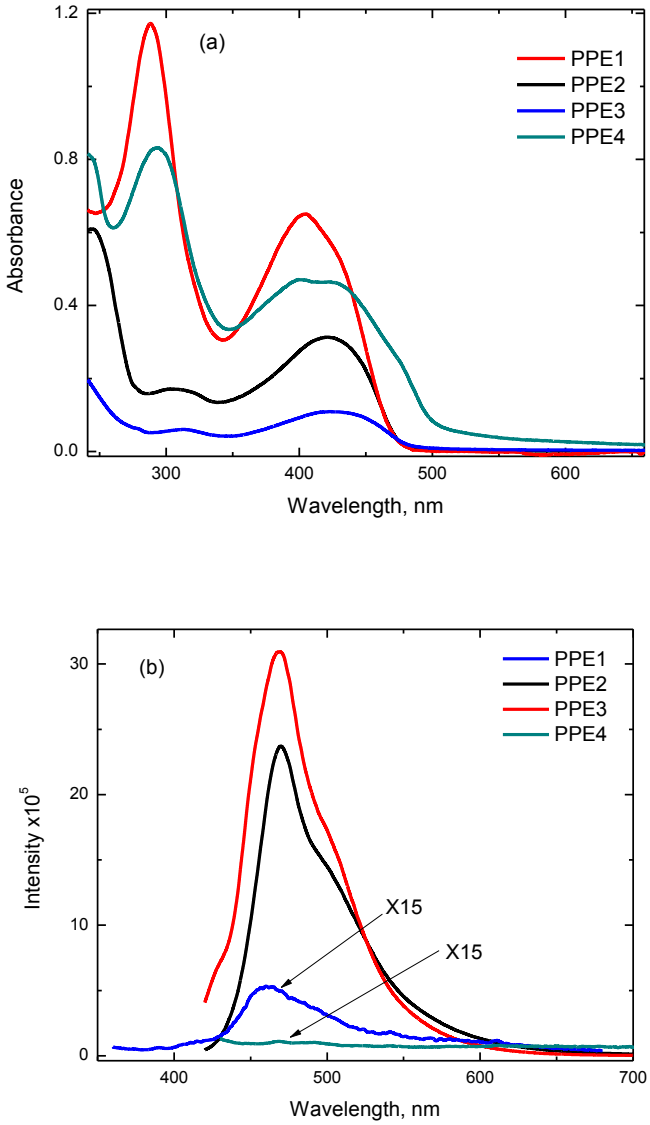

Figure 5.21. A comparison of (a) absorption and (b) emission spectra of PPE[1], PPE[2] PPE[3] and PPE[4]. For lucidity, the emission spectra of PPE[1] and PPE[4] was enhanced by a factor of 15. The data for PPE[1], PPE[2] PPE[3] were acquired in THF and PPE[4] in deionised H_2O at 298 ± 3 K. λ_{exc} for PPE[2], PPE[3] and PPE[4] = 400 nm and λ_{exc} for PPE[1] = 370 nm. The concentration of polymers was set to 100 µg mL^{-1}.

Table 5.4. Ground-and excited-state parameters of PPE polymers.

Entry	PPE[1][b]	PPE[2][b]	PPE[3][b]	PPE[4][a]
$\lambda_{max}^{S_0 \rightarrow S_1}$, nm	404	422	430	412
$E_{op}^{S_0 \rightarrow S_1}$, cm^{-1}	24750	23700	23250	24270
$\lambda_{em}^{S_1 \rightarrow S_0}$, nm	460	470	468	487
$E_{em}^{S_1 \rightarrow S_0}$, cm^{-1}	21740	21280	21360	20530
E_{SS}, cm^{-1}	3010	2420	1890	3740
$\phi_{em}^{S_1 \rightarrow S_0}$	0.038	0.29	0.74	0.0024
τ, ns	5.1	6.4	7.9	11.6
k_r, s^{-1}	7.4×10^6	4.5×10^7	9.3×10^7	2.0×10^5
k_{nr}, s^{-1}	$\mathbf{1.8 \times 10^8}$	$\mathbf{1.1 \times 10^8}$	$\mathbf{3.2 \times 10^7}$	$\mathbf{8.6 \times 10^7}$

[a] Data acquired in N_2 saturated deionized H_2O (λ_{exc} = 370 nm), the concentration of polymer was set to 100 µg mL^{-1} at 298 ± 3 K. [b]Acquired in THF (λ_{exc} = 400 nm), the concentration of polymers was set to 100 µg mL^{-1} at 298 ± 3 K.

The absorption spectra of PPEs are usually broad, while the emission spectra are comparatively narrower.[51, 66] Interestingly, the emission spectra of PPE[1] and PPE[4] were found to be relatively broad. Although the emission and absorption spectra of PPEs show substantial asymmetry, they usually originate from $\pi \rightarrow \pi^*$ transition. As such, the values of radiative and non-radiative decay rate constants are calculated as described in Chapter 1. It is noteworthy, as well, that the values of Φ_{em} are much lower for PPE[1] and PPE[4] where both triazole and amino groups are present.

5.3.8. Cation Sensing in Water Using PPE^4

In order to assess the sensing abilities of PPE^4 in H_2O, it was titrated with six metal salts: $Cd(ClO_4)_2$, $NaClO_4$, $Zn(OTf)_2$, $Cu(OTf)_2$, $Ba(OTf)_2$, Li(OTf), and a Brønsted acid (TFA) (OTf is trifluoromethane sulfonate) and the resulting titration data are shown in Figures 5.23 to 5.29. The changes in the respective absorption and fluorescence spectra, with the addition of aliquots of the metal ions, were ascribed to interactions between PPE^4 and the responsive metal ions. PPE^2 and PPE^3 were highly fluorescent and were not considered suitable candidates for a turn-on sensing study. In order to achieve a turn-on sensing in water, PPE^4 was synthetically tuned by introducing sodium sulphonate groups to achieve solubility in H_2O, the dimethylamino moiety as an electron-donor and the triazole ring as acceptor, to achieve a weak emission by utilizing a PET quenching process—thus, the emission of PPE^4 was found to be very weak, but broad.[65]

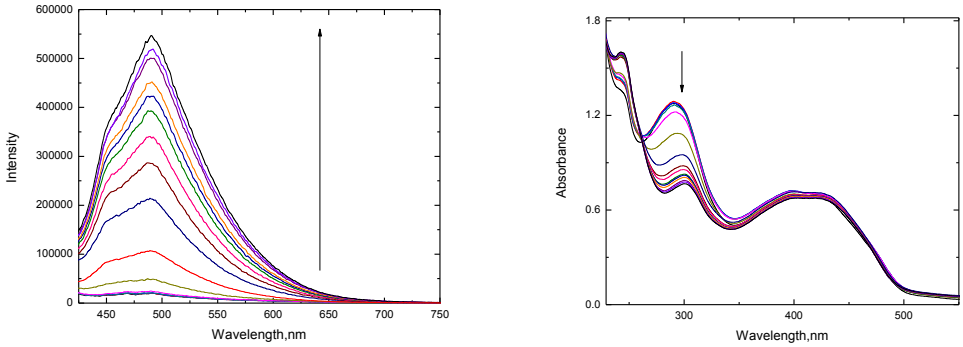

Figure 5.22. Emission (left) and absorption (right) spectra of PPE^4 obtained as a function of increasing aliquots of TFA in the following manner; 0.0, 0.12, 0.16, 0.18, 0.24, 0.32, 0.40, 0.44, 0.48, 0.52 , 0.56, 0.64, 0.80, 1.42, 1.52 and 2.0 mM titrated in deionized H_2O at 298 ± 3 K, λ_{exc} = 370 nm. The arrows indicate the direction of response after the addition of analyte. The concentration of PPE^4 was set to 100 µg mL^{-1}.

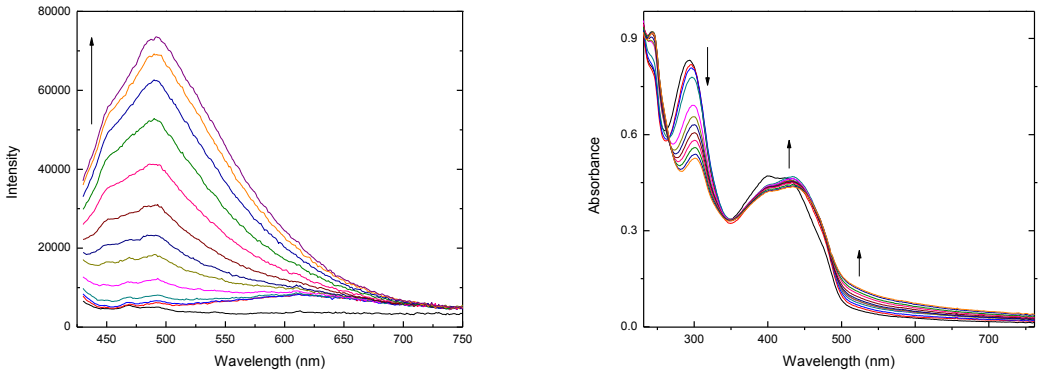

Figure 5.23. Emission (left) and absorption (right) spectra of PPE[4] obtained as a function of increasing aliquots of $Cd(ClO_4)_2$ in the following manner: 0, 2.0, 2.4, 2.8, 3.2, 3.6, 4.0, 4.8, 6.0, 8.0, 12, 20, and 28 mM titrated in deionized H_2O at 298 ± 3 K, λ_{ex} = 370 nm. The arrows indicate the direction of response after the addition of analyte. The concentration of PPE[4] was set to 100 µg mL^{-1}.

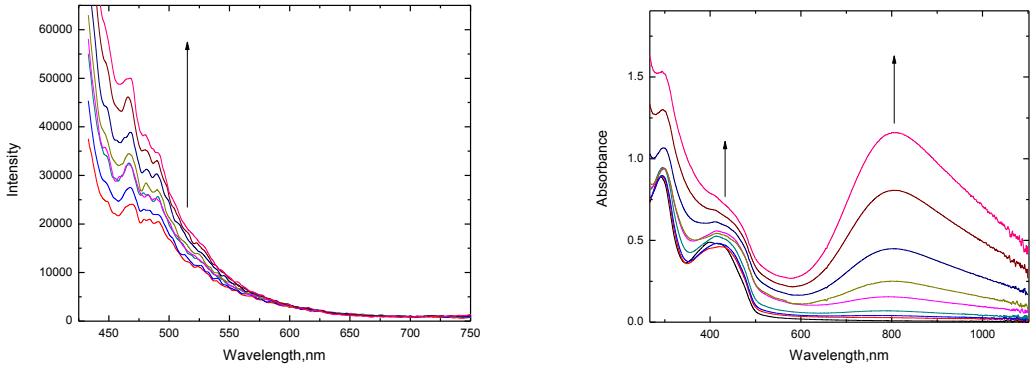

Figure 5.24. Emission (left) and absorption (right) spectra of PPE[4] obtained as a function of increasing aliquots of $Cu(OTf)_2$ in the following manner: 0.0 , 0.8, 2.4, 5.6, 12, 24.8, 50.4, and 101.6 mM titrated in deionized H_2O at 298 ± 3 K, λ_{ex} = 370 nm. The arrows indicate the direction of response after the addition of analyte. The concentration of PPE[4] was set to 100 µg mL^{-1}.

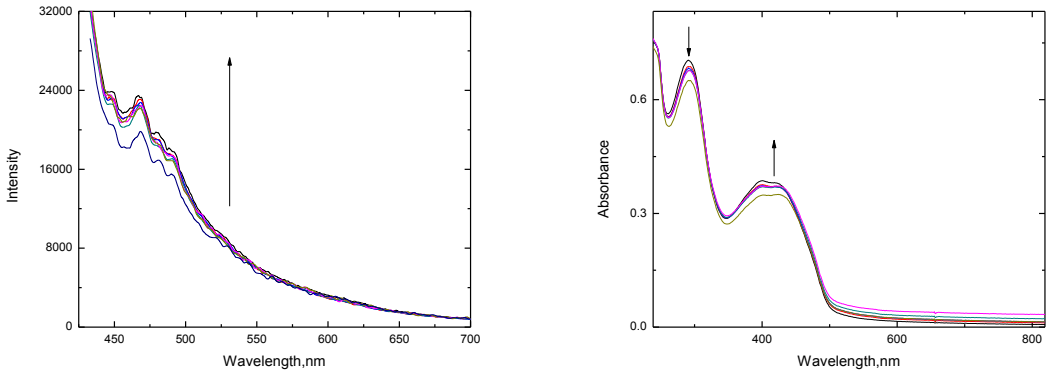

Figure 5.25. Emission (left) and absorption (right) spectra of PPE^4 obtained as a function of increasing aliquots of LiOTf in the following manner: 0.0 , 0.8, 2.4, 5.6, 12, 24.8 and 50.4 mM in deionized H_2O at 298 ± 3 K, λ_{ex} = 370 nm. The arrows indicate the direction of response after the addition of analyte. The concentration of PPE^4 was set to 100 µg mL^{-1}.

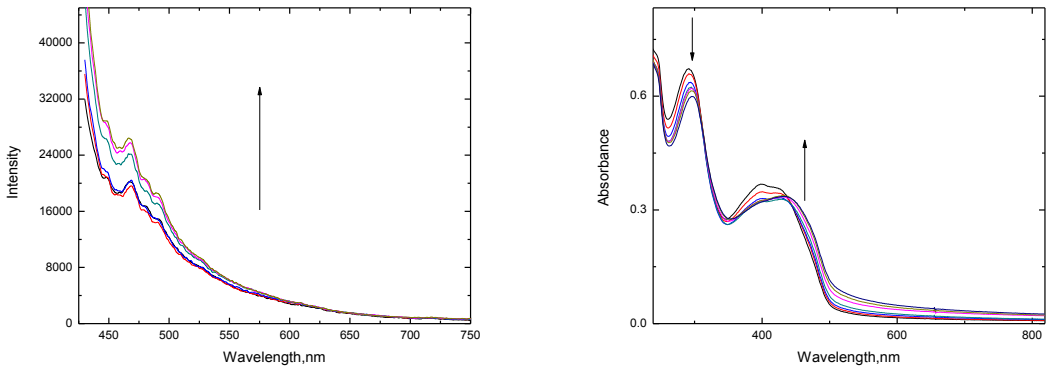

Figure 5.26. Emission (left) and absorption (right) spectra of PPE^4 obtained as a function of increasing aliquots of $Zn(OTf)_2$ in the following manner: 0.0 ,0.8, 2.4, 5.6, 12 and 25.6 mM in deionized H_2O at 298 ± 3 K, λ_{ex} = 370 nm. The arrows indicate the direction of response after the addition of analyte. The concentration of PPE^4 was set to 100 µg mL^{-1}.

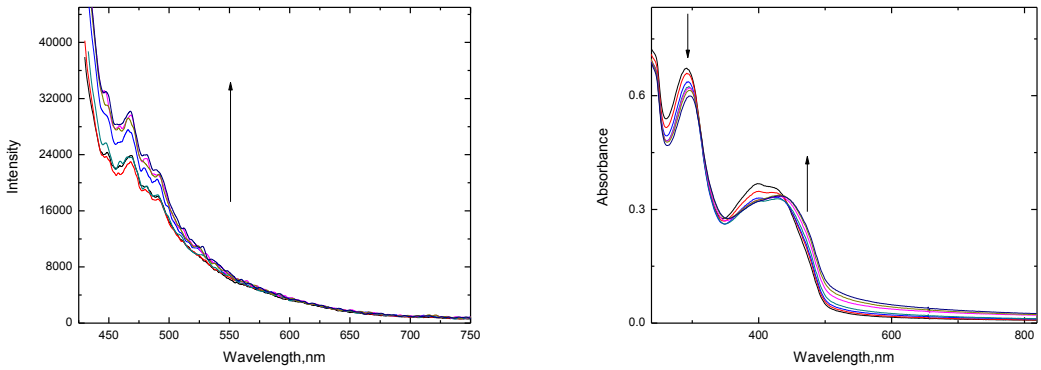

Figure 5.27. Emission (left) and absorption (right) spectra of PPE^4 obtained as a function of increasing aliquots of $Ba(OTf)_2$ in the following manner: 0.0 , 0.8, 2.4, 5.6, 12, 24.8 and 50.4 mM in deionized H_2O at 298 ± 3 K, λ_{ex} = 370 nm. The arrows indicate the direction of response after the addition of analyte. The concentration of PPE^4 was set to 100 µg mL^{-1}.

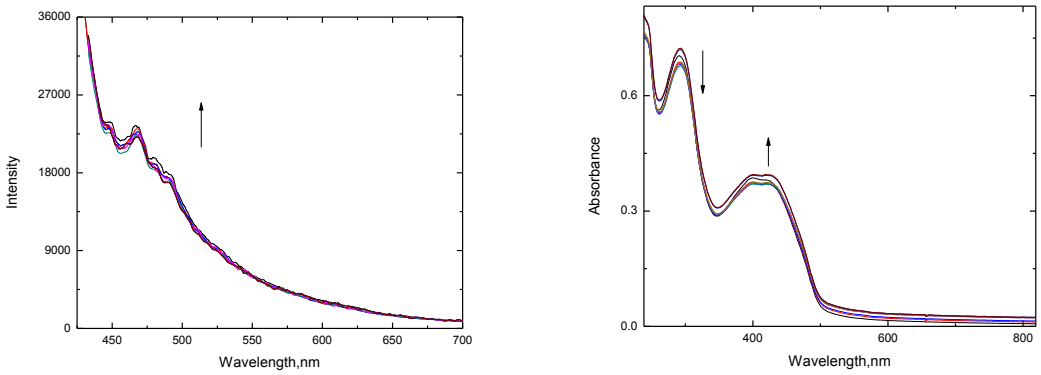

Figure 5.28. Emission (left) and absorption (right) spectra of PPE^4 obtained as a function of increasing aliquots of $NaClO_4$ in the following manner: 0.0 , 6.5, 13.0, 28.0, 60.0, 120, 180 and 380 mM in deionized H_2O at 298 ± 3 K, λ_{ex} = 370 nm. The arrows indicate the direction of response after the addition of analyte. The concentration of PPE^4 was set to 100 µg mL^{-1}.

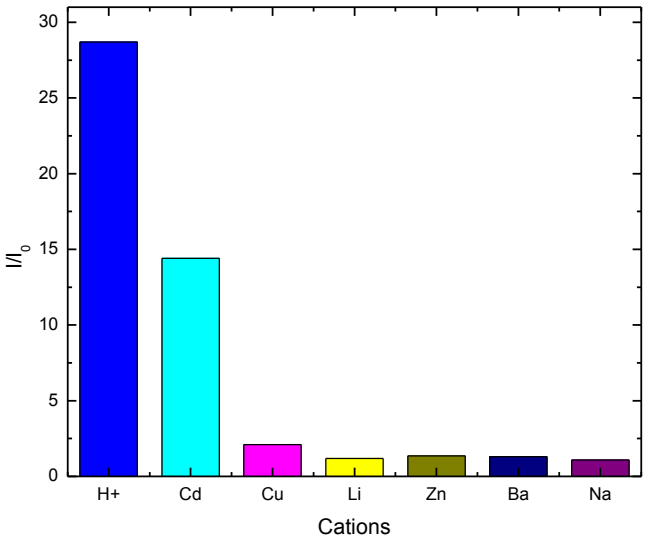

Figure 5.29. A comparison of the fluorescence enhancement of PPE^4 at 490 nm in response to various cations, calculated from the emission titration data in Figure 5.23 to 5.29. Noticeably, the greatest enhancement was for $Cd(ClO_4)_2$ and TFA.

A considerable enhancement in the fluorescence intensity was observed when $Cd(ClO_4)_2$ was added to a solution containing PPE^4. After the addition of aqueous 20 mM of $Cd(ClO_4)_2$, a ca. 14-fold enhancement was recorded at ca. 492 nm (Figure 5.30). Furthermore, a new broad and featureless band appeared centered at ca. 640 nm after the addition of just 2.0 to 3.0 mM $Cd(ClO_4)_2$ (Figure 5.24). A very similar response was observed, as well, when TFA was added to PPE^4, where the emission intensity was enhanced by ca. 29 fold after addition of ca. 2.0 mM of TFA. Interestingly, the broad and featureless band observed in the case of titration with $Cd(ClO_4)_2$ was not observed: this behaviour might be due the fact that there appears to be two distinct coordinating sites, namely, the triazole (pKa = 9.26) and amino groups (pKa = 4.87).[67] Since the amine will

be more basic in nature than the triazole, H^+ will prefer to bind at the amino site. On the other hand, however, Cd^{2+} can also bind to a triazole nitrogen in one step and then bind to the amine in a subsequent step. To further elucidate this idea, a monomer was prepared (Figure 5.31) and its ^1H NMR chemical shifts were observed upon addition of Cd^{2+}. It was observed that the triazolyl and aminophenyl protons were shifted downfield, and it was more pronounced in the aminophenyl protons—confirming that both of these coordinating sites are taking part in the binding with Cd^{2+} as well as with H^+.[65]

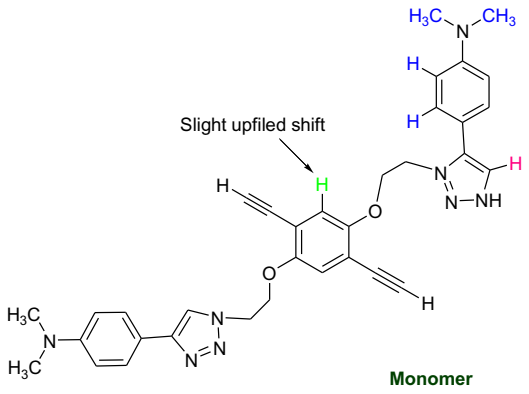

Figure 5.30. Structure of the monomer and the corresponding proton's which exhibits change in NMR chemical shifts upon addition of Cd^{2+}.[65]

5.3.9. The Turn-on Sensing Mechanism in PPE Polymers

The sensing mechanism can be explained via a new energy-transfer sensitization mechanism as depicted in Scheme 5.6. In this mechanism, PPE serves primarily as a fluorophore unit: following the irradiation (λ_{exc} = 400 nm), PPE captures a photon and reaches first singlet excited-state (S_1). Meanwhile, rapid-energy transfer from PPE sensitizes the donor (amino) group. As a result, the amino moiety undergoes an

intramolecular charge transfer (ICT) to the triazole group. Due to the existence of this donor (amino)-acceptor (triazole) ICT, energy-transfer and sensitization process, the fluorescence of PPE^4 remains very weak and broad. This idea is, furthermore, confirmed by the observation of PPE^2 and PPE^3 emission where either a D or A is missing—thus proving that no ICT is expected and, as a result, the fluorescence of these two polymers is very intense. Once Cd^{2+} binds to the amino group, it reduces the electron-donating ability of the donor amino group and ICT is non-tenable. As a result of this cessation of ICT, then, the fluorescence from PPE unit gets revived and observed as fluorescence enhancement upon $Cd(ClO_4)_2$ addition.

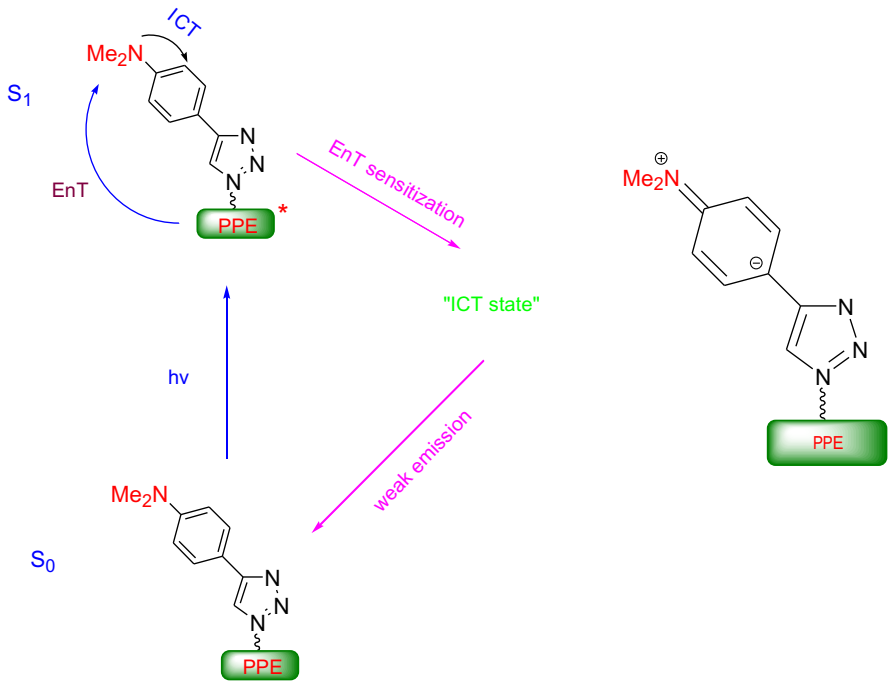

Scheme 5.6. A schematic illustration of the energy-transfer sensitization mechanism of metal sensing in PPE^4, where, following photoexcitation, PPE undergoes rapid energy transfer and sensitizes the amino group. Consequently, the amino group becomes a donor and ICT from amino to acceptor triazole occurs. Moreover, this ICT is responsible for the weak emission of the PPE^4 polymer. Here, EnT depicts energy transfer.[65]

5.3.10. Sensing Using Tetrathiafulvelene (TTF) Based Molecules

TTF based molecules have been proven to be excellent building blocks for numerous CT processes.[68] The discovery of 7,7,8,8 – tetracyanoquinodimethane (TCNQ) (Figure 5.32) spurred TTF's potential to be used as an excellent platform in the redox processes. The TTF-TCNQ marriage opened new avenues for the organic-based conductors.[69] Furthermore, the CT salts of TCNQ showed conductance at temperatures as low as 56 K.[70] TTF-based compounds are particularly of interest because of their low HOMO-LUMO gaps, which can be modulated by designing the synthesis accordingly.

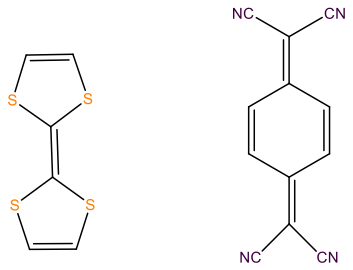

Figure 5.31. The basic building blocks of TTF CT chemistry, TTF (left) and TCNQ (right).

TTF-based molecules have been reviewed several times quite extensively.[71] [68, 72-78] The featured properties which make them lucrative in the study of CT reactions are:

- Owing to their electron-rich structures, they are excellent electron donors.
- They can undergo sequential oxidation into a radical cation and dication to form stable $6\pi e^{-}$, 1,3-dithiolium cations with oxidation potentials of $E_{1/2}^{a}$ = +0.35 V and $E_{1/2}^{b}$ = +0.71 V (vs. Ag/AgCl, MeCN/$TBAPF_6$), respectively. Furthermore,

conversion from cis to trans after forming the dication is also a unique feature (Scheme 5.7).

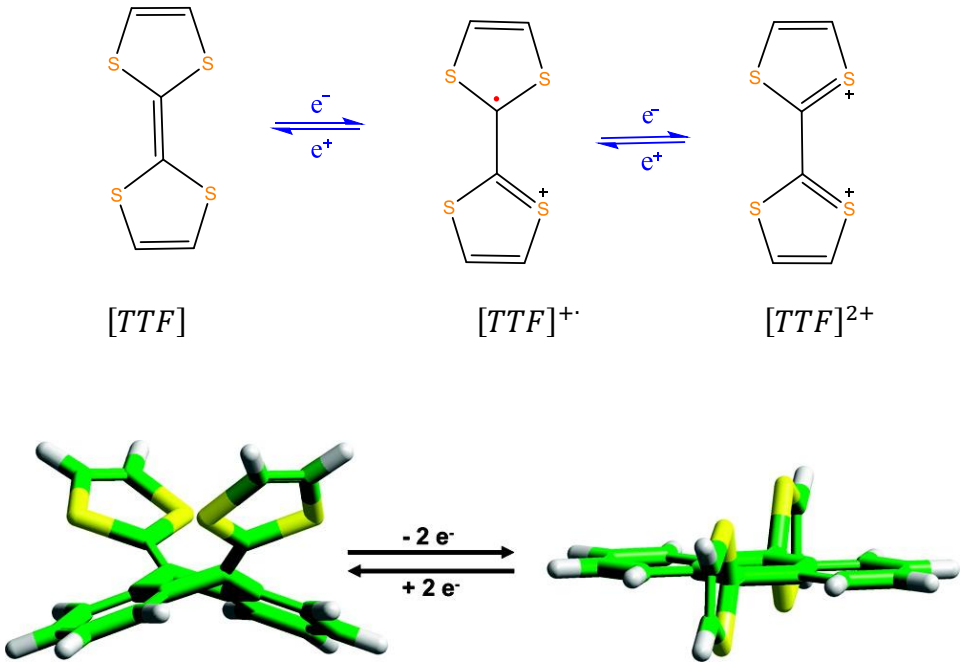

Scheme 5.7. The sequential and fully reversible oxidation of TTF into $TTF^{\cdot+}$ and TTF^{2+} (top) and geometry of ex-TTF (extended TTF) and ex-TTF^{2+} (bottom). Reprinted in part with permission from Martín, N.; Sánchez, L.; Herranz, M. A. Á.; Illescas, B.; Guldi, D. M. Acc. Chem. Res. 2007, 40, 1015.[68]

- The oxidation potential of TTF can be tuned directly from the synthesis via an embedded electron-withdrawing group (EWG) and an electron-donating group (EDG).
- TTF molecules are highly stable, except when treated with a strong acid or base.

- The UV-Vis spectra of TTF, $TTF^{\cdot+}$, and $TTF^{2+}$are distinctly different, making data interpretation easy.

TTF molecules can be extended by adding diverse π-spacers forming ex-TTF (extended TTF derivatives).[71] Chen et al. have been particularly successfully to exploit properties of TTF, by designing a wide array of TTF-based molecules involving ex-TTF, anthracene, and pyrene-appended TTF to achieve remarkable sensing properties via synthetic control.[79-82] Figure 5.33 shows some of the conjugated oligoyne-ex-TTF molecules reported by Chen et al., where the HOMO-LUMO gaps have been tuned by the targeted synthesis of the molecules. DFT calculations suggested that the HOMO's are evenly

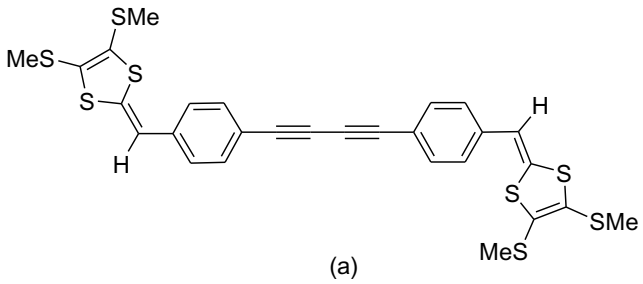

(a)

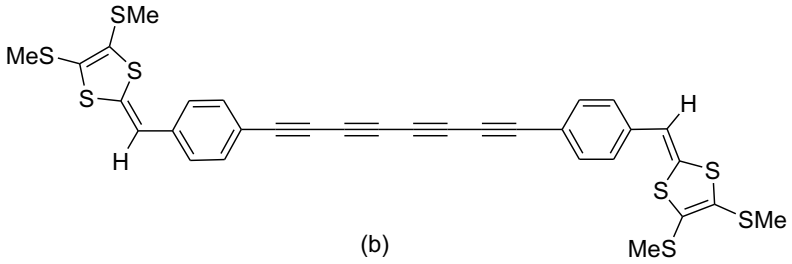

(b)

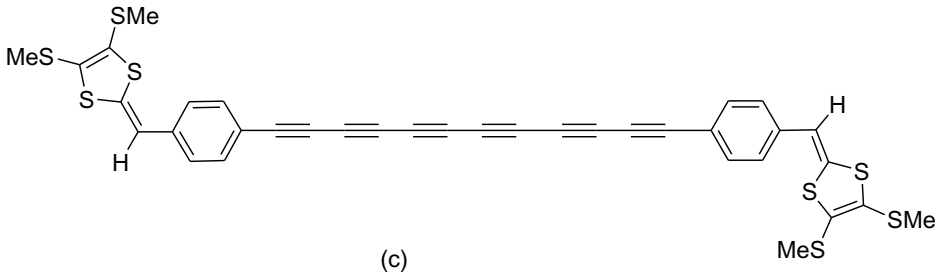

(c)

Figure 5.32. Showing the structures of conjugated, oligoyne-ex-TTF molecules.[79]

distributed across the whole π framework while the LUMO's are centralized on the oligoyne moiety as the chain length increases. Furthermore, the optical band gaps (E_g) of oligoyne–ex-*TTF's* are dependent upon the chain length of the central oligoyne moiety. It was concluded, then, that the electron-accepting ability of the oligoyne increases with increasing length of the oligoyne moiety. Table 5.5 lists the HOMO-LUMO gaps and corresponding E_g values of the oligoyne-ex-TTF molecules.[79]

Table 5.5. The electronic properties of oligoyne ex-TTF molecules shown in Figure 5.33. [79]

ex-TTF	λ_{abs}, nm ($\varepsilon \times 10^4$ M^{-1} cm^{-1})	E_{HOMO} (eV)	E_{LUMO} (eV)	$\Delta E_{H\text{-}L}$ (eV)	E_g (eV)
a	423 (6.69), 332 (2.23)	-5.08	-2.04	3.04	2.61
b	467 (8.39), 3.7 (6.58)	-5.08	-2.33	2.75	2.39
c	506, 467, 458, 431, 346, 326, 303	-5.21	-2.71	2.50	2.25

ex-TTF can be further divided into two different classes: (i) TTFAQ – composed of an anthraquinoid conjugated π-linkage between the two thiole rings.[83] (ii) TTFV (tetrathiafulvalene vinylogues) - composed of two C = C bonds between the dithiole rings.[71, 84] TTFAQ undergoes conformational switching during redox process and form a stable dication species. In order to mitigate the repulsion between sulfur atoms and the hydrogen of the anthraquinoid moiety it acquires a conformation in which the central part becomes planar and the dithiole rings becomes perpendicular to the central plane.[85, 86]

Similarly, TTFV also undergoes conformational changes upon oxidation. TTFV remains in a non-planar conformation in its neutral state and upon oxidation it acquires a planar conformation. The non-planar conformation dodges the repulsion between the dithiole rings and planar conformation as well as favours the formation of dication species by reducing any steric interactions.[71]

5.3.11. TTF Based Metal Sensors

As alluded to earlier, synthetically-tuned TTF molecules with embedded redox moieties can be designed to achieve selective metal sensing. While sensing studies using TTF began with crown ethers, crown-ether appended TTF molecules are still one of the favoured structural motifs in anion and cation recognition. In 1992, for example, a crown ether was attached to TTF and found to complex with Na^+.[87] As well, a mono-crown ether TTF was reported by Moore et al. and selective detection of Li^+ and K^+ was achieved to a moderate level while a noticeable response to Ag^+ was observed.[88, 89] Le Derf et al. reported a Ba^{2+} sensor (Figure 5.34), where interaction of Ba^{2+} was observed by changes in ^1H NMR, UV-Vis, and interestingly by X-ray crystallography.[90, 91]

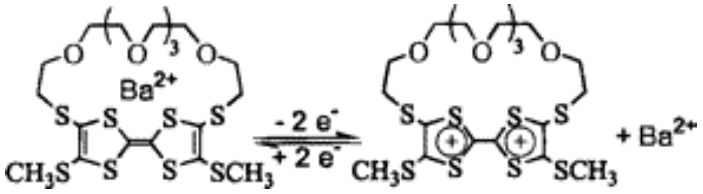

Figure 5.33. A TTF based, crown ether appended Ba^{2+} receptor. [91] Reprinted with permission from Derf, F.; Mazari, M.; Mercier, N.; Levillain, E.; Richomme, P.; Becher, J.; Garín, J.; Orduna, J.; Gorgues, A.; Sallé, M. Inorg. Chem. 1999, 38, 6096.

Shao et al. have successfully demonstrated Ba^{2+} sensing using a biscrown-annulated ex-TTF sensor.[81] The sensor involves appended anthracene and two crown ether moieties attached to the TTF (Figure 5.35). In this molecular assembly TTF is an electron donor and anthracene is an electron acceptor and the clever synthetic design uses these features to facilitate the PET process. Moreover, the fluorescence remains dark because of the PET from the TTF to the anthracene, and as soon as a metal ion is trapped between the two crown ethers, the PET shuts down and the fluorescence from anthracene appears. A binding constant analysis using SPECFIT afforded a 1:1 and 1:2 type of two-step binding equilibrium, with the highest binding constant for Ba^{2+} over the other cations tested i.e. Mg^{2+}, Ag^{+} and Li^{+}.

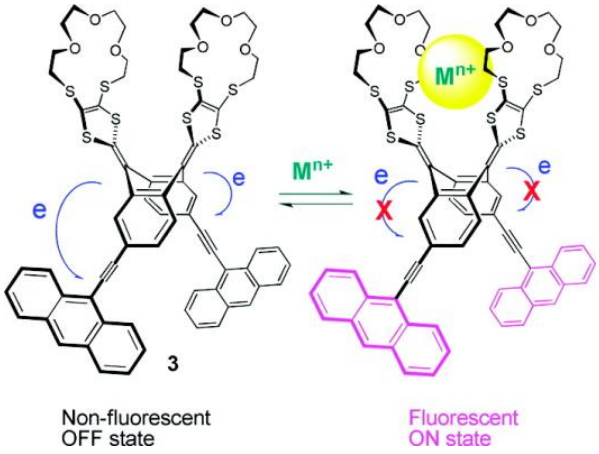

Figure 5.34. A Biscrown-annulated ex-TTF sensor. Metal trapped in the space between crown ethers shuts down PET affording fluorescence revival.[81] Reprinted with permission from Shao, M.; Dongare, P.; Dawe, L. N.; Thompson, D. W.; Zhao, Y. Org. Lett. 2010, 12, 3050.

Shao et al. argue that Ba^{2+}, owing to its larger size than the other cations analysed in the same study (Mg^{2+}, Ag^{+} and Li^{+}), could fit best into the space between the two crown ethers and provide the best fluorescence response.

5.3.11.1. A Dianthryl Tetrathiafulvalene Vinylogue (TTFV) Molecule as a Metal Ion Sensor

A dianthryl TTFV molecule which has been used as a metal ion sensor is shown in Figure 5.36. The molecule involves triazole rings, which function as good linkers or ligands, a pair of anthracenes working as fluorophores as well as an electron acceptor, and TTFV (TTF vinylogue) as an electron donor. Like many other PET-based turn-on sensors, this molecule also shows a low-intensity emission in THF ($\Phi_{\mathrm{em}} = 9 \times 10^{-3}$). However, once the metal ions are added, they preferably bind to the triazole nitrogen and raise the

energy of the bridge between the donor and acceptor and attenuate the PET from TTFV to anthracene.[82] As a result, the fluorescence from anthracene revives. Thus, the fluorescence enhancement reveals three main bands, the characteristics of the anthracene $S_1 \rightarrow S_0$ transition ($\pi \rightarrow \pi^*$ in nature), and the corresponding vibronic progressions.

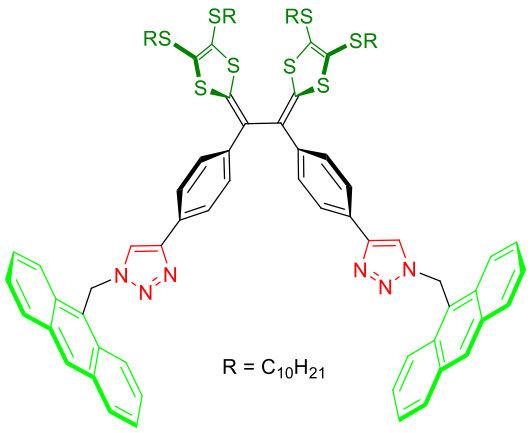

Figure 5.35. The structure of a click-assembled dianthryl TTFV molecule (tweezer).

The fluorescence spectra of the TTFV molecule a function of added $Cu(OTf)_2$ and $Cd(ClO_4)_2$ are shown in Figures 5.37.[82] Here, the emission spectra clearly show a fluorescence pattern of the anthracene fluorophore with a $\pi \rightarrow \pi^*$ transition at 395 nm and the corresponding vibronic progressions at 415 and 440 nm. Although the sensor was very sensitive towards the Cd^{2+} ion, the highest enhancements were observed for the Cu^{2+} ion (ca. 26–fold enhancement at 415 nm). Based on these observations, then, this molecule can be attributed as a Cu^{2+} sensor. The detailed emission and absorption titration data, along with the corresponding Stern-Volmer plots, are provided in the Appendix (Figures S19-S26).

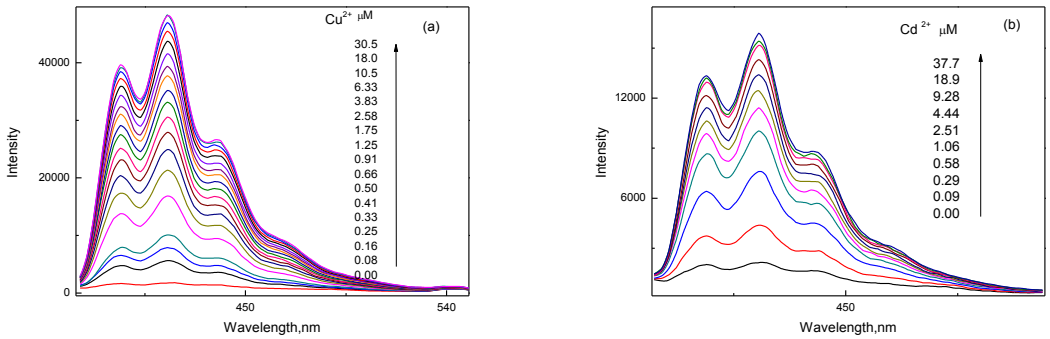

Figure 5.36. (a) Fluorescence spectra of TTFV tweezer obtained as a function of increasing concentration of $Cu(OTf)_2$. (b) fluorescence spectra obtained as a function of increasing concentration of $Cd(OTf)_2$ in THF at 298 ± 3 K. [TTFAn] = (5.5 μM) and λ_{ex} = 350 nm. The arrows indicate the trend for the increasing metal ion concentration.[82]

5.3.12. Analysis of Association Constants

To examine the binding equilibria and the corresponding equilibrium constants, the emission titration data was subjected to SVD using SPECFIT/32 and the detailed results of the SVD analysis are provided in the Appendix (Figures S27-S34). The analysis reveals three different coloured species and three dominating species.[82] Moreover, this result reveals the existence of a 1:1-and 1:2-type of step-wise binding equilibria for all analytes as well as the equilibrium constants for binding between TTFV and cations. The two-step binding is proposed to be from the triazole rings which act as both linkages and receptors. The literature values of the standard electrode potentials (E^0) of metal ions (in H_2O) along with the extracted association constants are displayed in Table 5.6.

Table 5.6. The association constants (K_A) for the dianthryl TTF molecule and cations along with the standard electrode potentials (E^0) of the cations.[82]

Cation	log β_{11}[a]	log β_{12}[a]	E^0, V[b]
Cu^{2+}	7.12 ± 0.7	12.1 ± 0.8	+0.33 ($Cu^{2+}\rightarrow Cu^0$)
Cd^{2+}	5.22 ± 0.6	9.75 ± 0.6	-0.39 ($Cd^{2+}\rightarrow Cd^0$)
Zn^{2+}	4.78 ± 0.2	8.59 ± 0.3	-0.76 ($Zn^{2+}\rightarrow Zn^0$)
Fe^{2+}	4.62 ± 0.4	10.8 ± 0.2	-0.42 ($Fe^{2+}\rightarrow Fe^0$)
Mn^{2+}	4.58 ± 0.1	7.56 ± 0.1	-1.20 ($Mn^{2+}\rightarrow Mn^0$)
Ag^{+}	3.57 ± 0.1	6.67 ± 0.1	+0.80 ($Ag^{+}\rightarrow Ag^0$)
Hg^{+}	2.72 ± 0.2	4.47 ± 0.2	+0.79 ($Hg^{2+}\rightarrow Hg^0$)
Pb^{2+}	1.72 ± 0.2	2.46 ± 0.3	-0.12 ($Pb^{2+}\rightarrow Pb^0$)
H^{+}	1.63 ± 0.5	2.95 ± 0.6	+0.00 ($H^{+}\rightarrow H_2$)

[a] The quantity β represents the overall association constant. [b]E^0 values are relative to standard hydrogen electrode and were acquired in H_2O at 298 K; adapted from Vanýsek, P. In Handbook of Chemistry and Physics; 93 ed.; Chemical Rubber Company, 2012; Vol. 1 and Standard Potentials in Aqueous Solutions; Bard, A. J.; Parsons, R.; Jordan, J., Marcel Dekker New York, 1985; Vol. 1.[92, 93]

The association constants qualitatively follow the fluorescence response in titration experiments—i.e. association constants were largest for Cu^{2+} and smallest for H^{+}.

Further analysis of the equilibrium constants was performed by plotting the equilibrium constants vs. standard electrode potentials (E^0, V) of the metal ions (Figure 5.38). The resulting plots unveil some very interesting aspects, and based on these plots the metal ions can be classified into two separate categories: the most responsive metal ions i.e. Cu^{2+}, Fe^{2+}, and Cd^{2+} show a linear correlation and fall in one group, while the less responsive or less selective metal ions, such as $Ag^{+}, Zn^{2+}, Hg^{2+}, Pb^{2+}$, and H^{+}(TFA) show a linear correlation and fall into another group. Moreover, the correlations can be interpreted in terms of Pearson's Hard and Soft Acid Base (Lewis) theory (HSAB) theory.[94, 95] According to the HSAB theory, the less responsive cations (Ag^{+}, Hg^{2+} and Pb^{2+}) are categorized as the soft acids with the

exception of H^+ (hard acid) and Zn^{2+} (borderline acid). On the other hand the highly responsive cations Cu^{2+} and Fe^{2+} are categorized as borderline acids, with the exception of Cd^{2+} (soft acid). As such, the borderline acids tend to have a larger size and small electronegativity than the hard acids. However, a detailed and more focused investigation is required to completely delineate the origin of such effects.

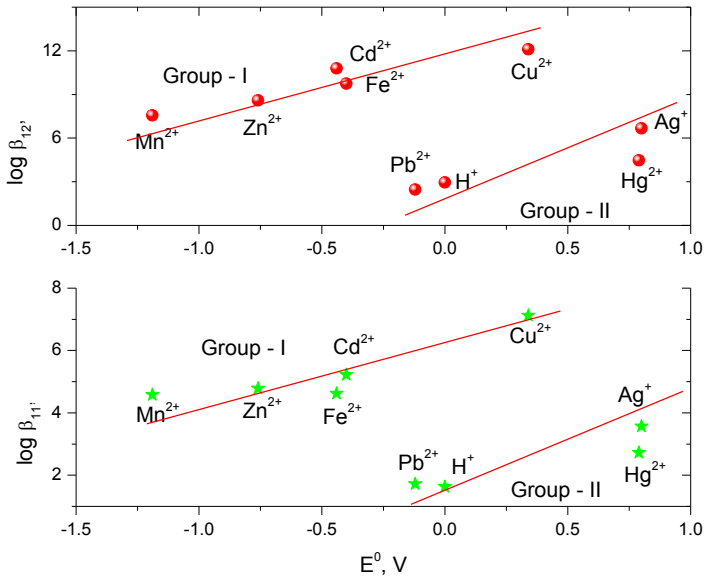

Figure 5.37. Showing correlation between the equilibrium constants for the binding of the cation with TTFV molecule and the reduction potential of cations.[82] Reduction potential of the cations are adapted from Vanýsek, P. In Handbook of Chemistry and Physics; 93 ed.; Chemical Rubber Company, 2012; Vol. 1 and Standard Potentials in Aqueous Solutions; Bard, A. J.; Parsons, R.; Jordan, J., Marcel Dekker New York, 1985; Vol. 1.[92, 93]

Nevertheless, the borderline bases are easily reducible and have a high positive E^0 which enhances the possibilities of the CT from TTFV to anthracene. As a result, the PET

shuts down more quickly which is observed as a greater fluorescence enhancement. This analysis implies that the PET sensors can be designed by employing HSAB theory.

Lever has documented the electrode potentials of metal complexes and related them to the association constants of ligand binding. In this treatment, $Ru^{III/II}$ or $Re^{I/II}$ redox couples and the relative binding strength of a ligand with the two oxidation states was studied. The potential of a given redox couple reflects the relative binding strength of the two oxidation states to the ligand concerned. This is illustrated in the following free energy cycle proposed by Lever (Scheme 5.8).[96, 97]

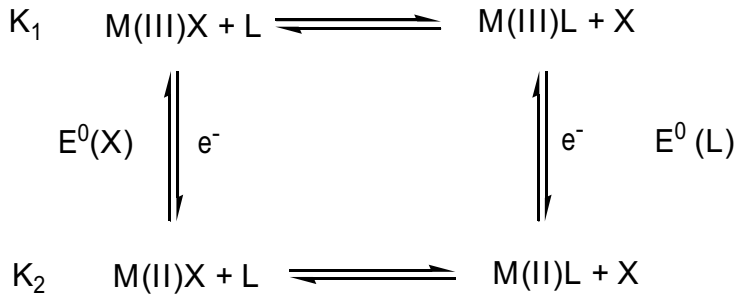

Scheme 5.8. The free energy cycle proposed by Lever for $Ru^{III/II}$ or $Re^{I/II}$ redox couples. M = host (in this case a metal ion), X = redox active site of the metal center, L = guest (in this case a ligand), e^- = electron.

Equation 5.2 relates the redox potential of both the ligand and metal ion with the association constants.[96, 97]

$$E^0(L) - E^0(X) = (RT/nF)\, ln\, (K_2/K_1) \qquad [5.2]$$

In a similar fashion, one can relate the redox potential of both the TTF tweezer and analyte with association constants. The electrode potential of an analyte under investigation reflects its relative binding strength with the tweezer i.e. the more positive potential of analyte is, the larger the association constant.[82] A free energy cycle pertinent to the case is shown in Scheme 5.9 to further illustrate the arguments.

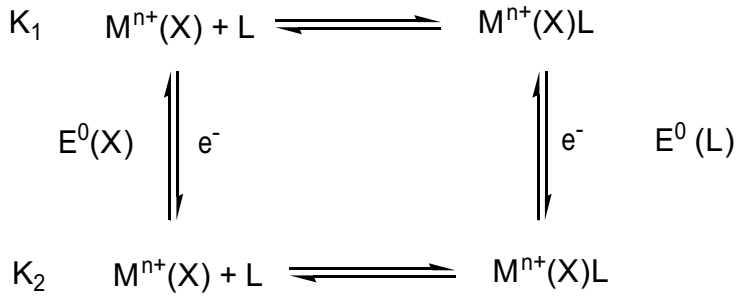

Scheme 5.9. Presenting the free energy cycle of tweezer binding with analyte. Here, M = host (in this case the tweezer), X = redox active site of tweezer, L = guest (in this case an analyte), e^- = electron.

Equation 5.2 can be considered to relate the redox potential of both the analyte and the tweezer with the association constants by considering $E^0(L)$ as the redox potential of the analyte (listed in Table 5.6) and $E^0(X)$ redox potential of the tweezer.

5.4. Concluding Remarks

This chapter provides arguments for an understanding of the design of new molecular sensors. Clever synthetic design can be utilized to tune the excited-state properties of a molecule, and a slight change in the oligomer structure (hmers, in this case) results in a dramatic change in their excited-state behaviour towards diols. Moreover,

hmers provide an opportunity to understand the saccharide sensing of oligomers with multiple $B(OH)_2$ groups: both the hmer oligomers provide selectivity towards fructose under physiological conditions.

The triazole-based PPE polymer sensors exhibit a new sensing mechanism for the turn-on sensing. Among all the PPE molecules, PPE^4 and PPE^1 contain both amino and triazole groups—thus making them weakly fluorescent and ideal for turn-on sensing studies. Furthermore, a new energy-transfer sensitization mechanism operates in the turn-on sensing of metal ions by the PPE^4 polymer. On the other hand, however, the remaining PPE polymers in the series are highly fluorescent and cannot be considered fit for turn-on sensing studies. This lent insight into the possible design of a sensor.

A triazole-based TTFV sensor shows high sensitivity towards a variety of metal ions. Furthermore, the sensor is very selective towards Cu^{2+} even at μM concentrations. The triazole moiety here acts as a linker and ligand in this molecule, showing that triazoles are "non-innocent linkers". The correlation between standard electrode potential and association constants, moreover, reveals that the sensing response can potentially be fine tuned by consideration of HSAB theory.

References

[1] Hulanicki, A.; Glab, S.; Ingman, F., Pure Appl. Chem., (1991) 63, 1247.

[2] McDonagh, C.; Burke, C. S.; MacCraith, B. D., Chem. Rev., (2008) 108, 400.

[3] McQuade, D. T.; Pullen, A. E.; Swager, T. M., Chem. Rev., (2000) 100, 2537.

[4] Stokes, G. G., Phil. Trans. Soc. (1852) 142, 463.

[5] de Silva, A. P.; Moody, T. S.; Wright, G. D., Analyst, (2009) 134, 2385.

[6] Wu, J.; Liu, W.; Ge, J.; Zhang, H.; Wang, P., Chem. Soc. Rev., (2011) 40, 3483.

[7] Lackowicz, J. R. Ed. Principles of Fluorescence Spectroscopy, Springer: (2009); Vol. 3.

[8] Lorand, J. P.; Edwards, J. O., J. Org. Chem., (1959) 24, 769.

[9] Soundararajan, S.; Badawi, M.; Kohlrust, C. M.; Hageman, J. H., Anal. Biochem., (1989) 178, 125.

[10] Nakatani, H.; Morita, T.; Hiromi, K., Biochim. Biophys. Acta, (1978) 525, 423.

[11] Nakatani, H.; Hiromi, K., Biochim. Biophys. Acta, (1978) 524, 413.

[12] Yoon, J.; Czarnik, A. W., J. Am. Chem. Soc., (1992) 114, 5874.

[13] Ludwig, R.; Harada, T.; Ueda, K.; James, T. D.; Shinkai, S., Perkin Trans. 1, (1994), 697.

[14] Murakami, H.; Nagasaki, T.; Hamachi, I.; Shinkai, S., Perkin Trans. 1, (1994), 975.

[15] Imada, T.; Kijima, H.; Takeuchi, M.; Shinkai, S., Tetrahedron Lett., (1995) 36, 2093.

[16] Imada, T.; Kijima, H.; Takeuchi, M.; Shinkai, S., Tetrahedron, (1996) 52, 2817.

[17] Takeuchi, M.; Yoda, S.; Imada, T.; Shinkai, S., Tetrahedron, (1997) 53, 8335.

[18] Kimura, T.; Arimori, S.; Takeuchi, M.; Nagasaki, T.; Shinkai, S., Perkin Trans. 1, (1995), 1889.

[19] Shinkai, S., Nato Adv. Sci. Inst. Ser., C, Math. Phys. Sci., (1997) 492, 37.

[20] Shinmori, H.; Takeuchi, M.; Shinkai, S., Tetrahedron, (1995) 51, 1893.

[21] Shinmori, H.; Takeuchi, M.; Shinkai, S., Perkin Trans. 1, (1996), 1.

[22] Suenaga, H.; Arimori, S.; Shinkai, S., Perkin Trans. 1, (1996), 607.

[23] Suenaga, H.; Nakashima, K.; Hamachi, O.; Shinkai, S., Tetrahedron Lett., (1997) 38, 2479.

[24] Takeuchi, M.; Mizuno, T.; Shinmori, H.; Nakashima, M.; Shinkai, S., Tetrahedron, (1996) 52, 1195.

[25] Suenaga, H.; Mikami, M.; Sandanayake, K. R. A. S.; Shinkai, S., Tetrahedron Lett., (1995) 36, 4825.

[26] James, T. D.; Sandanayake, K. R. A. S.; Shinkai, S., J. Chem. Soc., Chem. Comm., (1994) 122, 477.

[27] James, T. D.; Sandanayake, K. R. A. S.; Shinkai, S., Angew. Chem.Int. Ed., (1994) 33, 2207.

[28] James, T. D.; Sandanayake, K.; Shinkai, S., Nature, (1995) 374, 345.

[29] Scrafton, D. K.; Taylor, J. E.; Mahon, M. F.; Fossey, J. S.; James, T. D., J. Org. Chem., (2008) 73, 2871.

[30] Mulla, K.; Dongare, P.; Thompson, D. W.; Zhao, Y., Manuscript in Preparation, (2013),

[31] Mulla, K.; Dongare, P.; Zhou, N.; Chen, G.; Thompson, D. W.; Zhao, Y., Org. Biomol. Chem., (2011) 9, 1332.

[32] Dowlut, M.; Hall, D. G., J. Am. Chem. Soc., (2006) 128, 4226.

[33] Lakowicz, J. R., Springer, (2006),

[34] Hirakawa, K.; Segawa, H., J. Photochem. Photobiol. A: Chemistry, (1999) 123, 67.

[35] Liu, L. T.; Yaron, D.; Sluch, M. I.; Berg, M. A., J. Phys. Chem. B, (2006) 110, 18844.

[36] Sluch, M. I.; Godt, A.; Bunz, U. H. F.; Berg, M. A., J. Am. Chem. Soc., (2001) 123, 6447.

[37] Karabunarliev, S.; Bittner, E. R.; Baumgarten, M., J. Chem. Phys., (2001) 114, 5863.

[38] de Miguel, G.; Wielopolski, M.; Schuster, D. I.; Fazio, M. A.; Lee, O. P.; Haley, C. K.; Ortiz, A. L.; Echegoyen, L.; Clark, T.; Guldi, D. M., J. Am. Chem. Soc., (2011) 133, 13036.

[39] Kim, T. Y.; Elliott, A. B. S.; Shaffer, K. J.; John McAdam, C.; Gordon, K. C.; Crowley, J. D., Polyhedron, (2013) 52, 1391.

[40] Wang, Z.; Zhang, D. Q.; Zhu, D. B., J. Org. Chem., (2005) 70, 5729.

[41] Binstead, R. A.; Stultz, L. K.; Meyer, T. J., Inorg. Chem., (1995) 34, 546.

[42] Binstead, R. A.; McGuire, M. E.; Dovletoglou, A.; Seok, W. K.; Roecker, L. E.; Meyer, T. J., J. Am. Chem. Soc., (1992) 114, 173.

[43] Gagliardi, C. J.; Binstead, R. A.; Thorp, H. H.; Meyer, T. J., J. Am. Chem. Soc., (2011) 133, 19594.

[44] Lebeau, E. L.; Binstead, R. A.; Meyer, T. J., Abstracts of Papers of the American Chemical Society, (1995) 209, 244.

[45] James, T. D.; Sandanayake, K. R. A. S.; Iguchi, R.; Shinkai, S., J. Am. Chem. Soc., (1995) 117, 8982.

[46] Phillips, M. D.; Fyles, T. M.; Barwell, N. P.; James, T. D., Chem. Commun., (2009), 6557.

[47] Zhang, X.; Chi, L.; Ji, S.; Wu, Y.; Song, P.; Han, K.; Guo, H.; James, T. D.; Zhao, J., J. Am. Chem. Soc., (2009) 131, 17452.

[48] Galbraith, E.; James, T. D., Chem. Soc. Rev., (2010) 39, 3831.

[49] Anderson, C. P.; Salmon, D. J.; Meyer, T. J.; Young, R. C., J. Am. Chem. Soc., (1977) 99, 1980.

[50] Luo, J. D.; Xie, Z. L.; Lam, J. W. Y.; Cheng, L.; Chen, H. Y.; Qiu, C. F.; Kwok, H. S.; Zhan, X. W.; Liu, Y. Q.; Zhu, D. B.; Tang, B. Z., Chem. Commun., (2001),

[51] Swager, T. M.; Gil, C. J.; Wrighton, M. S., J. Phys. Chem., (1995) 99, 4886.

[52] VanVeller, B.; Robinson, D.; Swager, T. M., Angew. Chem.Int. Ed., (2012) 51, 1182.

[53] Bunz, U. H. F., Synthesis and structure of PAEs, In Poly(Arylene Ethynylenes): From Synthesis to Application, Weder, C. Ed. (2005); Vol. 177, pp 1.

[54] Kim, I. B.; Dunkhorst, A.; Bunz, U. H. F., Langmuir, (2005) 21, 7985.

[55] Kim, I. B.; Dunkhorst, A.; Gilbert, J.; Bunz, U. H. F., Macromolecules, (2005) 38, 4560.

[56] Kim, I. B.; Erdogan, B.; Wilson, J. N.; Bunz, U. H. F., Chem. Eur. J., (2004) 10, 6247.

[57] Kim, I. B.; Wilson, J. N.; Bunz, U. H. F., Chem. Commun., (2005), 1273.

[58] Wilson, J. N.; Wang, Y. Q.; Lavigne, J. J.; Bunz, U. H. F., Chem. Commun., (2003), 1626.

[59] Kraft, A.; Grimsdale, A. C.; Holmes, A. B., Angew. Chem. Int. Ed., (1998) 37, 402.

[60] Xu, Y. F.; Berger, P. R.; Wilson, J. N.; Bunz, U. H. F., App. Phys. Lett., (2004) 85, 4219.

[61] Kleiman, V. D.; Melinger, J. S.; McMorrow, D., J. Phys. Chem. B, (2001) 105, 5595.

[62] Fan, L. J.; Jones, W. E., J. Am. Chem. Soc., (2006) 128, 6784.

[63] Fan, L.-J.; Zhang, Y.; Jones, W. E., Macromolecules, (2005) 38, 2844.

[64] Sluch, M. I.; Godt, A.; Bunz, U. H. F.; Berg, M. A., J. Am. Chem. Soc., (2001) 123, 6447.

[65] Pourghaz, Y.; Dongare, P.; Thompson, D. W.; Zhao, Y. M., Chem. Commun., (2011) 47, 11014.

[66] Swager, T. M., Acc. Chem. Res., (1998) 31, 201.

[67] Gross, K. C.; Seybold, P. G., Int. J. Quant. Chem., (2000) 80, 1107.

[68] Martín, N.; Sánchez, L.; Herranz, M. a. Á.; Illescas, B.; Guldi, D. M., Acc. Chem. Res., (2007) 40, 1015.

[69] Ferraris, J.; Cowan, D. O.; Walatka, V.; Perlstein, J. H., J. Am. Chem. Soc., (1973) 95, 948.

[70] Wudl, F.; Wobschall, D.; Hufnagel, E. J., J. Am. Chem. Soc., (1972) 94, 670.

[71] Zhao, Y. M.; Chen, G.; Mulla, K.; Mahmud, I.; Liang, S.; Dongare, P.; Thompson, D. W.; Dawe, L. N.; Bouzan, S., Pure Appl. Chem., (2012) 84, 1005.

[72] Enoki, T.; Miyazaki, A., Chem. Rev., (2004) 104, 5449.

[73] Iyoda, M.; Hasegawa, M.; Miyake, Y., Chem. Rev., (2004) 104, 5085.

[74] Jérome, D., Chem. Rev., (2004) 104, 5565.

[75] Kobayashi, A.; Fujiwara, E.; Kobayashi, H., Chem. Rev., (2004) 104, 5243.

[76] Miyagawa, K.; Kanoda, K.; Kawamoto, A., Chem. Rev., (2004) 104, 5635.

[77] Rovira, C., Chem. Rev., (2004) 104, 5289.

[78] Shibaeva, R. P.; Yagubskii, E. B., Chem. Rev., (2004) 104, 5347.

[79] Chen, G.; Mahmud, I.; Dawe, L. N.; Daniels, L. M.; Zhao, Y., J. Org. Chem., (2011) 76, 2701.

[80] Chen, G.; Zhao, Y. M., Tetrahedron Lett., (2006) 47, 5069.

[81] Shao, M.; Dongare, P.; Dawe, L. N.; Thompson, D. W.; Zhao, Y., Org. Lett., (2010) 12, 3050.

[82] Mulla, K.; Dongare, P.; Thompson, D. W.; Zhao, Y., Org. Biomol. Chem., (2012) 10, 2542.

[83] Martin, N., Chem. Commun., (2013) 49, 7025.

[84] Shao, M.; Dongare, P.; Dawe, L. N.; Thompson, D. W.; Zhao, Y., Org. Lett., (2010) 12, 3050.

[85] Grimm, B.; Santos, J.; Illescas, B. M.; Munoz, A.; Guldi, D. M.; Martin, N., J. Am. Chem. Soc., (2010) 132, 17387.

[86] Day, P.; Kurmoo, M., J. Mater. Chem., (1997) 7, 1291.

[87] Hansen, T. K.; Joergensen, T.; Stein, P. C.; Becher, J., J. Org. Chem., (1992) 57, 6403.

[88] Dieing, R.; Morisson, V.; Moore, A. J.; Goldenberg, L. M.; Bryce, M. R.; Raoul, J.-M.; Petty, M. C.; Garin, J.; Saviron, M.; Lednev, I. K.; Hester, R. E.; Moore, J. N., Perkin Trans. 2, (1996) 0, 1587.

[89] Moore, A. J.; Goldenberg, L. M.; Bryce, M. R.; Petty, M. C.; Moloney, J.; Howard, J. A. K.; Joyce, M. J.; Port, S. N., J. Org. Chem., (2000) 65, 8269.

[90] Trippé, G.; Le Derf, F.; Lyskawa, J.; Mazari, M.; Roncali, J.; Gorgues, A.; Levillain, E.; Sallé, M., Chem. Eur. J., (2004) 10, 6497.

[91] Le Derf, F.; Mazari, M.; Mercier, N.; Levillain, E.; Richomme, P.; Becher, J.; Garín, J.; Orduna, J.; Gorgues, A.; Sallé, M., Inorg. Chem., (1999) 38, 6096.

[92] Vanýsek, P., Electrochemical Series, In Handbook of Chemistry and Physics, Chemical Rubber Company: (2012); Vol. 1.

[93] Bard, A. J.; Parsons, R.; Jordan, J. Eds., Standard Potentials in Aqueous Solutions, Marcel Dekker New York, (1985); Vol. 1.

[94] Pearson, R. G., J. Am. Chem. Soc., (1963) 85, 3533.

[95] Pearson, R. G., J. Chem. Ed., (1968) 45, 581.

[96] Lever, A. B. P., Inorg. Chem., (1990) 29, 1271.

[97] Lever, A. B. P., Inorg. Chem., (1991) 30, 1980.

Chapter - 6

Concerted Electron-Proton Transfer Using Re(I) MLCT Excited-States

In this study, a mechanistic investigation of the reactions between three homologous heteroleptic Re(I) polypyridyl complexes and $(tBu)_2PhOH$ was performed using optical spectroscopy. The study mainly focuses on the excited-state EPT, ET and PT events occurring between them.

6.1. Introduction

Re(I) polypyridyl complexes are one of the most-extensively documented metal complexes and have been continuously attracting the attention of chemists since the discovery of their interesting excited-state properties by Wrighton in the mid 1970s.[1-3] Ever since, they have been recognized as excellent chromophoric scaffolds for the study of electron transfer (ET), proton transfer (PT), energy transfer (E_NT) as well as concerted-EPT (electron-proton transfer) or proton-coupled electron transfer (PCET) reactions.[4, 5] fac-$[(CO)_3Re(bpy)(L)]^+$ (bpy is 2,2'-bipyridine and L = 4,4'-bipyridine, 4-ethylpyridine and 4-phenylpyridine type of ligand, Figure 6.1) complexes possess stereochemistry which makes them attractive molecular assemblies to study inter- and intra-molecular charge-transfer reactions.[6-8]

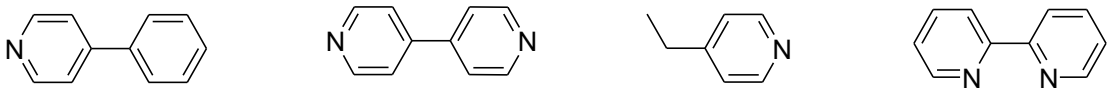

Figure 6.1. The structures of the pyridyl ligands mentioned in the main text.

The synthetic chemistry of Re polypyridyl complexes is well-developed, allowing the tuning of the excited-state properties through systematic synthetic modifications.[9, 10] This family of complexes has been used to establish the Energy Gap Law,[11, 12] and photoinduced electron-[13] and energy-transfer in the inverted region[14, 15] by employing several spectroscopic methods to probe the excited-state dynamics.[16, 17]

6.1.1. Terminology of Proton Coupled Electron Transfer (PCET)

The term PCET was first coined by T. J. Meyer in the 1980s, for the reactions in which proton (H^+)-transfer accompanies electron (e^-)-transfer.[18] PCET is a general term given to a broad set of electron-proton transfer reactions. Meyer has proposed a specific vocabulary to delineate the difference between various PCET reactions.[19, 20] A PCET reaction can occur through following distinct pathways:

(i) Stepwise electron transfer followed by proton transfer (ET-PT)

(ii) Stepwise proton transfer followed by electron transfer (PT-ET)

(iii) Concerted electron-proton transfer (CPET).

To describe some key points in understanding the PCET process, the photosystem II (PSII) of green plants can be used. In this process the oxidation of tyrosine (Tyr161) Histidine (His190) pair (Y_z) by the reaction center, photo-oxidized P_{680}^+ occurs. Figure 6.2

illustrates the events of this process where the initial proton transfer produces the anionic species before being oxidized and in the case of initial ET the tyrosine radical cation is formed before losing its proton to produce tyrosine radical. Each of these initial stepwise products are high-energy intermediates that can become damaging inside PSII. Therefore, a third mechanistic pathway, electron-proton transfer (EPT) becomes relevant. In this mechanism, the movement of protons and electrons is in concert, thus avoiding high energy anionic and cationic intermediates. However, EPT is mechanistically more complex than the stepwise ET/PT mechanisms because of the simultaneous transfer of two particles: the proton and electron.

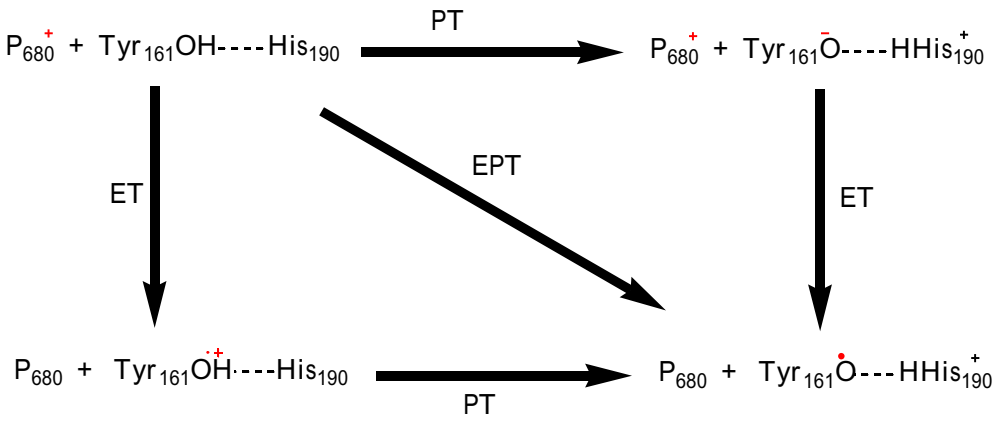

Figure 6.2. A simplified description of ET-PT, PT-ET and EPT events in the oxidation of the Y_z pair in PSII.[20]

CPET is further classified into the following categories based on donor (D) and acceptor (A) orbitals: (a) EPT: In this mechanism, the reaction occurs between different donors and acceptors for the proton and electron. (b) Hydrogen atom transfer (HAT): In

this mechanism both the electron and proton are transferred to the same orbital. Figure 6.3 illustrates the difference between HAT and EPT processes. (c) Multisite-EPT (MS-EPT): An electron-proton donor transfers electrons and protons to spatially-separated acceptors, or an electron-proton acceptor accepts electrons from spatially-separated donors.[20]

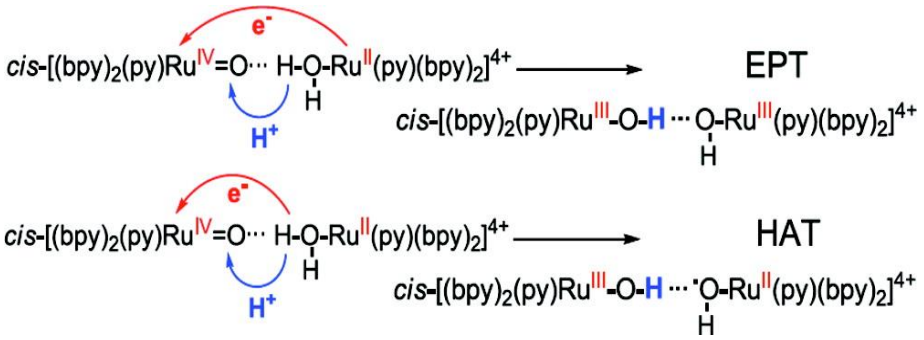

Figure 6.3. An example illustrating the difference between HAT and EPT reactions.[20] Reprinted with permission from Weinberg, D. R.; Gagliardi, C. J.; Hull, J. F.; Murphy, C. F.; Kent, C. A.; Westlake, B. C.; Paul, A.; Ess, D. H.; McCafferty, D. G.; Meyer, T. J. Chem. Rev. 2012, 112, 4016.

.

6.1.2. Photoinduced Electron Transfer in Re(I) Polypyridyl Complexes

As discussed in Section 6.1, Re(I) polypyridyl complexes have been extensively employed to study PET processes. The first case discussed in this section presents an interesting case where charge separation is demonstrated in two organic moieties covalently attached to the Re metal center. The complex fac-$[(CO)_3Re(DEAS\text{-}bpy)(L)]^+$ (L = 1,10-bis(4-pyridyl)-3,8-dimethyl-1,3,5,7,9-decapentaene and DEAS-bpy = 4,4'-

bis[p-(diethyl-amino)-α-styryl]-2,2'-bipyridine, Figure 6.4) was found to show long-lived charge separation in the mononuclear complex at room temperature.[21, 22]

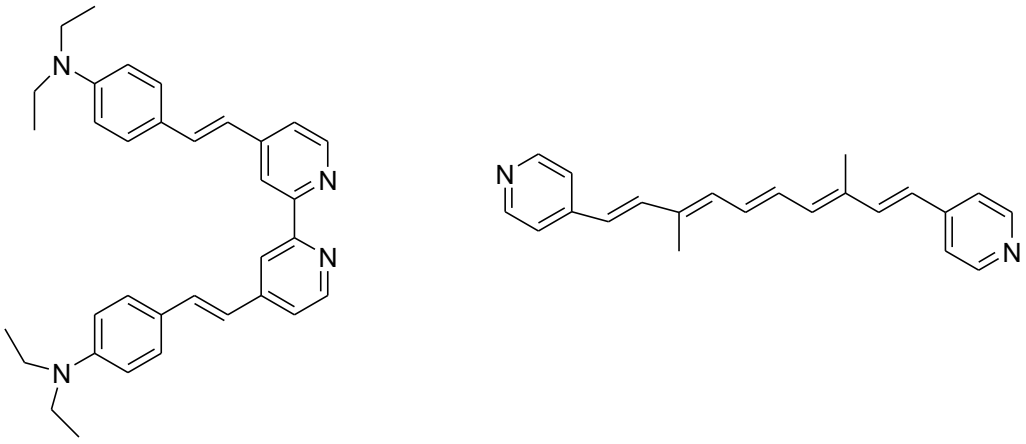

DEAS-bpy **L**

Figure 6.4. 1,10-bis(4-pyridyl)-3,8-dimethyl-1,3,5,7,9-decapentaene (L) and 4,4'-bis[p-(diethyl-amino)-α-styryl]-2,2'-bipyridine (DEAS-bpy) ligands.

Initially a weak, ligand-centered luminescence was reported for the fac-$[(CO)_3Re(DEAS\text{-}bpy)(Cl)]^+$ complex at room temperature.[23] However, when chloride was replaced by the BPP ligand the luminescence at room temperature of the complex was quenched. Detailed ground-and excited-state spectral investigations revealed the formation of a charge-separated fac-$[(CO)_3Re(DEAS\text{-}bpy^{+\cdot})(L^{-\cdot})]^+$ species decaying with the lifetime of 4.3 μs (k_{CR} = 2.3 × 10^5 s^{-1}). Based on the available data, the reaction was predicted to occur in the Marcus inverted region and hence a slow rate of back-electron transfer was observed.

In another interesting case, Vlĉek delineated the mechanism of electron transfer in the fac-$[(CO)_3Re(4,4'\text{-}(X)_2\text{-}bpy)(MQ)^+]^{2+}$ (X = CH_3, bpy = 2,2'-bipyridine and MQ^+ = N-Methyl-4,4'-bipyridinium ligand) complex.[24] Photoexcitation of fac-$[(CO)_3Re(4,4'\text{-}(X)_2\text{-}bpy)(MQ)^+]^{2+}$ populates the Re → 4,4'-$(X)_2$-bpy ^{3}MLCT excited-state to yield fac-$[(CO)_3Re^{II}(4,4'\text{-}(X)_2\text{-}bpy^{-\cdot})(MQ)^+]^{2+}$ which then undergoes an ultrafast interligand electron transfer (ILET) 4,4'-$(X)_2$-$bpy^{-\cdot}$ → MQ^+ with a lifetime of 8 ps in CH_3CN and 14 ps in glycerol (Figure 6.5).[24, 25]

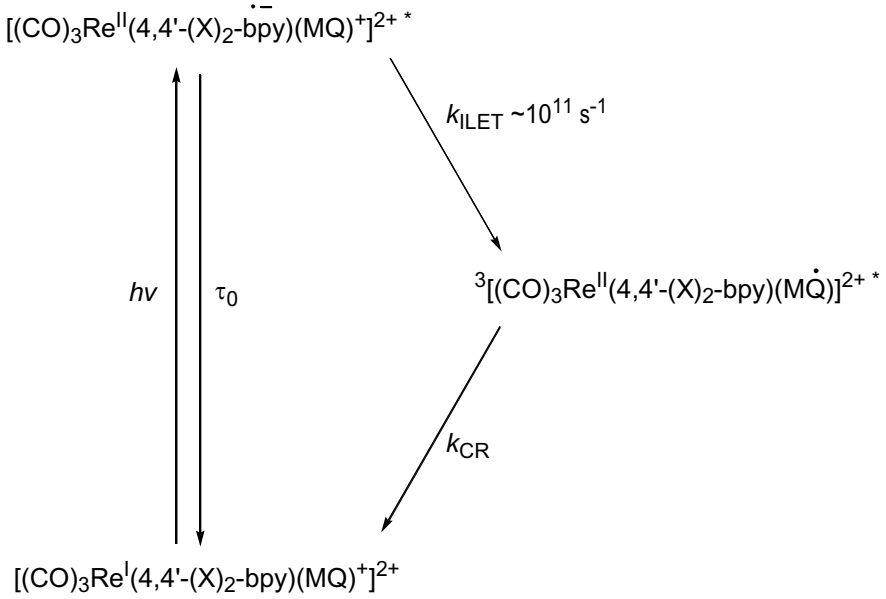

Figure 6.5. Photoinduced Interligand electron transfer (ILET) (4,4'-$(X)_2$-$bpy^{-\cdot}$ → MQ^+) in fac-$[(CO)_3Re(4,4'\text{-}(X)_2\text{-}bpy)(MQ)^+]^{2+}$, k_{ILET} = rate of interligand electron transfer and k_{CR} = rate of charge recombination.[24]

A solvent-dependent study has also been reported by Vlĉek et al. in fac-$[(CO)_3Re(4,4'\text{-}(X)_2\text{-}bpy)(MQ)^+]^{2+}$ complex. In this study, the back electron-transfer (k_{CR}) ($MQ^{\cdot}$ → Re^{II}) was found to be dependent upon the molecular nature of the solvent. The

observations were ascribed to the interactions between solvent and the positively-charged MQ^+ where the polar solvents may align themselves to accommodate the positive charge of MQ^+.[26] Furthermore, the positive charge of the MQ^+ may induce dipoles in solvents that are polarisable.

It was reported that the ILET in fac-$[(CO)_3Re(4,4'\text{-}(X)_2\text{-bpy})(4,4'\text{-bpy})]^+$ (X = H, CH_3, NH_2, CO_2Et) complexes are thermodynamically uphill.[9, 27, 28] However, the presence of an axial ligand of the MQ^+ type $(4,4'\text{- bpyH}^+)$ has been reported to provide the driving force for ILET.[28] Furthermore, the driving force for ILET was changed when the substituents at the $4,4'$ position of $2,2'$- bpy were varied.[29] The ILET driving force of $-\Delta G^0$ = 1.0 eV for X = NH_2; 0.49 eV for X = H; ~0.1 eV for X = CO_2Et_2 and 0.45 eV for X = CH_3 was calculated and reported by Meyer et al.[28] It was concluded that if substituent X is an electron-donating group, the driving force for ILET is higher and vice-versa. Equation 6.1 shows the ILET in a fac-$[(CO)_3Re(4,4'\text{-}(X)_2\text{-bpy})(MQ)^+]^{2+}$ complex.

$$[(CO)_3Re^{I}(4,4'\text{-}(X)_2\text{-bpy})(MQ)^+]^{2+} \xrightarrow{hv} {}^3[(CO)_3Re^{II}(4,4'\text{-}(X)_2^{\bullet -}\text{-bpy})(MQ)^+]^{2+*}$$

$$\xrightarrow{ILET} {}^3[(CO)_3Re^{II}(4,4'\text{-}(X)_2\text{-bpy})(M\dot{Q})]^{2+*}$$

[6.1]

A study involving Re(I) polypyridyl complexes with a reductive quencher ligand has been reported by Chen et al.[13, 30] Excitation of fac-$[(CO)_3Re(bpy)(py\text{-}PTZ)]^+$ (py-PTZ = 10-(4-picolyl)phenothiazine, Figure 6.6 and bpy = $2,2'$-bipyridine) leads to the

formation of the fac-$^3[(CO)_3Re^{II}(bpy^{-\cdot})(py\text{-}PTZ)]^{+*}$ excited-state followed by a rapid electron-transfer quenching from py-PTZ $\rightarrow Re^{II}$ ($k_q = 4.8 \times 10^9$ s^{-1}) forming the fac-$^3[(CO)_3Re^{I}(bpy^{-\cdot})(py\text{-}PTZ^{+\cdot})]^{+*}$ charge-separated state. This is viewed as a ligand-to-ligand charge transfer (py-PTZ $\rightarrow Re^{II}$) excited-state which decays to the ground-state by intramolecular charge transfer ($bpy^{-\cdot} \rightarrow py\text{-}PTZ^{+\cdot}$) with a rate of 4.0×10^6 s^{-1} in CH_3CN at room temperature. Figure 6.6 illustrates the process.

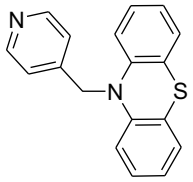

py-PTZ

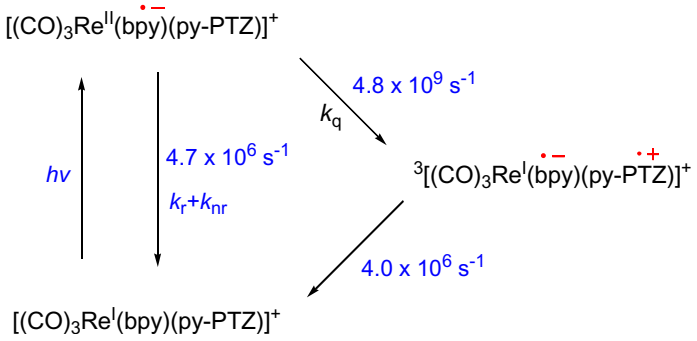

Figure 6.6. Structure of py-PTZ (top) and the mechanism of intramolecular electron transfer in fac-$[(CO)_3Re(bpy)(py\text{-}PTZ)]^+$ (bottom).[13, 30]

6.1.3. EPT Reactions Involving Phenols

EPT reactions are ubiquitous in nature and are found in many enzymatic and photosynthesis reactions.[19, 31, 32] A number of EPT reactions (especially involving phenols) have been examined in considerable detail.[33-37] Several systems have been reported which involve EPT and ET-PT or PT-ET pathways.[19, 20] An account of EPT reaction mechanisms and its theory has been outlined in Chapter 1.

Phenols and their derivatives are continuously under intense study in the context of EPT mechanistic pathways.[33, 36-40] A MS-EPT process has been demonstrated by using phenols and C_{60}, where phenols were utilized as good redox agents to carry out EPT by avoiding high energy intermediates.[41] Equations 6.2 - 6.5 show a MS-EPT process where $^3C_{60}$ acts as an electron acceptor, B is a base (proton acceptor) and phenol (PhOH) works as an electron donor as well as a proton donor.

$$C_{60} \xrightarrow{h\nu} {}^1C_{60}{}^* \qquad [6.2]$$

$${}^1C_{60} \xrightarrow{k_{isc}} {}^3C_{60}{}^* \qquad [6.3]$$

$${}^3C_{60} + PhOH - B \rightarrow C_{60}^{-\cdot} + PhO^{\cdot} + BH^+ \qquad [6.4]$$

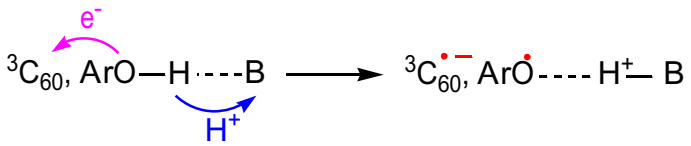

[6.5]

Recently Stewart et al. published EPT studies where hydroquinone (H_2Q) was used to reductively quench the fac-$[(CO)_3Re(bpy)(4,4'\text{-bpy})]^+$ excited-state along with a concomitant PT from H_2Q to the pyridinic nitrogen (Scheme 6.1).[42] Competing ET-PT and EPT pathways were proposed based on the time-resolved spectroscopic data.

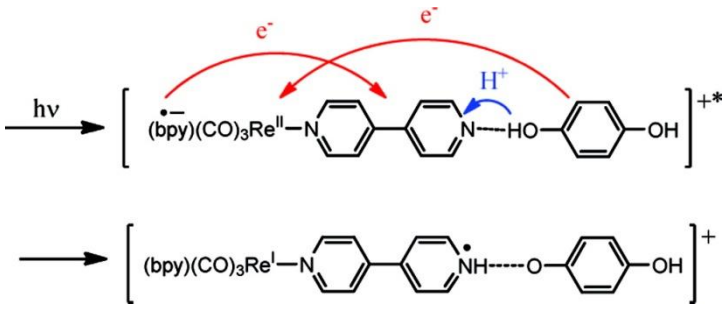

Scheme 6.1. EPT reactions in fac-$[(CO)_3Re(bpy)(4,4'\text{-bpy})]^+$ and H_2Q reported by Stewart et al.[42] Reprinted with permission from Stewart, D. J.; Brennaman, M. K.; Bettis, S. E.; Wang, L.; Binstead, R. A.; Papanikolas, J. M.; Meyer, T. J. J. Phys. Chem. Lett. 2011, 2, 1844.

Substituted phenols with sterically bulky groups have been reported to reductively quench the excited-state of $^3[Ru(bpy)_3]^{2+*}$ and $Ru(H_2dcbpy)_3$ (H_2dcbpy = 4,4'-dicarboxy-2,2'-bipyridine) complexes via a PCET reaction.[43] Similarly, Mayer has demonstrated a distance dependence in PCET reactions using 2,4,6-tri-tert-butylphenol and Ru terpyridine-4'-carboxylate complex (Figure 6.7).[44]

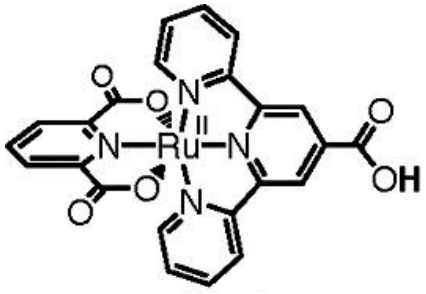

Figure 6.7. Ru terpyridine-4'-carboxylate complex.[44]

However, the mechanistic aspects of EPT involving sterically bulky phenolic compounds have not been studied as much as for the other phenols.

6.2. Objectives and Methodology

In this work 2,6-di-tert-butylphenol $(tBu)_2PhOH$ from herein, (Figure 6.8) was utilized to quench the metal-to-ligand-charge-transfer (MLCT) excited-states of fac-$[(CO)_3Re(4,4'\text{-}(X)_2\text{-}bpy)(4,4'\text{-}bpy)]^+$ (X = H, CH_3, NH_2, Figure 6.8) complexes. The effect of change in the ILET driving force on the overall photochemical reaction between fac-$[(CO)_3Re(4,4'\text{-}(X)_2\text{-}bpy)(4,4'\text{-}bpy)]^+$ and $(tBu)_2PhOH$ will also be analyzed. The use of $(tBu)_2PhOH$ provides an opportunity to study the EPT reactions involving a sterically bulky phenol. In addition, $(tBu)_2PhOH$ also exhibits spectral markers that can be easily identified in the absorption and emission spectral data.[45]

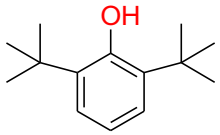

$(tBu)_2PhOH$

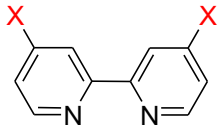

$4,4'\text{-}(X)_2\text{-bpy}$ $X = NH_2, H, CH_3$

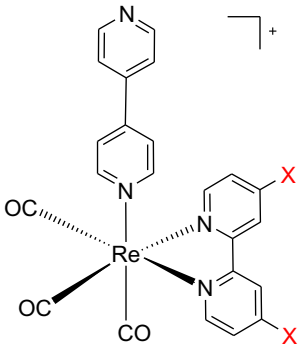

$X = NH_2, H, CH_3$

fac-$[(CO)_3Re(4,4'\text{-}(X)_2\text{-bpy})(4,4'\text{-bpy})]^+$

Figure 6.8. Structural formulae and abbreviations used in the descriptions.

6.3. Results

6.3.1 Ground-State Properties

6.3.1.1 Absorption

The absorption spectra of fac-[$(CO)_3$Re(4,4'-$(X)_2$-bpy)(4,4'-bpy)]$^+$ are shown in Figure 6.9. All the Re(I) polypyridyl complexes undergo $Re(d\pi)^6 \rightarrow \pi^*$(4,4'-$(X)_2$-bpy) transition between 330 to 430 nm.[10]

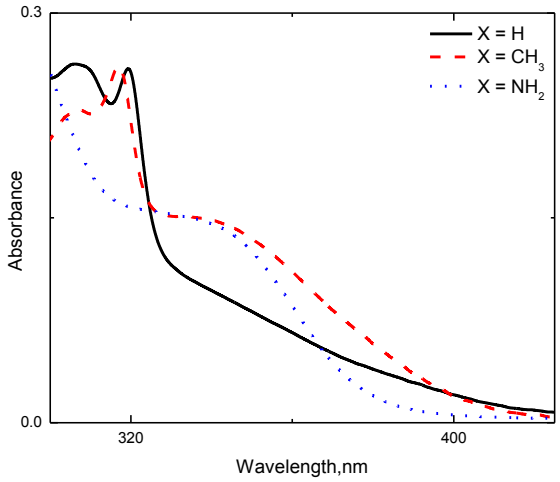

Figure 6.9. Electronic spectra of fac-[$(CO)_3$Re(4,4'-$(X)_2$-bpy)(4,4'-bpy)]$^+$. Acquired in CH_3CN (1 atm N_2) at 298 ±3 K. [X = H] = 65 µM, [X = CH_3] = 29 µM and [X = NH_2] = 46 µM.

The position of the MLCT absorption band depends on the type of substituents on the bpy.[46] The electron-donating substituents increase the energy of the π^*(bpy) acceptor orbitals to a greater degree than they do for Re(dπ) orbitals.[10] The absorption spectra of Re(I) complexes are known to be complicated due to the overlap of $Re(d\pi)^6 \rightarrow \pi^*$(4,4'-

$(X)_2$-bpy), $Re(d\pi)^6 \rightarrow \pi^*$(4,4'-bipyridine) and intraligand 4,4'-$(X)_2$-bpy based $\pi \rightarrow \pi^*$ transitions.[29] Furthermore, by systematically changing substituents (X) by synthetic tuning of a metal complex, one can expect a change in the energy of HOMO-LUMO i.e. [ΔE (HOMO-LUMO)] of the (4,4'-$(X)_2$-bpy).[9]

Addition of $(tBu)_2$PhOH brings negligible change in the electronic spectra of fac-$[(CO)_3Re(4,4'\text{-}(X)_2\text{-}bpy)(4,4'\text{-}bpy)]^+$ complexes. The absorption spectra of fac-$[(CO)_3Re(4,4'\text{-}(X)_2\text{-}bpy)(4,4'\text{-}bpy)]^+$ acquired as a function of increasing $(tBu)_2$PhOH in CH_3CN at 298 K are shown in Figure 6.10.

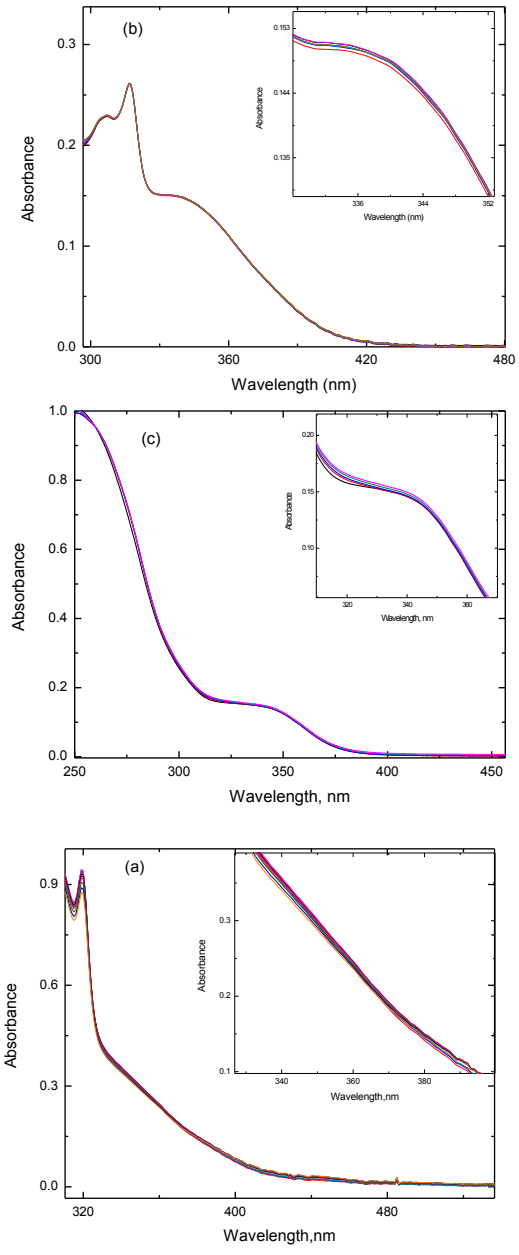

Figure 6.10. The electronic spectra of fac-$[(CO)_3Re(4,4'\text{-}(X)_2\text{-}bpy)(4,4'\text{-}bpy)]^+$ obtained as a function of increasing $(tBu)_2PhOH$. (a) X = H at concentrations of 0.0, 0.079, 0.15, 0.31, 1.26, 1.88, 2.50, 4.87, 9.26 and 17.0 mM. (b) X = CH_3 at concentrations of 0.0, 1.50, 3.70, 3.60, 5.30 and 8.60 mM. (c) X = NH_2 at concentrations of 0.0, 4.0, 11.0 and 23.0 and 42.0 mM of $(tBu)_2PhOH$, acquired in CH_3CN at 298 ±3 K. [X = H] = 65 μM, [X = CH_3] = 29 μM and [X = NH_2] = 46 μM. The changes occurring in the MLCT band are shown in the insets.

A slight increase in the absorption intensity of both $(4,4'\text{-}(X)_2\text{-bpy})\pi \rightarrow (4,4'\text{-}(X)_2\text{-bpy})\pi^*$ (290 – 330 nm) and MLCT bands (~345 nm) was observed with each addition of $(tBu)_2PhOH$. Similar spectral changes are documented previously by Stewart et al. for fac-$[(CO)_3Re(bpy)(4,4'\text{-bpy})]^+$ and 1,4-dihydroquinone (H_2Q) and are ascribed to a preassociation, but the changes were too small to measure an equilibrium constant.[47]

6.3.2. Excited-State Properties

6.3.2.1. Luminescence

Luminescence spectra of fac-$[(CO)_3Re(4,4'\text{-}(X)_2\text{-bpy})(4,4'\text{-bpy})]^+$ acquired in CH_3CN by exciting at 370 nm are shown in Figure 6.11 and are consistent with previously reported spectra for fac-$[(CO)_3Re(4,4'\text{-}(X)_2\text{-bpy})(L)]^+$ (L = 4,4'-bipyridine, 4-ethylpyridine and 4-phenylpyridine) complexes.[10, 48]

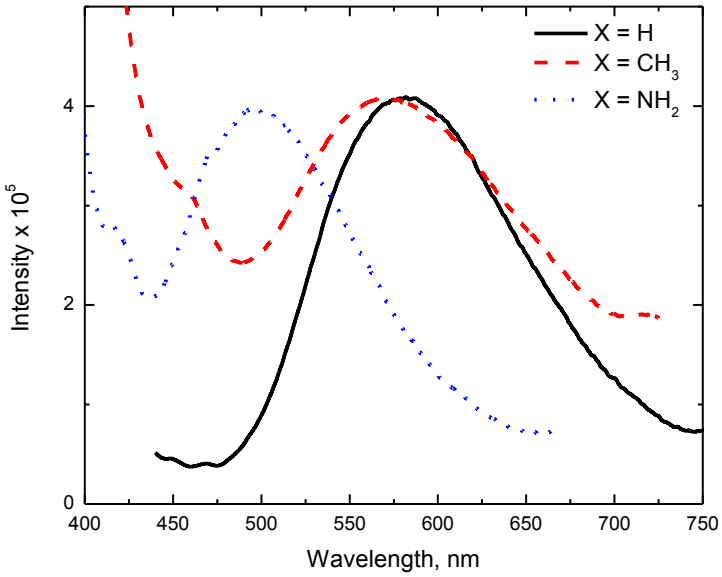

Figure 6.11. Normalized emission spectra of fac-$[(CO)_3Re(4,4'\text{-}(X)_2\text{-}bpy)(4,4'\text{-}bpy)]^+$ acquired in CH_3CN (1 atm N_2) at 298 ±3 K, λ_{exc} = 370 nm. [X = H] = 65 μM, [X = CH_3] = 29 μM and [X = NH_2] = 46 μM.

Figure 6.11 shows that the lowest-lying excited-state is emissive in all three metal complexes with broad and featureless bands assigned previously to a ^{3}MLCT → G.S. transition.[9] The complexes emit with different quantum yields (Φ_{em}), with X = H being the most emissive (Φ_{em} = 0.11) followed by X = CH_3 (Φ_{em} = 0.042) and X = NH_2 (Φ_{em} = 0.021). Table 6.1 lists the ground and excited-state properties of these complexes.

Table 6.1. Ground and excited-state photophysical properties of fac-[$(CO)_3$Re(4,4'-$(X)_2$-bpy)(4,4'-bpy)]$^+$.

Entry	X = H	X = NH_2	X = CH_3
λ_{MLCT}^{abs}, nm[a]	350	343	340
$\varepsilon \times 10^3\ M^{-1}cm^{-1}$	4.3	3.0	5.0
E_{op}, cm^{-1}	28500	29100	29400
λ_{em}, nm	580	500	560
E_{em}, cm^{-1}	17200	20000	17800
E_{SS}, cm^{-1}[b]	11300	9100	11600
ϕ_{em}	0.11	0.021	0.042
τ , ns	251	562	344
$k_r \times 10^5$, s^{-1}	4.3	0.37	1.2
$k_{nr} \times 10^6$, s^{-1}	4.3	1.7	2.7

[a]The MLCT absorption manifold is very broad in these metal complexes, ranging from 300 to 450 nm. [b]Stokes shift. Data was acquired in N_2 saturated CH_3CN at 298 ± 3 K.

The emission energy was highest for X = NH_2 and least for X = H. The excited-state luminescence lifetimes (τ) were acquired in CH_3CN (1 atm N_2) at 298 ±3 K. The τ values are primarily dictated by non-radiative decay because $k_{nr} > k_r$. A cursory glance at Table 6.1 suggests that the lifetimes decrease as the energy gap between the excited and ground-state decrease; this observation being consistent with previous literature reports.[49]

The presence of substituents on the bpy can significantly influence the energy of the MLCT excited-state as well as the ground-state.[9, 10, 13, 50] As presented earlier in

Section 6.3.1.1, the electron-donating substituents (X = NH_2, NEt_2) on the bpy increase the energy of the π^* acceptor orbitals to a greater extent than they do for the Re($d\pi$) orbitals. In contrast, the presence of electron-withdrawing substituents (X = CO_2H, CO_2Et) stabilizes the π^* acceptor level of the bpy resulting in a red shift in the absorption and luminescence spectra.[9]

6.3.2.2. Effect of $(tBu)_2PhOH$ Addition on the Excited-State Properties of fac-$[(CO)_3$**Re(4,4'-$(X)_2$-bpy)(4,4'**-bpy)$]^+$

The emission spectra of fac-$[(CO)_3$Re(4,4'-$(X)_2$-bpy)(4,4'-bpy)$]^+$ complexes obtained as a function of $[(tBu)_2PhOH]$ are shown in Figure 6.12.

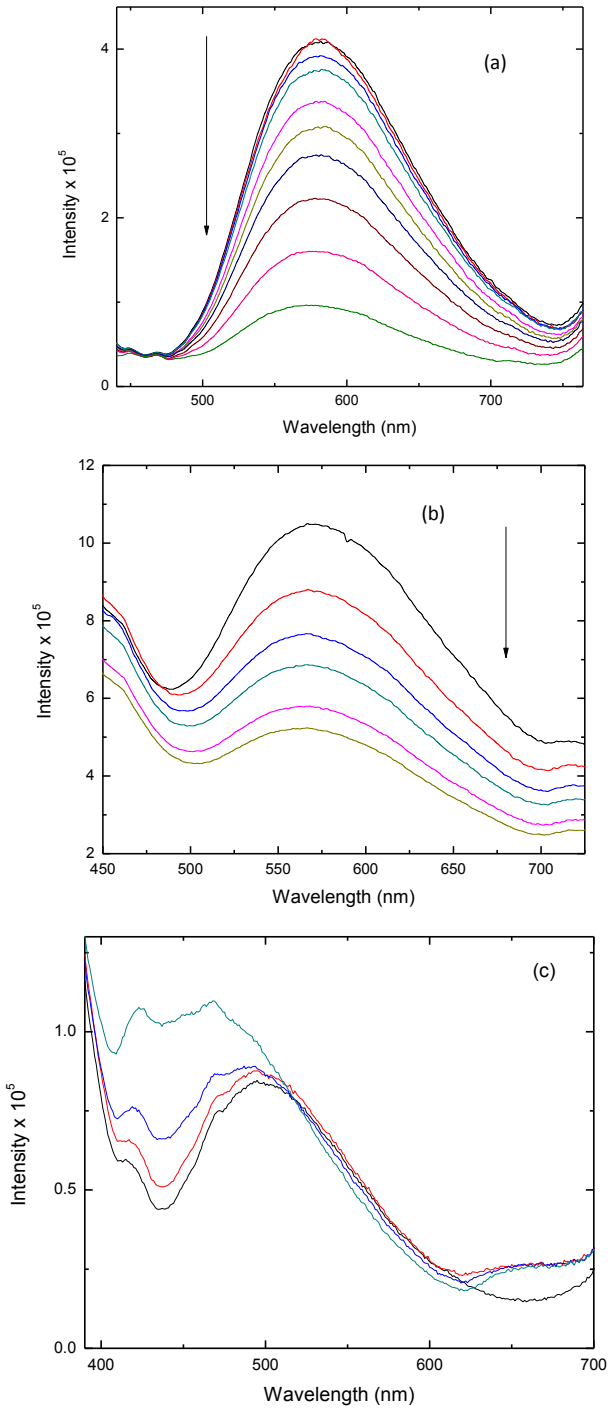

Figure 6.12. Emission spectra of fac-$[(CO)_3Re(4,4'\text{-}(X)_2\text{-}bpy)(4,4'\text{-}bpy)]^+$ obtained as a function of increasing $[(tBu)_2PhOH]$. (a) X = CH_3 at concentrations of 0.0, 1.50, 3.70, 3.60, 5.30 and 8.60 mM. (b) X = H at concentration of 0.0, 0.079, 0.15, 0.31, 1.26, 1.88, 2.50, 4.87, 9.26 and 17.0 mM. (c) X = NH_2 at concentration of 0.0, 4.0, 11.0 and 23.0 mM of $(tBu)_2PhOH$, acquired in CH_3CN at 298 ±3 K. [X = H] = 65 μM, [X = CH_3] = 29 μM and [X = NH_2] = 46 μM. The weak band at 725 nm in the case of X = CH_3 is an instrumental artifact.

Addition of $(tBu)_2PhOH$ significantly attenuates the emission intensity of fac-$[(CO)_3Re(4,4'\text{-}(X)_2\text{-}bpy)(4,4'\text{-}bpy)]^{+*}$ (X = H, CH_3) complexes. The complex with X = NH_2 exhibits new transitions centered at 425 nm and 660 nm with the disappearance of the broad ^{3}MLCT band at 500 nm. This observation is consistent with previous reports where no, or very weak, MLCT-based emission is observed for the fac-$[(CO)_3Re(4,4'\text{-}(NH_2)_2\text{-}bpy)(MQ)^+]^{2+}$ complex at room temperature.[27, 28] At this time a careful interpretation of these new transitions can be described as follows: The new transition at 660 nm is presumably due to the emission from the higher-lying protonated fac-$[(CO)_3Re(4,4'\text{-}(NH_2)_2\text{-}bpy)(4,4'\text{-}bpyH)^+]^{2+*}$ species.[27] Similarly, the high energy structured band at 425 nm that appears after addition of $(tBu)_2PhOH$ can be tentatively assigned to a phenoxyl radical based on the emission spectrum of 2,4,6-tri-tert-butylphenoxyl radical reported by Okamura et al.[51] The reason why the transitions at 660 and 425 nm are not observed in the case of fac-$[(CO)_3Re(4,4'\text{-}(X)_2\text{-}bpy)(4,4'\text{-}bpy)]^{+*}$ (X = H, CH_3) is due to the fact that $(4,4'\text{-}(NH_2)_2\text{-}bpy)$ has a very substantial ILET driving force (ΔG^0 = -1.0 eV) which presumably attenuates the rate constant for the charge recombination. In contrast, the driving force of ILET for fac-$[(CO)_3Re(4,4'\text{-}(X)_2\text{-}bpy)(4,4'\text{-}bpy)]^{+*}$ (X = H, CH_3) are ΔG^0 = -0.49 eV (X = H) and (ΔG^0 = -0.45 eV) (X= CH_3) which allows comparatively faster back electron transfer and this may be a reason why new transitions are not observed in the case where substitutents H and CH_3 are present. Furthermore, the interpretation of the dramatic changes in the emission spectra of fac-$[(CO)_3Re(4,4'\text{-}(NH_2)_2\text{-}bpy)(4,4'\text{-}bpy)]^+$ upon addition of $(tBu)_2PhOH$ as compared to X = H, CH_3 gets further complicated, probably due to the protonation of the available multiple protonable sites.[9]

The emission lifetimes of pure fac-$[(CO)_3Re(4,4'\text{-}(X)_2\text{-}bpy)(4,4'\text{-}bpy)]^+$ acquired in N_2-saturated 1:1 CH_3CN/H_2O (λ_{exc} = 337 nm) are listed in Table 6.1. In general, the addition of $(tBu)_2PhOH$ to fac-$[(CO)_3Re(4,4'\text{-}(X)_2\text{-}bpy)(4,4'\text{-}bpy)]^+$ shortens the luminescence lifetimes significantly. Notably, a decrease from 251 to 116 ns for X = H, 344 to 171 ns for X = CH_3 and 562 to 332 ns for X = NH_2 was observed. Furthermore, all (unless otherwise noted) luminescence decay traces gave satisfactory fit to a single exponential kinetic function. Representative luminescence decay traces for fac-$[(CO)_3Re(4,4'\text{-}(CH_3)_2\text{-}bpy)(4,4'\text{-}bpy)]^+$ with varying $[(tBu)_2PhOH]$ are shown in Figure 6.13.

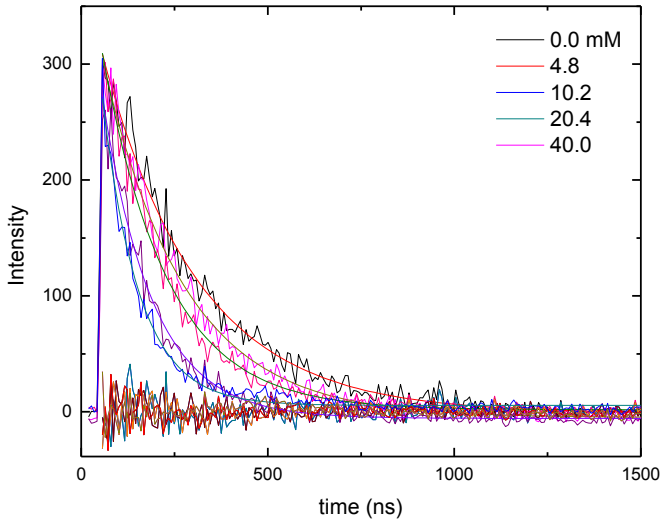

Figure 6.13. Luminescence decay traces for fac-$[(CO)_3Re(4,4'\text{-}(CH_3)_2\text{-}bpy)(4,4'\text{-}bpy)]^+$ with varying $[(tBu)_2PhOH]$ (indicated in the Figure). λ_{exc} = 337 nm in N_2 saturated 1:1 v/v CH_3CN/H_2O solution at 298 ± 3 K. The red curves are the single exponential fits of the decay traces, and noise in the bottom curves are due to the residuals.

6.3.2.3. Transient Absorbance

Transient absorption (TA) difference spectra of fac-[$(CO)_3$Re(4,4'-$(X)_2$-bpy)(4,4'-bpy)]$^+$ at t = 0 and a representative decay trace are shown in Figure 6.14. Transient spectra were recorded by exciting a deoxygenated CH_3CN/H_2O (1:1 v/v) solution of fac-[$(CO)_3$Re(4,4'-$(X)_2$-bpy)(4,4'-bpy)]$^+$ at 355 nm.

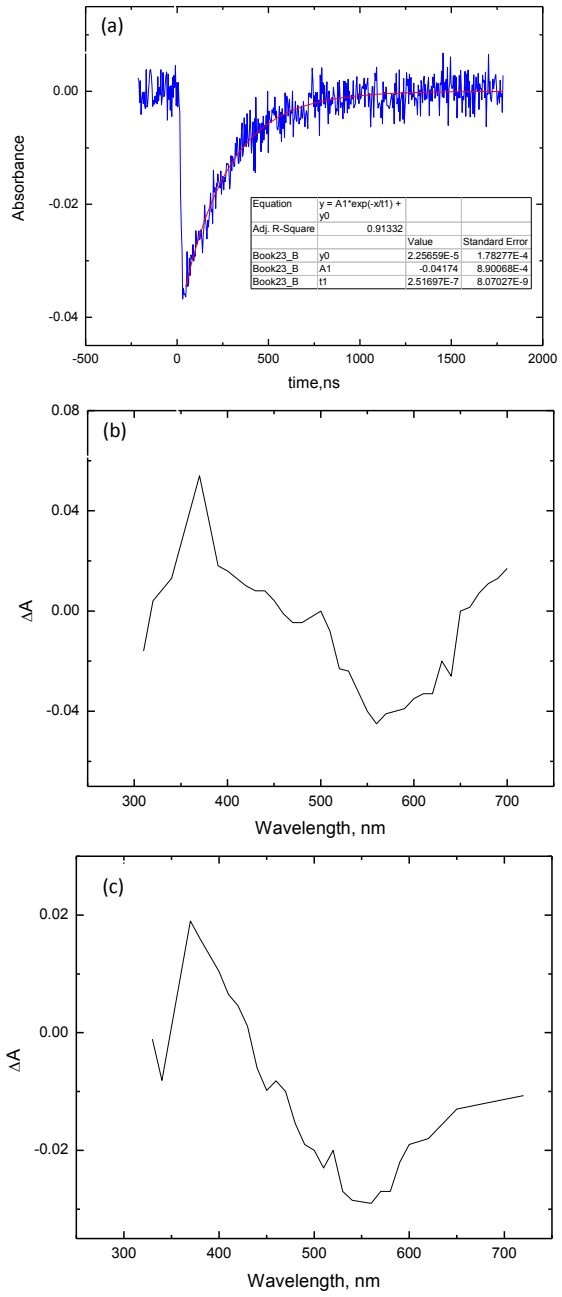

Figure 6.14. (a) A representative decay trace and corresponding fit obtained for complex with X = H at 550 nm; (b) transient absorption spectra following excitation of fac-$[(CO)_3Re(4,4'\text{-}(X)_2\text{-}bpy)(4,4'\text{-}bpy)]^+$, X = H; (c) X = CH_3 constracted by following the trace at t = 0 (constructed by recording the absorbance of individual decay traces at t = 0). The data was acquired in a N_2-saturated 1:1 v/v CH_3CN/H_2O solution of polypyridyl complex by exciting at 355 nm at 298 ± 3 K. [X = H] = 15 μM and [X = CH_3] = 20 μM.

The TA spectrum of fac-$[(CO)_3Re(4,4'\text{-}(X)_2\text{-}bpy)(4,4'\text{-}bpy)]^+$ (X = H, CH_3) complexes exhibit TA that is typical of ^{3}MLCT-excited Re(I) tricarbonyl complexes, as explained below.[9, 28] A ground-state bleach at 300 nm with prompt positive absorption in the 350-450 nm range arising from a $\pi \rightarrow \pi^*$ transition in the MLCT-reduced $4,4'\text{-}(X)_2\text{-}bpy^{-\cdot}$ radical (Equation 6.6).[9, 26] The second feature is a broad ^{3}MLCT emission in the range of 450-700 nm from the lowest lying excited-state ($4,4'\text{-}(X)_2\text{-}bpy$) of the complex as evident from the emission spectra (Figure 6.12).[13, 42, 52]

$$[(CO)_3Re^{I}(4,4'\text{-}X_2\text{-}bpy)(4,4'\text{-}bpy)]^+ \xrightarrow{hv} [(CO)_3Re^{II}(4,4'\text{-}X_2\text{-}\dot{b}\bar{p}y)(4,4'\text{-}bpy)]^{+*} \quad [6.6]$$

The rates of excited-state decay were found to be within experimental error of the rates observed from the luminescence lifetime measurements with ($k = 1/\tau$) k = 3.9 (±0.8) $\times 10^6$ s^{-1} for X = H (at 550 nm and τ = 251 ns) and k = 2.9 (±1.1)$\times 10^6$ s^{-1} for X = CH_3 (at 550 nm and τ = 340 ns).

TA spectra of fac-$[(CO)_3Re(4,4'\text{-}(X)_2\text{-}bpy)(4,4'\text{-}bpy)]^+$ (X = H, CH_3) with $(tBu)_2PhOH$ were also acquired by adding 10.0 mM CH_3CN solution of $(tBu)_2PhOH$ directly into a CH_3CN/H_2O (1:1 v/v) solution of each Re polypyridyl complex separately. For illustration, the single exponential fits of individual decay traces were loaded into Reactlab software program and the 3D plots were obtained (Figure 6.15).

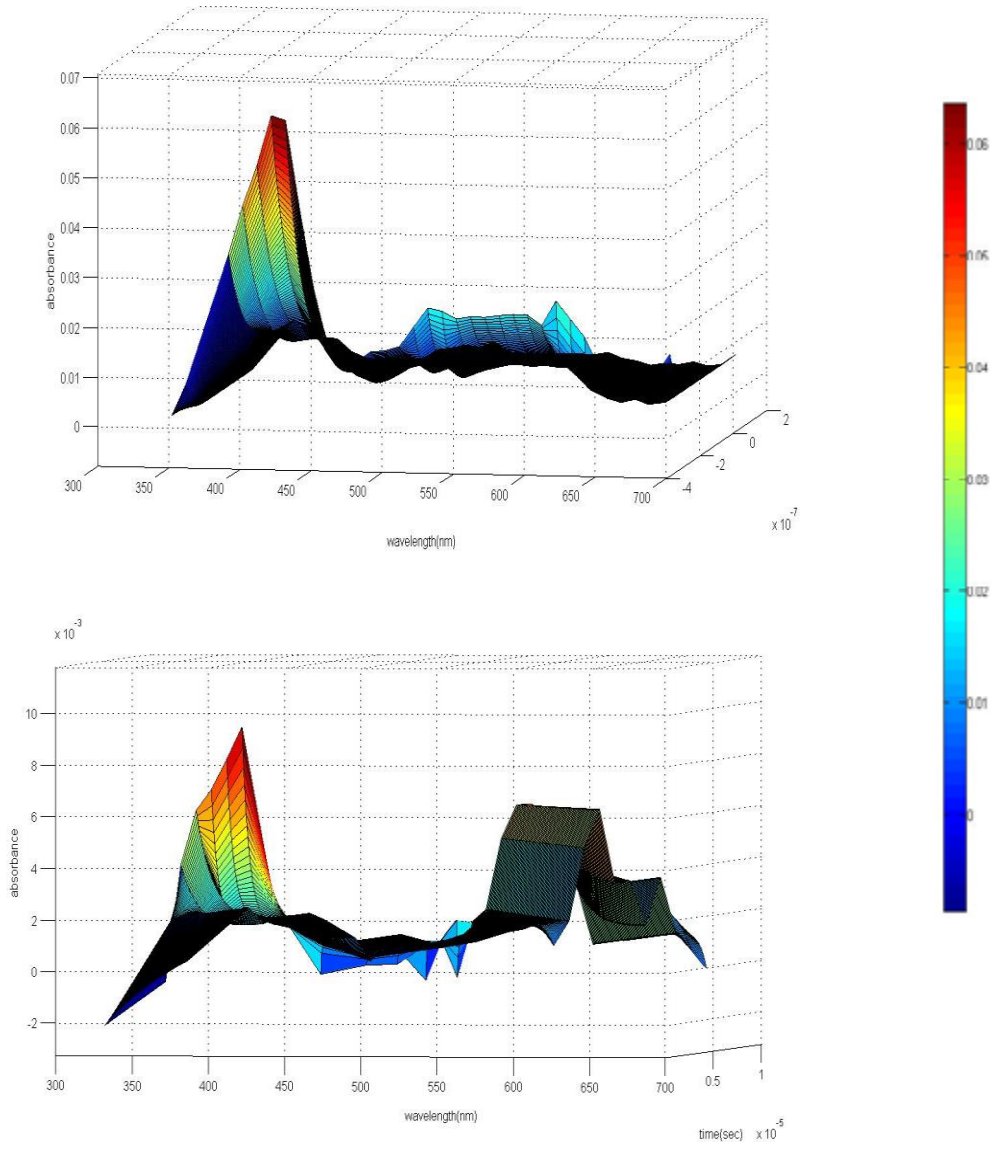

Figure 6.15. The transient absorption spectra of fac-$[(CO)_3Re(4,4'\text{-}(X)_2\text{-}bpy)(4,4'\text{-}bpy)]^+$ (a) X = H, and (b) X = CH_3, acquired after addition of 10 mM of $(tBu)_2PhOH$. The data was acquired in a nitrogen saturated (1:1 v/v) CH_3CN/H_2O solution of polypyridyl complex by exciting at 355 nm at 298 ± 3 K. The bar in the right presents the colour coding for the graphs, where the numbers represent the absorbance for the indicated colour.

Upon addition of $(tBu)_2PhOH$ significant spectral changes were observed in the TA spectra of X = H and X = CH_3 complexes. The excited-state dynamics following irradiation are expected to be different because of proton binding and competitive electron-transfer quenching. When fac-$[(CO)_3Re(4,4'\text{-}(X)_2\text{-}bpy)(4,4'\text{-}bpy)]^+$ was excited, a new broad absorption peak appears at 500 – 650 nm in the case of X = H and 550 – 650 nm in the case of X = CH_3. In numerous literature reports the origin of this broad absorption has been previously ascribed to an intraligand $\pi \rightarrow \pi^*$ absorption of singly-reduced protonated pendent 4,4'-bipyridine (Scheme 6.2).[9, 26, 42, 53]

The pendent pyridine has been reported to become protonated by phenols such as H_2Q and $(tBu)_2PhOH$.[42, 43, 54] The protonation creates sufficient driving force to reduce the 4,4'-bipyridine via an interligand electron transfer (ILET) of $\pi^*(4,4'\text{-}(X)_2\text{-}bpy) \rightarrow \pi^*(4,4'\text{-bipyridine})$ origin.[9, 42, 43]

The observation of a noticeable kinetic isotope effect (KIE) for excited-state quenching of fac-$[(CO)_3Re(4,4'\text{-}(X)_2\text{-}bpy)(4,4'\text{-}bpy)]^+$ by $(tBu)_2PhOH$ (Section 6.3.4) is also in line with protonation of the pendent 4,4'-bipyridine ligand in fac-$[(CO)_3Re(4,4'\text{-}(X)_2\text{-}bpy)(4,4'\text{-}bpy)]^+$ by $(tBu)_2PhOH$. The excited-state quenching of fac-$[(CO)_3Re(4,4'\text{-}(X)_2\text{-}bpy)(4,4'\text{-}bpy)]^+$ initiated by proton transfer also makes sense by considering the fact that ILET is thermodynamically uphill in fac-$[(CO)_3Re(4,4'\text{-}(X)_2\text{-}bpy)(4,4'\text{-}bpy)]^+$ complexes.[9, 27, 28] Protonation of the pendent 4,4'-bipyridine ligand also stabilizes the higher energy fac-$[(CO)_3Re^{II}(4,4'\text{-}(X)_2\text{-}bpy^{-\cdot})(4,4'\text{-}bpyH)]^{+*}$ state by providing the driving force for ILET.[26, 42]

6.3.3. Stern-Volmer Analysis

The luminescence spectra of fac-$[(CO)_3Re(4,4'\text{-}(X)_2\text{-}bpy)(4,4'\text{-}bpy)]^+$ (X = H, CH_3) obtained as a function of increasing $(tBu)_2PhOH$ (Figure 6.12) were used to construct Stern-Volmer plots. The dramatic decrease in Φ_{em} of fac-$[(CO)_3Re(4,4'\text{-}(X)_2\text{-}bpy)(4,4'\text{-}bpy)]^+$ after adding $(tBu)_2PhOH$ is consistent with the excited-state quenching and has been documented previously.[47] The effect of $(tBu)_2PhOH$ addition on fac-$[(CO)_3Re(4,4'\text{-}(X)_2\text{-}bpy)(4,4'\text{-}bpy)]^+$ is clearly reflected in the Stern-Volmer plots (Figure 6.16), where I_0 is the luminescence intensity of fac-$[(CO)_3Re(4,4'\text{-}(X)_2\text{-}bpy)(4,4'\text{-}bpy)]^+$ in the absence of the quencher $(tBu)_2PhOH$, and I is the intensity in the presence of $(tBu)_2PhOH$. The plot for X = H, CH_3 shows that the emission intensity decreases dramatically with increasing concentration of $(tBu)_2PhOH$.

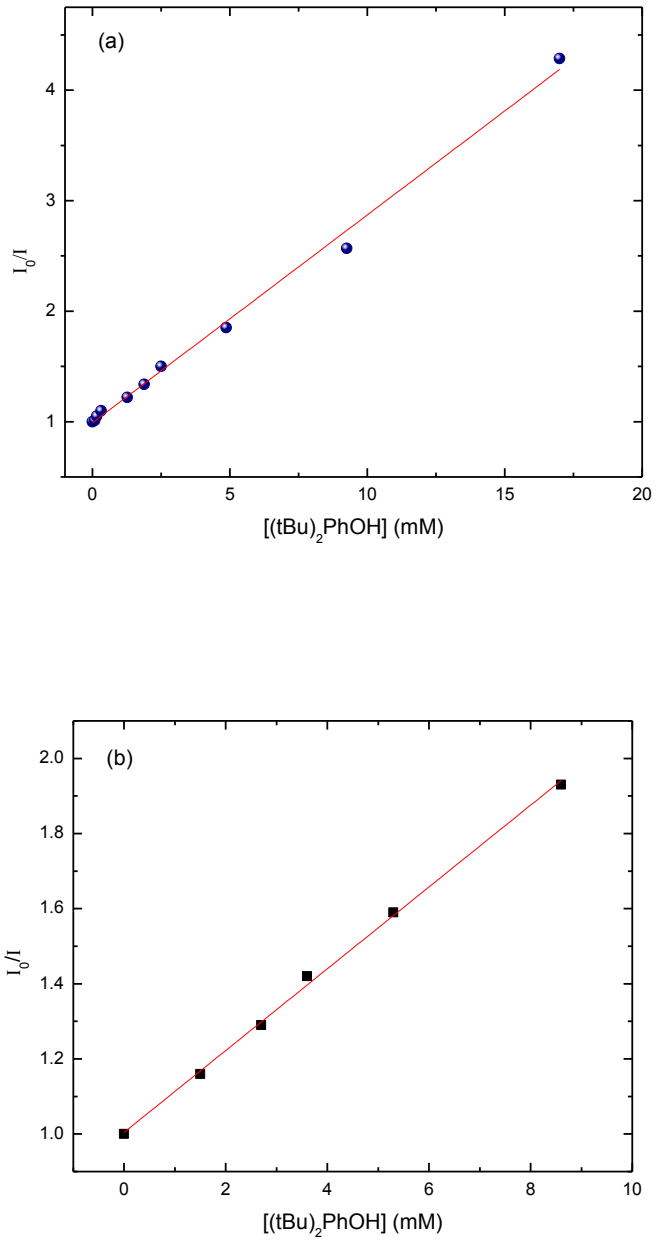

Figure 6.16. Stern-Volmer plots based on the luminescence titration data shown in Figure 6.12 (a) X = H, R^2 = 0.99, monitored at 580 nm; (b) X = CH_3, R^2 = 0.99, monitored at 560 nm. The red line is a linear fit to the data points. The K_{SV} values are given in Table 6.2.

Similarly, when luminescence lifetimes of fac-[$(CO)_3Re(4,4'\text{-}(X)_2\text{-}bpy)(4,4'\text{-}bpy)]^+$ (X = H, CH_3, NH_2) were recorded as a function of [$(tBu)_2PhOH$], a noticeable drop in the lifetimes were observed.

The Stern-Volmer plots of change in τ_0/τ vs. [$(tBu)_2PhOH$] are shown in Figure 6.18, where τ_0 is the lifetime of fac-[$(CO)_3Re(4,4'\text{-}(X)_2\text{-}bpy)(4,4'\text{-}bpy)]^+$ in the absence of $(tBu)_2PhOH$ and τ is the lifetime in the presence of the $(tBu)_2PhOH$.

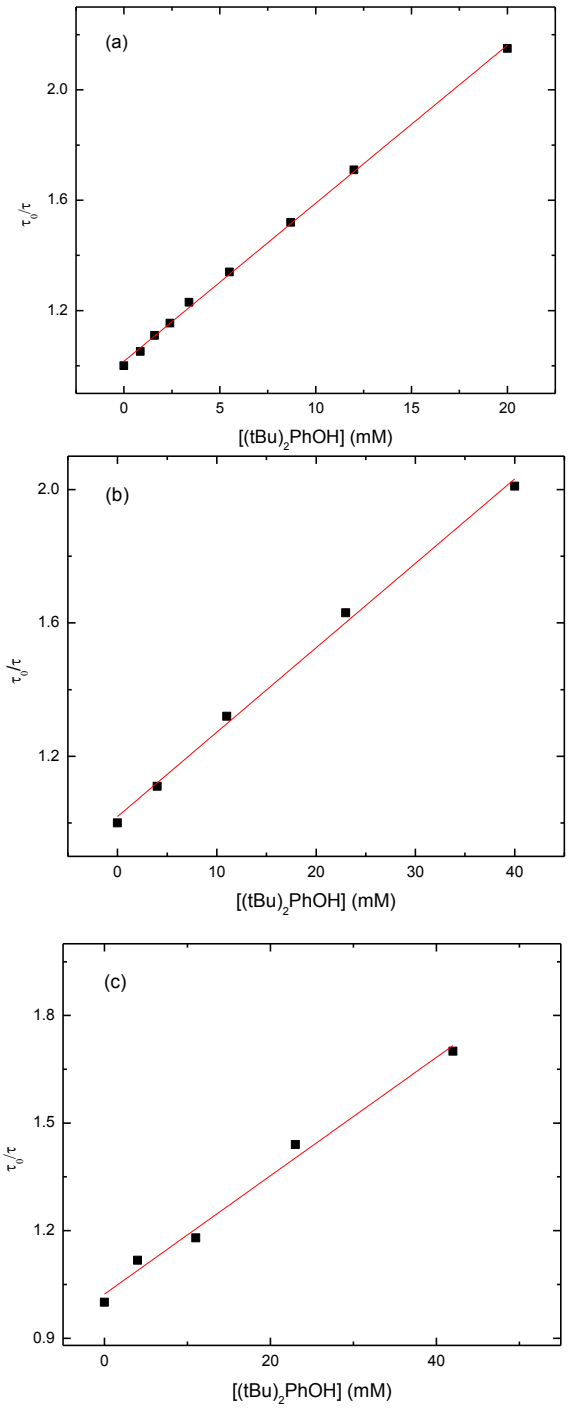

Figure 6.18. Stern-Volmer plots based on the luminescence lifetime titration data. Data was acquired in CH_3CN/H_2O (1:1 v/v) solution of fac-$[(CO)_3Re(4,4'\text{-}(X)_2\text{-}bpy)(4,4'\text{-}bpy)]^+$ by exciting at 337 nm at 298 ± 3 K. (a) X = H, R^2 = 0.99 (b) X = CH_3, R^2 = 0.99 (c) X = NH_2, R^2 = 0.98. The K_{SV} values are given in Table 6.2.

From a linear regression analysis of the luminescence lifetime (Equation 6.7) as well as intensity data (Equation 6.8), one can find the Stern-Volmer constants (K_{SV}) for fac-[$(CO)_3$Re(4,4'-$(X)_2$-bpy)(4,4'-bpy)]$^+$ complexes.

$$\frac{\tau_0}{\tau} = 1 + \tau_0 k_q[(tBu)_2PhOH] \qquad [6.7]$$

$$\frac{I_0}{I} = 1 + \tau_0 k_q[(tBu)_2PhOH] \qquad [6.8]$$

Furthermore, by considering the ^{3}MLCT luminescence lifetime of the pure metal complex it is possible to calculate bimolecular quenching constants (k_q). A similar method has been successfully utilized in numerous literature reports, to calculate k_q values in different systems.[42, 55-58]

A list of K_{SV} and k_q values is given in Table 6.2. For X = H, $k_q = 2.2 \times 10^8\ M^{-1}s^{-1}$, for X = CH_3, $k_q = 1.8 \times 10^8\ M^{-1}s^{-1}$and for X = NH_2, $k_q = 2.8 \times 10^8\ M^{-1}s^{-1}$ was calculated from luminescence lifetime data. The Stern-Volmer analysis of the luminescence intensity data leads to similar k_q values. The calculated rates of bimolecular quenching (k_q) in this work are consistent with the previous observations reported by Swarnalatha et al. where slower rates are observed when bulky groups are present at the 2,6-positions of a phenol, as compared to the reactions where phenols such as H_2Q are used.[43, 47]

Table 6.2. A list of k_q and KIE values calculated for fac-[$(CO)_3$Re(4,4'-X_2-bpy)(4,4'-bpy)]$^+$ complexes.

Entry	Exp. type	X = H	X = CH_3	X = NH_2
$K_{SV, I}$ (M^{-1})	luminescence	88 ± 2.8	72 ± 2.5	-
$K_{SV, H}$ (M^{-1})	lifetime	57 ± 2.6	63 ± 2.3	16 ± 0.9
$K_{SV, D}$ (M^{-1})[a]	lifetime	49 ± 2.0	45 ± 1.8	9 ± 0.6
$k_q \times 10^8$ (M^{-1} s^{-1}), I[a]	luminescence	3.5 ± 0.2	2.1 ± 0.8	-
$k_q \times 10^8$ (M^{-1} s^{-1}), H[b]	lifetime	2.2 ± 0.2	1.8 ± 0.6	2.8 ± 0.4
$k_q \times 10^8$ (M^{-1} s^{-1}), D[c]	lifetime	1.9 ± 0.1	1.3 ± 0.4	1.6 ± 0.5
KIE		1.1 ± 0.1	1.4 ± 0.1	1.7 ± 0.1
τ_0 (ns)		251	340	562

[a] Data obtained from luminescence intensity plot [b]acquired in CH_3CN/H_2O (1:1 v/v) mixture [c]acquired in CH_3CN/D_2O (1:1 v/v).

6.3.4. Kinetic Isotope Effect

Experiments analogous to that of Section 6.3.3 were performed in a CH_3CN/D_2O (1:1 v/v) mixture and the resulting Stern-Volmer analysis plots are shown in Figure 6.19.

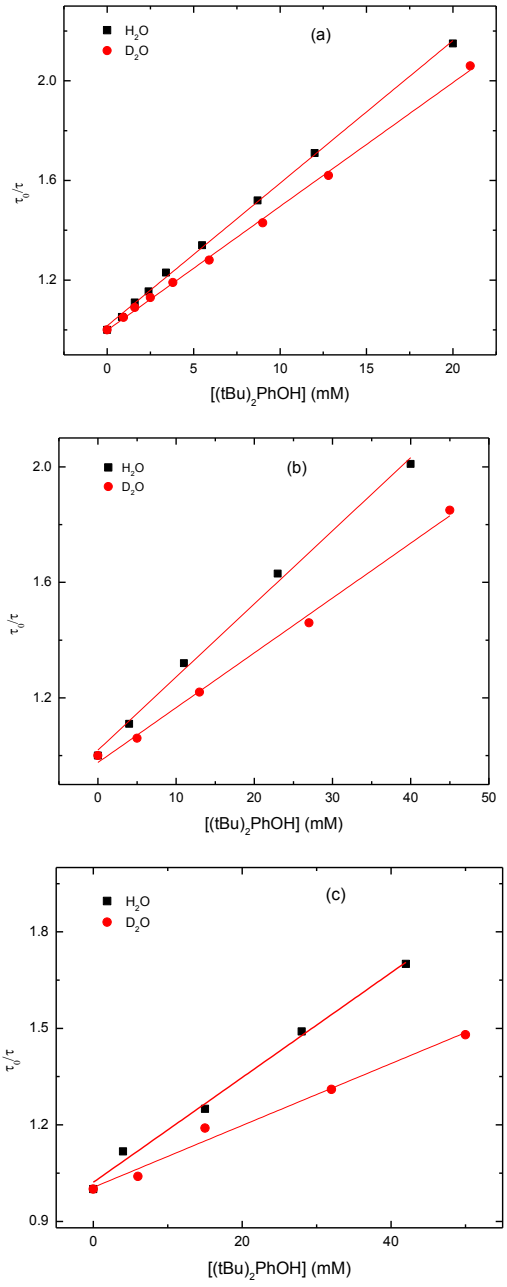

Figure 6.19. A comparison of Stern-Volmer plots for the luminescence lifetime data acquired in CH_3CN/D_2O (1:1 v/v) mixture and CH_3CN/H_2O (1:1 v/v) mixture at 298 ± 3 K by exciting at 337 nm. (a) X = H (b) X = CH_3 and (c) NH_2. The red line is a linear fit to the data points. The K_{SV} values are given in Table 6.2.

Table 6.2 lists the KIE and k_q values for the photochemical reactions between fac-$[(CO)_3Re(4,4'\text{-}(X)_2\text{-}bpy)(4,4'\text{-}bpy)]^+$ and $(tBu)_2PhOH$. Comparatively reduced rates of bimolecular quenching (k_q) were observed when data was acquired in 1:1 v/v CH_3CN/D_2O mixture. This result shows the existence of a primary KIE of 1.15 for X = H, 1.48 for X = CH_3 and 1.75 for X = NH_2. Furthermore, the KIE observed for X = H was found to be well in agreement with the previously-reported value of 1.1 for an EPT reaction between complex with X = H and H_2Q.[47]

Similarly, from the observation of KIE and calculated k_q values from luminescence lifetime as well as intensity data a PT and ET event can be predicted. Furthermore, the TA observed at ~600 nm indicates the presence of a 4,4'-bpyH$^{\cdot}$ species formed as a result of ILET upon protonation of pendent 4,4'-bpy. Thus, based on the experimental data presented so far, and available literature models for similar systems an overall scheme can be proposed for all the possible photochemical events (Scheme 6.2).[20, 42, 56]

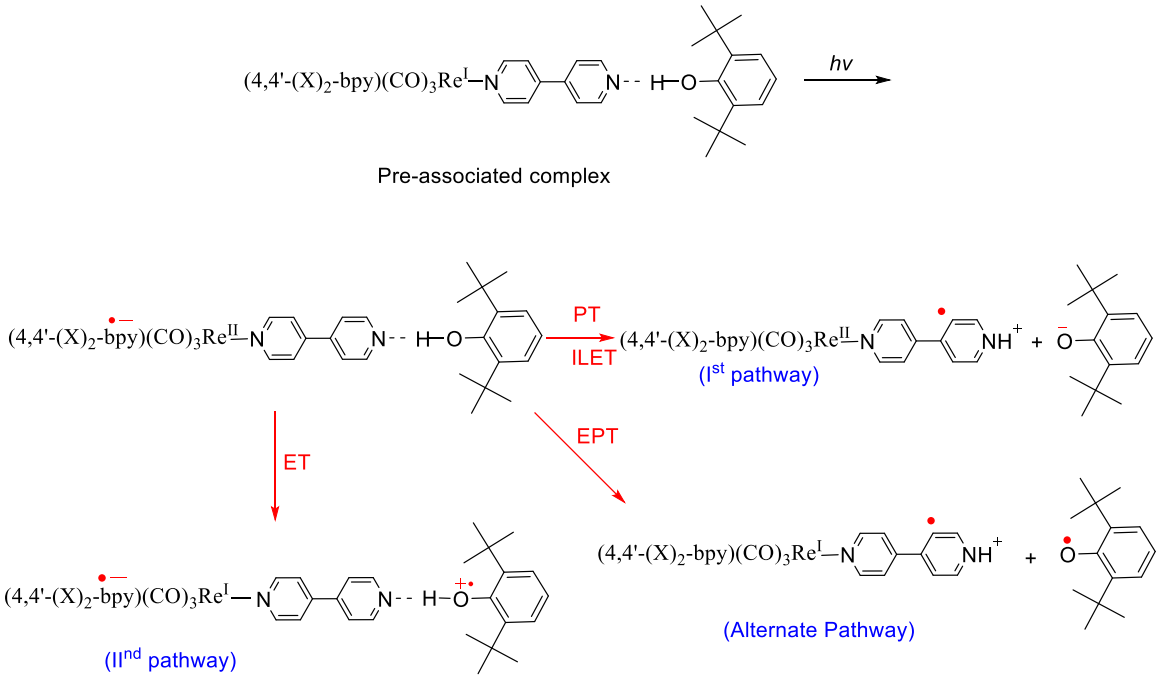

Scheme 6.2. Proposed EPT reaction pathways in fac-$[(CO)_3Re(4,4'\text{-}(X)_2\text{-}bpy)(4,4'\text{-}bpy)]^+$ complexes.[47, 59]

In Scheme 6.2, three pathways are predicted: In the first pathway, following MLCT, a PT from $(tBu)_2PhOH$ to the pendent pyridine can occur followed by an ILET. In the second pathway, one-electron oxidation of $(tBu)_2PhOH$ by Re(II) has been proposed. In an alternate pathway, PT from $(tBu)_2PhOH$ to the pendent pyridine can occur concomitantly with the ILET and oxidation of $(tBu)_2PhOH$ by the Re(II) center. The third pathway (alternate pathway) makes sense because this pathway has been reported to avoid high-energy intermediates and hence it can be assumed as a preferred pathway.[20]

6.3.5. Correlations of the Driving Force and Exited-State Properties

The values of bimolecular quenching (k_q) calculated for fac-[$(CO)_3$Re(4,4'-$(X)_2$-bpy)(4,4'-bpy)]$^+$ (X = H, NH_2 and CH_3) from Stern-Volmer analysis were plotted vs. ΔG^0 (eV) of ILET (obtained from previous literature reports).[9, 13, 27, 28, 42, 48, 52] Similarly, a plot of k_H/k_D values of fac-[$(CO)_3$Re(4,4'-$(X)_2$-bpy)(4,4'-bpy)]$^+$ vs. ΔG^0 (eV) of ILET was made and interesting correlations were observed. As seen from Figure 6.20, X = NH_2 exhibits the largest k_q value and has the highest driving force for ILET as compared to other two metal complexes. Furthermore, X = NH_2 also shows a larger KIE, whereas for X = H and X = CH_3 these have similar driving forces for ILET and display comparatively slower rates of the bimolecular quenching and smaller KIE values. These are very important and unprecedented observations which need to be explored further in detail.

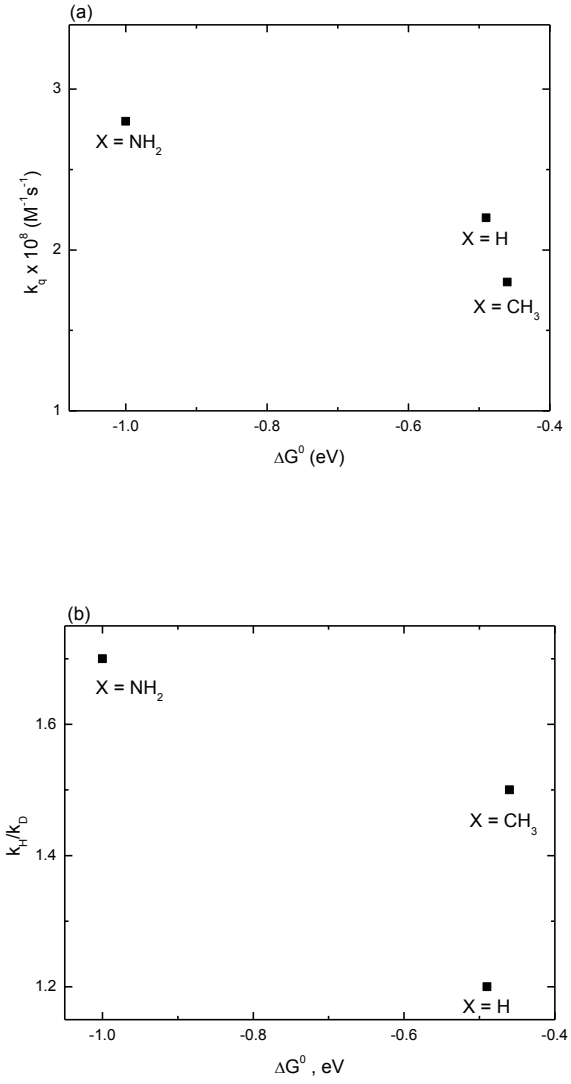

Figure 6.20. Plots of correlations between (a) bimolecular quenching vs. driving force of ILET (b) kinetic isotope effect vs. driving force of ILET. The k_q values calculated from luminescence lifetime data were used in plots a and b.

One possible reason for the high k_q for the ligand with the NH_2 could be due to the fact that it has the highest driving force (ΔG^0 = -1.0 eV) for ILET.[60] However, in a situation where the amino group gets protonated along with the pendent pyridine, it forms

an ammonium group ($-NH_3^+$) it changed from an electron-donating to a electron-withdrawing group. In this situation, the driving force is expected to drop, and then this assumption falls apart. At this juncture, the study was limited to only three metal complexes and is therefore not sufficient to establish clear correlations. A detailed study using a series of complexes with varying substituents from donating-to withdrawing groups, such as NH_2, NEt_2, $NHCOCH_3$, OCH_3, CH_3, H, Cl, Ph, CO_2Et, COOH and NO_2 will be required to completely understand the correlations of k_q, k_H/k_D and ΔG^0. In short, this study provides a new significant insight into EPT chemistry involving Re polypyridyl complexes with respect to the variation of susbstituents on the bpy.

6.4. Conclusion

The original goal of this study was to analyze the mechanistic aspects of the photochemical reaction between fac-$[(CO)_3Re(bpy)(4,4'\text{-bpy})]^+$ and $(tBu)_2PhOH$. However, when a series of homologous metal complexes was studied, some very significant properties were revealed. Values of k_q and KIE (Table 6.2) vary according to the substituents on the 4,4'-$(X)_2$-bpy. The rates of bimolecular quenching are consistent with the previous observations reported by Swarnalatha et al. where slower rates are observed when bulky groups are present at the 2,6 positions of a phenol as compared to the reactions where phenols such as H_2Q are used.[43, 47]

Moreover, an electron transfer from the phenolate moiety to the oxidized Re^{II} center takes place. The experimental data also suggests protonation of the pendant pyridine moiety of the 4,4'-bipyridine ligand by $(tBu)_2PhOH$. Consequently, an ILET

occurs that is consistent with thermodynamic arguments and previously published reports on similar systems.[26, 47]

An EPT pathway appears to be the most plausible reaction mechanism for the photochemical reaction between $(tBu)_2PhOH$ and fac-$[(CO)_3Re(4,4'\text{-}(X)_2\text{-}bpy)(4,4'\text{-}bpy)]^+$. However, competing ET-PT and PT-ET pathways cannot be overruled completely. In addition, correlations of ILET driving force with k_q and KIE (Figure 6.20) were discovered which can be explored further.

The metal complex with X = NH_2 displays spectral properties very different from the other two analogous metal complexes (X = H, CH_3). It presents a very challenging case for further studies to completely delineate the reaction mechanism behind such behaviour. Thus, this study has not become as clear mechanistically as one would expect but some interesting aspects such as, similar k_q and KIE values with similar reaction rates were revealed even though X = H and X = CH_3 have different excited-state structure than X = NH_2 in a sense that it has multiple protonable sites compared to the other two metal complexes.

References

[1] Wrighton, M. S.; Ginley, D. S., J. Am. Chem. Soc., (1975) 97, 2065.

[2] Wrighton, M. S.; Morse, D. L.; Gray, H. B.; Ottesen, D. K., J. Am. Chem. Soc., (1976) 98, 1111.

[3] Wrighton, M. S.; Morse, D. L.; Pdungsap, L., J. Am. Chem. Soc., (1975) 97, 2073.

[4] Reece Steven, Y.; Nocera Daniel, G., J. Am. Chem. Soc., (2005) 127, 9448.

[5] Reece, S. Y.; Seyedsayamdost, M. R.; Stubbe, J.; Nocera, D. G., J. Am. Chem. Soc., (2007) 129, 13828.

[6] Feliz, M.; Ferraudi, G., Inorg. Chem., (1998) 37, 2806.

[7] Servaas, P. C.; Stor, G. J.; Stufkens, D. J.; Oskam, A., Inorg. Chim. Acta, (1990) 178, 185.

[8] Lucia, L. A.; Burton, R. D.; Schanze, K. S., Inorg. Chim. Acta, (1993) 208, 103.

[9] Tapolsky, G.; Duesing, R.; Meyer, T. J., Inorg. Chem., (1990) 29, 2285.

[10] Worl, L. A.; Duesing, R.; Chen, P.; Della Ciana, L.; Meyer, T. J., J. Chem. Soc., Dalton Trans.: Inorg. Chem. (1972-1999), (1991), 849.

[11] Caspar, J. V.; Kober, E. M.; Sullivan, B. P.; Meyer, T. J., J. Am. Chem. Soc., (1982) 104, 630.

[12] Caspar, J. V.; Meyer, T. J., J. Phys. Chem., (1983) 87, 952.

[13] Chen, P.; Duesing, R.; Tapolsky, G.; Meyer, T. J., J. Am. Chem. Soc., (1989) 111, 8305.

[14] Wang, Y. S.; Schanze, K. S., Inorg. Chem., (1994) 33, 1354.

[15] Jones, W. E.; Baxter, S. M.; Strouse, G. F.; Meyer, T. J., J. Am. Chem. Soc., (1993) 115, 7363.

[16] Bakova, R.; Chergui, M.; Daniel, C.; Vlcek, A., Jr.; Zalis, S., Coord. Chem. Rev., (2011) 255, 975.

[17] Stufkens, D. J.; Vlcek, A., Jr., Coord. Chem. Rev., (1998) 177, 127.

[18] Binstead, R. A.; Moyer, B. A.; Samuels, G. J.; Meyer, T. J., J. Am. Chem. Soc., (1981) 103, 2897.

[19] Huynh, M. H. V.; Meyer, T. J., Chem. Rev., (2007) 107, 5004.

[20] Weinberg, D. R.; Gagliardi, C. J.; Hull, J. F.; Murphy, C. F.; Kent, C. A.; Westlake, B. C.; Paul, A.; Ess, D. H.; McCafferty, D. G.; Meyer, T. J., Chem. Rev., (2012) 112, 4016.

[21] Ziessel, R.; Juris, A.; Venturi, M., Inorg. Chem., (1998) 37, 5061.

[22] Ziessel, R.; Juris, A.; Venturi, M., Chem. Commun., (1997), 1593.

[23] Juris, A.; Campagna, S.; Bidd, I.; Lehn, J. M.; Ziessel, R., Inorg. Chem., (1988) 27, 4007.

[24] Liard, D. J.; Vlcek, A., Inorg. Chem., (2000) 39, 485.

[25] Vlcek, A.; Busby, M., Coord. Chem. Rev., (2006) 250, 1755.

[26] Liard, D. J.; Kleverlaan, C. J.; Vlcek, A., Inorg. Chem., (2003) 42, 7995.

[27] Chen, P.; Danielson, E.; Meyer, T. J., J. Phys. Chem., (1988) 92, 3708.

[28] Jones, W. E.; Chen, P.; Meyer, T. J., J. Am. Chem. Soc., (1992) 114, 387.

[29] Chen, P. Y.; Curry, M.; Meyer, T. J., Inorg. Chem., (1989) 28, 2271.

[30] Chen, P.; Westmoreland, T. D.; Danielson, E.; Schanze, K. S.; Anthon, D.; Neveux, P. E.; Meyer, T. J., Inorg. Chem., (1987) 26, 1116.

[31] Gagliardi, C. J.; Binstead, R. A.; Thorp, H. H.; Meyer, T. J., J. Am. Chem. Soc., (2011) 133, 19594.

[32] Mayer, J. M., Annu. Rev. Phys. Chem., (2004) 55, 363.

[33] Markle, T. F.; Rhile, I. J.; Mayer, J. M., J. Am. Chem. Soc., (2011) 133, 17341.

[34] Mayer, J. M., Annu. Rev. Phys. Chem., (2004) 55, 363.

[35] Rhile, I. J.; Mayer, J. M., J. Am. Chem. Soc., (2004) 126, 12718.

[36] Saouma, C. T.; Kaminsky, W.; Mayer, J. M., J. Am. Chem. Soc., (2012) 134, 7293.

[37] Schrauben, J. N.; Cattaneo, M.; Day, T. C.; Tenderholt, A. L.; Mayer, J. M., J. Am. Chem. Soc., (2012) 134, 16635.

[38] Markle, T. F.; Tronic, T. A.; DiPasquale, A. G.; Kaminsky, W.; Mayer, J. M., J. Phys. Chem. A, (2012) 116, 12249.

[39] Tronic, T. A.; Kaminsky, W.; Coggins, M. K.; Mayer, J. M., Inorg. Chem., (2012) 51, 10916.

[40] Warren, J. J.; Menzeleev, A. R.; Kretchmer, J. S.; Miller, T. F.; Gray, H. B.; Mayer, J. M., J. Phys. Chem. Lett., (2013) 4, 519.

[41] Biczok, L.; Linschitz, H., J. Phys. Chem., (1995) 99, 1843.

[42] Stewart, D. J.; Brennaman, M. K.; Bettis, S. E.; Wang, L.; Binstead, R. A.; Papanikolas, J. M.; Meyer, T. J., J. Phys. Chem. Lett., (2011) 2, 1844.

[43] Swarnalatha, K.; Rajkumar, E.; Rajagopal, S.; Ramaraj, R.; Banu, I. S.; Ramamurthy, P., J. Phys. Org. Chem., (2011) 24, 14.

[44] Manner, V. W.; DiPasquale, A. G.; Mayer, J. M., J. Am. Chem. Soc., (2008) 130, 7210.

[45] Owsik, I.; Kolarz, B.; Jezierska, J., Catal Lett, (2006) 107, 197.

[46] Knight, T. E.; McCusker, J. K., J. Am. Chem. Soc., (2010) 132, 2208.

[47] Stewart, D. J.; Brennaman, M. K.; Bettis, S. E.; Wang, L.; Binstead, R. A.; Papanikolas, J. M.; Meyer, T. J., J. Phys. Chem. Letters, (2011) 2, 1844.

[48] Tapolsky, G.; Duesing, R.; Meyer, T. J., J. Phys. Chem., (1991) 95, 1105.

[49] Barbara, P. F.; Meyer, T. J.; Ratner, M. A., J. Phys. Chem., (1996) 100, 13148.

[50] Chen, P. Y.; Duesing, R.; Graff, D. K.; Meyer, T. J., J. Phys. Chem., (1991) 95, 5850.

[51] Okamura, T.; Yip, R. W., Bull. Chem. Soc. Jpn., (1978) 51, 937.

[52] Strouse, G. F.; Schoonover, J. R.; Duesing, R.; Meyer, T. J., Inorg. Chem., (1995) 34, 2725.

[53] Liard, D. J.; Busby, M.; Farrell, I. R.; Matousek, P.; Towrie, M.; Vlcek, A., Jr., J. Phys. Chem. A, (2004) 108, 556.

[54] Wenger, O. S., Acc. Chem. Res., (2010) 44, 25.

[55] Gagliardi, C. J.; Binstead, R. A.; Thorp, H. H.; Meyer, T. J., J. Am. Chem. Soc., (2011) 133, 19594.

[56] Wenger, O. S., Acc. Chem. Res., (2013) 46, 1517.

[57] Lebedeva, N. V.; Schmidt, R. D.; Concepcion, J. J.; Brennaman, M. K.; Stanton, I. N.; Therien, M. J.; Meyer, T. J.; Forbes, M. D. E., J. Phys. Chem. A, (2011) 115, 3346.

[58] Gagliardi, C. J.; Westlake, B. C.; Kent, C. A.; Paul, J. J.; Papanikolas, J. M.; Meyer, T. J., Coord. Chem. Rev., (2010) 254, 2459.

[59] Kuss-Petermann, M.; Wolf, H.; Stalke, D.; Wenger, O. S., J. Am. Chem. Soc., (2012) 134, 12844.

[60] Chen, P. Y.; Duesing, R.; Graff, D. K.; Meyer, T. J., J. Phys. Chem., (1991) 95, 5850.

Chapter – 7

Summary and Future Work

7.1. General Conclusions

This dissertation encompasses the investigation of excited-state properties of systematically-designed molecular assemblies and novel chromophores. The studies reported herein set out to explore how slight synthetic modifications can bring astounding variations in the excited-state properties of a system. The studies also sought to know how the excited-state of a molecule responds towards a specific analyte. The studies reveals that all of the studied systems examined exhibit rich excited-state properties.

7.1.1. Empirical Findings

The first part of this Thesis (Chapter 1-2) is dedicated to a review of important photochemistry concepts, a review of instrumental techniques and synthetic procedures. The main empirical findings are chapter-specific and were summarized within the respective empirical chapters (Chapter 3 to Chapter 6).

In Chapter 3, a detailed analysis of the spectral data was performed using the Franck-Condon band-shape analysis and the emission spectral-fitting procedure. As a result, the following conclusions were made: The lower-energy absorption manifold arises due to underlying transitions which lead to both emission as well as non-radiative decay. It

was found that pyrenophane (O-C_4-O) exhibits properties that are quite different from those of the remaining pyrenophanes in the series. At the present time, it can be considered that the anomaly in (O-C_4-O) can be attributed to its relatively bent structure. It was also concluded that vibrational mixing between the ^1L_a and ^1L_b transitions which leads to discernible difference in the properties of (O-C_n-O) (n = 4, 5, 6) pyrenophanes, as compared to pyrene itself. Moreover, based on the existing literature reports it can be proposed that there is an inversion of the energetics in these molecules. It is very striking that a cursory glance of the spectral data show very little differences between the three pyrenophanes, however, a detailed analysis reveals some much unexpected aspects. The literature on this subject and specifically in the context of excited-state behaviour of bent pyrenophane molecules is inconclusive on several vital questions. The key empirical findings can be concluded as follows:

i. The pyrenophane molecules show considerable dipole moment and charge-transfer character.

ii. The Huang-Rhys factor (S_M) which reflects the vibrational reorganization energy (λ_i), decreases from n = 6 to n = 4.

iii. The $\hbar\omega_M$ value is higher in (O-C_4-O) due to the increased contributions in the excited-state decay from a number of symmetrical ν(Pyr) stretching modes, mainly C=C in character. This is a key observation because in the one-mode limit, the excited-state is distributed over many nuclear coordinates.

Chapter 4 provides the spectroscopic characterization and understanding of proton transfer (PT) equilibria in pyrene-based shape persistent macrocycles. Pyr_{in}, Pyr_{out}, Pyr_{in}-half, pyr_{out}-half, and Pyr_{ben} can be considered as structurally different members of a new class of pyrene-based shape-persistent macrocycles that incorporate nitrogen heterocyclic rings (with the exception of Pyr_{ben}). The following major conclusion can be made from this study.

i. Despite their highly conjugated frameworks, Beer's law plots rule out any sign of aggregation in these macrocycles.

ii. Addition of TFA results in substantial changes in the spectral properties of all of the investigated systems, suggesting that the protons bind to all the macrocycles and half-cycles.

iii. In Pyr_{in}, Pyr_{out} and their half counterparts, the pyridinic nitrogens are protonated first, because they are more basic than the other possible binding sites (enol ether), in accordance with pKa values from the literature sources.

iv. The equilibrium constants suggest stepwise binding in macrocycles and single-step binding in the half-cycles. Moreover, the equilibrium constants for half-cycles were slightly larger than those of macrocycles.

Chapter 5 describes the sensing behaviour and underlying mechanism in triazole based oligomers. In the first segment of the Chapter, interactions of some medically-important saccharides with triazole-based, phenylboronic acid-containing π-conjugated

OPV oligomers (named ‘‘hmer’’) were studied. In hmers, the OPV serves both as the fluorophore and structural backbone, the phenylboronic acid moiety serving as a receptor for incoming saccharides.

The second segment reports the triazole-based metal ion sensors. Specifically, triazole-based PPE polymers and triazole-based TTFV oligomers were studied. The following key conclusions can be made from this study:

i. Saccharide sensing was demonstrated in neutral aqueous media. The hmer oligomers show similar responses towards fructose and galactose with similar equilibrium constants. On the other hand, the responses towards ribose and glucose are quite distinctive.

ii. SVD analysis reveals that the hmers bind with the saccharides in stepwise 1:2 and 1:4 equilibria.

iii. This study provides an understanding of new sensor design and their tuning to improve the performance of oligomeric chemo-and bio-sensors.

iv. The PPE^4 polymer was designed to achieve turn-on metal sensing behaviour in aqueous media and selective Cd^{2+} sensing was demonstrated.

v. A new energy-transfer sensitization mechanism was discovered for metal ion sensing in PPE^4 polymer.

vi. A turn-on sensing behaviour towards metal ions was achieved in THF using a dianthryl-TTFV sensor. SVD analysis suggests binding of metal ions in a sequential 1:1 and 1:2 manner.

vii. Lever's treatment and HSAB theory was utilized to explain the response of dianthryl-TTFV (tweezer) towards metal ions. The results from this analysis can be particularly useful in the architecture of new sensors for the sensing of a specific target analyte.

viii. It is noteworthy that a triazole functional group plays a very important role in the structure-property relationship in all the sensors studied in this Chapter. The triazole unit is not just a synthetic tool, but it also works as a spacer, linker and ligand.

Chapter 6 deals with EPT reactions between fac-$[(CO)_3Re(4,4'\text{-}(X)_2\text{-bpy})(4,4'\text{ bpy})]^+$ (X = H, NH_2, CH_3) and a sterically bulky phenol, $(tBu)_2PhOH$. The salient points concluded in this study are given below:

i. Three analogous, heteroleptic Re polypyridyl complexes were synthesized and characterized. In each complex Re(I) MLCT excited-state work as a powerful oxidant.

ii. Luminescence (lifetime and intensity) and transient absorption data confirms that the protonation of the pendent 4,4'-bipyridine pyridine by $(tBu)_2PhOH$ occurs.

iii. Variation of substituents at the 4,4' position of the 2,2'-bpy alters the driving force for ILET which ultimately affects the reduction of the Re^{II} oxidized state by $(tBu)_2PhOH$.

iv. The rates of bimolecular quenching are consistent with the previous observations reported by Swarnalatha et al. where slower rates are observed when bulky groups are present at the 2,6 positions of a phenol as compared to the reactions where phenols such as H_2Q are used.

v. Referring to the experimental data and previous literature reports, preferred EPT pathway can be proposed for the photochemical reactions between fac-$[(CO)_3Re(4,4'\text{-}(X)_2\text{-}bpy)(4,4'\text{-}bpy)]^+$ and $(tBu)_2PhOH$.

7.2. Recommendations for Future Work

The study has offered an evaluative perspective on the excited-state behaviour of novel aromatic chromophores and molecular assemblies. However, the scale of this study is extensive and multifaceted. Therefore, some recommendations for future work can be made.

7.2.1. Chapter 3

i. The present study is limited to only three pyrenophanes and in order to get further insights into the structure-property relationship the pyrenophane series can be extended to establish the energy gap correlations and the effect of bend angle on the transition moment.

ii. TD-DFT calculations can be done to assign the individual transitions.

iii. Raman and resonance Raman studies need to be done to identify the vibrational modes coupled to the LUMO-HOMO transitions. These studies need to be extended to systems where the tether length is systematically varied.

7.2.2. Chapter 4

i. The CT dynamics in pyrene macrocycles and half-cycles can be investigated using ultrafast laser spectroscopy. Insights into the CT dynamics would also be helpful in understanding the origin of the new low-energy bands in absorption and emission titration data.

ii. Detailed ^{1}H, ^{13}C NMR and COSY spectra as a function of TFA should be acquired to verify the proposed protonation sites and equilibrium constants.

iii. Spectral data can be acquired in different solvents such as $CHCl_3$, CH_3CN, chlorobenzene to study the role of solvent polarity on the protonation processes.

iv. In order to check the reversibility of the protonation process, the spectral data can be acquired by additing a base to the protonated product.

7.2.3. Chapter 5

i. Determine how the sensing properties depend on the length of the π-conjugated oligomer and the number of boronic acid groups.

ii. AFM images of hmers with, and without, added saccharide can be acquired to verify the de-aggregation/solvation behaviour. Furthermore, dynamic laser scattering (DLS) and ultrafast laser spectroscopy techniques can be employed to elucidate the sensing mechanism.

iii. Determine how the monomer length affects the sensing behaviour of the π-conjugated PPE polymers.

iv. The role of the triazole unit as a linker and ligand can be investigated in detail using a series of triazole-based oligomers.

7.2.4. Chapter 6

i. The present study is limited to only three metal complexes, therefore, a detailed study using a series of complexes with varying substituents from donating-to withdrawing-groups such as NH_2, NEt_2, $NHCOCH_3$, OCH_3, CH_3, H, Cl, Ph, CO_2Et, COOH and NO_2 can be performed to understand the driving-force dependence on the EPT process.

ii. In addition to $(tBu)_2PhOH$, a study using several other phenols such as H_2Q, 2,4,6-tri-tert-butylphenol, p-cresol, catechol and resorcinol can be performed.

iii. Some experiments using ultrafast laser spectroscopy can be performed to acquire early-time PT kinetics and further insights into the kinetic isotope effect.

Appendix

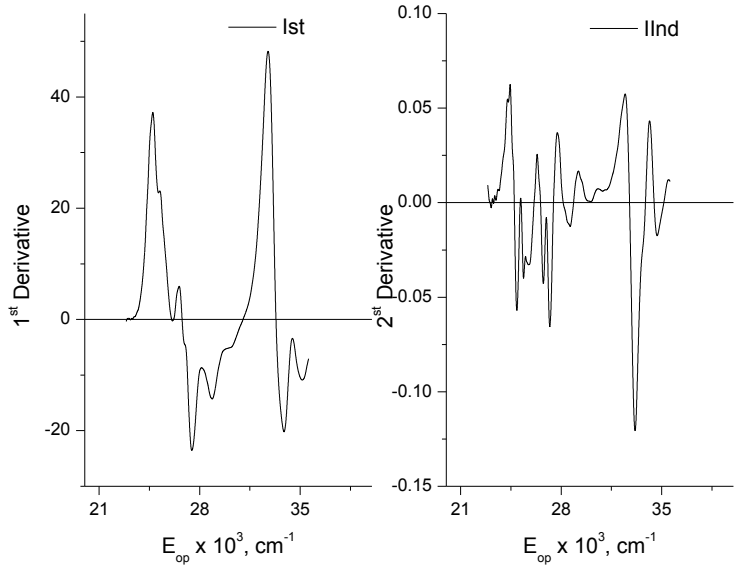

Figure S1. The first-and second-derivative plots for (O-C_4-O).

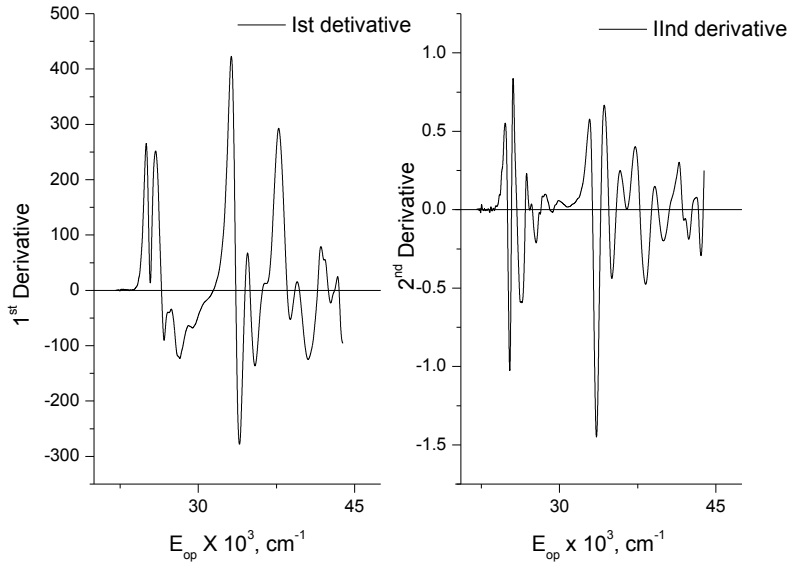

Figure S2. The first-and second-derivative plots for (O-C_5-O).

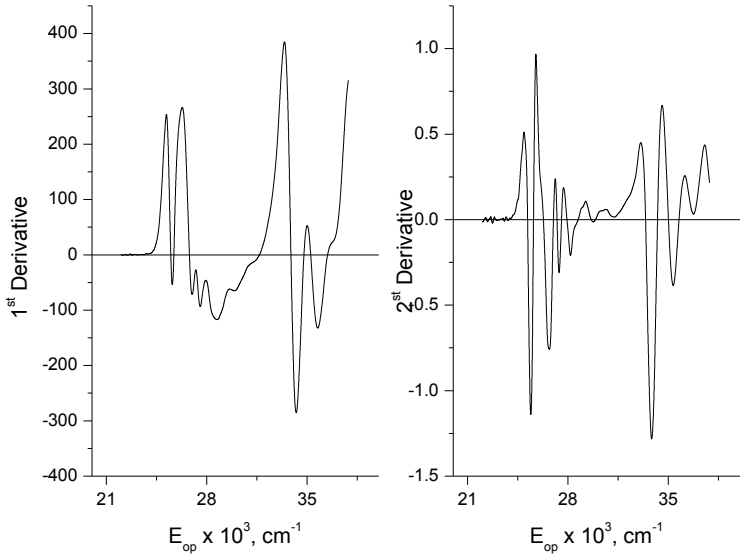

Figure S3. The first-and second-derivative plots for (O-C_6-O).

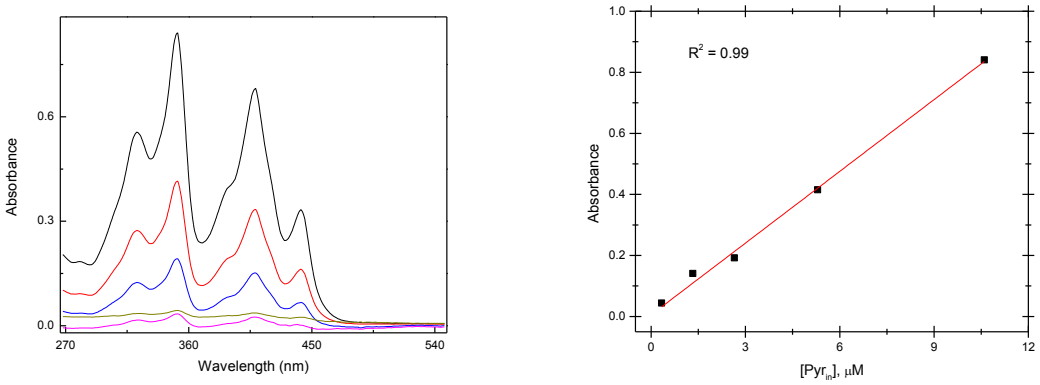

Figure S4. Absorption spectral data obtained as a function of [Pyr_{in}] in CH_2Cl_2 at 298 ± 3 K (left) and Beer's law plot of the absorbance at λ = 322 nm as a function of [Pyr_{in}] (right). The red line is the result of a linear least squares analysis of the data.

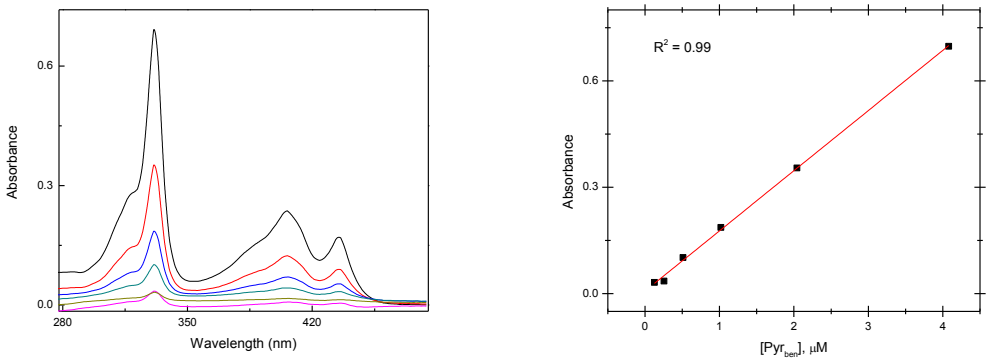

Figure S5. Absorption spectral data obtained as a function of [Pyr_{ben}] in CH_2Cl_2 at 298 ± 3 K (left) and Beer's law plot of the absorbance at λ = 326 nm as a function of [Pyr_{ben}] (right). The red line is the result of a linear least squares analysis of the data.

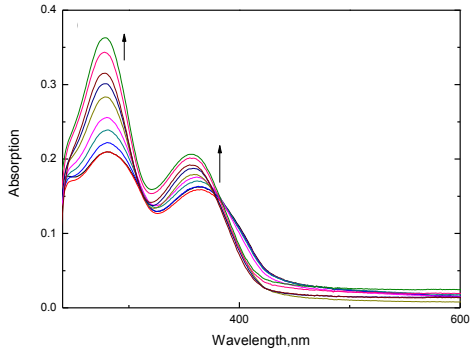

Figure S6. UV-Vis absorption spectra of compound C-hmer (7.6 μM) as a function of increasing amounts of D-fructose in aqueous PBS (pH = 7.4): at 0.00, 0.16, 0.38, 0.61, 0.89, 1.20, 1.50, 1.80, 2.30, 2.80 and 3.40 mM quantities, at a temperature of 298 ± 3 K.

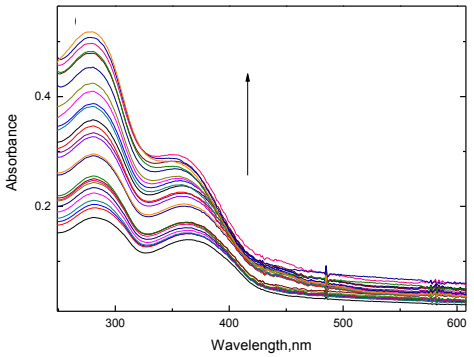

Figure S7. UV-Vis absorption spectra of compound C-hmer (7.6 μM) as a function of increasing amounts of D-galactose in aqueous PBS (pH = 7.4): at 0.00, 0.13, 0.33, 0.59, 0.92, 1.30, 1.90, 2.60, 3.40, 4.40, 5.60, 6.80, 8.20, 9.80, 11.60, 13.50, 15.50, 17.70, 20.0 and 24.90 mM quantities, at a temperature of 298 ± 3 K.

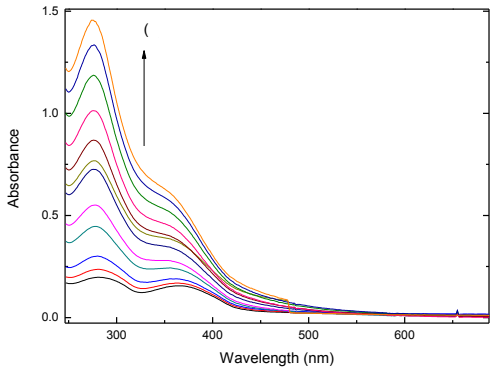

Figure S8. UV-Vis absorption spectra of compound C-hmer (7.6 μM) as a function of increasing amounts of D-ribose in aqueous PBS (pH = 7.4): at 0.00, 4.4, 13.0, 26.0, 39.0, 57.0, 79.0, 79.0, 79.0, 91.0, 130, 170, 240 and 330 mM quantities, at a temperature of 298 ± 3 K.

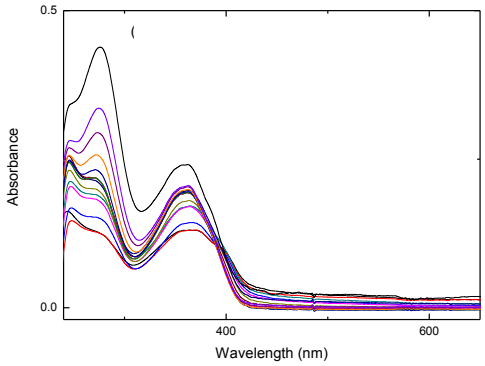

Figure S9. UV-Vis absorption spectra of compound O-hmer (7.3 μM) as a function of increasing amounts of D-fructose in aqueous PBS (pH = 7.4): at 0.00, 0.39, 1.20, 2.00, 2.70, 4.30, 7.50, 13.0, 26.0, 49.0 and 91.0 mM quantities, at a temperature of 298 ± 3 K.

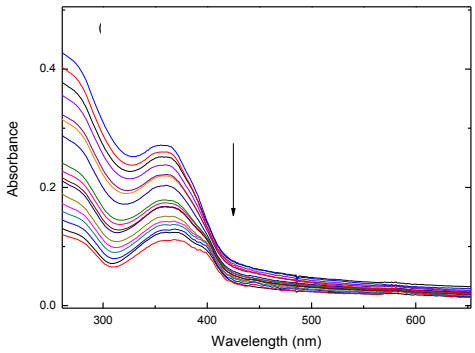

Figure S10. UV-Vis absorption spectra of compound O-hmer (7.3 μM) as a function of increasing amounts of D-galactose in aqueous PBS (pH = 7.4): at 0.00, 0.63, 3.60, 7.60, 13.0, 21.0, 32.0, 46.0, 61.0, 79.0, 99.0, 121, 145, 176, 209, 245 and 285 mM quantities, at atemperature of 298 ± 3 K.

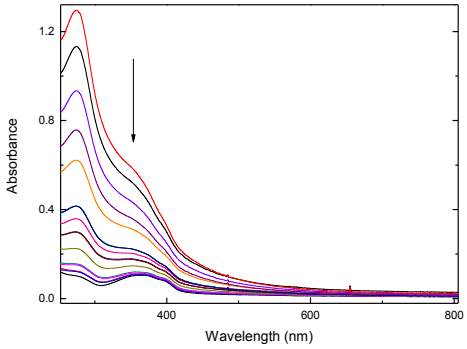

Figure S11. UV-Vis absorption spectra of compound O-hmer (7.3 μM) as a function of increasing amounts of D-ribose in aqueous PBS (pH = 7.4): at 0.00, 0.36, 11.0, 28.0, 52.0, 84.0, 121, 163, 211, 260, 309, 361 and 413 mM quantities, at a temperature of 298 ± 3 K

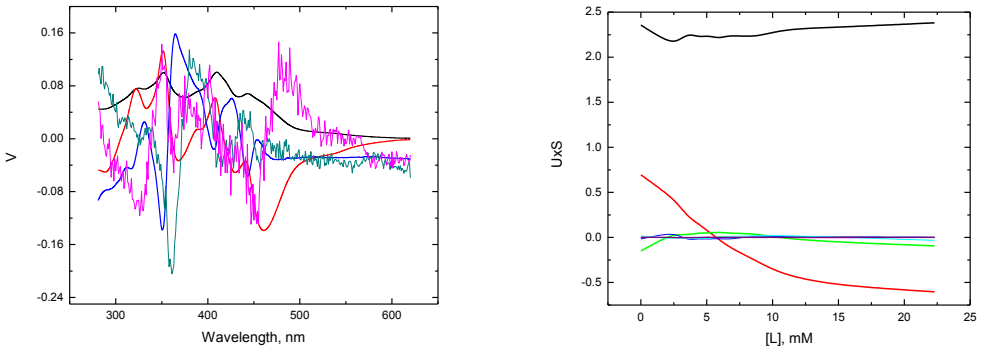

Figure S12. Representative eigen vectors extracted as a result of SVD of pyr_{in} absorption titration data: the first three spectral eigenvectors, V, (black, blue and red) are from the SVD analysis of the data matrix (left). The first three temporal eigenvectors (black, red and green) from $U \times S$, the remaining curves contains instrumental noise and noise from lamp source (right). By definition, the scan data can be reconstructed as $Y = U \times S \times V$.

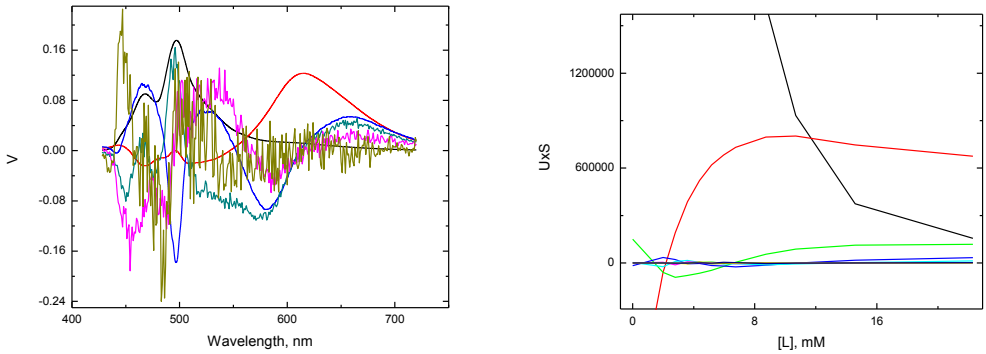

Figure S13. Representative eigen vectors extracted as a result of SVD of pyr_{in} emission titration data: the first three spectral eigenvectors, V, (black, blue and red) are from the SVD analysis of the data matrix (left). The first three temporal eigenvectors (black, red and green) from $U \times S$, the remaining curves contains instrumental noise and noise from lamp source (right). By definition, the scan data can be reconstructed as $Y = U \times S \times V$.

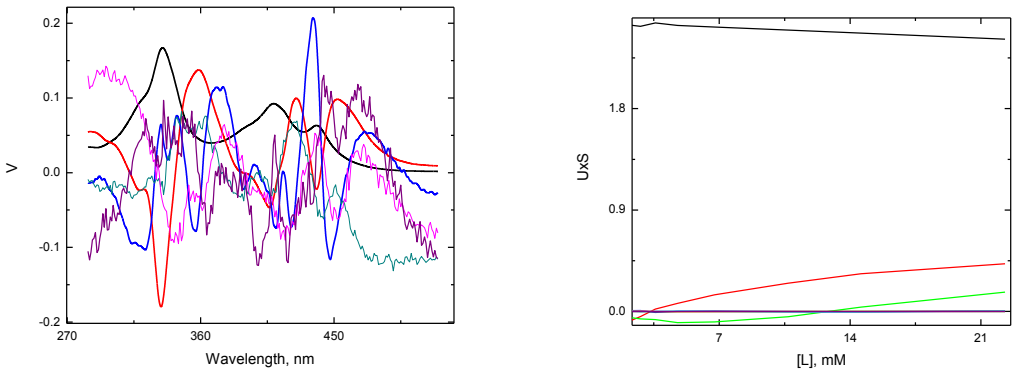

Figure S14. Representative eigen vectors extracted as a result of SVD of pyr_{out} absorption titration data: the first three spectral eigenvectors, V, (black, blue and red) are from the SVD analysis of the data matrix (left). The first three temporal eigenvectors (black, red and green) from $U \times S$, the remaining curves contains instrumental noise and noise from lamp source (right). By definition, the scan data can be reconstructed as $Y = U \times S \times V$.

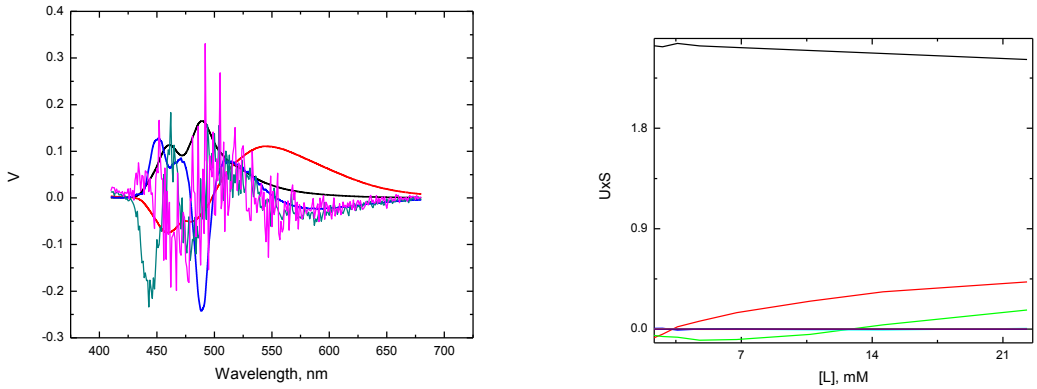

Figure S15. Representative eigen vectors extracted as a result of SVD of pyr_{out} absorption titration data: the first three spectral eigenvectors, V, (black, blue and red) are from the SVD analysis of the data matrix (left). The first three temporal eigenvectors (black, red and green) from $U \times S$, the remaining curves contains instrumental noise and noise from lamp source (right). By definition, the scan data can be reconstructed as $Y = U \times S \times V$.

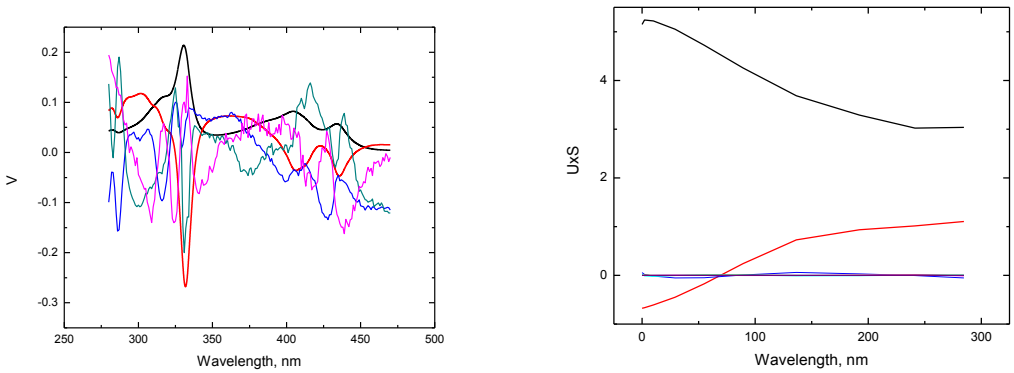

Figure S16. Representative eigen vectors extracted as a result of SVD of pyr_{ben} absorption titration data: the first three spectral eigenvectors, V, (black, blue and red) are from the SVD analysis of the data matrix (left). The first three temporal eigenvectors (black, red and green) from $U \times S$, the remaining curves contains instrumental noise and noise from lamp source (right). By definition, the scan data can be reconstructed as $Y = U \times S \times V$.

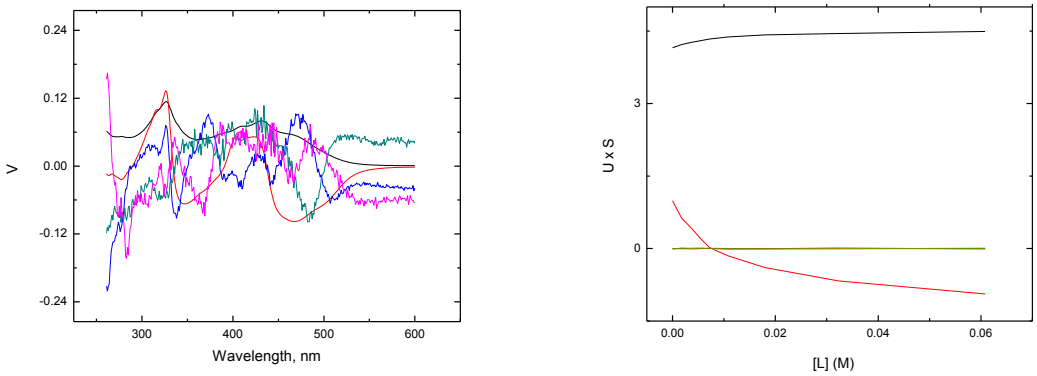

Figure S17. Representative eigen vectors extracted as a result of SVD of pyr_{in}-half absorption titration data: the first three spectral eigenvectors, V, (black and red) are from the SVD analysis of the data matrix (left). The first three temporal eigenvectors (black and red) from $U \times S$, the remaining curves contains instrumental noise and noise from lamp source (right). By definition, the scan data can be reconstructed as $Y = U \times S \times V$.

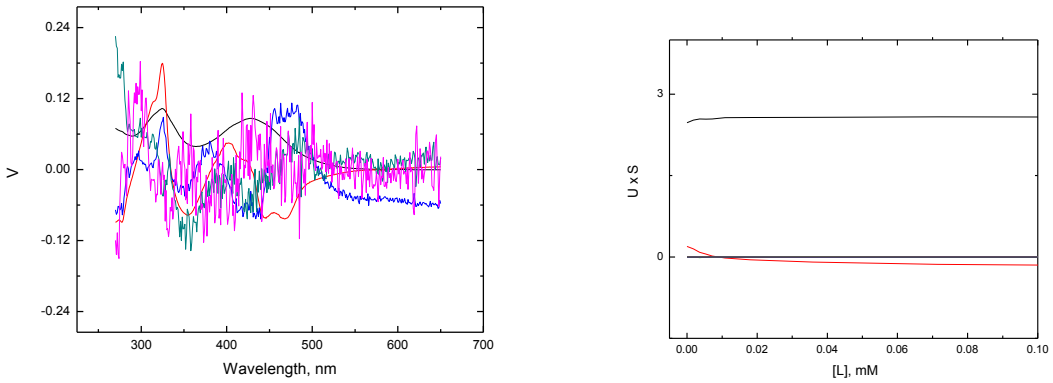

Figure S18. Representative eigen vectors extracted as a result of SVD of pyr_{out}-half absorption titration data: the first three spectral eigenvectors, V, (black and red) from the SVD analysis of the data matrix (left). The first three temporal eigenvectors (black and red) from $U \times S$, the remaining curves contains instrumental noise and noise from lamp source (right). By definition, the scan data can be reconstructed as $Y = U \times S \times V$.

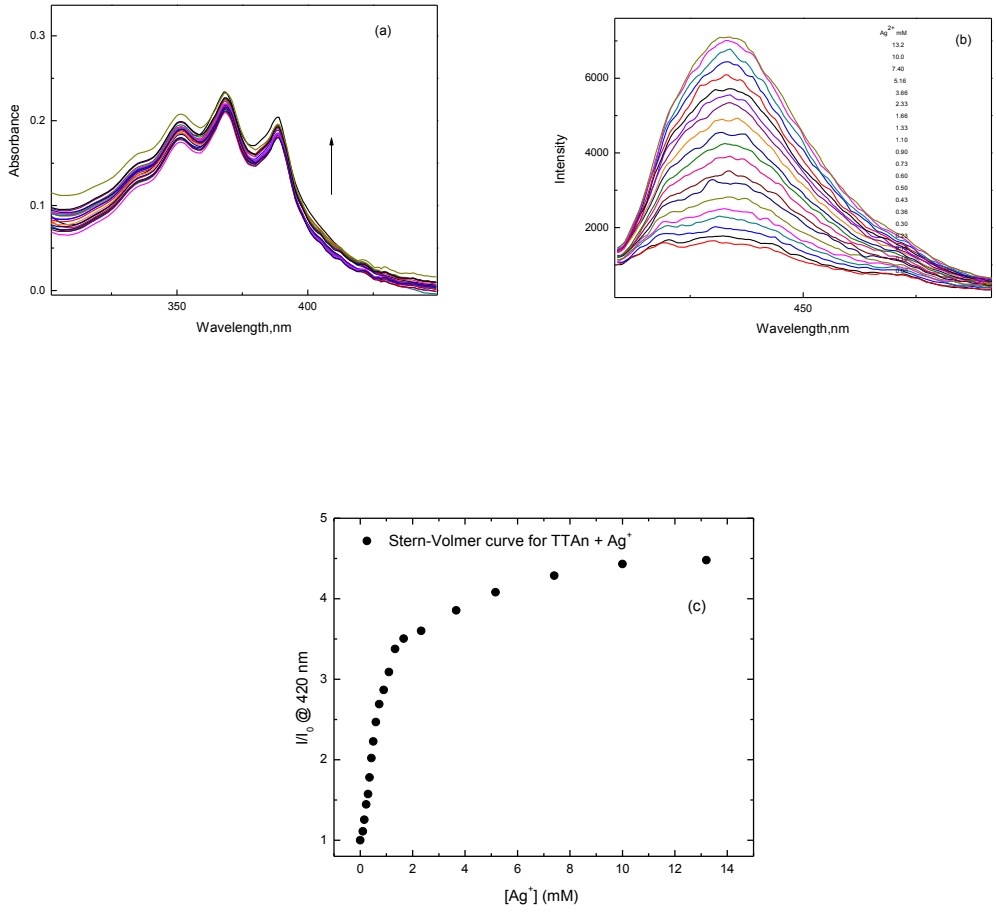

Figure S19. (a) UV-Vis absorption (b) Fluorescence spectra obtained as a function of increasing concentrations of AgOTf for TTFAn in THF at 298 ± 3 K. The arrows indicate the trend for increasing AgOTf. [TTFAn] = (5.9 μM) and λ_{exc} = 350 nm. (c) A plot of (I/I_0) vs. [AgOTf] obtained from λ_{exc} = 350 nm monitored at 420 nm.

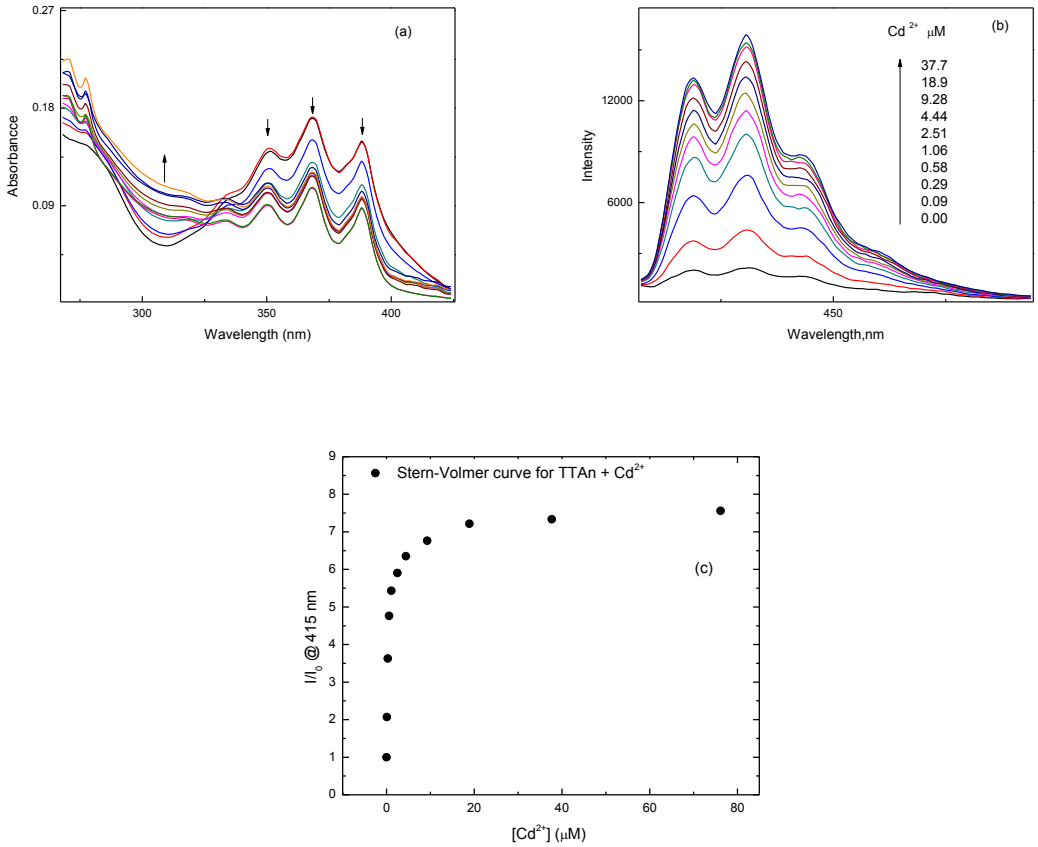

Figure S20. (a) UV-Vis absorption (b) Fluorescence spectra obtained as a function of increasing concentrations of $Cd(OTf)_2$ (2.89 mM) for TTFAn in THF at 298 ± 3 K. The arrows indicate the trend for increasing $Cd(OTf)_2$. [TTFAn] = (5.5 μM) and λ_{exc} = 350 nm. (c) A plot of (I/I_0) vs. $[Cd(OTf)_2]$ obtained from λ_{exc} = 350 nm monitored at 415 nm.

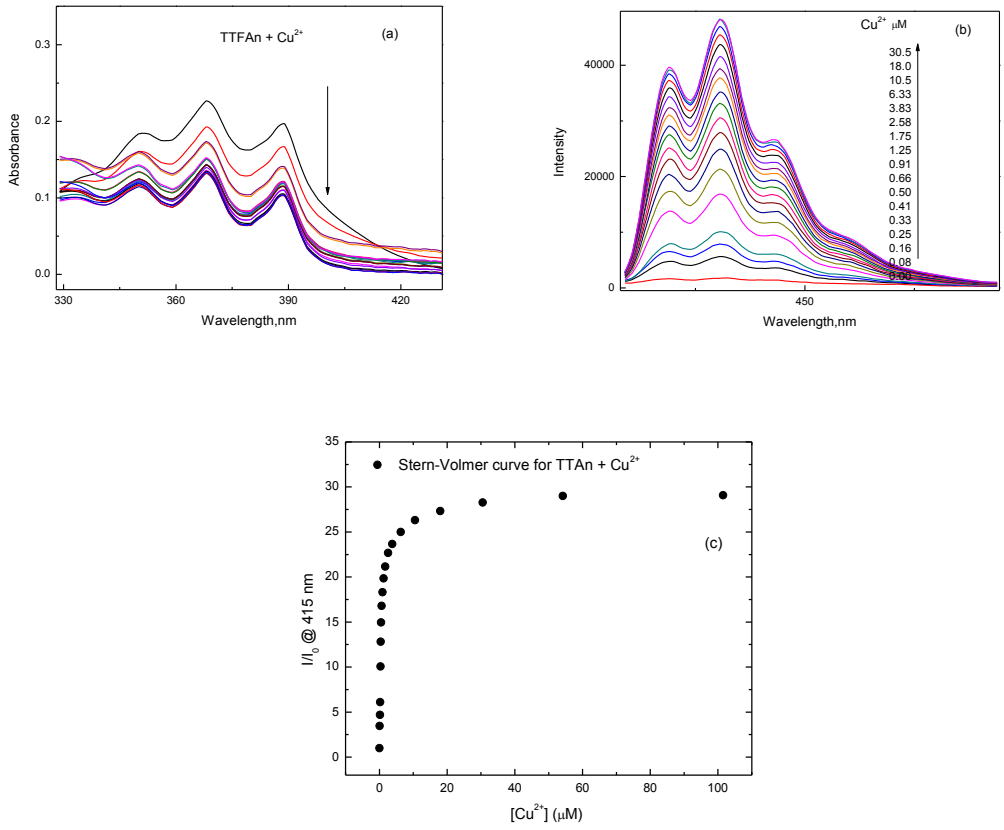

Figure S21. (a) UV-Vis absorption (b) Fluorescence spectra obtained as a function of increasing concentrations of $Cu(OTf)_2$ for TTFAn in THF at 298 ± 3 K. The arrows indicate the trend for increasing $Cu(OTf)_2$. [TTFAn] = (5.5 μM) and λ_{exc} = 350 nm. (c) A plot of (I/I_0) vs. $[Cu(OTf)_2]$ obtained from λ_{exc} = 350 nm monitored at 415 nm.

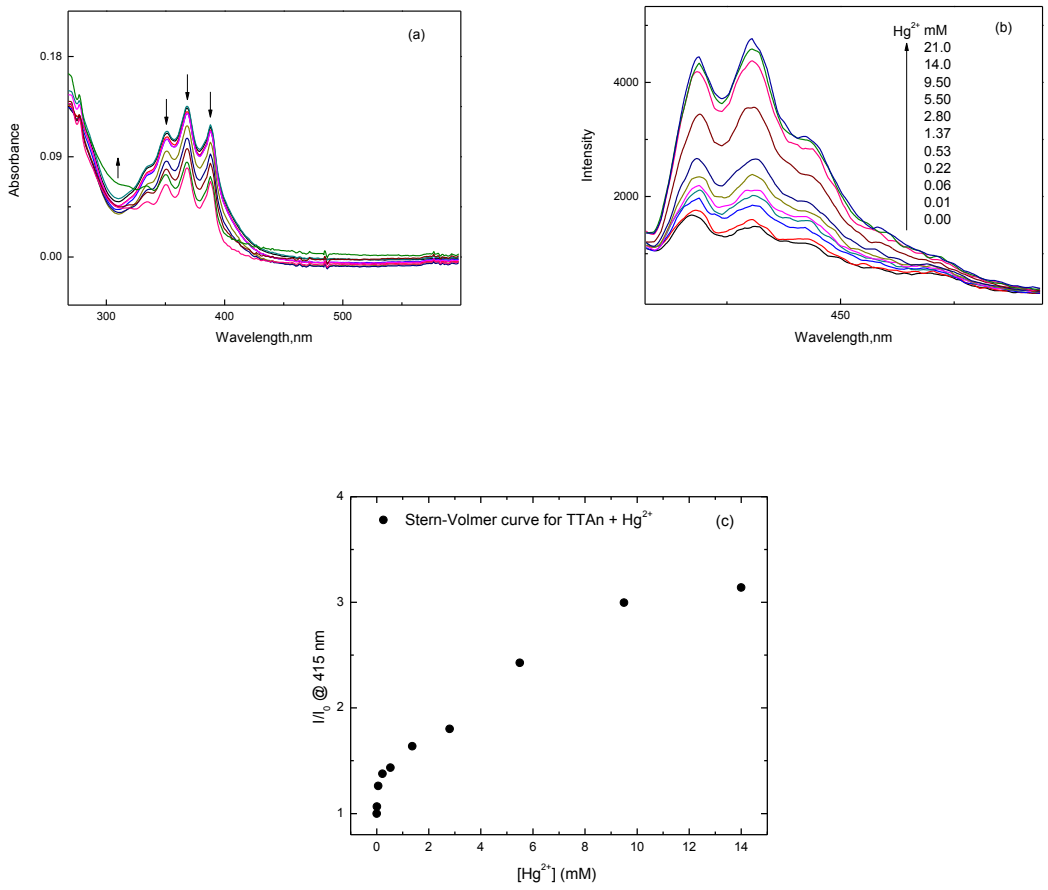

Figure S22. (a) UV-Vis absorption (b) Fluorescence spectra obtained as a function of increasing concentrations of $Hg(OTf)_2$ for TTFAn in THF at 298 ± K. The arrows indicate the trend for increasing $Hg(OTf)_2$. [TTFAn] = (5.0 μM) and λ_{exc} = 350 nm. (c) A plot of (I/I_0) vs. $[Hg(OTf)_2]$ obtained from λ_{exc} = 350 nm monitored at 415 nm.

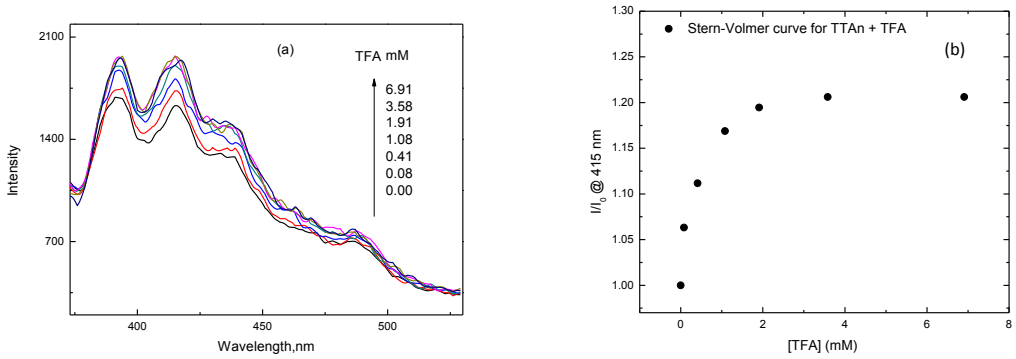

Figure S23. (a) Fluorescence spectra obtained as a function of increasing concentration of TFA (0.5 M) for TTFAn in THF at 298 ± 3 K. The arrows indicate the trend for increasing concentrations of TFA. [TTFAn] = (5.0 μM) and λ_{exc} = 350 nm. (b) A plot of (I/I_0) vs. [TFA] obtained from λ_{exc} = 350 nm monitored at 415 nm.

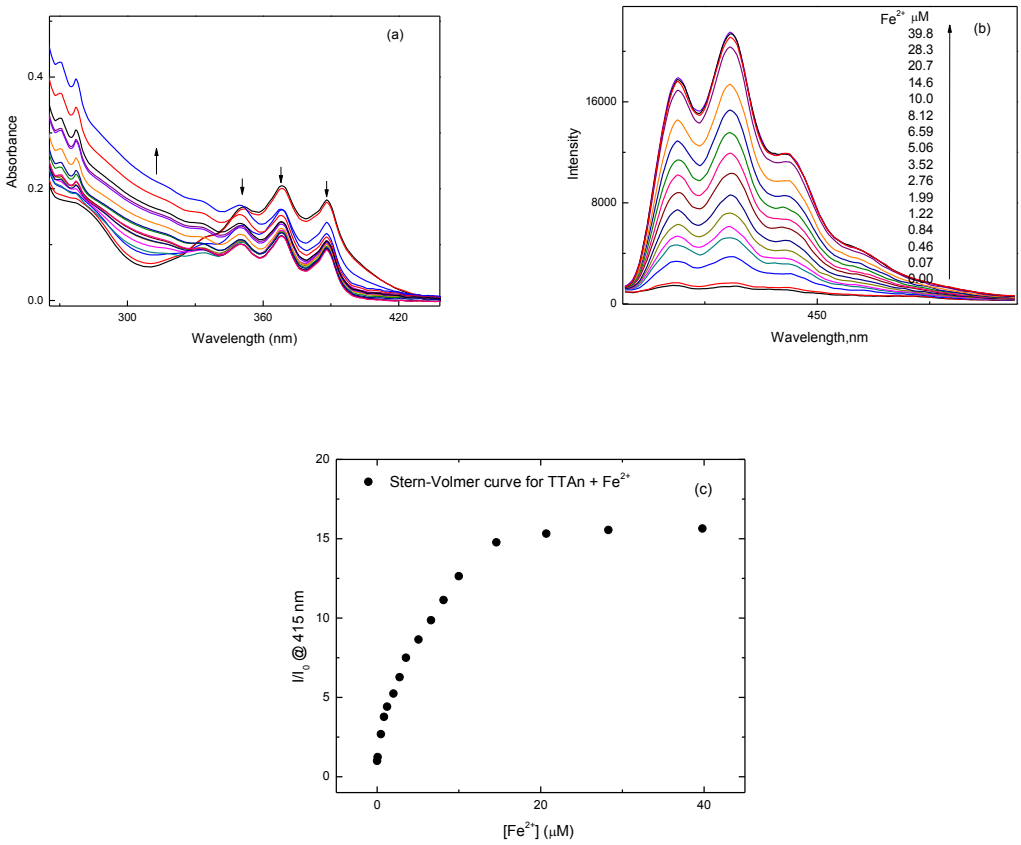

Figure S24. (a) UV-Vis absorption (b) Fluorescence spectra obtained as a function of increasing concentrations of $Fe(OTf)_2$ for TTFAn in THF at 298 ± 3 K. The arrows indicate the trend for increasing $Fe(OTf)_2$. [TTFAn] = (5.4 μM) and λ_{exc} = 350 nm. (c) A plot of (I/I_0) vs. $[Fe(OTf)_2]$ obtained from λ_{exc} = 350 nm monitored at 415 nm.

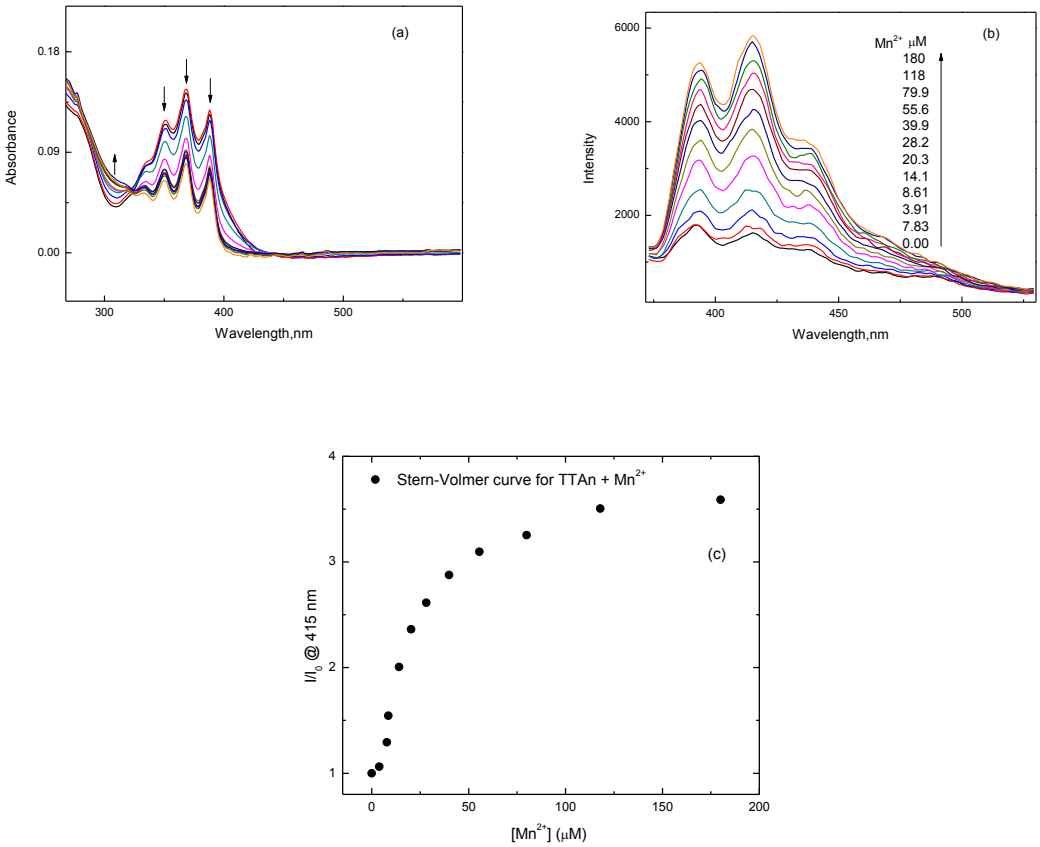

Figure S25. (a) UV-Vis absorption (b) Fluorescence spectra obtained as a function of increasing concentrations of $Mn(OTf)_2$ for TTFAn in THF at 298 ± 3 K. The arrows indicate the trend for increasing $Mn(OTf)_2$. [TTFAn] = (5.5 μM) and λ_{exc} = 350 nm. (c) A plot of (I/I_0) vs. $[Mn(OTf)_2]$ obtained from λ_{exc} = 350 nm monitored at 415 nm.

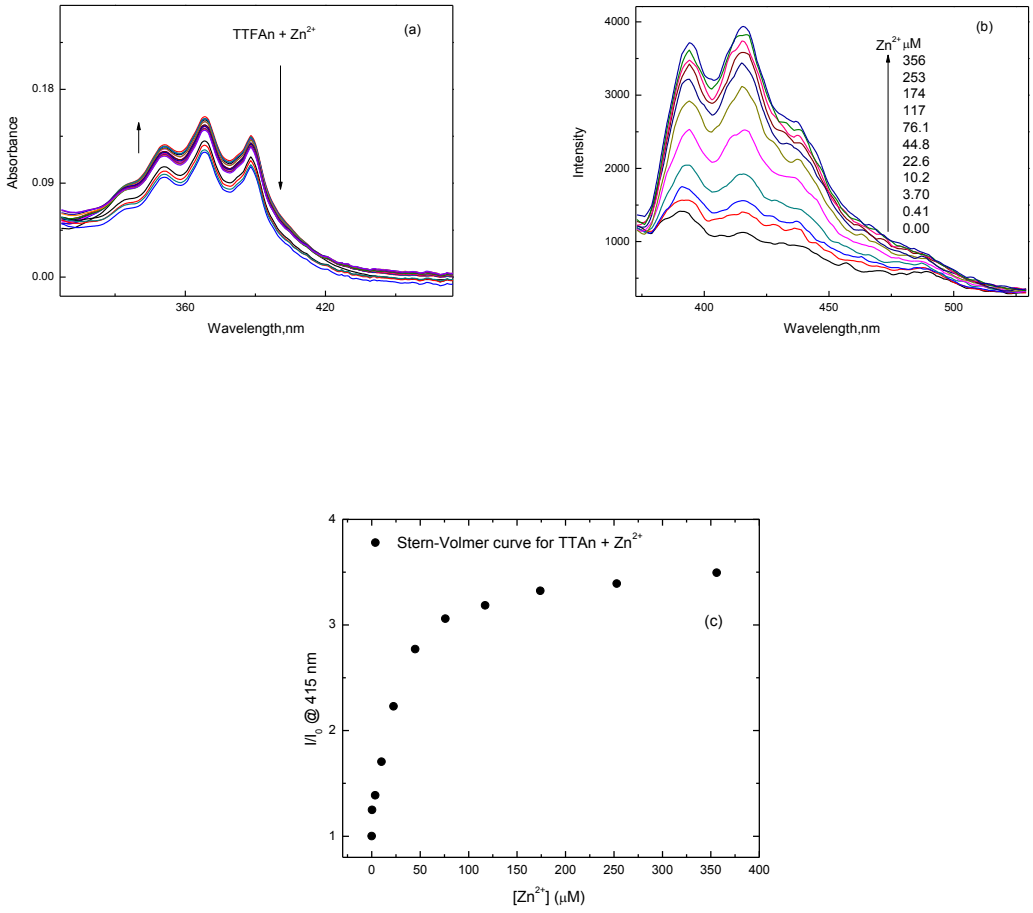

Figure S26. (a) UV-Vis absorption (b) Fluorescence spectra obtained as a function of increasing concentrations of $Zn(OTf)_2$ for TTFAn in THF at 298 ± 3 K. The arrows indicate the trend for increasing $Zn(OTf)_2$. [TTFAn] = (5.5 µM) and λ_{exc} = 350 nm. (c) A plot of (I/I_0) vs. $[Zn(OTf)_2]$ obtained from λ_{exc} = 350 nm monitored at 415 nm.

Extraction of Binding Constants for TTFAn and Metal Ions.

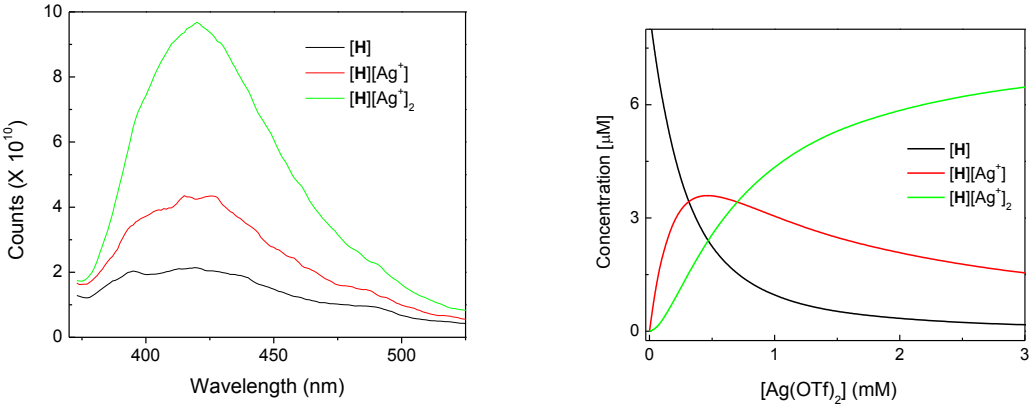

Figure S27. Deconvoluted spectra of coloured species (left) and correlation of the concentrations of coloured species versus Ag^{+} (right).

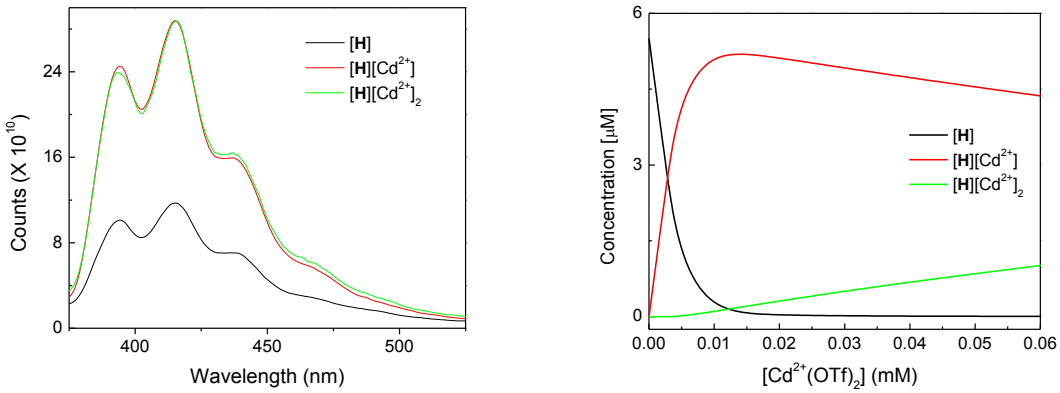

Figure S28. Deconvoluted spectra of coloured species (left) and correlation of the concentrations of coloured species versus Cd^{2+} (right).

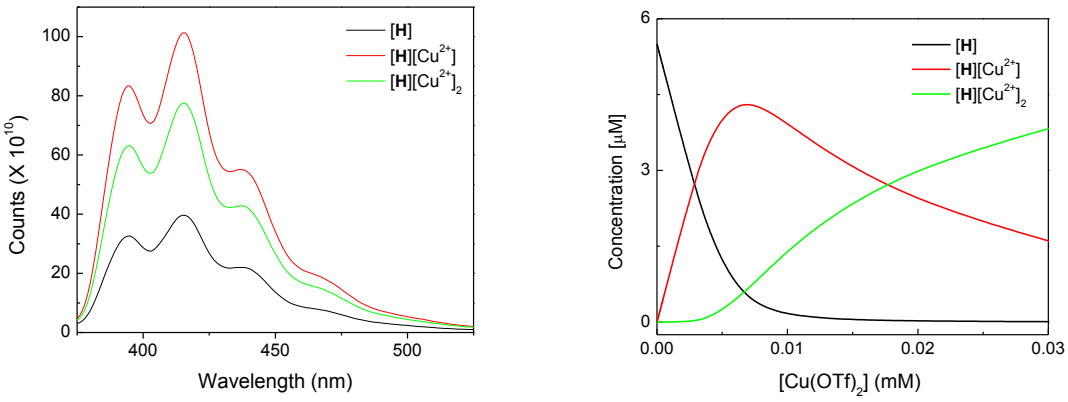

Figure S29. Deconvoluted spectra of coloured species (left) and correlation of the concentrations of coloured species versus Cu^{2+} (right).

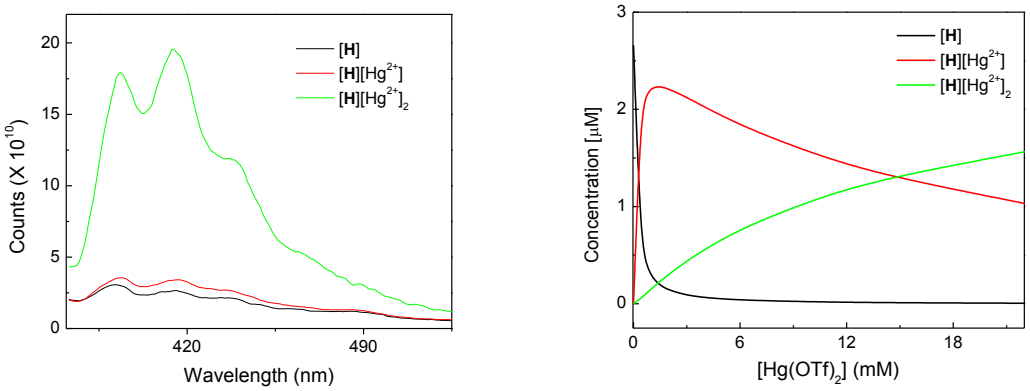

Figure S30. Deconvoluted spectra of coloured species (left) and correlation of the concentrations of coloured species versus Hg^{2+} (right).

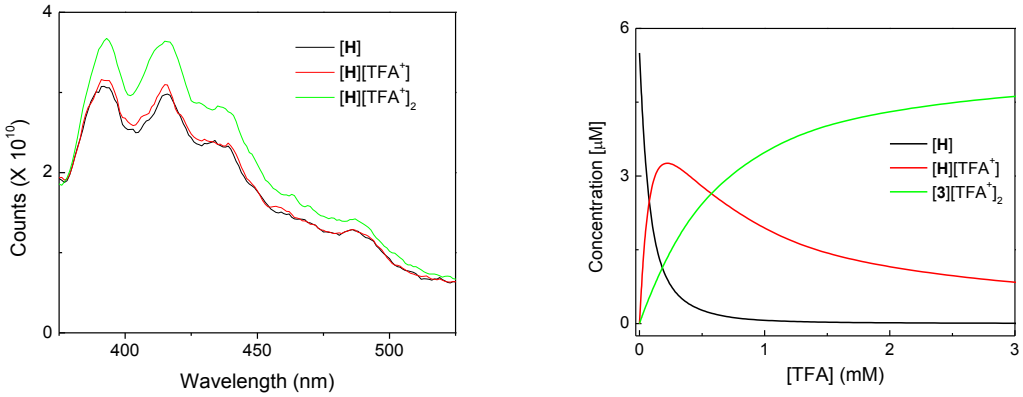

Figure S31. Deconvoluted spectra of coloured species (left) and correlation of the concentrations of coloured species versus TFA (right).

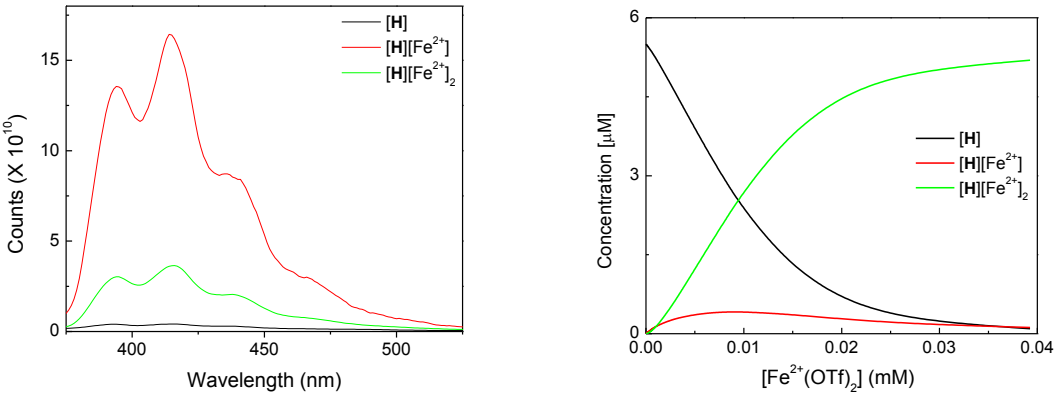

Figure S32. Deconvoluted spectra of coloured species (left) and correlation of the concentrations of coloured species versus Fe^{2+} (right).

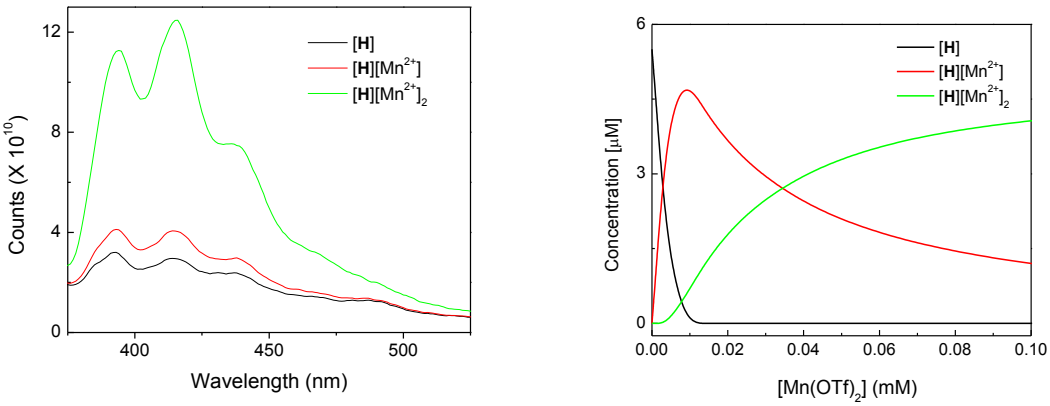

Figure S33. Deconvoluted spectra of coloured species (left) and correlation of the concentrations of coloured species versus Mn^{2+} (right).

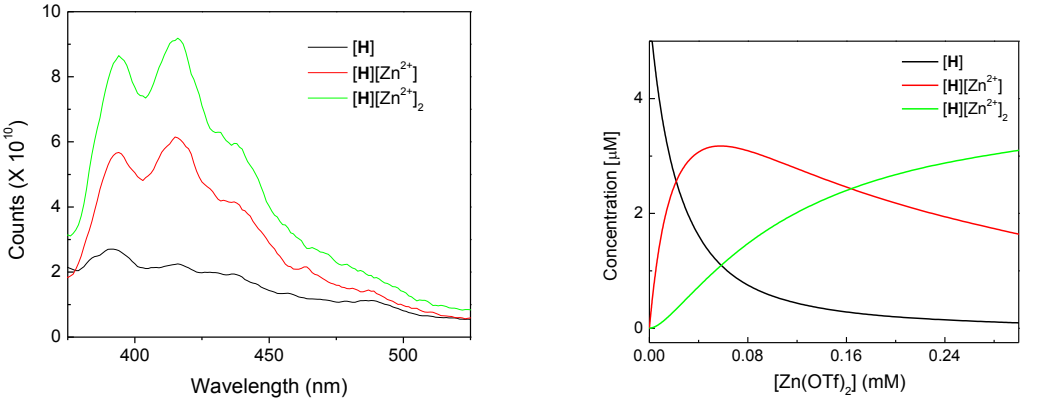

Figure S34. Deconvoluted spectra of coloured species (left) and correlation of the concentrations of coloured species versus Zn^{2+} (right).